

IAEA

International Atomic Energy Agency

Theoretical Foundations and Applications of Computational Fluid Dynamics in Nuclear Engineering

THEORETICAL FOUNDATIONS
AND APPLICATIONS OF
COMPUTATIONAL FLUID DYNAMICS
IN NUCLEAR ENGINEERING

The following States are Members of the International Atomic Energy Agency:

AFGHANISTAN	GEORGIA	PAKISTAN
ALBANIA	GERMANY	PALAU
ALGERIA	GHANA	PANAMA
ANGOLA	GREECE	PAPUA NEW GUINEA
ANTIGUA AND BARBUDA	GRENADA	PARAGUAY
ARGENTINA	GUATEMALA	PERU
ARMENIA	GUYANA	PHILIPPINES
AUSTRALIA	HAITI	POLAND
AUSTRIA	HOLY SEE	PORTUGAL
AZERBAIJAN	HONDURAS	QATAR
BAHAMAS	HUNGARY	REPUBLIC OF MOLDOVA
BAHRAIN	ICELAND	ROMANIA
BANGLADESH	INDIA	RUSSIAN FEDERATION
BARBADOS	INDONESIA	RWANDA
BELARUS	IRAN, ISLAMIC REPUBLIC OF	SAINT KITTS AND NEVIS
BELGIUM	IRAQ	SAINT LUCIA
BELIZE	IRELAND	SAINT VINCENT AND THE GRENADINES
BENIN	ISRAEL	SAMOA
BOLIVIA, PLURINATIONAL STATE OF	ITALY	SAN MARINO
BOSNIA AND HERZEGOVINA	JAMAICA	SAUDI ARABIA
BOTSWANA	JAPAN	SENEGAL
BRAZIL	JORDAN	SERBIA
BRUNEI DARUSSALAM	KAZAKHSTAN	SEYCHELLES
BULGARIA	KENYA	SIERRA LEONE
BURKINA FASO	KOREA, REPUBLIC OF	SINGAPORE
BURUNDI	KUWAIT	SLOVAKIA
CAMBODIA	KYRGYZSTAN	SLOVENIA
CAMEROON	LAO PEOPLE'S DEMOCRATIC REPUBLIC	SOUTH AFRICA
CANADA	LATVIA	SPAIN
CENTRAL AFRICAN REPUBLIC	LEBANON	SRI LANKA
CHAD	LESOTHO	SUDAN
CHILE	LIBERIA	SWEDEN
CHINA	LIECHTENSTEIN	SWITZERLAND
COLOMBIA	LITHUANIA	SYRIAN ARAB REPUBLIC
COMOROS	LUXEMBOURG	TAJIKISTAN
CONGO	MADAGASCAR	THAILAND
COSTA RICA	MALAWI	TOGO
CÔTE D'IVOIRE	MALAYSIA	TONGA
CROATIA	MALI	TRINIDAD AND TOBAGO
CUBA	MALTA	TUNISIA
CYPRUS	MARSHALL ISLANDS	TÜRKİYE
CZECH REPUBLIC	MAURITANIA	TURKMENISTAN
DEMOCRATIC REPUBLIC OF THE CONGO	MAURITIUS	UGANDA
DENMARK	MEXICO	UKRAINE
DJIBOUTI	MONACO	UNITED ARAB EMIRATES
DOMINICA	MONGOLIA	UNITED KINGDOM OF GREAT BRITAIN AND NORTHERN IRELAND
DOMINICAN REPUBLIC	MONTENEGRO	UNITED REPUBLIC OF TANZANIA
ECUADOR	MOROCCO	UNITED STATES OF AMERICA
EGYPT	MOZAMBIQUE	URUGUAY
EL SALVADOR	MYANMAR	UZBEKISTAN
ERITREA	NAMIBIA	VANUATU
ESTONIA	NEPAL	VENEZUELA, BOLIVARIAN REPUBLIC OF
ESWATINI	NETHERLANDS	VIET NAM
ETHIOPIA	NEW ZEALAND	YEMEN
FIJI	NICARAGUA	ZAMBIA
FINLAND	NIGER	ZIMBABWE
FRANCE	NIGERIA	
GABON	NORTH MACEDONIA	
GAMBIA	NORWAY	
	OMAN	

The Agency's Statute was approved on 23 October 1956 by the Conference on the Statute of the IAEA held at United Nations Headquarters, New York; it entered into force on 29 July 1957. The Headquarters of the Agency are situated in Vienna. Its principal objective is "to accelerate and enlarge the contribution of atomic energy to peace, health and prosperity throughout the world".

TRAINING COURSE SERIES No. 77

THEORETICAL FOUNDATIONS
AND APPLICATIONS OF
COMPUTATIONAL FLUID DYNAMICS
IN NUCLEAR ENGINEERING

INTERNATIONAL ATOMIC ENERGY AGENCY
VIENNA, 2023

COPYRIGHT NOTICE

All IAEA scientific and technical publications are protected by the terms of the Universal Copyright Convention as adopted in 1952 (Berne) and as revised in 1972 (Paris). The copyright has since been extended by the World Intellectual Property Organization (Geneva) to include electronic and virtual intellectual property. Permission to use whole or parts of texts contained in IAEA publications in printed or electronic form must be obtained and is usually subject to royalty agreements. Proposals for non-commercial reproductions and translations are welcomed and considered on a case-by-case basis. Enquiries should be addressed to the IAEA Publishing Section at:

Marketing and Sales Unit, Publishing Section
International Atomic Energy Agency
Vienna International Centre
PO Box 100
1400 Vienna, Austria
fax: +43 1 26007 22529
tel.: +43 1 2600 22417
email: sales.publications@iaea.org
www.iaea.org/publications

For further information on this publication, please contact:

Nuclear Knowledge Management Section
International Atomic Energy Agency
Vienna International Centre
PO Box 100
1400 Vienna, Austria
Email: Official.Mail@iaea.org

THEORETICAL FOUNDATIONS AND APPLICATIONS OF
COMPUTATIONAL FLUID DYNAMICS IN NUCLEAR ENGINEERING
IAEA, VIENNA, 2023
IAEA-TCS-77
ISSN 1018-5518

© IAEA, 2023

Printed by the IAEA in Austria
July 2023

FOREWORD

The IAEA supports human capacity development in its Member States by providing educational materials and offering training courses on a wide range of nuclear related topics. The IAEA also maintains a series of educational basic principle nuclear power plant simulators as well as part-task simulators, which can be used in educational and training courses and in nuclear engineering university curricula. The hands-on approach made possible by these simulators can help further trainees' practical and technical understanding of technologies.

The term computational fluid dynamics encompasses a vast range of numerical methods and practices for the simulation of fluid flow and heat and mass transfer that occur within nuclear systems on a broad range of spatial and temporal scales. These approaches represent an increasingly powerful tool that can aid academic institutions and industries in activities ranging from individual reactor component design and performance estimates to safety assessment at the plant level. In response to growing interest, the IAEA is providing education and training in the fundamentals of computational fluid dynamics in support of human capacity building efforts that may be of interest to Member States operating, constructing or planning the construction of nuclear power plants.

This publication is based on the course materials presented at the Joint ICTP–IAEA Course on Theoretical Foundations and Application of Computational Fluid Dynamics in Nuclear Engineering held in 2021. The course covered the basics of computational fluid dynamics in the field of nuclear engineering, from mathematical description to numerical representation and physical modelling. The concepts taught in course lectures were reinforced with practical hands-on virtual training exercises and demonstrations using open source software. The training materials from the course were compiled, edited and supplemented to create this publication as a resource for conducting similar training courses, as a reference for education and training programmes, and for direct use by trainees, university students and professors.

The IAEA is grateful for the contribution of H. ur Rehman (Pakistan) in drafting this publication. The IAEA officer responsible for this publication was T. Jevremovic of the Division of Nuclear Power.

EDITORIAL NOTE

This publication has been prepared from the original material as submitted by the contributors and has not been edited by the editorial staff of the IAEA. The views expressed remain the responsibility of the contributors and do not necessarily represent the views of the IAEA or its Member States.

Neither the IAEA nor its Member States assume any responsibility for consequences which may arise from the use of this publication. This publication does not address questions of responsibility, legal or otherwise, for acts or omissions on the part of any person.

The use of particular designations of countries or territories does not imply any judgement by the publisher, the IAEA, as to the legal status of such countries or territories, of their authorities and institutions or of the delimitation of their boundaries.

The mention of names of specific companies or products (whether or not indicated as registered) does not imply any intention to infringe proprietary rights, nor should it be construed as an endorsement or recommendation on the part of the IAEA.

The IAEA has no responsibility for the persistence or accuracy of URLs for external or third party Internet web sites referred to in this publication and does not guarantee that any content on such web sites is, or will remain, accurate or appropriate

CONTENTS

1.	INTRODUCTION	1
1.1.	BACKGROUND	1
1.2.	OBJECTIVE.....	2
1.3.	SCOPE.....	2
1.4.	STRUCTURE.....	2
2.	FUNDAMENTALS OF COMPUTATIONAL FLUID DYNAMICS	2
2.1.	BASICS OF VECTOR CALCUS AND GOVERNING EQUATIONS OF FLUID DYNAMICS	3
2.1.1.	Overview of the computational fluid dynamics procedure	
2.1.2.	Basics of vector algebra and vector calculus	
2.2.	LAGRANGIAN AND EULERIAN APPROACHES	11
2.2.1.	Lagrangian approach	
2.2.2.	Eulerian approach	
2.2.3.	Clarifying remarks on the Lagrangian and Eulerian approaches	
2.3.	GOVERNING EQUATIONS OF FLUID DYNAMICS	13
2.3.1.	Fluid flow representation models	
2.3.2.	Conservation equations	
2.3.3.	Considerations on the Navier–Stokes equations	
2.4.	IMPORTANCE OF THE NUMERICAL SOLUTION APPROACH	22
2.5.	NUMERICAL FRAMEWORKS	23
2.6.	FINITE VOLUME METHOD	24
2.6.1.	Discrete representation of a conservation equation	
2.6.2.	Examples of discretization practices in industrial computational fluid dynamics	
2.7.	INTRODUCTION TO NUMERICAL SOLUTION METHODS.....	32
2.7.1.	Solution of linear systems of equations	
2.8.	SOLUTION ALGORITHMS	36
2.8.1.	Solution algorithms of practical importance	
2.8.2.	Pressure implicit with splitting of operator method	
2.8.3.	Conclusive remarks	
3.	FUNDAMENTALS OF TURBULENCE MODELLING – FROM REYNOLDS AVERAGED NAVIER STOKES TO DIRECT NUMERICAL SIMULATION.....	41
3.1.	INTRODUCTION TO TURBULENCE AND TURBULENT FLOWS	41
3.1.1.	Types of turbulent flows	
3.1.2.	Fundamental concepts of turbulent flows	
3.2.	OVERVIEW OF PREDICTION METHODS FOR TURBULENT FLOWS..	44
3.2.1.	Direct numerical simulation	
3.2.2.	Reynolds averaged Navier–Stokes	
3.2.3.	Large eddy simulation	
3.2.4.	Hybrid approach	
3.3.	REYNOLDS AVERAGED NAVIER–STOKES.....	45
3.3.1.	Eddy viscosity models	
3.3.2.	Reynolds stress models	
3.3.3.	Near wall modelling	

4.	FUNDAMENTALS OF TWO PHASE FLOW MODELLING.....	55
4.1.	OVERVIEW OF TWO PHASE FLOW MODELLING APPROACHES	55
4.1.1.	Review of single phase computational fluid dynamics methods	
4.1.2.	Two phase flow features and averaging procedure	
4.1.3.	Two phase computational fluid dynamics approaches	
4.1.4.	Applicability limits of two phase computational fluid dynamics	
4.1.5.	Guidelines for the application of two phase computational fluid dynamics	
4.1.6.	Best practices guidelines	
4.1.7.	Conclusive remarks	
4.2.	INTERFACE RESOLVING TECHNIQUES	72
4.2.1.	The volume of fluid method	
4.2.2.	Volume of fluid method for phase change	
4.3.	EULERIAN–EULERIAN METHOD	80
4.3.1.	Introduction	
4.3.2.	Eulerian–Eulerian modelling theory	
4.3.3.	Interfacial transfer closure	
4.3.4.	Eulerian simulations of bubbly flow	
5.	APPLICATION OF COMPUTATIONAL FLUID DYNAMICS TO REACTOR DESIGN AND ANALYSES	104
5.1.	COMPUTATIONAL FLUID DYNAMICS FOR INNOVATIVE REACTORS	105
5.1.1.	Overview of advanced reactor concepts	
5.1.2.	Computational considerations on turbulence modelling	
5.1.3.	Reactor specific computational considerations	
5.1.4.	Summary	
5.2.	MULTI SCALE REACTOR SIMULATIONS	112
5.2.1.	Overview of multi scale reactor simulation models and modelling scales	
5.2.2.	Multi scale coupling algorithms	
5.2.3.	Verification and validation of multi scale simulations	
5.2.4.	Summary	
6.	UNCERTAINTY QUANTIFICATION AND ERROR ANALYSIS	125
6.1.	APPLICATION OF SINGLE PHASE COMPUTATIONAL FLUID DYNAMICS	126
6.2.	BEST ESTIMATE AND UNCERTAINTY APPROACH	127
6.2.1.	Nuclear reactor thermal hydraulics analysis	
6.2.2.	Process identification and ranking table	
6.2.3.	Scaling considerations	
6.2.4.	Verification and validation	
6.3.	METHODS FOR UNCERTAINTY QUANTIFICATIONS	130
6.3.1.	Uncertainty propagation based methods	
6.3.2.	Accuracy extrapolation methods	
6.3.3.	Verification and validation standards	
6.3.4.	Methods comparison	

6.4. APPLICATION OF AN UNCERTAINTY PROPAGATION METHOD	132
6.5. UNCERTAINTY QUANTIFICATION VIA ACCURACY EXTRAPOLATION	135
7. APPLICATIONS IN TRAINING AND EDUCATION	136
REFERENCES.....	137
CONTRIBUTORS TO DRAFTING AND REVIEW	147

1. INTRODUCTION

1.1. BACKGROUND

The behaviour of nuclear reactors depends on a complex interplay of physical phenomena that range from fluid dynamics, structural mechanics to neutron kinetics. With specific regard to the former, the prediction of momentum, heat and possibly mass transfer processes that affect the coolant and/or moderator is paramount to the design, performance, and safety assessment of nuclear reactors. Such predictions can be obtained via experimental or computational means. While experiments provide the ultimate benchmark, these can often be costly to set up, run and iterate to investigate the range of phenomena of interest. Conversely, computational approaches, are significantly cheaper to employ, both in material and temporal resource costs. However, the production of meaningful predictions via computational approaches is strongly dependent on a thorough understanding of all the elements that such approaches entail. These range from the governing physical laws (e.g., the conservation equations) to the geometric and temporal scales of the phenomena of interest, the mathematical models devised for their description as well as their limits of applicability, the steps required to obtain a time and space discrete description of a mathematical model starting from a time and space continuous formulation, the solution algorithms to be performed on the discrete model, and many more aspects.

Computational approaches can be fundamentally distinguished based on their dimensionality as well as target spatial resolution, which has important consequences on their limits of applicability. At the coarsest of the geometric scales, lumped parameter system codes rely primarily on a one dimensional (1D) fluid flow modelling to achieve a description of plant wide phenomena of interest. While the support for some degree of two dimensional (2D) and three dimensional (3D) flow modelling of certain components (e.g., the vessel) is increasing in some established system codes, their original 1D vocation stems from the historical constraints of the available hardware at the time of their development, dating back to several decades ago. At a finer geometric scale lie the subchannel and porous medium codes. These codes are generally employed for component level analyses that range in scale from a full core down to individual fuel elements, with a spatial resolution comparable to the fuel pin pitch. Further down the resolution scale lie Reynolds averaged Navier Stokes (RANS), large eddy simulation (LES) and direct numerical simulation (DNS) based approaches. These resolve the fluid flow in all physical dimensions down to the boundary layer thickness (RANS), down to the scale of some of the turbulent eddy scale (LES) or even further down the smallest of the turbulent eddy scales (DNS). The two most important trends to be considered when progressing towards higher spatially resolving approaches is that the computational cost of running simulations tends to increase significantly while the reliance on additional closure models (that make up for the lack of detail of coarser approaches) is reduced.

The computational approaches discussed so far formally belong to the broader category of computational fluid dynamics (CFD) approaches, which are otherwise transversal to many more fields of science and engineering, ranging from aeronautics to marine engineering. However, with specific regard to the nuclear field, the term CFD is often used to denote only the higher resolution approaches, namely RANS, LES, or DNS based CFD. The reason for this is that, as these approaches allow to resolve fluid flow down to or below the boundary layer size, most of the flow dynamics (which is shaped by what happens at these scales) can be resolved via first principles, i.e., without the use of case dependent correlations. On the other hand, coarser approaches require additional closure in the form of these case-dependent

correlations. For this document, the term CFD will be used in its nuclear vocation (unless specified differently), i.e., to encompass RANS, LES, and DNS methods.

The steady increase of available computational power, both in the form of desktop workstations as well as high performance computing clusters, enables the application of CFD methods to cases of research and industrial significance. This ties into the general trend towards higher fidelity simulations that has been witnessed in the nuclear field over the past decade, which is primarily driven by RANS based methods and, to a lesser extent, LES as well as so called hybrid RANS–LES methods. To this day, DNS methods remain very computationally expensive even for the investigation of small scale phenomena of operational relevance, yet interest in the field is set to grow as hardware capabilities progress.

1.2. OBJECTIVE

The objective of this publication is to build a theoretical understanding of the principal aspects related to CFD approaches. These aspects can be broadly summarized as: mathematical and physical foundations, governing equations, modelling of turbulence, the numerical discretization procedure of the physical domains and governing equations, and the solution algorithms. These aspects are covered for both single phase and multi phase flows and are provided further context via concrete examples of CFD applications in the field of nuclear engineering.

1.3. SCOPE

The domain of CFD approaches in nuclear engineering is vast and requires particular care when tackled from the perspective of gaining a sufficiently deep understanding of each aspect it entails while maintaining a broad outlook on the relationship among different aspects as well as of the overall CFD procedure. For this reason, the scope of this publication is to provide a clear overview of each aspect of the CFD approaches without aiming at the greatest possible depth of analysis, focusing rather on building a solid understanding on the connections in between different topics.

1.4. STRUCTURE

The fundamentals of CFD are described in Section 2, starting with the overview of basics in vector calculus of interest to later derivations of governing equations of fluid dynamics. The Lagrangian and Eulerian methods are described in detail. This section also provides the overview of numerical methods and solution algorithms. The fundamentals of turbulent modelling are described in Section 3, while Section 4 covers the fundamentals of two phase flow modelling. Section 5 provides descriptions and examples on the application of CFDs to reactor design and analysis. Section 6 provides brief overview of relating uncertainties and methods of error analysis.

2. FUNDAMENTALS OF COMPUTATIONAL FLUID DYNAMICS

This chapter focuses on introducing the most important concepts and procedures in CFD, which transcend any specific methodological declination. These concepts can be grouped in two domains: 1) the mathematical and physical foundations of fluid dynamics and its governing equations, and 2) the aspects related to translating a physical model described by a set of governing equations into a discrete model that can be solved and treated numerically.

2.1. BASICS OF VECTOR CALCUS AND GOVERNING EQUATIONS OF FLUID DYNAMICS

This section provides an overview of the CFD procedure and governing equations of fluid flow. It recalls basics of vector calculus and its utilization in modelling physical phenomena. In fluid dynamics, the description of fluid motion is an important aspect for analyzing any fluid flow problem. Two different approaches are used to describe fluid kinematics, namely Lagrangian and Eulerian approaches, which are also discussed in this section. Finally, the fluid flow models on which one can apply physical principle to derive governing equation of fluid dynamics followed by continuity, momentum and energy equations are discussed.

2.1.1. Overview of the computational fluid dynamics procedure

In fluid mechanics, conversation laws relating to mass, momentum, and energy conversation govern the fluid flows. These conversation laws are represented in the form of partial differential equations. To solve these equations numerically, these are first approximated to algebraic equations using CFD techniques. Various commercially available or specially developed software are utilized for this purpose. In CFD, different mathematical models, numerical methods, and soft tools are employed to analyze and predict fluid flows. The main advantage of the CFD over the experimental approach is that it provides valuable information about a physical phenomenon at a lower cost and in a lesser time. Furthermore, the information gained from a CFD analysis is more detailed as compared to an experimental one since measurement points are limited in experiments. In industries where the prediction of flow and process equipment is pertinent to the product design improvement, there is an increment in the CFD usage. Many CFD software packages offer the capability to capture fluid flow features like 3D, unsteady, turbulent, and even combustion – the features that are involved in most of the practical engineering problems related to fluid flows. The Navier–Stokes equations are of fundamental importance in a CFD analysis, these relate flow parameters like pressure, temperature, density, and velocity. The limited computational power or insufficient representation of the mathematical model often produces an approximate solution to a fluid flow problem. The following are the fundamental elements of a CFD simulation:

- Discretized flow field: Values at a finite number of nodes approximate the field variables (ρ, p, u , etc.);
- Motion equations are discretized: approximated by values at a finite number of nodes;
- Differential or integral equations: algebraic equations, as shown in Fig. 1;
- Resulting system of algebraic equations is solved to find values at the nodes.

The CFD codes provide a complete CFD analysis that consists of the following three steps (also refer to Fig. 2) [1]:

- *Pre-processing step*: In this step, the computational domain geometry and discretization (i.e., mesh) are defined and created, physical properties of the various materials involved in the simulation are defined, initial and boundary conditions are set, and simulation models and parameters are selected;
- *Solution step*: In this step, the governing equations that are representative of the investigated phenomenon are solved by the computer code, typically with

additional constitutive relationships that provide often required closure to the governing equations;

- *Post-processing step.* In this step, after the end of the simulation, results are extracted, processed, and interpreted in a wide variety of ways.

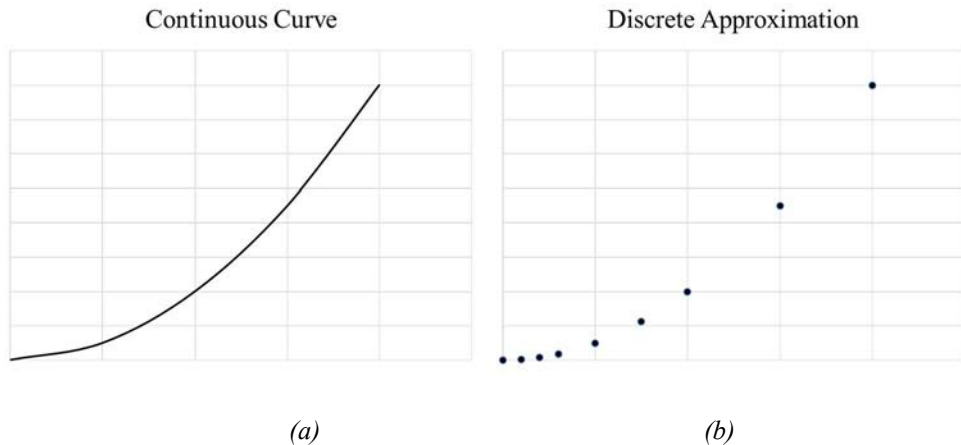


FIG. 1. (a) Continuous valued function and (b) discrete approximation of a function.

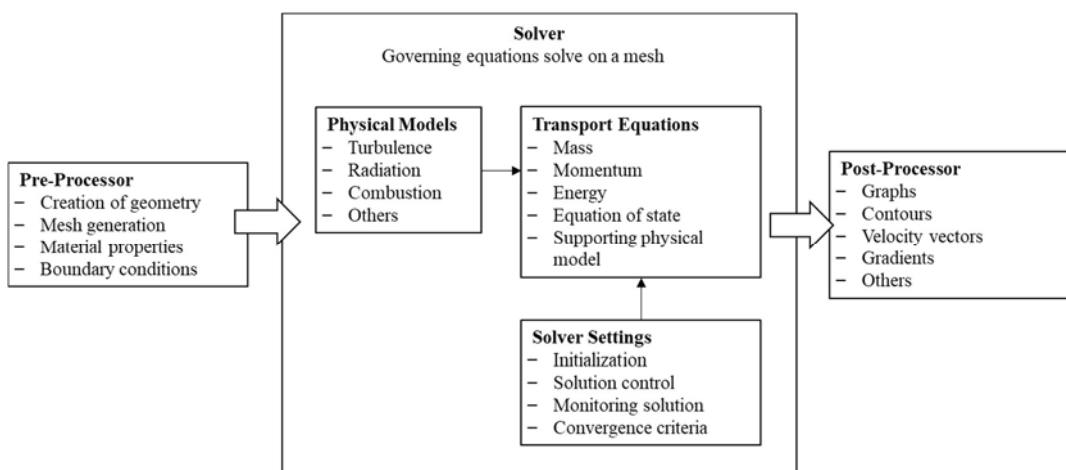


FIG. 2. Overall workflow and elements within the framework of a CFD approach.

2.1.2. Basics of vector algebra and vector calculus

Fluid dynamics is described with the quantities that have both, magnitude and direction, such as for example the velocity. This is a vector quantity, and as such, the mathematics involved behind fluid dynamics is most conveniently expressed in vector notation. This section provides an overview of basic relations of vector algebra and vector calculus [2].

2.1.2.1. Scalar and vector fields

A scalar quantity given as a function of three space coordinates and a time coordinate t is called a scalar field. The coordinates in space might be defined as cartesian (x, y, z), cylindrical (r, θ, z) or spherical (r, θ, φ). For example, pressure p , density ρ , and temperature T are all the scalar quantities that can be represented via scalar fields so that:

$$p = p(x, y, z, t) = p(r, \theta, z, t) = p(r, \theta, \varphi, t) \quad (1)$$

$$\rho = \rho(x, y, z, t) = \rho(r, \theta, z, t) = \rho(r, \theta, \varphi, t) \quad (2)$$

$$T = T(x, y, z, t) = T(r, \theta, z, t) = T(r, \theta, \varphi, t) \quad (3)$$

Similarly, a vector quantity given as a function of space and time coordinates is called a vector field. For example, velocity \mathbf{u} is a vector quantity that can be represented in terms of its scalar components u_i with respect to the basis vectors in the reference frame. In case of a cartesian reference frame with bases vectors ($\mathbf{e}_x, \mathbf{e}_y, \mathbf{e}_z$), velocity is defined as follows:

$$\mathbf{u} = u_x \mathbf{e}_x + u_y \mathbf{e}_y + u_z \mathbf{e}_z \quad (4)$$

wherein the individual components are scalar fields:

$$u_x = u_x(x, y, z, t) \quad (5)$$

$$u_y = u_y(x, y, z, t) \quad (6)$$

$$u_z = u_z(x, y, z, t) \quad (7)$$

Similarly, the fields of tensor quantities of any order can be defined; for example, a stress or a strain, which has magnitude, direction, and a plane in which it acts. Tensor (from Latin *tendere* that means *to stretch*) is a mathematical formalism used to solve physics problems. It is more general than vector, while zero tensor represent a scalar (number). Therefore, tensor is defined as an algebraic object over an n dimensional vector space obeying change-of-basis transformation law.

2.1.2.2. Scalar and vector products

Given two vector fields \mathbf{a} and \mathbf{b} , their scalar product is $\mathbf{a} \cdot \mathbf{b}$ while the vector product is $\mathbf{a} \times \mathbf{b}$. For a cartesian reference frame the vectors and products are defined as follows:

$$\mathbf{a} = a_x \mathbf{e}_x + a_y \mathbf{e}_y + a_z \mathbf{e}_z \quad (8)$$

$$\mathbf{b} = b_x \mathbf{e}_x + b_y \mathbf{e}_y + b_z \mathbf{e}_z \quad (9)$$

$$\mathbf{a} \cdot \mathbf{b} = a_x b_x + a_y b_y + a_z b_z \quad (10)$$

$$\begin{aligned} \mathbf{a} \times \mathbf{b} &= \begin{bmatrix} \mathbf{e}_x & \mathbf{e}_y & \mathbf{e}_z \\ a_x & a_y & a_z \\ b_x & b_y & b_z \end{bmatrix} \\ &= \mathbf{e}_x(a_y b_z - a_z b_y) + \mathbf{e}_y(a_z b_x - a_x b_z) + \mathbf{e}_z(a_x b_y - a_y b_x) \end{aligned} \quad (11)$$

When considering cylindrical or spherical reference frames, it is generally more convenient to perform a change of basis for both \mathbf{a} and \mathbf{b} from the original reference frame to a cartesian one. For a cylindrical reference frame, the change of basis to cartesian coordinates is:

$$a_x = a_r \cos\theta \quad (12)$$

$$a_y = a_r \sin\theta \quad (13)$$

$$a_z = a_z \quad (14)$$

wherein the θ angle is defined with respect to the x axis in the cartesian frame. For a transformation from a spherical reference frame:

$$a_x = a_r \cos\theta \sin\varphi \quad (15)$$

$$a_y = a_r \sin\theta \sin\varphi \quad (16)$$

$$a_z = a_r \cos\varphi \quad (17)$$

wherein the θ is defined with respect to the x axis in the cartesian frame, lying in the xy plane, while the φ angle is defined with respect to the z axis in the cartesian frame, lying in a plane perpendicular to the xy plane.

2.1.2.3. Gradient of a scalar field

Consider a scalar field p in the form specified by Eq. (1). The gradient of p , which is ∇p , at a given point in space is a vector such that:

- Its magnitude is the maximum rate of change of p per unit length of the coordinate space at the given point;
- Its direction is that along which p changes the most at the given point.

As an example, a 2D pressure field in Cartesian coordinates is sketched in Fig. 3. The solid curves are lines of constant pressure. Such lines are called isolines. An arbitrary point (x, y) is shown in Fig. 3. Moving away from this point in an arbitrary direction, p will in general, change because of moving to another location in space. Moreover, there will be some direction from this point along which p changes the most over a unit length in that direction. This defines the direction of the gradient of p . The magnitude of ∇p is the rate of change of p per unit length in that direction. Both, the magnitude, and direction of ∇p change from one point to another in the coordinate space. A line drawn in this space along which ∇p is tangent at every point is defined as a gradient line, as represented in Fig. 3. The gradient line and isoline through any given point in the coordinate space are perpendicular.

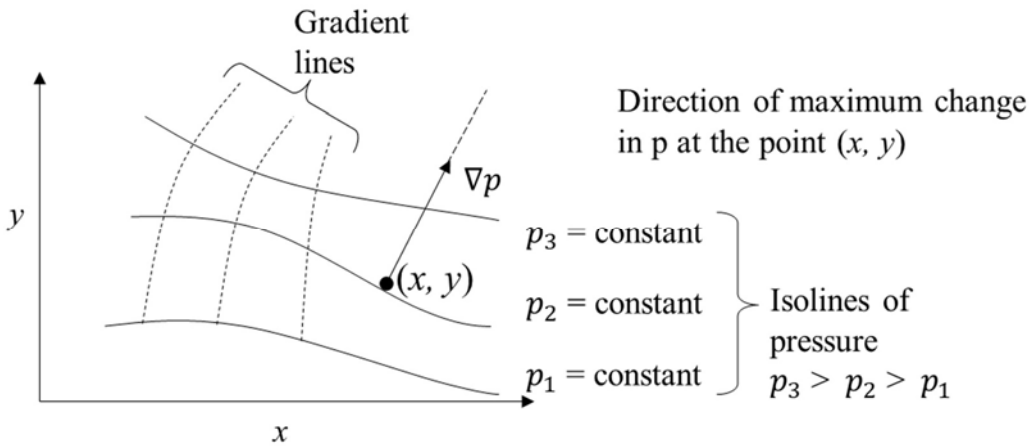


FIG. 3. Illustration of the concept of gradient of a scalar field.

The pressure gradient is hereby expressed in different reference frames, namely cartesian, cylindrical and spherical frames as follows:

$$\nabla p = \frac{\partial p}{\partial x} e_x + \frac{\partial p}{\partial y} e_y + \frac{\partial p}{\partial z} e_z \quad (18)$$

$$\nabla p = \frac{\partial p}{\partial r} e_r + \frac{1}{r} \frac{\partial p}{\partial \theta} e_\theta + \frac{\partial p}{\partial y} e_z \quad (19)$$

$$\nabla p = \frac{\partial p}{\partial r} \mathbf{e}_r + \frac{1}{r} \frac{\partial p}{\partial \theta} \mathbf{e}_\theta + \frac{1}{r \sin \theta} \frac{\partial p}{\partial \varphi} \mathbf{e}_\varphi \quad (20)$$

2.1.2.4. Divergence of a vector field

In fluid dynamics, one of the most relevant vector fields is the fluid flow velocity, often denoted with \mathbf{u} . For a fluid element of an infinitesimal volume of fluid moving along a streamline, a continuous 1D line in 3D space that is tangent to the velocity field at every point in space, the divergence of the velocity field denoted with $\nabla \cdot \mathbf{u}$, represents a scalar field that is the rate of change of a volume of a moving fluid element having a constant mass. The divergence of the velocity (or any vector field) for different reference frames, cartesian, cylindrical and spherical frames are defined as follows:

$$\nabla \cdot \mathbf{u} = \frac{\partial u_x}{\partial x} + \frac{\partial u_y}{\partial y} + \frac{\partial u_z}{\partial z} \quad (21)$$

$$\nabla \cdot \mathbf{u} = \frac{1}{r} \frac{\partial (r u_r)}{\partial r} + \frac{1}{r \sin \theta} \frac{\partial u_\theta}{\partial \theta} + \frac{\partial u_z}{\partial z} \quad (22)$$

$$\nabla \cdot \mathbf{u} = \frac{1}{r^2} \frac{\partial (r^2 u_r)}{\partial r} + \frac{1}{r \sin \theta} \frac{\partial (u_\theta \sin \theta)}{\partial \theta} + \frac{1}{r \sin \theta} \frac{\partial u_\varphi}{\partial \varphi} \quad (23)$$

2.1.2.5. Curl of a vector field

For the vector field \mathbf{u} defined in of Section 2.1.2.4., its curl, denoted with $\nabla \times \mathbf{u}$, is a vector field such that its value at any point in space is a vector that lies in a plane perpendicular to the flow streamline and is indicative of an overall rotation of the streamlines (i.e., of the velocity field) in space. The curl of the velocity (or any vector field) for a cartesian reference frame is given as follows:

$$\nabla \times \mathbf{u} = \begin{bmatrix} \mathbf{e}_x & \mathbf{e}_y & \mathbf{e}_z \\ \frac{\partial}{\partial x} & \frac{\partial}{\partial y} & \frac{\partial}{\partial z} \\ u_x & u_y & u_z \end{bmatrix} = \mathbf{e}_x \left(\frac{\partial u_z}{\partial y} - \frac{\partial u_y}{\partial z} \right) + \mathbf{e}_y \left(\frac{\partial u_z}{\partial x} - \frac{\partial u_x}{\partial z} \right) + \mathbf{e}_z \left(\frac{\partial u_y}{\partial x} - \frac{\partial u_x}{\partial y} \right) \quad (24)$$

2.1.2.6. Line integrals

For a vector field \mathbf{u} the line integral along any continuous open line defined between the two points a, b in space is defined as:

$$\int_a^b \mathbf{u} \cdot d\mathbf{l} \quad (25)$$

where $d\mathbf{l}$ is a vector of infinitesimal length dl along the integral domain. The integration domain might be represented by a closed line, and in such a case the line integral is expressed as:

$$\oint \mathbf{u} \cdot d\mathbf{l} \quad (26)$$

These two types of integrals are illustrated in Fig. 4. Line integrals of the velocity field on a closed domain are often used e.g., in the calculation of the circulation, a scalar quantity representing the degree of rotation that a fluid flow exhibits.

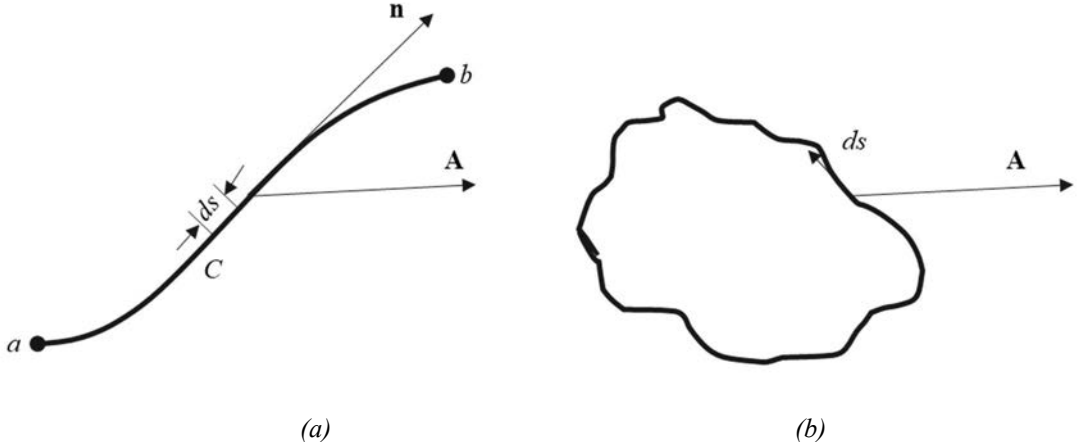


FIG. 4. Example of line integrals of a generic vector field \mathbf{A} on: (a) an open line defined between two points a , b and (b) a closed line C .

A line integral of a scalar field p is a scalar that can be calculated as:

$$\int_a^b p \, dl \quad (27)$$

or, for a closed line integral as follows:

$$\oint p \, dl \quad (28)$$

2.1.2.7. Surface integrals

Analogously to the line integrals introduced in Section 2.1.2.6, and with respect to vector fields such as e.g., the velocity field \mathbf{u} , the surface integral of a vector field is a scalar, and it can be defined as:

$$\iint_S \mathbf{u} \cdot d\mathbf{S} \quad (29)$$

wherein $d\mathbf{S}$ is the oriented infinitesimal surface area element on the surface S , and parallel to the surface normal \mathbf{n} at any point. In case the surface is closed, the normal is outwards from the domain enclosed by S , by convention. From the perspective of notation, integrals on closed surfaces can be denoted with \oint as an integration symbol, but typically the double integral notation (or even a single integral notation, if the integration domain is clearly indicated) suffice. An example of the integral domain with the relevant elements that partake in the definition of the integral are represented in Fig. 5.

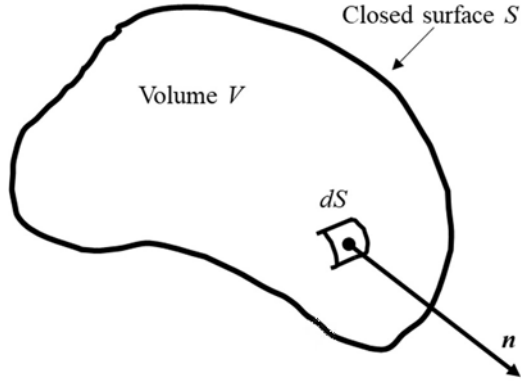


FIG. 5. Representation of a closed surface S encompassing a volume V , together with a representative infinitesimal oriented surface element dS parallel to the outwards normal \mathbf{n} .

Similarly, a surface integral for a scalar quantity p is defined as follows:

$$\iint_S p \, dS \quad (30)$$

The surface integrals, together with volume integrals and the Gauss theorem, provide the basis of the finite volume method, one of the most popular numerical discretization methods for obtaining a space and time-discrete representation of a continuous fluid flow problem. While other types of surface integrals are mathematically possible, such as the surface integral of a scalar field p yielding a vector $\iint_S p \, d\mathbf{S}$, or surface integrals of a vector field \mathbf{u} yielding a vector such as $\iint_S \mathbf{u} \, dS$ or $\iint_S \mathbf{u} \times d\mathbf{S}$, these are arguably quite rare in the domain of computational fluid dynamics as these do not offer particularly useful physical interpretations or numerical applications.

2.1.2.8. Volume integrals

The volume integral of \mathbf{u} , a vector field, in space over the volume V is defined as:

$$\iiint_V \mathbf{u} \, dV \quad (31)$$

Similarly, for a scalar field p , the volume integral results in a scalar and is defined as:

$$\iiint_V p \, dV \quad (32)$$

From the perspective of notation, given that in a 3D spatial domain, volumes are closed, the symbol \iiint can be used as well to represent the integration, but the meaning remains unchanged.

2.1.2.9. Relationship between line, surface, and volume integrals

The line integral of a vector field \mathbf{u} over closed line boundary C is related to the surface integral of \mathbf{u} over an open surface S by Stokes theorem. The representation of it is shown in Fig. 6.

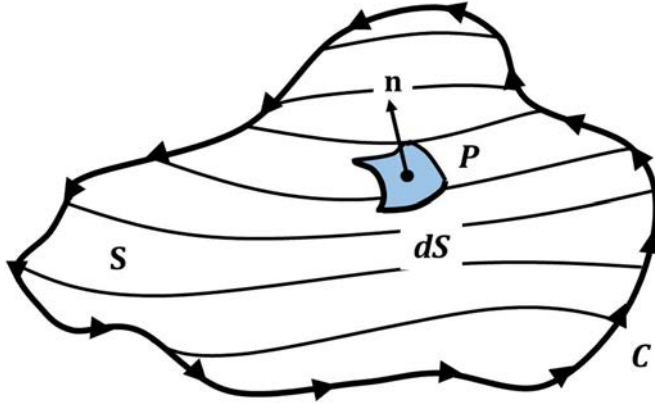


FIG. 6. Representation of an open surface S bounded by a closed line boundary C alongside a representative oriented infinitesimal surface element dS parallel to the surface normal \mathbf{n} at point P .

Stokes theorem is defined as follows:

$$\int_C \mathbf{u} \cdot d\mathbf{l} = \iint_S (\nabla \times \mathbf{u}) \cdot d\mathbf{S} \quad (33)$$

As shown in Fig. 5, if the volume V is enclosed within the closed surface S , the surface and volume integrals of the vector field \mathbf{u} are associated by the Gauss theorem, also known as the divergence theorem:

$$\iint_S \mathbf{u} \cdot d\mathbf{S} = \iiint_V (\nabla \cdot \mathbf{u}) dV \quad (34)$$

The significance of these two theorems, especially of the Gauss theorem, will become clear when discussing the tenets of the finite volume method.

2.1.2.10. Material derivative

The material derivative of a quantity, also known as substantial derivative, represents the rate of change per unit time as it is being transported (or advected) in space by a velocity field \mathbf{u} . It can be interpreted as a time derivative of a quantity as it is moving along a streamline. The quantity can be a scalar, vector, or tensor of any order, and the material derivative operator can be defined as:

$$\frac{D}{Dt} = \frac{\partial}{\partial t} + \mathbf{u} \cdot \nabla \quad (35)$$

By comparison, the partial derivative with respect to time $\partial / \partial t$, also known as local derivative, represents the rate of change of a quantity per unit time at a fixed point in space, regardless of advection. As an example, the material derivative of the density scalar field ρ is given with:

$$\frac{D\rho}{Dt} = \frac{\partial \rho}{\partial t} + \mathbf{u} \cdot (\nabla \rho) \quad (36)$$

2.2. LAGRANGIAN AND EULERIAN APPROACHES

Two distinct approaches for describing fluid motion through space are Lagrangian and Eulerian approaches. While the specific mathematical reference frames encountered so far, the cartesian, cylindrical and spherical ones, describe the space starting from a certain origin point, the Lagrangian and Eulerian approaches are concerned with how the perspective from which one is to describe the dynamics of a fluid.

2.2.1. Lagrangian approach

Collective motion of individual particles, as represented in Fig. 7, is described by laws of classical mechanics that can be applied to accurately define the motion and predict where these particles move and exchange momentum and kinetic energy with one another.

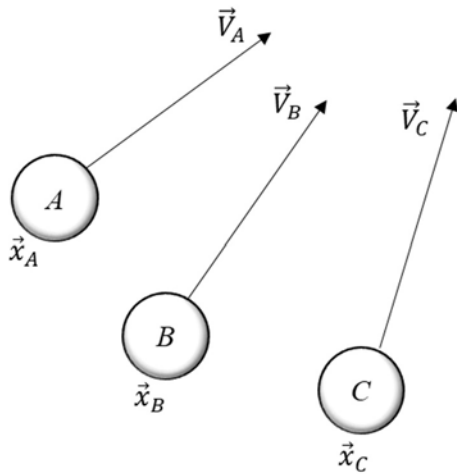


FIG. 7. Collection of particles whose state is described by the position vectors \mathbf{x} , and velocity vectors \mathbf{v} .

The kinematics refers to the position vectors \mathbf{x} and the velocity vectors \mathbf{v} of each particle as a function of time. When applied to tracking the evolution of the position and velocity of discrete fluid elements (or parcels) of constant mass, this approach is known as Lagrangian approach, named after Italian mathematician Joseph–Louis Lagrange (1736–1813). This method entails several difficulties: to define and identify fluid parcels as per their movement in the flow field, and for all cases of interest to nuclear engineering, fluids are assumed to be a continuum. As a result, interactions between neighboring fluid parcels are as easily described as the interactions between distinct particles. Despite these difficulties, there are numerous practical applications of Lagrangian approach, such as but not limited to rarefied flows, flow visualization and measurements based on particle tracking.

2.2.2. Eulerian approach

The Eulerian approach, named after Swiss mathematician Leonhard Euler (1707–1783), is more common method for describing fluid motion. The fluid properties are described in terms of continuous fields in space and time with reference to an observer that is not affected by the fluid flow. From a mathematical perspective, at each point \mathbf{x} and time t , these fields describe the various properties (pressure, velocity, density, etc.) of the fluid at a given location in space and time, regardless of which parcels of fluid pass through that location. From a physical perspective, as many fluid properties are statistical in nature, these fields describe fluid

properties in a neighborhood of a given point in space and time. Nonetheless, from a computational perspective, the domain of the fluid flow of interest is spanned by a grid of finite volumes or control volumes. The description of fluid flow becomes a description of the fluid inflow and/or outflow from each finite volume, as well as the change in flow properties in each cell arising from this inflow/outflow. This is described in the following sections.

2.2.3. Clarifying remarks on the Lagrangian and Eulerian approaches

The Lagrangian and Eulerian approaches are compared in the example of a generic fluid flow in a cartesian reference frame as shown in Fig. 8; in particular, the differences between the two approaches at three different moments in time t_0 , t_1 and t_2 .

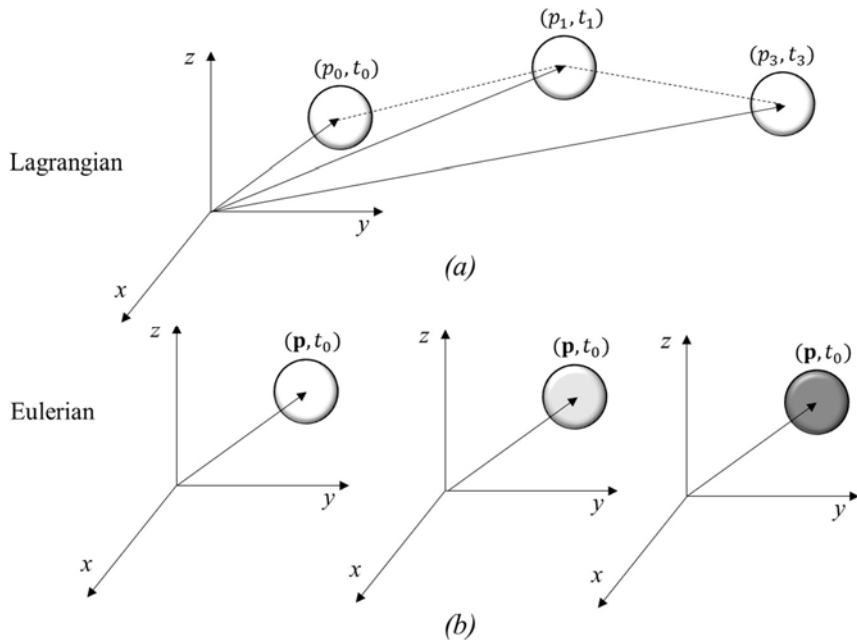


FIG. 8. Comparison of (a) Lagrangian) and (b) Eulerian approach in describing the fluid flow with respect to Cartesian reference frame at three separate moments in time, t_0, t_1 and t_2 .

The Lagrangian approach concerns itself with tracking the evolution of individual fluid parcels, which in case shown in Fig. 8, considers a fluid parcel in a neighbourhood of point \mathbf{p}_0 at time t_0 . As the parcel is advected through space, its position evolves accordingly, passing through points \mathbf{p}_1 and \mathbf{p}_2 at times t_1 and t_2 , respectively. The parcel's trajectory through time and space is presented by a dashed line. The fact that the fluid parcel is still the same as the starting one (i.e., composed of the same original molecules) is indicated by the colour of the parcels being not changed.

In contrast to this, in the Eulerian approach there is a collection of points of interest, in the neighbourhood of which the evolution of the fluid flow is tracked. As shown in Fig. 8, the concern is what happens in the neighbourhood of point \mathbf{p} (which never changes) at different times. The fluid within the neighbourhood is possibly changing as fluid flows through it; this is marked with different colours at different times in Fig. 8.

The reference frame is the same for both approaches and it is constant in time (though it does not necessarily need to be time independent), stressing the fact that the two approaches are independent of a coordinate system.

Despite, the Lagrangian approach provides valuable results in many cases, in fluid flow problems the Eulerian approach is more convenient and often used. Secondly, since velocity or pressure probes are usually installed at a specified location inside a wind tunnel, the Eulerian approach is more suitable for experimental measurement [3].

2.3. GOVERNING EQUATIONS OF FLUID DYNAMICS

Computational fluid dynamics is based on fundamental conservation laws, namely:

- Law of conservation of mass;
- Law of conservation of momentum (which follows from the second Newton's law);
- Law of conservation of energy.

The specific form, meaning the mathematical formulation, that the governing equations assume depends however on the chosen flow representation model. Representation model is the choice of a specific combination of flow reference frame (either Lagrangian or Eulerian) and a definition of the fluid neighborhood as discussed in Section 2.2. Two approaches for defining neighborhood in more rigorous terms are described in this section. These are a finite control volume approach and an infinitesimal fluid element approach. Thus, a total of four different flow models are possible [4].

2.3.1. Fluid flow representation models

Each of the four models are described by four different sets of governing equations, which nonetheless represent the same conservation laws. These flow models are shown in Fig. 9.

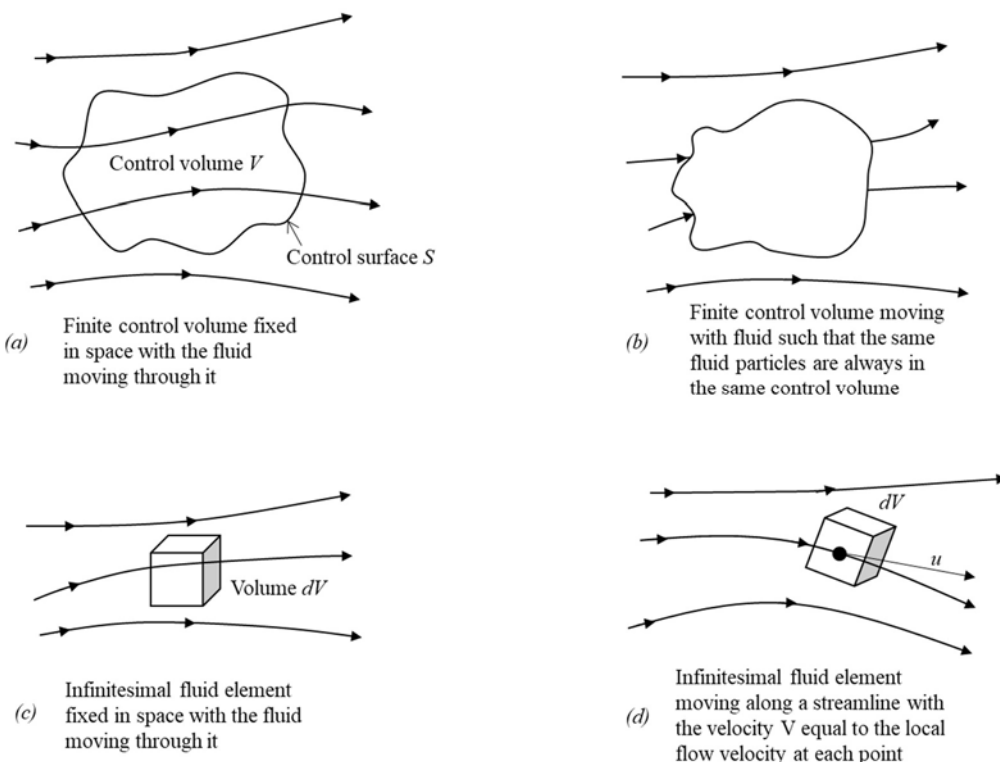


FIG. 9 Example of different flow models: (a) finite control volumes with Eulerian approach; (b) finite control volumes with Lagrangian approach; (c) infinitesimal fluid elements with Eulerian approach; (d) infinitesimal fluid elements with Lagrangian approach.

2.3.1.1. Eulerian, finite control volume based flow representation

A finite control volume together with Eulerian approach is used for the flow model illustrated in Fig. 9 (a). This control finite non infinitesimal volume V is bound by a boundary surface S . Consistently with a Eulerian approach, the control volume is not affected by the fluid as it flows through it. By applying the conservation laws to the fluid instantaneous contained in finite volume, it is possible to obtain conservation equations in an integral form. In other words, the conservation laws are expressed in terms of integrals of relevant quantities over the control volume V or the bounding surface S . The mathematical formulation does not separate derive terms into combinations of partial derivatives. While this is inconsequential from the perspective of mathematical notation, it is consequential from the perspective of an actual numerical representation of the equations.

2.3.1.2. Lagrangian, finite control volume based flow representation

Lagrangian approach for describing the flow via a finite control volume is illustrated in Fig. 9 (b). Consistently with a Lagrangian approach, the control volume is neither of constant volume nor of constant shape, as it intended to identify a specific collection of molecules as flow. By applying the conservation laws to the fluid within the control volume, the conservation equations take an integral form. The form is integral, as it was for the previously illustrated case, as the domain of interest is represented by a finite control volume. However, in a Lagrangian framework the form is said to be a non conservation one as, mathematically, some of the derivative terms that appear in the conservation form are separated in different individual derive terms. It is important to point out that the terms conservation and non conservation form are mathematical formalisms that describe the same exact physics but can lead to potential differences in numerical solutions of the equations.

2.3.1.3. Eulerian, infinitesimal fluid element based flow representation

An infinitesimal fluid element of volume dV treated with a Eulerian approach is illustrated in Fig. 9 (c). This infinitesimal volume is fixed in space with respect to selected coordinate system. In the limit of a vanishingly small volume, the conservation equations are in a differential, rather than an integral form. Thus, for a Eulerian reference frame, the final equations are in a differential conservation form.

2.3.1.4. Lagrangian, infinitesimal fluid element based flow representation

The fluid flow described via infinitesimal fluid elements dV in a Lagrangian reference frame is illustrated in Fig. 9 (d). Applying conservation laws to the fluid element, the conservation equations take a differential non conservation form. The actual equations for these different forms are presented in the following Section 2.3.2.

2.3.2. Conservation equations

2.3.2.1. Mass conservation equation

The mass conservation equation (or the continuity equation) describes conservation of mass to the volume of interest for a specified flow representation model. In the Eulerian reference frame, a finite control volume V is bounded by surface S . This corresponds to the flow representation model illustrated in Fig. 9 (a). In such a case, the mass conservation law states

that the total rate of fluid mass change within the volume V needs to correspond to the net mass flow into that volume through the surface boundary S . Thus, an integral conservation form of the continuity equation is as follows:

$$\frac{\partial}{\partial t} \iiint_V \rho \, dV + \iint_S \rho \mathbf{u} \cdot d\mathbf{S} = 0 \quad (37)$$

The volume integral of the fluid density over V equals the total fluid mass in the control volume. Conversely, while total mass inflow is given by an integral of the surface normal mass flow $\rho \mathbf{u} \cdot d\mathbf{S}$ over the bounding surface. It can help to think about these terms from a dimensional perspective. Namely, the term $\rho \mathbf{u}$ represents a mass flux, the amount of fluid mass flowing per unit time per unit surface through an imaginary surface perpendicular to the flow direction. Performing a scalar product of this quantity against an oriented surface gives the total mass flow across the surface, the total amount of fluid mass flowing per unit time through the surface. By performing this for all infinitesimal surface elements $d\mathbf{S}$ that compose the boundary and considering that the surface normal are by convention pointed outwards with respect to the volume enclosed, the resulting integral is a balance of the overall mass outflow from the volume (if the integral is < 0) or inflow into the volume (if the integral is > 0).

For the flow illustrated in Fig. 9 (c), the same logic applies to the derivation of integral form of the continuity equation. In this case however, the limit for $V \rightarrow 0$ needs to be considered. The problem posed by having to treat how $S \rightarrow 0$ as $V \rightarrow 0$ can be solved by formulating the surface integral in terms of volume integral using Gauss theorem (Section 2.1.2.9), Eq. (34), thus:

$$\iint_S \rho \mathbf{u} \cdot d\mathbf{S} = \iiint_V (\nabla \cdot \rho \mathbf{u}) \, dV \quad (38)$$

By taking the advantage of Eq. (38) and with the limit for $V \rightarrow 0$, based on Eq. (37), the differential conservation form of the continuity equation becomes:

$$\frac{\partial}{\partial t} \rho + \nabla \cdot (\rho \mathbf{u}) = 0 \quad (39)$$

For a finite control volume moving with the flow as represented in Fig. 9 (b), the mass conservation principle states that the total mass within the volume is constant in time, which stems from the definition of a control volume itself in a Lagrangian frame. Recalling the concept of material derivative introduced in Section 2.1.2.10, it represents the total rate of change of fluid mass within a moving fluid parcel. Thus, the conservation equation can be defined in its integral non-conservation form as:

$$\frac{D}{Dt} \iiint_V \rho \, dV = 0 \quad (40)$$

By applying the same logic adopted before when using the integral conservation form to derive the differential conservation form, the differential non-conservation form that describes the flow of an infinitesimal fluid element in a Lagrangian frame can be obtained as:

$$\frac{D}{Dt} \rho + \rho \nabla \cdot \mathbf{u} = 0 \quad (41)$$

By recalling the definition of material derivative provided by Eq. (35) and by recalling that $\nabla \cdot (\rho\mathbf{u}) = (\rho\nabla \cdot \mathbf{u}) + (\mathbf{u} \cdot \nabla \rho)$ due to the derivative of a product rules, the conservation and non-conservation forms of the continuity equation are mathematically identical. However, the advective term $\nabla \cdot (\rho\mathbf{u})$ is treated as a sum of separate terms in the non-conservation form. The differences between these forms arise only at the equation discretization step, as it is further elaborated in Section 2.4.

2.3.2.2. Momentum conservation equation

The momentum conservation equation (or the continuity equation) is a consequence of applying a formulation of Newton's second law to the volume of interest for a specified flow representation model. The total rate of change of a momentum within the volume (whether finite or infinitesimal) needs to be equal to a sum of: net momentum inflow in the volume, forces that act on the surface boundary of the volume, and the body forces (also known as bulk forces) acting on the volume from within (e.g., gravity). In the Eulerian reference frame, a finite control volume V is bounded by a surface S . This corresponds to the flow representation model illustrated in Fig. 9 (a). As the density represents a specific mass (i.e., mass per unit volume), specific momentum (i.e., momentum per unit volume) is then $\rho\mathbf{u}$. Thus, the rate of change of total momentum in the control volume can be calculated as:

$$\frac{\partial}{\partial t} \iiint_V \rho\mathbf{u} \, dV \quad (42)$$

The term $\rho\mathbf{u}$ can also be thought as the amount of mass that is advected by \mathbf{u} , namely a mass flux, while the term $\rho\mathbf{u} \cdot d\mathbf{S}$ represents the net mass flow through an infinitesimal oriented surface element $d\mathbf{S}$ on the bounding surface S . This is a scalar quantity that represent mass outflow from the volume V through $d\mathbf{S}$ if positive, inflow if negative. Starting from this, the net flow of momentum through $d\mathbf{S}$ can be defined as $\mathbf{u}(\rho\mathbf{u} \cdot d\mathbf{S})$. No specific mathematical considerations apply to this term in this form, as the term in parenthesis is scalar. Nonetheless, it is often more convenient to express this term as an outer product of the velocity terms, given that $\mathbf{u}(\rho\mathbf{u} \cdot d\mathbf{S}) = \rho(\mathbf{u} \otimes \mathbf{u}) \cdot d\mathbf{S}$. Finally, the net outward flow can be obtained as:

$$\iint_S \rho(\mathbf{u} \otimes \mathbf{u}) \cdot d\mathbf{S} \quad (43)$$

The momentum changes due to forces acting on the domain boundary surface. At each point on the surface, an infinitesimal force $d\mathbf{F}$ acting on an infinitesimal oriented surface area element $d\mathbf{S}$ can be defined. The oriented surface area element is given by $d\mathbf{S} = \mathbf{n} \, dS$, where \mathbf{n} being represents the surface normal and dS the surface area of the element. By defining a stress vector σ^n acting on the surface as :

$$\sigma^n = \frac{d\mathbf{F}}{dS} \quad (44)$$

it is possible to equate the total force acting on the surface S as:

$$\iint_S d\mathbf{F} = \iint_S \sigma^n \, dS \quad (45)$$

To abstract the description of the state of stress at each point in the fluid from a specific instance of a control volume, the Cauchy stress tensor $\boldsymbol{\sigma}$ is defined so that, for any possible infinitesimal surface $d\mathbf{S}$ of normal \mathbf{n} that passes through the point being considered, it is:

$$\boldsymbol{\sigma}^n = \mathbf{n} \cdot \boldsymbol{\sigma} \quad (46)$$

The Cauchy stress tensor fully describes the state of stress within each point of a fluid in a manner that is independent from the specific choice of a control volume and its bounding surface. In case of fluid, the stress tensor is always decomposed into a so called hydrostatic component that consists of (isotropic) pressure field p and a deviatoric stress tensor $\boldsymbol{\sigma}_d$ so that:

$$\boldsymbol{\sigma} = -p\mathbb{I} + \boldsymbol{\sigma}_d \quad (47)$$

where \mathbb{I} represents the identity tensor. In 3D space cartesian reference frame, the stress tensor is given by:

$$\boldsymbol{\sigma} = \begin{bmatrix} \tau_{xx} - p & \tau_{xy} & \tau_{xz} \\ \tau_{yx} & \tau_{yy} - p & \tau_{yz} \\ \tau_{zx} & \tau_{zy} & \tau_{zz} - p \end{bmatrix} \quad (48)$$

where the τ_{xy} values represent the nine components of the deviatoric stress tensor $\boldsymbol{\sigma}_d$. For a continuum, it can be shown that only six of these components are independent, as the principle of conservation of angular momentum applied to the control volume leads to $\tau_{ij} = \tau_{ji}$, meaning that the deviatoric stress tensor $\boldsymbol{\sigma}_d$ is symmetric. By substituting the stress vector $\boldsymbol{\sigma}^n$ with Eq. (46) in Eq. (45) and considering the definition of the stress tensor in terms of a hydrostatic and deviatoric components given by Eq. (47), the net rate of change of momentum due to forces acting on S becomes:

$$\iint_S d\mathbf{F} = \iint_S \mathbf{n} \cdot (-p\mathbb{I} + \boldsymbol{\sigma}_d) dS = - \iint_S p dS + \iint_S \mathbf{n} \cdot \boldsymbol{\sigma}_d dS \quad (49)$$

For Newtonian fluids, the deviatoric stress tensor is:

$$\boldsymbol{\sigma}_d = \mu(\nabla\mathbf{u} + (\nabla\mathbf{u})^T - \frac{2}{3}(\nabla \cdot \mathbf{u})\mathbb{I}) \quad (50)$$

where μ represents fluid molecular viscosity. Term $\boldsymbol{\sigma}_d$ in 3D space is obtained as follows:

$$\boldsymbol{\sigma}_d = \mu \begin{bmatrix} 2\frac{\partial u_x}{\partial x} - \frac{2}{3}\nabla \cdot \mathbf{u} & \frac{\partial u_y}{\partial x} + \frac{\partial u_x}{\partial y} & \frac{\partial u_z}{\partial x} + \frac{\partial u_x}{\partial z} \\ \frac{\partial u_x}{\partial y} + \frac{\partial u_y}{\partial x} & 2\frac{\partial u_y}{\partial y} - \frac{2}{3}\nabla \cdot \mathbf{u} & \frac{\partial u_z}{\partial y} + \frac{\partial u_y}{\partial z} \\ \frac{\partial u_x}{\partial z} + \frac{\partial u_z}{\partial x} & \frac{\partial u_y}{\partial z} + \frac{\partial u_z}{\partial y} & 2\frac{\partial u_z}{\partial z} - \frac{2}{3}\nabla \cdot \mathbf{u} \end{bmatrix} \quad (51)$$

For any specific bulk force \mathbf{f}_b its contribution is:

$$\iiint_V \mathbf{f}_b dV \quad (52)$$

By combining all of the contributions considered so far, namely: net momentum rate of change within V , given by Eq. (42), net momentum advected out of V , given by Eq. (43), net momentum change due to forces acting on S , given by Eq. (49), and net momentum change due to specific bulk forces given by Eq. (52), the final integral conservation form of the momentum equation becomes:

$$\frac{\partial}{\partial t} \iiint_V \rho \mathbf{u} dV + \iint_S \rho (\mathbf{u} \otimes \mathbf{u}) \cdot d\mathbf{S} = - \iint_S p d\mathbf{S} + \iint_S \mathbf{n} \cdot \boldsymbol{\sigma}_d dS + \iiint_V \mathbf{f}_b dV \quad (53)$$

Differential conservation form of the momentum equation is instead derived by applying the same logic to an infinitesimal fluid element dV fixed in space, consistent with Eulerian framework, as shown in Fig. 9 (c). This means that the governing equation would be given by Eq. (51) in the limit for $V \rightarrow 0$. As seen for the continuity equation, this limit is better handled if the surface integrals that appear in Eq. (53) are converted into volume integrals. By taking advantage of the divergence theorem, this can be accomplished for all relevant terms as follows:

$$\iint_S \rho (\mathbf{u} \otimes \mathbf{u}) \cdot d\mathbf{S} = \iiint_V \nabla \cdot (\rho \mathbf{u} \otimes \mathbf{u}) dV \quad (54)$$

$$\iint_S p d\mathbf{S} = \iiint_V \nabla p dV \quad (55)$$

$$\iint_S \mathbf{n} \cdot \boldsymbol{\sigma}_d dS = \iiint_V \nabla \cdot \boldsymbol{\sigma}_d dV \quad (56)$$

By substituting Eqs. (54)–(56) into Eq. (53) and taking the limit for $V \rightarrow 0$, the differential conservation form of the momentum conservation equation becomes:

$$\frac{\partial}{\partial t} \rho \mathbf{u} + \nabla \cdot (\rho \mathbf{u} \otimes \mathbf{u}) = -\nabla p + \nabla \cdot \boldsymbol{\sigma}_d + \mathbf{f}_b \quad (57)$$

Both, the integral and differential forms are vector valued equations, as the velocity \mathbf{u} is a vector. Thus, these can be also written as a group of equations, one for each component. Considering the differential form as an example, the momentum equation for the i^{th} component in a cartesian reference frame is:

$$\begin{aligned} \frac{\partial}{\partial t} \rho u_i + \sum_{j=1}^3 \frac{\partial}{\partial x_j} (\rho u_i u_j) \\ = -\frac{\partial}{\partial x_i} p + \sum_{j=1}^3 \frac{\partial}{\partial x_j} \left(\mu \left(\frac{\partial u_j}{\partial x_i} + \frac{\partial u_i}{\partial x_j} - \delta_{ij} \frac{2}{3} \sum_{k=1}^3 \frac{\partial u_k}{\partial x_k} \right) \right) + f_{b,i} \end{aligned} \quad (58)$$

where different axes along which the derivation is performed are indicated with x_i , with $x_1 = x$, $x_2 = y$ and $x_3 = z$. Furthermore, the Kronecker delta δ_{ij} equals 1 only when $i = j$ and is 0 otherwise. Thus, Eq. (57) consists of three scalar equations, that in case of a cartesian reference frame, assume the form specified by Eq. (58). For notational simplicity and abstraction from specific reference frames however, the momentum equation is often denoted in its vector form given by Eq. (57).

The system of coupled partial differential equations for continuity, Eq. (39), and for the conservation of momentum, Eq. (57), are referred to as the Navier–Stokes equations, governing the dynamics of fluid flow. The integral non–conservation formulation is:

$$\frac{D}{Dt} \iiint_V \rho \mathbf{u} \, dV = - \iint_S p \, d\mathbf{S} + \iint_S \mathbf{n} \cdot \boldsymbol{\sigma}_d \, dS + \iiint_V \mathbf{f}_b \, dV \quad (59)$$

The advective term is missing from the non–conservation formulation as the control volume is, at any point in time, always containing the same initial set of molecules over which it was defined. Thus, there is no net flow from or into the control volume. The force balances at the volume surface or within the volume itself still apply, resulting in the same formulation of the other source terms. With regards to its differential formulation, it can be obtained as:

$$\frac{D}{Dt} \rho \mathbf{u} + \rho \mathbf{u} (\nabla \cdot \mathbf{u}) = -\nabla p + \nabla \cdot \boldsymbol{\sigma}_d + \mathbf{f}_b \quad (60)$$

2.3.2.3. Energy conservation equation

The energy conservation equation is obtained by applying the first law of thermodynamics with the selected flow representation model. In practice, the energy balance is typically inclusive of internal, potential, and kinetic energy for the volume under investigation.

In the Eulerian frame the energy balance, i.e., the total energy change per unit time within a finite control volume V bounded by a surface S , such as the one represented in Fig. 9 (a) is defined as follows:

$$\frac{\partial}{\partial t} \iiint_V \rho \left(e + \frac{1}{2} \mathbf{u} \cdot \mathbf{u} \right) dV \quad (61)$$

where e is the specific internal energy (i.e., internal energy per unit mass) and $1/2 \mathbf{u} \cdot \mathbf{u}$ is the specific kinetic energy (i.e., kinetic energy per unit volume) of the fluid. The following energy balance change mechanisms are considered:

- *Advection*: fluid carrying energy in and out of the volume due to its own flow;
- *Heat conduction*: conduction of heat at the volume surface due to temperature differences;
- *Mechanical deformations* of fluid parcels due to fluid stress tensor;
- *Body heat source terms*, which might be due to chemical, nuclear reactions, emission or absorption of radiation in any spectrum;
- *Potential energy change* arising from the flow happening in the presence of a body force.

Following the same approach used for mass advection or momentum advection term, it can be shown that the advection energy source term is:

$$\iint_S \rho \left(e + \frac{1}{2} \mathbf{u} \cdot \mathbf{u} \right) \mathbf{u} \cdot d\mathbf{S} \quad (62)$$

Conduction takes place on the volume boundary surface S as it is driven by a temperature gradient ∇T at the surface. The total heat flow through the infinitesimal oriented surface $d\mathbf{S}$ of normal \mathbf{n} is given by Fourier's law and it is equal to $k\nabla T \cdot d\mathbf{S}$, where k is the fluid thermal conductivity at the surface. Thus, the total heat flow into the volume (if the normal is pointing out from the volume the surface encloses) is given by integrating Eq. (62) over the bounding surface, resulting in:

$$\iint_S k\nabla T \cdot d\mathbf{S} \quad (63)$$

The energy rate of change due to mechanical deformations, if the fluid is flowing at a velocity \mathbf{u} through an oriented surface $d\mathbf{S}$ with a normal \mathbf{n} , and the stress vector at location equals $\boldsymbol{\sigma}^n$, then the total mechanical power associated with this fluid flow under stress vector equals $\boldsymbol{\sigma}^n \cdot \mathbf{u} dS$. By recalling Eq. (46), this power can be expressed in terms of the stress tensor as $\mathbf{n} \cdot (\boldsymbol{\sigma} \cdot \mathbf{u}) dS$. Thus, the total deformation related energy change rate (i.e., power) is:

$$\iint_S \mathbf{n} \cdot (\boldsymbol{\sigma} \cdot \mathbf{u}) dS \quad (64)$$

For a specific body heat source term \dot{q} , namely a heat source per unit volume, the total resulting energy source per unit time over V is:

$$\iiint_V \dot{q} dV \quad (65)$$

About the effect of body force field \mathbf{f}_b , the energy change per unit time associated with the fluid moving through the potential field that gives rise to a force (e.g., gravity is $\mathbf{f}_b = \rho\mathbf{g}$) is:

$$\iiint_V \mathbf{f}_b \cdot \mathbf{u} dV \quad (66)$$

The integral conservation form of the energy conservation equation can thus be written as:

$$\begin{aligned} & \frac{\partial}{\partial t} \iiint_V \rho \left(e + \frac{1}{2} \mathbf{u} \cdot \mathbf{u} \right) dV + \iint_S \rho \left(e + \frac{1}{2} \mathbf{u} \cdot \mathbf{u} \right) \mathbf{u} \cdot d\mathbf{S} \\ &= \iint_S k\nabla T \cdot d\mathbf{S} + \iint_S \mathbf{n} \cdot (\boldsymbol{\sigma} \cdot \mathbf{u}) dS + \iiint_V \dot{q} dV + \iiint_V \mathbf{f}_b \cdot \mathbf{u} dV \end{aligned} \quad (67)$$

The differential formulation of the conservation form is obtained in the same manner as seen for the other conservation equations so far by taking the limit of the integral form for $V \rightarrow 0$ and expressing surface integrals in terms of volume integrals via the divergence theorem. The differential formulation thus is:

$$\begin{aligned} & \frac{\partial}{\partial t} \left(\rho e + \frac{1}{2} \rho \mathbf{u} \cdot \mathbf{u} \right) + \nabla \cdot \left(\left(\rho e + \frac{1}{2} \rho \mathbf{u} \cdot \mathbf{u} \right) \mathbf{u} \right) \\ &= \nabla \cdot (k\nabla T) + \nabla \cdot (\boldsymbol{\sigma} \cdot \mathbf{u}) + \dot{q} + \mathbf{f}_b \cdot \mathbf{u} \end{aligned} \quad (68)$$

Conversely, the integral non-conservation form of the energy conservation equation, that is applicable for a Lagrangian reference frame, can be written as:

$$\begin{aligned} \frac{D}{Dt} \iiint_V \rho \left(e + \frac{1}{2} \mathbf{u} \cdot \mathbf{u} \right) dV \\ = \iint_S k \nabla T \cdot d\mathbf{S} + \iint_S \mathbf{n} \cdot (\boldsymbol{\sigma} \cdot \mathbf{u}) dS + \iiint_V \dot{q} dV + \iiint_V \mathbf{f}_b \cdot \mathbf{u} dV \end{aligned} \quad (69)$$

To conclude with, the differential non-conservation form of the energy conservation equation is written as follows:

$$\begin{aligned} \frac{D}{Dt} \left(\rho e + \frac{1}{2} \rho \mathbf{u} \cdot \mathbf{u} \right) + \left(\left(\rho e + \frac{1}{2} \rho \mathbf{u} \cdot \mathbf{u} \right) \right) (\nabla \cdot \mathbf{u}) \\ = -\nabla \cdot (\kappa \nabla T) + \nabla \cdot (\boldsymbol{\sigma} \cdot \mathbf{u}) + \dot{q} + \mathbf{f}_b \cdot \mathbf{u} \end{aligned} \quad (70)$$

It should be stressed that energy equations often vary depending on which energy transfer terms are considered and which are not. It is not uncommon in the domain of CFD to neglect e.g., frictional heating associated with the stress power term $\nabla \cdot (\boldsymbol{\sigma} \cdot \mathbf{u})$. These considerations need to be made based on the expected magnitudes of the different terms, which can vary from application to application and can differ from one another significantly. It is not uncommon, for certain applications where heat transfer processes dominate over kinetic energy change processes, to e.g., neglect the kinetic energy contribution altogether.

In conclusion to this section, it was shown how to construct conservation equations for different quantities that are fundamental to fluid flow based on the adopted choice of a flow representation model. It should nonetheless be noticed that, for the purposes of computational fluid dynamics, the conservation form (i.e., Eulerian based) representations of the fluid flow are significantly more common than the Lagrangian approaches, which conversely enjoy some degree of popularity for the description of multi phase fluid flows.

2.3.3. Considerations on the Navier–Stokes equations

When referring to the Navier–Stokes equations, one generally refers specifically to the coupled system of equations represented by the continuity equation and the momentum conservation equation. These equations commonly appear in simplified forms compared to what has been discussed so far, depending on the flow properties.

At the most fundamental level, flows are categorized as incompressible flows and as compressible flows. Incompressible flows are time independent flows with the fluid density parcel advected by the flow. This is equivalent to stating that the material derivative of the density is null:

$$\frac{D}{Dt} \rho = 0 \quad (71)$$

By recalling the definition of the material derivative provided by Eq. (35) it can be shown that for incompressible flows the continuity equation becomes (in its differential form):

$$\nabla \cdot \mathbf{u} = 0 \quad (72)$$

A consequence of Eq. (71) is that all flows with constant density are incompressible, while not all incompressible flows have a constant density. Conversely, compressible flows are all flows that are not incompressible in the sense described by Eq. (71) and Eq. (72). This has consequences on the form of a momentum equation as well, specifically referring to the divergence of the deviatoric stress tensor $\nabla \cdot \boldsymbol{\sigma}_d$, i.e., momentum diffusion. For the most general case of a compressible flow, it follows:

$$\nabla \cdot \boldsymbol{\sigma}_d = \nabla \cdot \left(\mu \left(\nabla \mathbf{u} + (\nabla \mathbf{u})^T - \frac{2}{3} (\nabla \cdot \mathbf{u}) \mathbb{I} \right) \right) \quad (73)$$

For an incompressible flow however, this can be simplified via Eq. (72) to obtain:

$$\nabla \cdot \boldsymbol{\sigma}_d = \nabla \cdot (\mu (\nabla \mathbf{u} + (\nabla \mathbf{u})^T)) \quad (74)$$

If the flow, in addition to being incompressible with $\nabla \cdot \mathbf{u} = 0$, is also characterized by a constant molecular viscosity μ , and by considering the fact that $\nabla \cdot ((\nabla \mathbf{u})^T) = \nabla (\nabla \cdot \mathbf{u})$, the deviatoric stress tensor can be modelled in an even more concise manner as:

$$\nabla \cdot \boldsymbol{\sigma}_d = \mu \nabla \cdot (\nabla \mathbf{u}) = \mu \nabla^2 \mathbf{u} \quad (75)$$

The symbol ∇^2 is the vector Laplacian operator and, in 3D cartesian coordinate system, it yields a vector given by:

$$\nabla^2 \mathbf{u} = \begin{bmatrix} \frac{\partial^2 u_x}{\partial x^2} + \frac{\partial^2 u_x}{\partial y^2} + \frac{\partial^2 u_x}{\partial z^2} \\ \frac{\partial^2 u_y}{\partial x^2} + \frac{\partial^2 u_y}{\partial y^2} + \frac{\partial^2 u_y}{\partial z^2} \\ \frac{\partial^2 u_z}{\partial x^2} + \frac{\partial^2 u_z}{\partial y^2} + \frac{\partial^2 u_z}{\partial z^2} \end{bmatrix} \quad (76)$$

As a conclusive example, for the case of an incompressible fluid flow with constant viscosity (which is an example to be reconsidered in Section 2.8), the Navier–Stokes equations in their differential, conservation form are written as follows:

$$\nabla \cdot \mathbf{u} = 0 \quad (77)$$

$$\frac{\partial}{\partial t} \rho \mathbf{u} + \nabla \cdot (\rho \mathbf{u} \otimes \mathbf{u}) = -\nabla p + \mu \nabla^2 \mathbf{u} + \mathbf{f}_b \quad (78)$$

2.4. IMPORTANCE OF THE NUMERICAL SOLUTION APPROACH

The aim of any solution approach is to find an approximate solution to a set of equations generated from fundamental conservation laws governing fluid behavior. In practice, solution procedures consist of:

- Discretization, whose purpose is to generate, from the basic fluid conservation laws, a set of equations amenable to being solved numerically;
- Solution algorithm containing the sequence of steps to tackle solution of each of the equations;
- Use of numerical methods to solve the equations.

These three aspects are interconnected to the extent that the choice of discretization methods and solution algorithms is important not just for the accuracy of numerical solutions but may also crucially determine if the equations generated can be solved numerically, or how fast these can be solved depending on numerical method. The remainder of this section provides an overview of discretization practices commonly used in CFD to help a reader understand the importance of discretization parameters in relation to numerical solution, and to illustrate the main principle behind solution algorithms used in current CFD approaches.

2.5. NUMERICAL FRAMEWORKS

There are several numerical frameworks developed to model the behavior of fluids. The idea common to most of these frameworks is to subdivide the region of space where the fluid is to be studied into smaller subregions and to develop, for every subregion, a relationship between the yet unknown value of a fluid property of interest in one subregion to the values at neighboring subregions. The system of equations (one for each subregion) so generated is then processed numerically to calculate the actual values of the property in each subregion. Three various approaches are sketched in Fig. 10.

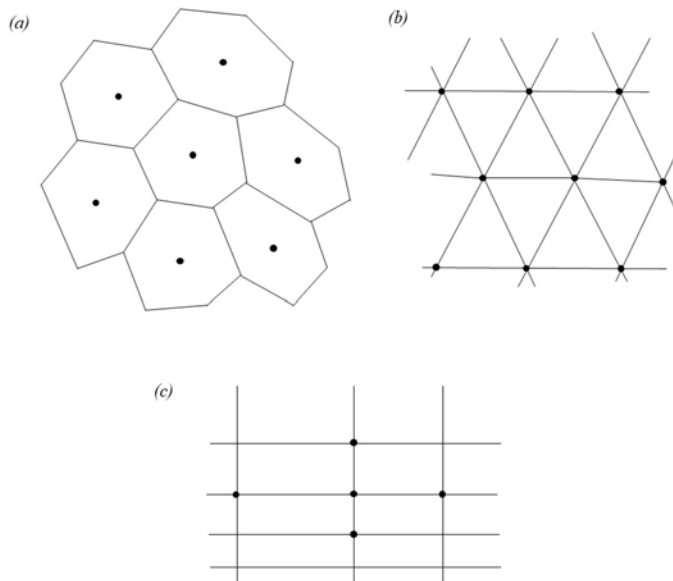


FIG. 10. Arrangement of variables on the computational domain according to different numerical frameworks: (a) finite volume method, (b) finite element method, (c) finite difference method.

With the finite volume method shown in Fig. 10 (a), the region of space of interest (simulation domain) is subdivided into control volumes of arbitrary shapes; the fluid property (or flow variable) is evaluated at the geometrical centroid of the control volume, and it is assumed to prevail inside the control volume. With the finite element method, shown in Fig. 10 (b) the simulation domain is subdivided into elements of arbitrary shapes and fluid property is evaluated at the element corner points. With finite difference methods as sketched in Fig. 10 (c), flow variables are arranged at the points of intersections of orthogonal grid lines. All these mesh based approaches are fundamentally best suited for a Eulerian description of the fluid flow. All the equations that are derived in this section and discussed are obtained in their conservation form, as discussed in Section 2.3.1. assuming the Eulerian description of the fluid flow. The finite volume method is the dominant approach for CFD applications due to its flexibility, relative ease of implementation and applicability to model flows in complex

geometries of typical engineering problems, among which are nuclear thermal hydraulic applications.

2.6. FINITE VOLUME METHOD

For CFD applications, the aim is to use the finite volume method to generate a set of linear algebraic equations linking the value of fluid property of interest at a control volume to the values in neighbouring control volumes. The finite volume method subdivides the simulation domain into (typically, but not necessarily) stationary, arbitrary shaped control volumes, as shown in Fig. 11, where P is the geometrical centroid of the control volume. The value of a property at P is assumed to prevail inside the control volume (also called *mesh cell* or simply *cell*). The cell has a volume V and is bounded by surface S . Due to a simplified computational representation, mesh cells always consist of polyhedra, meaning that the bounding surface of each cell consists of a collection of flat surfaces, referred to as faces. Each face f is characterized by a surface area vector \mathbf{S}_f of normal \mathbf{n}_f and magnitude S_f , which by convention points outwards from the volume enclosed by overall cell bounding surface S .

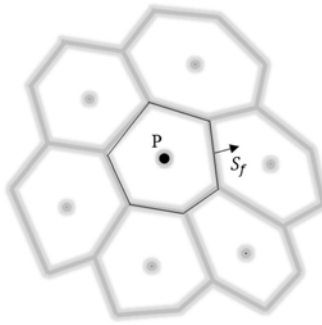


FIG. 11. Generic representation of a finite volume. For generic cell (in the center of this figure) any value of interest is represented by an average value that is constant throughout the cell and that is stored at the cell centroid.

The conservation of a generic fluid property ϕ is enforced via integral transport equations, linking the rate of change of a fluid property within V to different phenomena, which can be broadly categorized as of:

- Advection, i.e., the transport of ϕ by the fluid velocity field \mathbf{u} ;
- Diffusion i.e., the transport of ϕ due to molecular diffusive processes even in absence of a macroscopic net advection;
- Source term i.e., physical processes that result in a net generation or removal of ϕ from the volume.

While the conservation equations for the specific cases of mass, momentum and energy conservation have been derived in their various forms in Section 2.3.2, the integral form of the transport equation for a generic fluid property ϕ is presented here from the perspective of using it as a starting point to discuss the finite volume method.

2.6.1. Discrete representation of a conservation equation

The integral formulation of the transport equation for a generic mass intensive fluid property ϕ can be derived considering the discussion in Section 2.3.2. Its integral formulation over the

volume of a mesh cell V is considered. The triple and double integral notations are simplified to a single integral notation. The equation can be thus written as:

$$\frac{\partial}{\partial t} \int_V \rho \phi dV + \int_S \rho \phi \mathbf{u} \cdot d\mathbf{S} = - \int_S \mathbf{J}_\phi \cdot d\mathbf{S} + \int_V f_\phi dV \quad (79)$$

in which the two terms on the left hand side correspond to the net rate of change of $\rho\phi$ in V and the outflow of $\rho\phi$ due to advection through the boundary surface S respectively, while the two terms on the right hand side represent the diffusion of $\rho\phi$ into V through the bounding surface, governed by a diffusion flux \mathbf{J}_ϕ , and the volume source of $\rho\phi$ due to a source term f_ϕ . Note that if ϕ were to be a vector quantity, the relevant gradient and dot product operations would need to be adequately replaced (by substituting those with divergences and outer products to preserve dimensionality). Different integral forms of various conservation equations that have been previously discussed in Section 2.3.2 can be derived from Eq. (79):

- Continuity equation can be obtained by setting $\phi = 1, \mathbf{J}_\phi = \mathbf{0}, f_\phi = 0$;
- Momentum conservation equation can be obtained by setting $\phi = \mathbf{u}, \mathbf{J}_\phi = -\boldsymbol{\sigma}$, namely the fluid stress tensor, and $f_\phi = \mathbf{f}_b$;
- Energy conservation equation can be obtained by setting $\phi = e + \frac{1}{2}\mathbf{u} \cdot \mathbf{u}, \mathbf{J}_\phi = -k\nabla T - \boldsymbol{\sigma} \cdot \mathbf{u}$ and $f_\phi = \dot{q} + \mathbf{f}_b \cdot \mathbf{u}$.

In order to obtain a finite volume discretization of the integral governing equation defined within a control volume, one primarily takes advantage of the definition of a mean volume and surface values, as well as the divergence (or Gauss) theorem. As it was previously introduced, the finite volume method assumed that all values of any fluid quantity ϕ within the mesh volume can be reasonably approximated by a certain value stored at the cell centroid. This value consists of the volume average, so that for a cell labelled P of volume V :

$$\phi_P = |\phi|_V = \frac{1}{V} \int_V \phi dV \quad (80)$$

The same averages can be defined for surface values as:

$$|\phi|_S = \frac{1}{S} \int_S \phi dS \quad (81)$$

The goal of a finite volume method is to derive (algebraic) governing equations that apply to discrete collection of average values, since those are the values that being numerically processed. For the time derivative term, it can be seen that:

$$\frac{\partial}{\partial t} \int_V \rho \phi dV = \frac{\partial}{\partial t} (V |\rho \phi|_V) \quad (82)$$

The product of average terms is a good approximation to the average of the product. With this approximation, it is possible to obtain:

$$\frac{\partial}{\partial t} \int_V \rho \phi dV \simeq \frac{\partial}{\partial t} (V |\rho|_V |\phi|_V) \quad (83)$$

This logic can be applied to surface integrals as well. As the mesh cells are always polyhedral, the integral can be decomposed into a sum of integrals over each flat face f of surface area S_f and surface normal \mathbf{n}_f :

$$\int_S \rho \phi \mathbf{u} \cdot d\mathbf{S} = \sum_f \int_f \rho \phi \mathbf{u} \cdot d\mathbf{S} \quad (84)$$

By expressing the surface integral in terms of a surface average it follows:

$$\int_f \rho \phi \mathbf{u} \cdot d\mathbf{S} = S_f |\rho \phi \mathbf{u}|_f \cdot \mathbf{n}_f \quad (85)$$

By substituting the average of the product with the product of the averages, the advective term can be re-written as follows:

$$\int_f \rho \phi \mathbf{u} \cdot d\mathbf{S} \approx \sum_f S_f |\phi|_f |\rho \mathbf{u}|_f \cdot \mathbf{n}_f \quad (86)$$

However, in computational framework, where field variables are available only at cell centroids, the face averaged values $|\phi|_f$ are not generally directly available. Thus, need to be reconstructed from the cell center average values $|\phi|_V$ of the cells that share each face f via adequate interpolation methods. However, a continuous problem in a continuous space is translated into a discrete problem (i.e., a discrete collection of governing equations for ϕ , one per mesh cell) that is fundamentally reducible to a set of algebraic relationships between cell centered average values $|\phi|_V$, which are what the numerical solution ultimately consists of.

2.6.2. Examples of discretization practices in industrial computational fluid dynamics

The finite volume method is used to generate a set of linear equations, one for each control volume, amenable to numerical solution. Various spatial and temporal discretization practices can be plugged into the finite volume method framework to generate the linear equations. Discretization practices are here illustrated with simple 1D convection diffusion problems. A 1D flow configuration is considered where the flow velocity \mathbf{u} is known. To derive the coefficients of the linear equation, the properties of each control volume of interest are linked with nearby control volumes as is transported by velocity \mathbf{u} (convection) and by molecular processes (diffusion). The simulation domain is assumed to consist of a series of mesh cells of equal size aligned in the flow direction, as shown in Fig. 12, where the computational molecule consisting of the control volume P , for which an algebraic equation is derived, and its neighbor control volumes W (west) and E (east) are indicated.

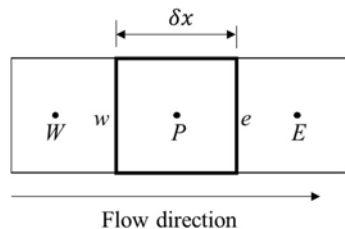


FIG. 12. Computational molecule in 1D uniform grid made of cubic cells. The control volume with centroid P as well as its two neighbors W and E are labelled.

2.6.2.1. Spatial discretization

The steady state advection diffusion example for ϕ in a fluid of constant density as given by Eq. (79) is considered. By steady state it is assumed that the final distribution of ϕ is time independent so that the time derivative term is always null. It is assumed that the flux \mathbf{J}_ϕ can be related to the gradient of ϕ as $\mathbf{J}_\phi = -c_\phi \nabla \phi$ with c_ϕ being a certain diffusion coefficient and that the source term $f_\phi = 0$. Thus the problem reduces to finding a solution ϕ to:

$$\int_S \rho \phi \mathbf{u} \cdot d\mathbf{S} = \int_S c_\phi \nabla \phi \cdot d\mathbf{S} \quad (87)$$

At the same time, the fluid flow itself, meaning its density and velocity distribution, should satisfy the conservation of fluid mass, namely a steady state version of Eq. (37) that reduces to:

$$\int_S \rho \mathbf{u} \cdot d\mathbf{S} = 0 \quad (88)$$

However, as the density is taken as a constant for the case under exam, it is the velocity field alone that should satisfy Eq. (88). For clarity regarding the problem statement, the differential forms of Eq. (87) and Eq. (88) can be obtained by applying the divergence theorem and taking the limit for $V \rightarrow 0$, which results in:

$$\nabla \cdot (\rho \phi \mathbf{u}) = \nabla \cdot (c_\phi \nabla \phi) \quad (89)$$

$$\nabla \cdot (\rho \mathbf{u}) = 0 \quad (90)$$

By reformulating Eq. (87) in terms of surface averages, it follows:

$$\sum_f S_f |\phi|_f |\rho \mathbf{u}|_f \cdot \mathbf{n}_f = \sum_f S_f |c_\phi \nabla \phi|_f \cdot \mathbf{n}_f \quad (91)$$

Based on the example provided in Fig. 12 a focus is on the cell of centroid P . The summation over the cell faces consists of two terms for each of the two cell faces, namely w and e , so that the Eq. (91) can be written as follows:

$$S_e |\phi|_e |\rho \mathbf{u}|_e - S_w |\phi|_w |\rho \mathbf{u}|_w = S_e \left| c_\phi \frac{\partial}{\partial x} \phi \right|_e - S_w \left| c_\phi \frac{\partial}{\partial x} \phi \right|_w \quad (92)$$

The negative sign on the terms evaluated at the w face arises from the fact that, for the considered scenario, both the velocity vector and the gradients on the face are antiparallel to the face normal, which is outwards oriented from the cell by convention. The important aspect to stress here is that Eq. (92) is a discretized version of Eq. (89).

It is customary to introduce a face flux variable in the discretized equations that govern fluid flow. This face flux is a scalar quantity denoted with F and, for the 1D case, it is defined on each cell face f as follows:

$$F_f = |\rho \mathbf{u}|_f \quad (93)$$

Physically, it represents the net mass flux through the face f and has the dimension of $\text{kg}/\text{m}^2\text{s}$. By employing this result, Eq. (92) is then written as:

$$S_e |\phi|_e F_e - S_w |\phi|_w F_w = S_e \left| c_\phi \frac{\partial}{\partial x} \phi \right|_e - S_w \left| c_\phi \frac{\partial}{\partial x} \phi \right|_w \quad (94)$$

By applying the same procedure for the discretization of the continuity equation, Eq. (88) in cell with centroid P , it follows:

$$S_e F_e - S_w F_w = 0 \quad (95)$$

For simplicity, it is assumed that the velocity field is known a priori and requires no solution (also considering that Eq. (95) alone does not suffice, as one needs to solve a momentum conservation equation as well, not presently discretized). Thus, the focus is on obtaining a field ϕ that consists of the cell center values of ϕ , so that ϕ satisfies Eq. (94) in each cell of the mesh. However, Eq. (94) is still not expressed in terms of cell centered values, rather in terms of face centered values $|\phi|_f$ as well as face centered gradients $|\partial\phi/\partial x|_f$. In order to be able to solve the collective system of equations, each in form of Eq. (94) for each cell, these terms need to be expressed as functions of cell centered quantities of the cell under consideration and, possibly, the cell centered quantities of neighboring cells. This is done via adequate so called differencing (also known as interpolation) schemes.

2.6.2.2. Differencing schemes

The most fundamental differencing schemes is summarized in this section. The central differencing scheme employs a linear interpolation to approximate a property at a generic face f that is shared by cells P and N , so that:

$$\phi_f \simeq \frac{\delta_P \phi_P + \delta_N \phi_N}{\delta_P + \delta_N} \quad (96)$$

where δ_i is the distance between the cell center and the face center for each cell i . For a uniform mesh, this reduces to:

$$\phi_f \simeq \frac{\phi_P + \phi_N}{2} \quad (97)$$

Similarly, with a central differencing scheme the gradient at the face is approximated as follows:

$$\left| \frac{\partial}{\partial x} \phi \right|_f \simeq \frac{\phi_N - \phi_P}{\delta x} \quad (98)$$

with δx being the distance between centers of P and N cells. By employing Eqs. (97) and (98), and assuming a uniform mesh, Eq. (94) can be rewritten as:

$$S_e F_e \left(\frac{\phi_P + \phi_E}{2} \right) - S_w F_w \left(\frac{\phi_P + \phi_W}{2} \right) = S_e |c_\phi|_e \left(\frac{\phi_E - \phi_P}{\delta x} \right) - S_w |c_\phi|_w \left(\frac{\phi_P - \phi_W}{\delta x} \right) \quad (99)$$

Eq. (99) relates the cell center value ϕ_P to the neighboring cell center values ϕ_E , ϕ_W and contains no other unknowns expressed at face centers (recall that a velocity distribution is assumed to be known, and thus face fluxes are known as well). For reasons that will be explained later, it is often convenient to arrange the terms with respect to the unknowns into coefficients, so that Eq. (99) can be expressed as:

$$a_P \phi_P = a_E \phi_E + a_W \phi_W \quad (100)$$

with the coefficients expressed as, in this case:

$$a_E = S_e \left(\frac{|c_\phi|_e}{\delta x} - \frac{F_e}{2} \right) \quad (101)$$

$$a_W = S_w \left(\frac{|c_\phi|_w}{\delta x} + \frac{F_w}{2} \right) \quad (102)$$

$$a_P = a_W + a_E + (S_e F_e - S_w F_w) \quad (103)$$

These are the coefficients that result from a central differencing scheme. As anticipated, this is not the only possible differencing scheme, and the scheme introduced next consist of the upwind interpolation scheme. The essence of the upwind scheme is that, for a face f that is shared between two cells P and N , the value of ϕ_f at a face is set equal to either cell center value ϕ_P or ϕ_N , depending on the flow direction. It is set equal to the cell center value of the cell that lies upstream (or upwind, hence the name) of the fluid flow. In particular:

$$\phi_f \simeq \begin{cases} \phi_P & \text{if } F_f > 0 \\ \phi_N & \text{if } F_f < 0 \end{cases} \quad (104)$$

This differencing scheme is often applied to the advective term, but rarely to the diffusive terms, which are treated here with a central differencing scheme. Thus, with reference to Fig. 12 for information regarding the flow direction, Eq. (94) can be written with an upwind differencing scheme for the advective term as:

$$S_e F_e \phi_P - S_w F_w \phi_W = S_e |c_\phi|_e \left(\frac{\phi_E - \phi_P}{\delta x} \right) - S_w |c_\phi|_w \left(\frac{\phi_P - \phi_W}{\delta x} \right) \quad (105)$$

which can in turn be expressed in the form of Eq. (100) with the following coefficients:

$$a_E = S_e \frac{|c_\phi|_e}{\delta x} \quad (106)$$

$$a_W = S_w \left(\frac{|c_\phi|_w}{\delta x} + F_w \right) \quad (107)$$

$$a_P = a_W + a_E + (S_e F_e - S_w F_w) \quad (108)$$

While the number of differencing schemes that have been historically devised that are currently in use is considerable, the central and upwind schemes are the two most fundamental ones which enjoy a large degree of application for a large variety of cases, which is why the present discussion will not introduce further schemes.

2.6.2.3. Considerations on the accuracy of differencing schemes

The approximation implicit in the upwind scheme contains information from fewer cells than the centered differencing scheme i.e., there are fewer cells in the upwind computational molecule than in the molecule generated by the centered differencing scheme. For a given number of mesh cells, a larger computational molecule has the advantage of a higher spatial accuracy due to using more cell centroid points for the interpolation of the flow property. In this sense, the central differencing scheme can be characterized as having a higher order of accuracy if compared to the upwind scheme. In developing discretization schemes, the requirements to maintain accuracy of the calculation are the main drive to formulate discretization schemes as a blend of upwind schemes i.e., the schemes that calculate interpolation parameters based on different estimates of the local convective velocity and higher order schemes i.e., schemes that use information from increasingly large computational molecules.

2.6.2.4. Temporal discretization

The temporal derivative term that figures within any equation is usually approximated with the mean value theorem via taking the mean value of the temporal derivative prevailing inside a control volume as the value at the centroid P of the control volume, according to Eq. (80), so that:

$$\frac{\partial}{\partial t} \int_V \rho \phi dV = \int_V \frac{\partial}{\partial t} \rho \phi dV \simeq V \left| \frac{\partial}{\partial t} \rho \phi \right|_v \quad (109)$$

As for the spatial differencing scheme discussed in Section 2.6.2.2, numerous temporal differencing schemes exists as well. For introductory purposes, the Euler scheme is presented. Recalling that the volume average $|\phi|_V$ over cell P is denoted with ϕ_P , the time derivative is approximated as follows:

$$\left| \frac{\partial}{\partial t} \rho \phi \right|_v \simeq \frac{\rho_P \phi_P - \rho_P^0 \phi_P^0}{\delta t} \quad (110)$$

where the superscript 0 denotes that the given quantity is evaluated at the previous (or old) time step, while the absence of a superscript denotes the variable at the current time step, i.e., the unknown. For a constant density case, it follows:

$$\left| \frac{\partial}{\partial t} \rho \phi \right|_v \simeq \rho_P \frac{\phi_P - \phi_P^0}{\delta t} \quad (111)$$

However, the chosen time differencing scheme affects the treatment of all terms in governing equation. To better explain this, it is assumed that the discretized transport equation for ϕ in cell P is unsteady in nature, meaning it accounts for temporal changes. By adding the discretized time derivative term to the upwind-discretized steady transport equation, the Eq. (105) then becomes:

$$V \rho_P \frac{\phi_P - \phi_P^0}{\delta t} + S_e F_e \phi_P - S_w F_w \phi_W = S_e |c_\phi|_e \left(\frac{\phi_E - \phi_P}{\delta x} \right) - S_w |c_\phi|_w \left(\frac{\phi_P - \phi_W}{\delta x} \right) \quad (112)$$

By considering all the ϕ terms in the equation, except ϕ^0 to be the unknown new time step values that need to be solved for, the overall resulting time differencing scheme takes the name of backwards Euler scheme and is an instance of an implicit method. The implicit means that the unknown value of ϕ_P at the time step under exam depends not only on the old time step values, such as ϕ_P^0 , but also on the unknown values of ϕ in the neighboring cells, namely ϕ_E and ϕ_W . The construction of a system of equations is aided by grouping the coefficients of the unknown terms, as it will be explained later. In particular, the Eq. (112) is rearranged as:

$$a_P \phi_P = a_W \phi_W + a_E \phi_E + b_P \quad (113)$$

where the term b_P is the source term. The coefficients assume the following form for the case of Eq. (112):

$$a_E = S_e \frac{|c_\phi|_e}{\delta x} \quad (114)$$

$$a_W = S_w \left(\frac{|c_\phi|_w}{\delta x} + \frac{F_w}{2} \right) \quad (115)$$

$$a_P = a_W + a_E + (S_e F_e - S_w F_w) + V \frac{\rho_P}{\delta t} \quad (116)$$

$$b_P = V \frac{\rho_P}{\delta t} \phi_P^0 \quad (117)$$

Another temporal discretization scheme consists of the forward Euler scheme. While the actual time derivative term is treated via Eq. (111), all the other ϕ terms are treated with their old time step values, so that the unsteady discretized transport equation becomes:

$$V \rho_P \frac{\phi_P - \phi_P^0}{\delta t} + S_e F_e \phi_P^0 - S_w F_w \phi_W^0 = S_e |c_\phi|_e \left(\frac{\phi_E^0 - \phi_P^0}{\delta x} \right) - S_w |c_\phi|_w \left(\frac{\phi_P^0 - \phi_W^0}{\delta x} \right) \quad (118)$$

In this case, the solution for ϕ_P is trivial since all values are known. This category of temporal discretization schemes, wherein the new time step values exclusively depend on known old time step values, are called explicit schemes, and while significantly faster in principle compared to implicit scheme, these are severely constrained by the limitations of the maximum admissible value for the time step δt , as it will be shown. Therefore, it is useful to express Eq. (118) in the following way:

$$a_P \phi_P = a_P^0 \phi_P^0 + b_P \quad (119)$$

where

$$a_P = V \frac{\rho}{\delta t} \quad (120)$$

$$a_P^0 = V \frac{\rho}{\delta t} - S_e F_e - S_e |c_\phi|_e \frac{1}{\delta x} - S_w |c_\phi|_w \frac{1}{\delta x} \quad (121)$$

$$b_P = S_w F_w \phi_W^0 + S_e |c_\phi|_e \frac{\phi_E^0}{\delta x} + S_w |c_\phi|_w \frac{\phi_W^0}{\delta x} \quad (122)$$

2.7. INTRODUCTION TO NUMERICAL SOLUTION METHODS

When using the finite volume method, the simulation domain is subdivided into control volumes of arbitrary shapes. The integral form of the fundamental conservation law applied to each control volume generates a system of linear equations, linking neighbor control volumes, to be solved numerically.

2.7.1. Solution of linear systems of equations

A system of n linear algebraic equations for an unknown ϕ can be expressed in matrix notation as:

$$\mathbf{A}\phi = \mathbf{b} \quad (123)$$

with

$$\mathbf{A} = \begin{bmatrix} a_{11} & \cdots & a_{1n} \\ \vdots & \ddots & \vdots \\ a_{n1} & \cdots & a_{nn} \end{bmatrix} \quad (124)$$

$$\phi = \begin{bmatrix} \phi_1 \\ \vdots \\ \phi_n \end{bmatrix} \quad (125)$$

$$\mathbf{b} = \begin{bmatrix} b_1 \\ \vdots \\ b_n \end{bmatrix} \quad (126)$$

where a_{ij} are the matrix coefficients, ϕ_i the unknown and b_i the source term for the i -th equation.

2.7.1.1. Iterative solution approaches

Linear system of equations can always be solved via a direct method, however particular features of convection-diffusion equations and of their discretization with the finite volume method generate large linear system of equations i.e., systems with many (often millions) equations, characterized by sparse matrices i.e., matrices whose only non zero coefficients are the diagonal and near diagonal coefficients. This is due to a nature of numerical frameworks considered that subdivide the simulation domain in many subregions and that result in discretized equations linking a subregion to its neighboring subregions. The typical equation for control volume P can be used to infer the basic features of the matrix \mathbf{A} corresponding to the linear system containing the equations for all control volumes in the computational domain. As an example, a discretized transport equation in the form of Eq. (113) would figure in the linear system as:

$$\mathbf{A} = \begin{bmatrix} \ddots & & 0 & & 0 \\ 0 & -a_W & a_P & -a_E & 0 \\ 0 & & 0 & & \ddots \end{bmatrix} \quad (127)$$

$$\boldsymbol{\phi} = \begin{bmatrix} \vdots \\ \phi_W \\ \phi_P \\ \phi_E \\ \vdots \end{bmatrix} \quad (128)$$

$$\mathbf{b} = \begin{bmatrix} \vdots \\ b_P \\ \vdots \end{bmatrix} \quad (129)$$

For solving a linear system with a large sparse coefficient matrix, an iterative solution method is more convenient than a direct solution method i.e., an iterative numerical method requires less computational time than a direct method (such considerations apply also to numerical frameworks alternative to the finite volume method).

Iterative methods seek to find an approximate solution $\boldsymbol{\phi}^m$ to the system of equations $\mathbf{A}\boldsymbol{\phi}^m = \mathbf{b}^m$ via repeatedly updating $\boldsymbol{\phi}$ a given number m of times, starting from an initial guess $\boldsymbol{\phi}^0$, typically multiplying the approximate solution by an iteration matrix \mathbf{M} computed from \mathbf{A} as in $\boldsymbol{\phi}^{m+1} = \mathbf{M}(\mathbf{A})\boldsymbol{\phi}^m$. The approximate solution $\boldsymbol{\phi}^m$ at iteration m satisfies the following:

$$\mathbf{A}\boldsymbol{\phi}^m = \mathbf{b} - \mathbf{r}^m \quad (130)$$

where the quantity \mathbf{r}^m is called residual and is defined as:

$$\mathbf{r}^m = \mathbf{A}(\boldsymbol{\phi} - \boldsymbol{\phi}^m) \quad (131)$$

The requirement that any iterative method must fulfill is that \mathbf{r}^m decreases for increasing numbers of iterations, and that for any sufficiently large m one has $\boldsymbol{\phi}^m \approx \boldsymbol{\phi}$, so that $\boldsymbol{\phi}^m$ can be considered as an approximation of the true solution $\boldsymbol{\phi}$ to $\mathbf{A}\boldsymbol{\phi} = \mathbf{b}$. Since the fundamental solution $\boldsymbol{\phi}$ is ultimately unknown during the solution process, one generally relies on a pseudo residual rather than the residual defined by Eq. (131). This pseudo residual is defined as:

$$\mathbf{r}^m = \mathbf{A}(\boldsymbol{\phi}^m - \boldsymbol{\phi}^{m-1}) \quad (132)$$

The residual itself depends on the coefficient matrix \mathbf{A} ; such matrix is generally required to have certain properties if the desired behavior for \mathbf{r}^m is for it to get smaller as the number of iterations m increases. This behavior is also known as convergence of the iterative solution.

2.7.1.2. Impact of matrix coefficient properties on linear system convergence

The rigorous determination of requirements on matrix coefficient for guaranteeing applicability and performance of iterative numerical methods is a complex subject. Here only two fundamental results from this vast area of mathematical research are explained, which can be used to derive recommendations of practical use for determining discretization parameters δx and δt . Referring to the example matrix \mathbf{A} , a sufficient condition that guarantees convergence of at least one iterative method is that:

$$|a_P| \geq |a_W| + |a_E| \quad (133)$$

This concept is known in linear algebra as diagonal dominance. A matrix is diagonally dominant if the magnitude of the terms on the diagonal (i.e., the a_P term for every matrix row)

are greater or equal to the sum of the magnitudes of the off-diagonal terms (i.e., a_W , a_E) for each matrix row. This condition, while being sufficient, is not necessary.

A further condition that has consequences on CFD applications is that all coefficients of the discretized equations have the same sign. This condition has a physical interpretation; if property ϕ increases in cell P , then it must also increase in the neighboring cells W and E . In practice, if the signs are not all equal, the solution exhibits oscillations in space (i.e., from cell to cell) in an unphysical manner. Such a solution typically oscillates from iteration to iteration as well for any given cell, and the iterative approach fails to determine a solution.

The condition related to diagonal dominance applies to most numerical methods commonly used in engineering, while the second one is a bit more subtle, and, in that it has important implications in CFD.

2.7.1.3. *Deriving conditions on spatial and temporal discretization*

Among the platitude of parameters that shape the convergence properties of the linear system as well as the accuracy of the numerical solution, the mesh size δx and time step size δt play an important role.

In principle, the mesh size and time step size should be refined (i.e., reduced) until the obtained numerical solution stops changing with any further refinements being performed. Such a solution is said to be mesh independent and time step independent. However, certain values of time step and mesh size are not guaranteed to yield a solution at all, as the iterative solution process might become unstable and diverge, rather than converge towards a well defined solution. This topic is broadly known as numerical stability analysis, and it deals with establishing valid ranges for these parameters that are necessary, but not necessarily sufficient, for convergence.

Some specific examples are presented to illustrate the overall logic and results of stability analysis. First, a steady state convection–diffusion problem for a quantity ϕ , spatially interpolated with a central differencing scheme is considered, i.e., in the form of Eq. (99). A viscous flow oriented along the 1D x axis is considered, so that $F_w > 0$ and $F_e > 0$. The continuity equation imposes $F_e - F_w = 0$ for every cell. In addition to this, it was previously stated that one of the conditions to be respected is that all matrix coefficients need to have the same sign. Recalling that the matrix coefficients for this case are given by Eq. (101)–Eq. (103), the following considerations can be made: $a_W = S_w (|c_\phi|_w / \delta x + F_w / 2)$, which is always positive. Thus, all other coefficients need to be positive. Conversely, for $a_E = S_e (|c_\phi|_e / \delta x - F_e / 2)$ to be positive it is required:

$$\frac{F_e \delta x}{|c_\phi|_e} < 2 \quad (134)$$

which need to hold true for all cells in the domain. By recalling the definition of face flux provided by Eq. (93) and considering that one cell's E face is the neighboring cell's W face, Eq. (134) can be better formulated as:

$$Pe_\phi = \frac{\rho u \delta x}{c_\phi} < 2 \quad (135)$$

where Pe_ϕ is the Peclet number of the convection–diffusion problem of quantity ϕ , meaning the ratio between the advective and diffusive components of the overall transport of quantity ϕ . Thus, a necessary condition for the stability of the solution algorithm when solving Eq. (99) via an iterative process is given by Eq. (135), for each mesh cell. Thus, returning to the original problem that deals with a given velocity field, Eq. (135) can be employed to derive the maximum allowable size of the mesh δx for the solution process to converge.

We now consider an unsteady 1D convection dominated flow with $F_w > 0$, $F_e > 0$ that is discretized spatially with an upwind scheme and temporally with a forward Euler (i.e., explicit) scheme. This would be equivalent to the model described by Eq. (118). However, an analogy can be drawn: as the stability of an implicit method (as iterations are performed) for each time step depends on the relationship between coefficients of neighboring cells in space (i.e., coefficients of ϕ_W and/or ϕ_E , depending on the spatial differencing scheme), the stability of an explicit method (as the time steps are advanced) depends on the coefficients of neighboring cells in time (i.e., the coefficient of ϕ_P^0 for a forward Euler scheme). This parallelism is represented in FIG. 13.

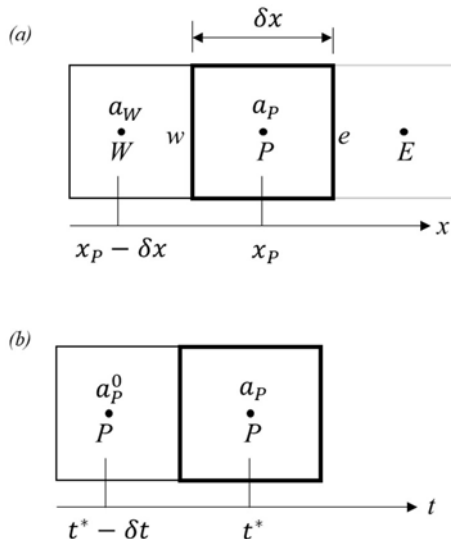


FIG. 13. (a) Representation of a neighbourhood of a cell P in space, and (b) and time. An upwind spatial discretization, only the upwind cell W is highlighted in the spatial neighbourhood case. In the temporal neighbourhood case, the case is spatially the same (cell P) but seen at two different moments in time, with different associated coefficients.

A criterion necessary but not sufficient for the stability of an explicit scheme as new solutions are obtained for each new time step t^* is that the coefficients that multiply the different field values at different time steps (i.e., ϕ_P , ϕ_P^0 in this case) for any given cell all have the same sign. These coefficients consist of a_P given by Eq. (120), which is always positive, so that a_P^0 given by Eq. (121) needs to be always positive as well for the criterion to hold. This results in:

$$V \frac{\rho}{\delta t} - S_e F_e - S_e |c_\phi|_e \frac{1}{\delta x} - S_w |c_\phi|_w \frac{1}{\delta x} > 0 \quad (136)$$

For the initially made assumption that the transport is dominated by convection (i.e., that $F_f \gg |c_\phi|_f$ everywhere in the domain), and by generalizing for any face f , Eq. (136) reduces to:

$$S_f F_f < V \frac{\rho}{\delta t} \quad (137)$$

By recalling the definition of face flux F_f given by Eq. (93) as well by defining a characteristic dimension $L = V/S_f$ for the fluid flow, it follows:

$$Co = \frac{u \delta t}{L} < 1 \quad (138)$$

which constitutes the definition of Courant number Co as well as a necessary (but not sufficient) condition, also known as the Courant–Friedrichs–Lowy condition, for the stability of an explicit solution scheme with a forward Euler approach. For the case of a mesh where all the cell surface areas S_f are equal, then $L = \delta x$, and for the case in which that does not hold, the mesh size δx is still a good approximation of the characteristic size L . This condition sets a maximum value on the allowable time step size δt for any choice of mesh size δx , and this constraint can often be quite severe for explicit solution approaches that seek a high spatial resolution. In cases wherein diffusive phenomena are not negligible, it can be shown that the constraints on the time step size are loosened, but Eq. (159) still represents a very useful indicator when choosing a particular time step for a simulation.

2.8. SOLUTION ALGORITHMS

This section focuses on the solution of Navier–Stokes equations describing fluid flow, namely the solution of the coupled systems of equations for mass conservation (continuity) and momentum conservation. For simplicity, the focus is on an incompressible, constant viscosity formulation of Navier–Stokes equations in their differential, conservation form, represented by Eq. (77) and Eq. (78) which are here repeated, however without any additional external momentum source terms:

$$\nabla \cdot \mathbf{u} = 0 \quad (139)$$

$$\frac{\partial}{\partial t} \rho \mathbf{u} + \nabla \cdot (\rho \mathbf{u} \otimes \mathbf{u}) = -\nabla p + \mu \nabla^2 \mathbf{u} \quad (140)$$

For simplicity, it is assumed that density is constant so that the advective term in the momentum equation can further be simplified as follows:

$$\nabla \cdot (\rho \mathbf{u} \otimes \mathbf{u}) = \rho \nabla \cdot (\mathbf{u} \otimes \mathbf{u}) = \rho (\mathbf{u} (\nabla \cdot \mathbf{u}) + \mathbf{u} \cdot (\nabla \mathbf{u})) = \rho \mathbf{u} \cdot (\nabla \mathbf{u}) \quad (141)$$

The kinematic viscosity ν is defined with:

$$\nu = \frac{\mu}{\rho} \quad (142)$$

so that the momentum equation can be now expressed as:

$$\frac{\partial}{\partial t} \mathbf{u} + \mathbf{u} \cdot (\nabla \mathbf{u}) = -\frac{1}{\rho} \nabla p + \nu \nabla^2 \mathbf{u} \quad (143)$$

The principal issue with the Navier–Stokes equations is that pressure p is not dependent variable to be solved (in Eq. (139) and Eq. (143)): the continuity relation is expressed in terms of velocity and the set of equations that does not contain an equation that could be explicitly

solved for the pressure. The approach to deal with such a problem is to solve the momentum and continuity equations sequentially and to enforce continuity through a derived equation for the pressure (effectively a pressure equation). This solution strategy is called a segregated solution approach in that it relies on sequential solution of the equations.

An effective pressure equation is derived by taking the divergence of the momentum equation. The momentum equation here considered contains numerical approximations of the differential operators and temporal derivative:

$$\frac{\mathbf{u} - \mathbf{u}^0}{\delta t} + \mathbf{u} \cdot (\nabla_n \mathbf{u}) = -\frac{1}{\rho} \nabla_n p + \nu \nabla_n^2 \mathbf{u} \quad (144)$$

where subscript n denotes numerical approximation of the differential operators and the temporal derivative is approximated with the Euler scheme. In this form, the equation does not imply errors due to the yet unspecified segregated procedure used to solve it and is referred to as the exact equation even though it is expressed in terms of numerical approximations of its component terms. By taking the divergence of Eq. (144) it follows:

$$\begin{aligned} \nabla \cdot \left(\frac{\mathbf{u} - \mathbf{u}^0}{\delta t} + \mathbf{u} \cdot (\nabla_n \mathbf{u}) \right) &= \nabla \cdot \left(-\frac{1}{\rho} \nabla_n p + \nu \nabla_n^2 \mathbf{u} \right) \\ \rightarrow \frac{\nabla_n \cdot \mathbf{u} - \nabla_n \cdot \mathbf{u}^0}{\delta t} + \nabla_n \cdot (\mathbf{u} \cdot (\nabla_n \mathbf{u})) &= -\frac{1}{\rho} \nabla_n \cdot (\nabla_n p) + \nu \nabla_n^2 (\nabla_n \cdot \mathbf{u}) \end{aligned} \quad (145)$$

Since $\nabla_n \cdot \mathbf{u} = 0$ and $\nabla_n \cdot \mathbf{u}^0 = 0$, and considering that $\nabla_n \cdot (\nabla_n p) = \nabla_n^2 p$, Eq. (145) becomes:

$$\nabla_n^2 p = -\rho (\nabla_n \cdot (\mathbf{u} \cdot \nabla_n \mathbf{u})) \quad (146)$$

2.8.1. Solution algorithms of practical importance

The rationale behind segregated solution methods is to enforce continuity $\nabla_n \cdot \mathbf{u} = 0$ via generating an effective equation for the pressure. The pressure calculated via solving such an effective pressure equation is used to correct the velocity and therefore enforce that the velocity so corrected satisfies continuity. Segregated solutions methods are illustrated here using a popular solution algorithm, the semi-implicit method for pressure linked equations (SIMPLE) [5], as an example. Historically, the SIMPLE method is the first of a numerous group of segregated solution algorithms based on the same principle, often referred to as the SIMPLE family of methods. Another important method of the SIMPLE family is the pressure implicit with splitting of operators (PISO) method [6], which is described next.

The core idea of the SIMPLE method can be summarized with the following steps:

1. Use a guess value for the pressure field p^* to solve a momentum equation in the form of Eq. (144). This step is called velocity predictor as it yields a velocity \mathbf{u}^* that is not guaranteed to satisfy the continuity equation, namely $\nabla_n \cdot \mathbf{u} = 0$.
2. Construct a pressure equation from the continuity equation and solve it to yield a pressure field p .
3. Use the new pressure field to correct the velocity with a correction term \mathbf{u}' so to have a velocity $\mathbf{u}^{**} = \mathbf{u}^* + \mathbf{u}'$. This step is called velocity corrector.

4. Repeat the process starting from the first step (step 1.) until the convergence criteria are met.

This whole set of steps is repeated for each time step, although it should be stressed out that the SIMPLE method was originally devised for steady state scenarios. The following is a discussion in greater details regarding each of these steps.

The idea behind the velocity predictor is to solve an equation in the following form:

$$\frac{\mathbf{u}^* - \mathbf{u}^0}{\delta t} + \hat{\mathbf{u}} \cdot (\nabla_n \mathbf{u}^*) = -\frac{1}{\rho} \nabla_n \hat{p} + \nu \nabla_n^2 \mathbf{u}^* \quad (147)$$

where quantities under the hat symbol $\hat{\cdot}$ represent the latest available values or a guess value. The advective term uses the latest available velocity $\hat{\mathbf{u}}$ so that it can be linearized with respect to \mathbf{u}^* . The solution of Eq. (147) yields \mathbf{u}^* which is not guaranteed to satisfy continuity. Thus, the next step is to find a pressure correction p' such that the pressure field $p^* = \hat{p} + p'$ gives rise to a velocity field $\mathbf{u}^{**} = \mathbf{u}^* + \mathbf{u}'$ that does satisfy $\nabla_n \cdot \mathbf{u}^{**} = 0$. Ideally, the field also satisfies the momentum equation, such that:

$$\frac{\mathbf{u}^{**} - \mathbf{u}^0}{\delta t} + \mathbf{u}^{**} \cdot (\nabla_n \mathbf{u}^{**}) = -\frac{1}{\rho} \nabla_n p^* + \nu \nabla_n^2 \mathbf{u}^{**} \quad (148)$$

However, as the difference between \mathbf{u}^{**} and \mathbf{u}^* diminishes as iterations are performed (as the solutions progresses towards convergence), it proves to be more useful to require \mathbf{u}^{**} to satisfy a slightly modified version of the momentum conservation equation:

$$\frac{\mathbf{u}^{**} - \mathbf{u}^0}{\delta t} + \hat{\mathbf{u}} \cdot (\nabla_n \mathbf{u}^*) = -\frac{1}{\rho} \nabla_n p^* + \nu \nabla_n^2 \mathbf{u}^* \quad (149)$$

The reason why this requirement is deemed useful is that it enables to derive an explicit equation that relates the velocity correction \mathbf{u}' and the pressure correction p' . By subtracting Eq. (147) from Eq. (149) it is obtained:

$$\frac{\mathbf{u}^{**} - \mathbf{u}^*}{\delta t} = -\frac{1}{\rho} \nabla_n (p^* - \hat{p}) \quad (150)$$

This result is used to compute the velocity correction $\mathbf{u}' = \mathbf{u}^{**} - \mathbf{u}^*$ from the pressure correction $p' = p^* - \hat{p}$, in the step 3. of the algorithm, while the pressure correction itself is computed from a pressure equation constructed from taking the divergence of both sides of Eq. (150) while considering that $\nabla_n \cdot \mathbf{u}^{**} = 0$, so that:

$$\begin{aligned} \nabla_n \cdot \left(\frac{\mathbf{u}^{**} - \mathbf{u}^*}{\delta t} \right) &= \nabla_n \cdot \left(-\frac{1}{\rho} \nabla_n (p^* - \hat{p}) \right) \rightarrow \\ \nabla_n^2 (p^* - \hat{p}) &= \frac{\rho}{\delta t} \nabla_n \cdot \mathbf{u}^* \end{aligned} \quad (151)$$

This is the pressure correction equation that is solved at step 2. to obtain $p' = p^* - \hat{p}$. Thus, the algorithm that is executed at every time step may be more accurately formulated as:

1. Use the latest available pressure field \hat{p} to solve Eq. (147) for \mathbf{u}^* , which does not in principle satisfy the continuity equation.
2. Use \mathbf{u}^* to solve a pressure correction equation in the form of Eq. (151) for $p' = p^* - \hat{p}$.
3. Use the pressure correction p' to compute the velocity correction \mathbf{u}' via Eq. (150), which is used to correct the velocity $\mathbf{u}^{**} = \mathbf{u}^* + \mathbf{u}'$ that is divergence-free.
4. Repeat the process starting from step 1. Until some convergence criteria are met. The final velocity and pressure distributions are given by \mathbf{u}^{**} and p^* , respectively.

Many iterations of the loop are required within every time step; therefore, the SIMPLE method is often referred to as an iterative method. For steady problems, an under relaxation parameter replaces the time step. The underrelaxation parameter has no physical meaning and its value is typically set to the largest value that guarantees stability of the SIMPLE procedure to maximize the computational speed.

Finally, while the incompressible, constant viscosity formulation used for illustration purposes to describe the algorithm, the SIMPLE method can be adopted for the simulation of any flow type.

2.8.2. Pressure implicit with splitting of operator method

The principal issue with the SIMPLE method concerns typically slow convergence of the $\nabla_n \cdot \mathbf{u}^*$ term in the pressure correction equation, Eq. (151), which should vanish as the iterations are performed within each time step. It should vanish as, ultimately, for a converged solution one has $\mathbf{u}^{**} \approx \mathbf{u}^*$ within a certain tolerance, and \mathbf{u}^{**} satisfies continuity by construction, namely that $\nabla_n \cdot \mathbf{u}^{**} = 0$. In practice, the term $\nabla_n \cdot \mathbf{u}^*$, arises in the pressure correction equation, Eq. (151), from the fact that the momentum equation for \mathbf{u}^{**} that is used for its construction, Eq. (149), uses the precited velocity \mathbf{u}^* , which does not satisfy continuity, for the formulation of the advective and diffusive terms.

To further illustrate why this is a problem, it can be useful to build a pressure equation for p^* and compare it with the exact pressure equation, Eq. (146). By taking the divergence of the Eq. (149) and considering $\nabla_n \cdot \mathbf{u}^{**} = 0$ it follows:

$$\begin{aligned} \nabla \cdot \left(\frac{\mathbf{u}^{**} - \mathbf{u}^0}{\delta t} + \hat{\mathbf{u}} \cdot (\nabla_n \mathbf{u}^*) \right) &= \nabla \cdot \left(-\frac{1}{\rho} \nabla_n p^* + \nu \nabla_n^2 \mathbf{u}^* \right) \\ \rightarrow \frac{\nabla_n \cdot \mathbf{u}^{**} - \nabla_n \cdot \mathbf{u}^0}{\delta t} + \nabla_n \cdot (\hat{\mathbf{u}} \cdot (\nabla_n \mathbf{u}^*)) &= -\frac{1}{\rho} \nabla_n \cdot (\nabla_n p^*) + \nu \nabla_n^2 (\nabla_n \cdot \mathbf{u}^*) \rightarrow \quad (152) \\ \rightarrow \nabla_n^2 p^* &= \frac{\rho}{\delta t} (\nabla_n \cdot (\hat{\mathbf{u}} \cdot (\nabla_n \mathbf{u}^*))) - \nu \nabla_n^2 (\nabla_n \cdot \mathbf{u}^*) \end{aligned}$$

Compared to the exact pressure equation, namely Eq. (146), the previous equation contains the $-\nu \nabla_n^2 (\nabla_n \cdot \mathbf{u}^*)$ term, which tends to 0 as iterations progress, but its presence can increase the overall number of iterations required to reach convergence within a time step. This is a limitation of the SIMPLE approach.

The idea behind the PISO approach is to take the overall logic of the SIMPLE approach, but to construct further corrections to the velocity and pressure fields. The reason why this is advantageous is now illustrated. A further set of corrected fields is defined as velocity $\mathbf{u}^{***} =$

$\mathbf{u}^{**} + \mathbf{u}''$ and pressure $p^{**} = p^* + p''$. Just as \mathbf{u}^{**} is constructed so that $\nabla_n \cdot \mathbf{u}^{**} = 0$, \mathbf{u}^{***} is also constructed so to enforce $\nabla_n \cdot \mathbf{u}^{***} = 0$. In a similar manner, this is done by constructing a momentum equation for \mathbf{u}^{***} in the same way as for \mathbf{u}^{**} :

$$\frac{\mathbf{u}^{***} - \mathbf{u}^0}{\delta t} + \hat{\mathbf{u}} \cdot (\nabla_n \mathbf{u}^{**}) = -\frac{1}{\rho} \nabla_n p^{**} + \nu \nabla_n^2 \mathbf{u}^{**} \quad (153)$$

There is a formal equivalence between Eq. (153) (i.e., the momentum equation for \mathbf{u}^{***}) and Eq. (149) (i.e., the momentum equation for \mathbf{u}^{**}). However, and this is the crucial aspect of the PISO approach, \mathbf{u}^{**} in Eq. (153) satisfies continuity by construction, while \mathbf{u}^* in Eq. (149) does not. Thus, to construct a pressure equation for p^{**} by taking the divergence of Eq. (153), a pressure equation is then obtained in the following form:

$$\nabla_n^2 p^{**} = \frac{\rho}{\delta t} (\nabla_n \cdot (\hat{\mathbf{u}} \cdot (\nabla_n \mathbf{u}^{**})) - \nu \nabla_n^2 (\nabla_n \cdot \mathbf{u}^{**})) = \frac{\rho}{\delta t} \nabla_n \cdot (\hat{\mathbf{u}} \cdot (\nabla_n \mathbf{u}^{**})) \quad (154)$$

which, unlike Eq. (157), is formally equivalent to the exact pressure equation defined by Eq. (146). Practical consequence of this, due to the absence of terms such as $-\nu \nabla_n^2 (\nabla_n \cdot \mathbf{u}^{**})$ that slowly converge to 0, is that having a second pressure correction and velocity correction step after the first one can significantly reduce the number of iterations required to reach convergence within each time step. Historically, it is important to note that it is precisely the PISO algorithm that enabled feasible transient (i.e., unsteady) simulations.

The relationship between the second velocity correction \mathbf{u}'' and the second pressure correction p'' , as well as the second pressure correction equation is derived as follows. The relationship between the correction fields is obtained by subtracting the momentum equation for \mathbf{u}^{**} , Eq. (149) from the momentum equation for \mathbf{u}^{***} , Eq. (153):

$$\frac{\mathbf{u}^{***} - \mathbf{u}^{**}}{\delta t} + \hat{\mathbf{u}} \cdot (\nabla_n \mathbf{u}') = -\frac{1}{\rho} \nabla_n (p^{**} - p^*) + \nu \nabla_n^2 \mathbf{u}' \quad (155)$$

This equation relates the second pressure correction field $\mathbf{u}'' = \mathbf{u}^{***} - \mathbf{u}^{**}$ to the second pressure correction field $p'' = p^{**} - p^*$ and is explicit in \mathbf{u}'' as all other fields are known.

To derive the pressure correction equation, a divergence of Eq. (155) in combination with $\nabla_n \cdot \mathbf{u}^{***} = 0$ and $\nabla_n \cdot \mathbf{u}^{**} = 0$ leads to:

$$\nabla_n^2 (p^{**} - p^*) = \rho \nabla_n \cdot (\nu \nabla_n^2 \mathbf{u}' - \hat{\mathbf{u}} \cdot (\nabla_n \mathbf{u}')) \quad (156)$$

The PISO algorithms with two corrector steps can be now fully described. The first three steps are the same as for the SIMPLE algorithm:

1. Use the latest available pressure field \hat{p} to solve Eq. (147) for \mathbf{u}^* , which does not in principle satisfy the continuity equation.
2. Use \mathbf{u}^* to solve the first pressure correction equation in the form of Eq. (151) for $p' = p^* - \hat{p}$.
3. Use the pressure correction p' to compute the velocity correction \mathbf{u}' via Eq. (150), which is used to correct the velocity $\mathbf{u}^{**} = \mathbf{u}^* + \mathbf{u}'$ that is divergence-free.
4. Use \mathbf{u}' to solve the second pressure correction equation in the form of Eq. (161) for $p'' = p^{**} - p^*$.

5. Use the pressure correction p'' to compute the velocity correction \mathbf{u}'' via Eq. (155), which is used to correct the velocity $\mathbf{u}^{***} = \mathbf{u}^{**} + \mathbf{u}''$.
6. Repeat the process starting from step 1. until some convergence criteria are met. The final velocity and pressure distributions are given by \mathbf{u}^{***} and p^{**} respectively.

The PISO algorithm can be expanded to any number of correction steps, generally called PISO iterations. This is achieved by repeating steps 4., and 5. an arbitrary number of times by setting $\mathbf{u}' = \mathbf{u}''$, $\mathbf{u}^{**} = \mathbf{u}^{***}$ $p^* = p^{**}$ after the end of step 6., before the start of step 5.

2.8.3. Conclusive remarks

It was demonstrated [6] that two PISO steps are in practice sufficient to drive the error introduced by the PISO procedure to a small enough value i.e., to an amount no larger than that the discretization error associated with the temporal derivative. Due to such an attractive feature, the PISO method enables a drastic reduction of computation times compared to the SIMPLE method. Similar segregated solution algorithms [7] e.g., SIMPLER, PRESTO, etc., are developed by combining different aspects of fundamental SIMPLE and PISO approaches. As the basic principle of the segregated solution strategy is originally laid out by the SIMPLE method of Patankar, segregated solution algorithms are often referred to as the SIMPLE family of methods. Merged PISO–SIMPLE (PIMPLE) is the name given to the popular PISO implementation available in many CFD solvers in the popular OpenFOAM library of CFD analysis. As a further example, recent versions of the STAR–CCM+ code offer an implementation of the PISO method for some applications.

Choice of the appropriate solution algorithm depends on the specific problem under consideration. For steady state problems, the performance of the SIMPLE method with under relaxation is often comparable to the PISO method. For unsteady problems, the SIMPLE method requires a very large number of iterations, when compared to the PISO approach to attain accuracy within a time step, which makes the method unsuitable for time dependent simulation, wherein the PISO approach is preferred. Drastic reduction of simulation times that can be attained by using the PISO method effectively enabled realistic scale resolving time dependent simulation, such as large eddy simulations or pseudo–direct numerical simulation, and their application to industrially relevant flows in complex geometries. In this context, the success of PISO based solution methodologies available in actual CFD codes is at least in part due to implementations of the PISO method specific to the various solvers available in the OpenFOAM CFD toolbox.

3. FUNDAMENTALS OF TURBULENCE MODELLING – FROM REYNOLDS AVERAGED NAVIER STOKES TO DIRECT NUMERICAL SIMULATION

This chapter describes the turbulence modelling, and it is focused on RANS and unsteady RANS (URANS) modelling. It covers the basics of turbulence and turbulent flows and describes different types of turbulent flows. Prediction methods used to predict such flows are described. The RANS/URANS approach is discussed in detail as well as various turbulence models used to close the governing equations of RANS/URANS modelling.

3.1. INTRODUCTION TO TURBULENCE AND TURBULENT FLOWS

Mostly fluid flows are turbulent. The transport and mixing of matter, momentum, and heat in a fluid flow is of prime importance in many industrial engineering applications and turbulence

considerably improves the rates of these processes. This motivates engineers to study turbulent flows. In turbulent flows, there exist the continuous mixing of adjacent layers of the fluid. The mixing of fluid elements from different mean velocity layers causes the net momentum transfer which is far more effective as compared to the transfer resulting from viscous stresses. Subsequently, in a turbulent flow, the mean velocity profile becomes more uniform.

There is no easy way to define turbulence. It is mostly described by investigating the dissipative and non local flow features at high Reynolds numbers including irregularity, diffusivity, and rotational features. It is a continuum phenomenon that is not a property of fluid but fluid flow. Unsteadiness, convection, production, diffusion, and dissipation are a few physical processes that are involved in turbulent flows [8].

In 1922, Richardson presented the energy cascade mechanism – a hypothesis that shows the characterization of turbulent flows at an infinite number of time and length scales. The eddies of different sizes also describe the turbulence. The sizes of eddies vary from the flow length scale L to the smallest eddies. There exists a characteristic velocity $u(l)$ and timescale $t(l) = u(l)/l$ of an eddy of length size l . The largest eddies exist at length scales near to the flow length scale L . Each eddy has a Reynold number and large eddies have large Reynold numbers hence negligible viscous effects. The smaller eddies gain energy produced from the breaking up of large eddies and then the smaller ones undergo the same disintegration and so on. This goes on and the energy cascades until the Reynold number is small enough that the eddies have stable motion and molecular viscosity causes energy dissipation i.e., energy is dissipated only by viscous effects. In 1941, Kolmogorov proposed the smallest energy dissipating scales in the flow. These are Kolmogorov length scale η , velocity scale u_η and time scale t_η and are calculated as follows:

$$\eta = \left(\frac{\nu^3}{\varepsilon} \right)^{0.25} \quad (157)$$

$$u_\eta = (\varepsilon \nu)^{0.25} \quad (158)$$

$$t_\eta = \left(\frac{\nu}{\varepsilon} \right)^{0.5} \quad (159)$$

The unsteady nature, the presence of a wide range of eddies, and its strong dependence on initial conditions make the computation of the turbulent flow a challenging task. Proper computational modelling requires addressing all these features.

3.1.1. Types of turbulent flows

Turbulent flows are mainly divided into three groups: boundary layers or wall bounded flows, shear layers, and grid generated turbulent flows. In wall bounded turbulent flows, near the wall is where most of the kinetic energy of a turbulent flow is produced. The wall bounded turbulent flows are often categorized into turbulent boundary layers or fully developed turbulent flows. A surface and a free stream bound turbulent boundary layers while in fully developed turbulent flows it is bounded by a wall e.g., channel or a pipe. In the case of turbulent shear layers, flow grows up in a streamwise direction and develops self preserving universal characteristics. This type of flow may be categorized into three different types i.e., free shear layers, jets, and wakes. Typical mean velocity profiles of shear flows are shown in Fig. 14.

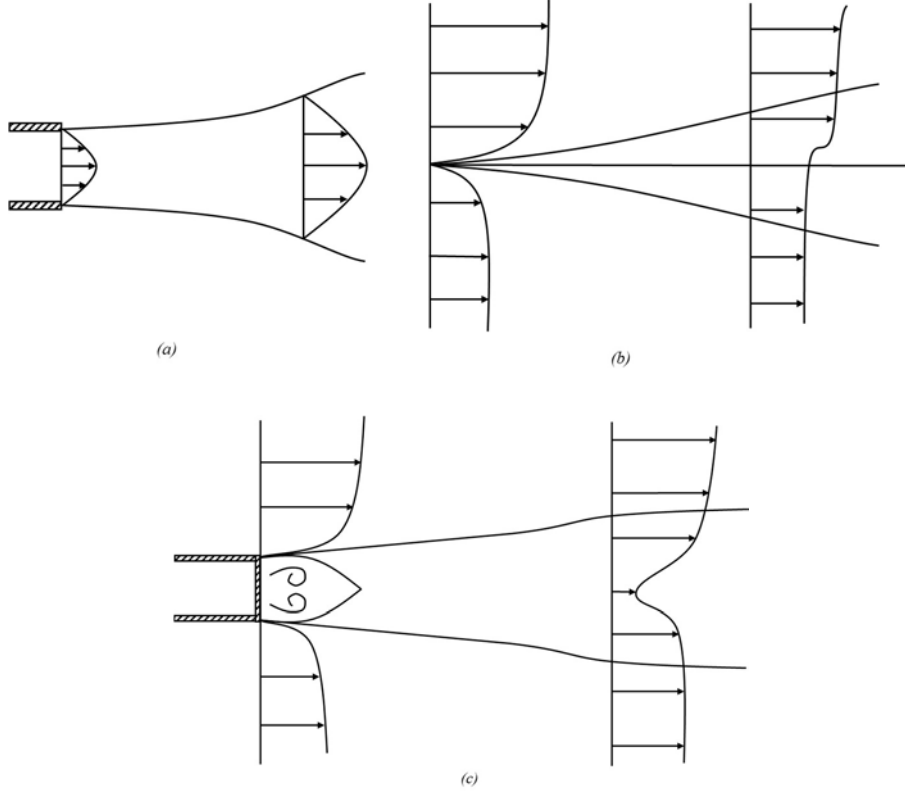


FIG. 14. Representation of three principal types of turbulent flows: (a) jet flow; (b) free shear layer flow; (c) wake flow (adapted from [8]).

3.1.2. Fundamental concepts of turbulent flows

Usually, a turbulent boundary layer is divided into regions and in each region, the turbulence behavior is described. The first region is a very thin layer of fluid near the surface that is known as a viscous sublayer and the second region is the outer layer where the fluid flow is turbulent, called a fully turbulent region. The region in between the two is referred to as a buffer zone. Turbulent flows are described by these three regions. The turbulent boundary layers can also be divided into inner and outer regions. The viscous sublayer, buffer zone, and a portion of the fully turbulent zone make up the inner region while the rest of the part lies in the outer region. To identify the various regions within the turbulent boundary layer, a non dimensional velocity u^+ and a normalized wall distance y^+ are defined as follows:

$$u^+ = \frac{u}{u_\tau} \quad (160)$$

$$y^+ = y \frac{u_\tau}{v} \quad (161)$$

where y is the real wall distance coordinate, v is fluid kinematic viscosity, and u_τ is frictional velocity defined with:

$$u_\tau = \sqrt{\frac{\tau_w}{\rho}} \quad (162)$$

where τ_w is the shear stress value at the wall. The normalized wall distance is useful for identifying different regions of the boundary layer flow. In particular, the region of the fluid

flow that lies within the $y^+ \leq 2\sim 8$ range is known as viscous sublayer, the one in the $2\sim 8 < y^+ < \sim 50$ range is known as a buffer zone, and in the $y^+ > \sim 50$ range is known as fully turbulent zone [9].

3.2. OVERVIEW OF PREDICTION METHODS FOR TURBULENT FLOWS

In CFD, different predication methods are used for computing turbulent flows. The most important ones consist of DNS, RANS, LES, and hybrid methods which consists of a blending of different approaches, such as RANS–LES hybrid methods.

3.2.1. Direct numerical simulation

Under the hypothesis of continuum, the Navier-Stokes equations solely can describe all fluid flows including turbulent flows. In DNS, time dependent Navier-Stokes equations are solved resolving all the spatial and turbulence temporal scales. If used as a technique for design and analysis, there are two challenges to consider. To solve complex problems at high Re numbers, current computers lack required memory and computational speed. The number of grid points has to be proportional to $Re^{0.75}$ in case of a 2D problem, while representing the fluid flows in 3D it needs to be proportional to $Re^{2.25}$. Parallel processing can be used to increase performance and computational speed. The other important challenge is to develop a solution algorithm without numerical error. This is related to selected grid system, numerical scheme, and boundary conditions. To use DNS, it is recommended to generate higher order grids and apply higher order numerical schemes. The use of DNS in practical problems is still limited. However, in transition and turbulent flows that are difficult to analyze experimentally, the DNS still provides useful data. Therefore, in understanding turbulence and its degree of practical applicability to problems of engineering interests, the DNS plays an important role [8].

3.2.2. Reynolds averaged Navier–Stokes

In the RANS, the technique decomposes solution variables in the Navier-Stokes equation into mean and fluctuating components with respect to time. As a result of this, some additional unknowns appear in the equations making the system of governing equation more complex to model. In order to close the system of governing equations, additional relations known as turbulence models are used.

3.2.3. Large eddy simulation

DNS method focusses on resolution of all scales of turbulence, whereas in RANS all scales are not directly resolved but modelled. Large eddy simulations provide a compromise between DNS and RANS. As most of the eddy energy is contained outside the dissipation range i.e., the smallest scales, the core idea of LES is to model these small scales that have universal characteristics while fully resolving the larger scales. In LES, large scales are resolved and the small scales (subgrid, i.e., smaller than the mesh cell size) are modeled. Sub grid scale models are used for sub grid turbulent scales and are applicable to an extensive range of flow regimes and are used for subgrid turbulent scales. Fig. 15 shows how the LES approach provides better results to resolve shorter length scales compared to RANS approach at the cost of more computational power.

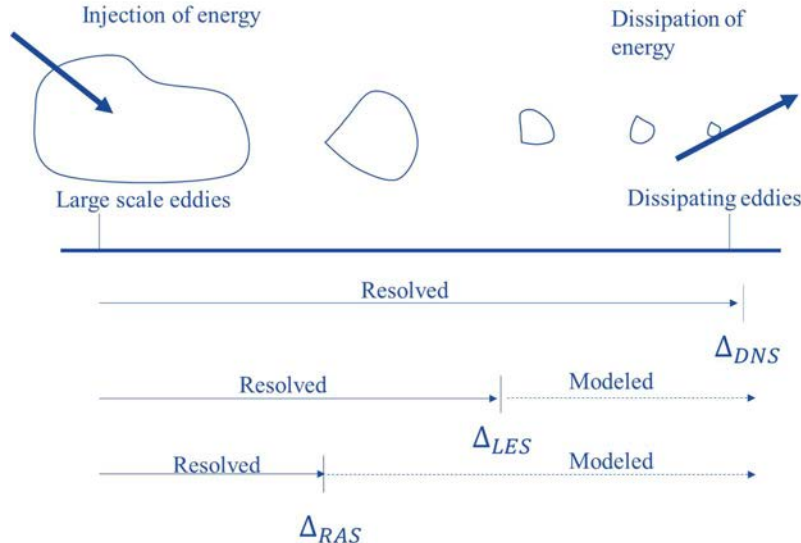


FIG. 15. Spatial ranges of what can be resolved versus what needs to be modelled for each type of turbulence modelling approach (conceived from [10]).

3.2.4. Hybrid approach

In a hybrid approach put forth by Spalart et al. [11] in 1997, regions with turbulent length scales less than the grid dimensions are solved using the RANS, and regions with length scales higher than the grid dimensions are solved using the LES. A suitable interface is used to switch between RANS and LES and therefore, cost of computing is therefore lower than LES.

3.3. REYNOLDS AVERAGED NAVIER–STOKES

To consider turbulence effects in flow fields, the governing equations of fluid flow are revised. The approach discussed here is how to obtain a set of governing equations that describe, and model turbulence based on the RANS approach. The application of this approach to the initial Navier–Stokes equations results in the so called RANS equations.

For simplicity, but without losing generality in the derivation, the constant density, constant viscosity, incompressible Navier–Stokes equations in their differential form, namely Eq. (77) and Eq. (78), are considered and formulated as follows:

$$\nabla \cdot \mathbf{u} = 0 \quad (163)$$

$$\frac{\partial}{\partial t} \mathbf{u} + \nabla \cdot (\mathbf{u} \otimes \mathbf{u}) = -\frac{1}{\rho} \nabla p + \nu \nabla^2 \mathbf{u} \quad (164)$$

As previously introduced, the idea behind Reynolds averaging is to first define each variable of interest ϕ in terms of a mean component $\bar{\phi}$ as well as a fluctuating component ϕ' . This is called Reynolds decomposition and consists of:

$$\phi(\mathbf{x}, t) = \bar{\phi}(\mathbf{x}, t) + \phi'(\mathbf{x}, t) \quad (165)$$

In the most general case, the mean component is given by an ensemble average operator $\bar{\phi} = \bar{\phi}^E$. The ensemble average assumes to conceptually perform an experiment under identical

conditions for a certain number of $N \rightarrow \infty$. Then, the ensemble average $\bar{\phi}^E(x, t)$ is the value that ϕ assumes at position x and time t averaged across all experimental realizations. Then, for the i -th realization with $\phi_i(x, t)$, it follows:

$$\bar{\phi}^E(x, t) = \lim_{N \rightarrow \infty} \frac{1}{N} \phi_i(x, t) \quad (166)$$

One can generally distinguish between steady flows and unsteady flows. These flows are distinguished based on the behavior of the ensemble average, such that steady flows are statistically steady in the sense that:

$$\frac{\partial}{\partial t} \bar{\phi}(x, t) = 0 \quad (167)$$

Conversely, unsteady flows do not necessarily satisfy Eq. (167) for all t and x . These two flow scenarios are illustrated in Fig. 16.

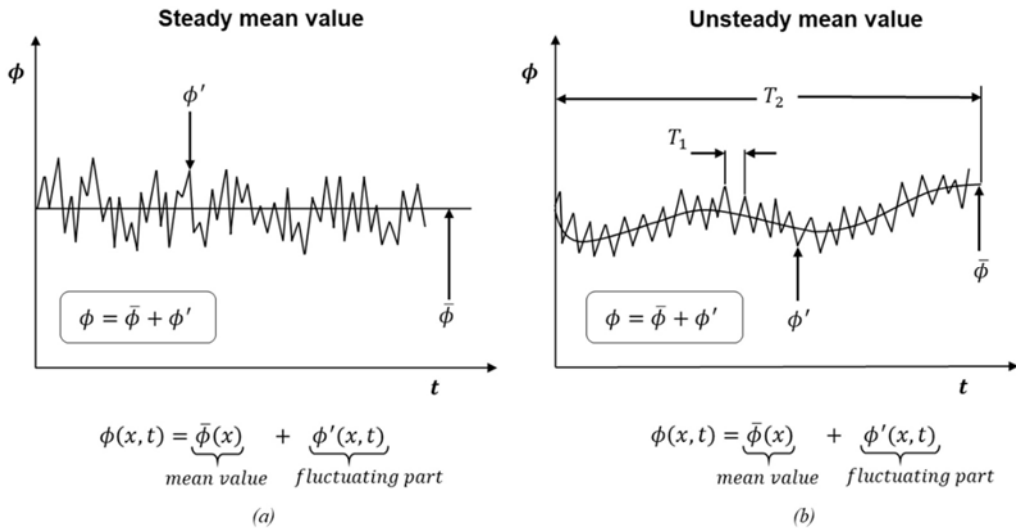


FIG. 16. Representation of (a) steady mean value and (b) unsteady mean values.

The equations obtained by applying the Reynolds decomposition and ensemble averaging to the equations governing an unsteady flow case are typically referred to as URANS equations. For completeness, it should be noted that in the steady case, the ensemble average corresponds to the time average $\bar{\phi}^E = \bar{\phi}^T$ so that:

$$\bar{\phi} = \bar{\phi}^E = \bar{\phi}^T(x) = \lim_{\Delta t \rightarrow \infty} \frac{1}{\Delta t} \int_0^{\Delta t} \phi(x, t) dt \quad (168)$$

The Reynolds averaging process relies on applying the ensemble averaging operator to all terms in the Navier–Stokes equations. As a consequence of the definition of such operator, for any two fields of interest ϕ and ψ , the following properties can be demonstrated:

$$\overline{\phi'} = 0 \quad (169)$$

$$\bar{\bar{\phi}} = \bar{\phi} \quad (170)$$

$$\overline{\bar{\phi} + \phi'} = \bar{\phi} \quad (171)$$

$$\overline{\phi + \psi} = \bar{\phi} + \bar{\psi} \quad (172)$$

$$\overline{\bar{\phi}\psi} = \bar{\phi}\bar{\psi} \quad (173)$$

$$\overline{\bar{\phi}\psi'} = 0 \quad (174)$$

$$\overline{\phi\psi} = \bar{\phi}\bar{\psi} + \overline{\phi'\psi'} \quad (175)$$

$$\overline{\phi'\psi'} \neq 0 \quad (176)$$

$$\overline{\phi'^2} \neq 0 \quad (177)$$

$$\overline{\frac{\partial}{\partial x}\phi} = \frac{\partial}{\partial x}\bar{\phi} \quad (178)$$

$$\int \phi dx = \int \bar{\phi} dx \quad (179)$$

It is significant to point out that the products of fluctuating terms do not average out to zeros in general. In fact, these are very relevant for turbulent flow modelling because of velocity fluctuations. Reynolds decomposition when applied to two unknowns, the velocity \mathbf{u} and pressure p in the Navier–Stokes equations represented by Eq. (163), Eq. (164) lead to:

$$\mathbf{u} = \bar{\mathbf{u}} + \mathbf{u}' \quad (180)$$

$$p = \bar{p} + p' \quad (181)$$

By applying the averaging operator to the Navier–Stokes equations it follows:

$$\nabla \cdot \bar{\mathbf{u}} = 0 \quad (182)$$

$$\frac{\partial}{\partial t} \bar{\mathbf{u}} + \nabla \cdot (\bar{\mathbf{u}} \otimes \bar{\mathbf{u}}) = -\frac{1}{\rho} \nabla \bar{p} + \nu \nabla^2 \bar{\mathbf{u}} + \frac{1}{\rho} \nabla \cdot \boldsymbol{\tau}_R \quad (183)$$

These equations are collectively known as the URANS equations when $\partial \bar{\mathbf{u}} / \partial t \neq 0$, and RANS equations otherwise. However, this use of the acronyms is not strict, and it is not unusual to encounter the URANS equations being called RANS equations. There are several differences between the RANS equation and the original Navier–Stokes equations, Eqs. (163) and (164) defined earlier. In the RANS equations, all the variables are (ensemble) averaged variables. In addition, the RANS equations give rise to an additional term in the momentum equations, namely the divergence of what is known as Reynolds stress $\boldsymbol{\tau}_R$. Physically, it represents macroscopic momentum exchange due to turbulence and can be interpreted as an additional shear stress, often called turbulent shear stress, as:

$$\boldsymbol{\tau}_R = \rho(\overline{\mathbf{u}' \otimes \mathbf{u}'}) = \rho \begin{bmatrix} \overline{u'_x u'_x} & \overline{u'_x u'_y} & \overline{u'_x u'_z} \\ \overline{u'_y u'_x} & \overline{u'_y u'_y} & \overline{u'_y u'_z} \\ \overline{u'_z u'_x} & \overline{u'_z u'_y} & \overline{u'_z u'_z} \end{bmatrix} \quad (184)$$

Reynolds stress fundamentally adds additional unknowns to the governing equations and has to be modelled in a way to close the system of RANS equations. Thus, additional relations known as turbulence models are used to complete the system of governing equations. These models use empirical constants derived from trials to connect the fluctuating variables with the

mean flow quantities. The RANS equations can be closed using two different categories of models, namely eddy viscosity models and Reynolds stress models.

3.3.1. Eddy viscosity models

Eddy viscosity models employ the Boussinesq approximation to relate the Reynolds stress $\boldsymbol{\tau}_R$ to the mean velocity gradients $\nabla \bar{\mathbf{u}}$, initially proposed by Boussinesq in 1877 [12]. This approximation states that the Reynolds stress is proportional to the mean strain rate tensor $\nabla \bar{\mathbf{u}} + (\nabla \bar{\mathbf{u}})^T$, multiplied by a constant which is known as eddy viscosity or turbulent viscosity μ_T . This hypothesis is like the one made when considering Newtonian fluids where the shear stresses are proportional to shear strain rate i.e., velocity gradient. The Boussinesq approximation simplifies the turbulence modelling and instead of having separate equations for the different components of the Reynolds stress, it determines the appropriate value of eddy viscosity or turbulent viscosity μ_T (and a kinematic turbulent viscosity $\nu_T = \mu_T/\rho$). It is important to note that turbulent viscosity is not a fluid property, rather, it is an artificial property of the flow which is devised to model the effects of turbulence. Mathematically, the Reynolds stress can be related with the mean strain rate tensor using the Boussinesq approximation as follows:

$$\boldsymbol{\tau}_R = -\rho(\bar{\mathbf{u}}' \otimes \bar{\mathbf{u}}') = \mu_T \left(\nabla \bar{\mathbf{u}} + (\nabla \bar{\mathbf{u}})^T - \frac{2}{3} \rho k \mathbb{I} \right) \quad (185)$$

or, in cartesian notation for the i, j component of $\boldsymbol{\tau}_R$:

$$\tau_{R,ij} = -\rho \bar{u}_i \bar{u}_j = \mu_T \left(\frac{\partial \bar{u}_i}{\partial x_j} + \frac{\partial \bar{u}_j}{\partial x_i} \right) - \frac{2}{3} k \delta_{ij} \quad (186)$$

where k is the turbulent kinetic energy, defined with:

$$k = \frac{1}{2} \bar{\mathbf{u}}' \cdot \bar{\mathbf{u}}' \quad (187)$$

Eddy viscosity models give reasonable results for large number of problems and require less computational power. The main downside of such models is to model μ_T as an isotropic scalar quantity which might not be always convenient. Eddy viscosity models are cornerstone of turbulence modelling and help in the computation of μ_T . The turbulence model is useful if it assures its wide applicability with accurate results and is enough simple for economical runs. From algebraic equations to systems partial differential equations to be solved, these models vary in terms of the degree of sophistication. The most common categories of models are the so called algebraic models (or zero equation models), one equation models and the two equations models. The number of equations signifies the number of additional partial differential equations to be solved.

3.3.1.1. Algebraic models

The turbulent fluctuating correlations are related to the mean flow field variables through the algebraic relations. The key assumption is that the local production rate and the dissipation rate of turbulence are equal (approximately). These do not include the convective transport of turbulence, which is conflicting to the physics of most flow fields since the of the flow history need to be considered. However, these models are mathematically simple, easy to implement,

and provide good predictions for simple flows where experimental correlations for mixing length exist. The Baldwin–Lomax model and the Cebeci–Smith model are used frequently for the external flow applications [8].

3.3.1.2. One equation models

These models typically solve a partial differential equation for turbulent kinetic energy k , whereas the turbulent viscosity μ_T is given by an algebraic relation involving turbulent kinetic energy as well as length scale l , which is specified algebraically. This length scale is generally assumed to be proportional to e.g., the thickness of the boundary layer, the width of a jet or a wake. The turbulent viscosity is thus typically modelled as:

$$\mu_T = \rho k^{0.5} l \quad (188)$$

The main disadvantage of this model is that it is not applicable to general flows since it is not likely to always find an algebraic expression for a length scale. The specific form of the transport equation for turbulent kinetic energy varies from model to model but it generally contains convective and diffusive transport as well as production and dissipation terms. This model is applicable to attached wall bounded flows, and the flows with mild separation recirculation. The Spalart–Allmaras model is the example of a one equation model [8].

3.3.1.3. Two equation models

Two equation turbulence models are presently the most used models in industrial applications as these overcome some of the previously illustrated limitations of the algebraic and one equation models. This is done by solving two additional transport equations for certain turbulence properties. Such properties generally consist of turbulent kinetic energy k and turbulent kinetic energy dissipation rate that is modelled either in absolute terms (ε , in J/kg/s) or specific terms (ω , in s⁻¹). In fluid mechanics applications, complex flow fields occur frequently. These include separated flows, unsteady flows as well as flows concerning multiple length scales. To better understand the physics of these complex flows, there exist two equation models. As for the previous models, many declinations of two equation models exist. Hereby, an overview of the most important two equation turbulence models is provided [8].

Whenever partial differential equations are to be solved, the boundary conditions need to be provided. One non-trivial issue that is faced by both one and two equation turbulence models is the specification of boundary conditions for the solved turbulence quantities at domain walls. Physically, the flow in the immediate vicinity of the wall is always viscous (as the viscous sublayer is the first layer in the wall vicinity regardless of the flow conditions in the bulk), meaning that there are no turbulent features in these regions. Setting appropriate boundary conditions might not be a problem for certain turbulence quantities (such as turbulence kinetic energy, which is physically null at the wall), but it might well be a problem for other quantities (such as turbulence dissipation rate ε). Additionally, as what happens nearby domain walls is crucial for the generation and dissipation of turbulence, one would in principle desire a computational domain that is able to fully resolve the near wall region (i.e., the full spatial domain represented in FIG. 15). However, this would generally lead to very large and dense computational meshes, thus leading to very large (possibly prohibitively so) computational costs. To circumvent both issues, RANS models typically employ so called wall functions. The idea is to avoid using prohibitively fine meshes in the near wall region, and to model what happens in between the mesh cell centres of the mesh cells that are adjacent to domain walls

and the domain walls themselves via a model as depicted in FIG. 15. However, care is generally required as the value of the y^+ coordinate of the boundary cell centers (which is not an exclusively geometric property but depends on flow properties as well) generally imposes the constraints on the usability of certain wall functions over the others.

Standard $k-\varepsilon$ model

The standard $k-\varepsilon$ model is a semi empirical model treating the turbulence kinetic energy k and its dissipation rate ε through transport equations. The transport equation for k is derived from mathematically exact transport equation, while the transport equation for ε contains additional empirically informed terms. In the derivation of the standard $k-\varepsilon$ model, it is assumed that the flow is completely turbulent, and molecular viscosity effects are insignificant [8]. The turbulent kinetic energy and its dissipation rate are governed by, [12]:

$$\frac{\partial}{\partial t} k + \nabla \cdot (\mathbf{u}k) = \boldsymbol{\tau}_R : \nabla \mathbf{u} - \varepsilon + \nabla \cdot \left(\left(\nu + \frac{\nu_T}{\sigma_k} \right) \nabla k \right) \quad (189)$$

$$\frac{\partial}{\partial t} \varepsilon + \nabla \cdot (\mathbf{u}\varepsilon) = C_{\varepsilon 1} \frac{\varepsilon}{k} \boldsymbol{\tau}_R : \nabla \mathbf{u} - C_{\varepsilon 2} \frac{\varepsilon^2}{k} + \nabla \cdot \left(\left(\nu + \frac{\nu_T}{\sigma_\varepsilon} \right) \nabla \varepsilon \right) \quad (190)$$

These equations are semi empirical and depend on empirical constants, which for the standard $k-\varepsilon$ model are $C_{\varepsilon 1} = 1.44$, $C_{\varepsilon 2} = 1.92$, $\sigma_k = 1.0$, $\sigma_\varepsilon = 1.3$. The closure relation that relates the turbulence kinetic energy to the turbulent kinematic viscosity ν_T is:

$$\nu_T = \frac{C_\mu k^2}{\varepsilon} \quad (191)$$

with $C_\mu = 0.09$ being a further empirical constant. We recall that the turbulent viscosity μ_T and kinematic turbulent viscosity are related by $\mu_T = \rho \nu_T$. Furthermore, the turbulence time scale (equivalent to the specific dissipation rate ω) and length scale l are defined as follows:

$$\omega = \frac{\varepsilon}{C_\mu k} \quad (192)$$

$$l = C_\mu \frac{k^{3/2}}{\varepsilon} \quad (193)$$

The standard $k-\varepsilon$ model is the most used turbulence model in industrial applications. In this model, the parameters are calibrated by utilizing data from the experiments. This model is robust and reasonably accurate for wide range of problems. However, it performs poorly for flows with larger pressure gradients, strong separation, and high swirling components. Furthermore, in regions of large strain rate, production of kinetic energy is excessive which can result in inaccurate model predictions.

Low Reynolds number $k-\varepsilon$ model

The difficulty with the standard $k-\varepsilon$ model is that equations become numerically unstable when the computational domain resolves the near wall region without the use of wall functions. Direct integration of the $k-\varepsilon$ equations for the viscous sublayer to the wall provides a better approach to overcoming that difficulty. Several revisions are introduced in the standard $k-\varepsilon$ model to allow the integration to the wall and to enhance its capability. The revised equations are called

the low Reynolds number $k-\varepsilon$ equations. The first model of this kind was formulated by Jones and Launder and later it was modified by several researchers. The low Reynolds number $k-\varepsilon$ model for a constant density case is written as follows [8].

$$\frac{\partial}{\partial t} k = \boldsymbol{\tau}_R : \nabla \mathbf{u} + L_k - \varepsilon + \nabla \cdot \left(\left(\nu + \frac{\nu_T}{\sigma_k} \right) \nabla k \right) \quad (194)$$

$$\frac{\partial}{\partial t} \varepsilon = C_{\varepsilon 1} \frac{\varepsilon}{k} f_1 \boldsymbol{\tau}_R : \nabla \mathbf{u} + L_\varepsilon - C_{\varepsilon 2} \frac{\varepsilon^2}{k} f_2 + \nabla \cdot \left(\left(\nu + \frac{\nu_T}{\sigma_\varepsilon} \right) \nabla \varepsilon \right) \quad (195)$$

with the same coefficients as the standard $k-\varepsilon$ model and:

$$\nu_T = \frac{f_\mu C_\mu k^2}{\varepsilon} \quad (196)$$

$$f_1 = 1 \quad (197)$$

$$f_2 = 1 - 0.3 e^{-Re_T^2} \quad (198)$$

$$f_\mu = e^{-\frac{2.5}{1+0.02Re_T}} \quad (199)$$

$$L_k = -2\nu(\nabla(k^{0.5}))^2 \quad (200)$$

$$L_\varepsilon = 2\nu\nu_T(\nabla^2 \mathbf{u})^2 \quad (201)$$

Renormalization group $k-\varepsilon$ model

The renormalization group $k-\varepsilon$ model (often abbreviated as RNG $k-\varepsilon$ model) is derived from the theory of renormalization group to the instantaneous Navier–Stokes equations. The constants are different from those in the standard $k-\varepsilon$ model, including the additional terms and functions in the transport equations for k and ε . This model has a structure that is similar to the conventional $k-\varepsilon$ model but adds more terms to the equation to address the interactions between mean shear and turbulence dissipation, the impact of swirl on turbulence, the impact of turbulent Prandtl number, and the impact of effective viscosity. This model provides improved predictions for high streamline curvature and strain rate, transitional flows and wall heat transfer. However, it generally fails to correctly predict the spreading of a round jet [9].

Realizable $k-\varepsilon$ model

The term realizable means that the model satisfies certain mathematical constraints on the normal stresses, consistent with the physics of turbulent flows [13]. This model has the same turbulent kinetic energy equation as in the standard $k-\varepsilon$ model. However, there are some improvements in the model that eliminate the discrepancies observed in the standard $k-\varepsilon$ model which include improved dissipation rate equation, and a variable C_μ in the eddy viscosity relationship [14]. Therefore, it provides better predictions for flows with planar and round jets, boundary layers subject to strong adverse pressure gradients or separation, recirculation, and strong streamline curvature.

$k-\omega$ model

This model includes one equation for turbulent kinetic energy and one equation for specific turbulent dissipation rate ω . In the $k-\varepsilon$ model, the k equation is derived from a transport

equation governed by the fluid flow. However, there is another approach to developing a transport equation in which the equation is formulated based on some known physical processes along with dimensional analysis. This approach is adopted for the development of ω transport equation. The ω is defined as the rate of dissipation per unit of turbulent kinetic energy. This dissipation of energy happens at the smallest eddies level and the rate of dissipation is equal to the rate of turbulence energy transfer to the smallest eddies. Thus, it depends upon the large eddy properties. The simplest physical meaning that can be attributed to ω is that it is the ratio of the rate of (absolute) turbulent dissipation to turbulent mixing. There are many versions of the model, including one proposed by Wilcox [15], which starts with the following:

$$\frac{\partial}{\partial t} k + \nabla \cdot (\mathbf{u}k) = \boldsymbol{\tau}_R : \nabla \mathbf{u} - \beta^* k \omega + \nabla \cdot ((\nu + \sigma^* v_T) \nabla k) \quad (202)$$

$$\frac{\partial}{\partial t} \omega + \nabla \cdot (\mathbf{u}\omega) = \alpha \frac{\omega}{k} \boldsymbol{\tau}_R : \nabla \mathbf{u} - \beta \omega^2 + \nabla \cdot ((\nu + \sigma v_T) \nabla \omega) \quad (203)$$

where $\alpha = 5/9$, $\beta = 0.075$, $\beta^* = 0.09$, $\sigma = \sigma^* = 0.5$ and:

$$v_T = \frac{k}{\omega} \quad (204)$$

$$\varepsilon = \beta^* \omega k \quad (205)$$

$$l = \frac{k^{0.5}}{\omega} \quad (206)$$

Transport equation for the specific ω can be obtained from the transport equation of the turbulence dissipation rate ε using Eq. (205), but it involves a significant number of further manipulations; these are not presented in this publication. Different variants of this model are: Wilcox (1998) $k-\omega$ model, Wilcox (2006) $k-\omega$, and Menter (2003) shear stress transport $k-\omega$ model [15]. Each variant is developed to overcome deficiencies of the previous formulations. The $k-\omega$ family of turbulence models are y^+ insensitive. These work by blending the viscous sublayer formulation and the logarithmic layer formulation based on y^+ . Unlike the standard $k-\varepsilon$ model, the $k-\omega$ model can be integrated through viscous sublayer without the need for wall functions. The wall boundary conditions for turbulent variables are obtained as follows:

$$k = 0 \quad (207)$$

$$\omega = \frac{6\nu}{\beta_0 d^2} \quad (208)$$

$$\beta_0 = 0.075 \quad (209)$$

Shear stress transport model

In the laminar sublayer and the logarithmic regions of the boundary layer, the $k-\omega$ model performs better than the $k-\varepsilon$ model. Though, outside the boundary layer $k-\omega$ model is shown to be sensitive to the specification of the freestream value of ω . Thus, in the wake region of the boundary layer $k-\omega$ model is not observed to be a better option. In contrast, the $k-\varepsilon$ model performs better for the outer and wake region of the boundary layer, and it is not a good option for the inner region as compared to $k-\omega$ model. The shear stress transport model applies the $k-\omega$ model for the inner region of the boundary layer and for the outer and the wake region, it utilizes the $k-\varepsilon$ model. It incorporates the two models using a blending function that is designed in a way that in the vicinity of the wall region it equals one, thus implementing the $k-\omega$ model,

and in the region far away from the wall it equals zero, thereby implementing the $k-\varepsilon$ model [8]. The model predicts well the flow even with the adverse pressure gradients.

3.3.2. Reynolds stress models

Unlike eddy viscosity models, the Reynolds stress models (RSM) provides for the Reynolds stress τ_R using transport equations that consist of six independent terms present in the Reynolds stress. This enables the RSM model to treat turbulence in a fully anisotropic manner, which contrasts with the definition of a scalar turbulent viscosity as seen in eddy viscosity model. This characterizes RSM model as the most complete classical description of turbulence. An equation for turbulent dissipation is also required for closure. Therefore, in 2D fluid flow five more equations and in 3D seven more equations are to be solved. In comparison to eddy viscosity models, these require more processing power and are a better choice for complex 3D turbulent fluid flow problems that include streamlined curvatures, swirl, rotation, and high strain rates such as cyclone flow, swirling combustor flows, rotating flow passages, and flows involving separation. The exact equation for the transport of each Reynolds stress component $\tau_{R,ij}$ is as follows:

$$\frac{\partial}{\partial t} \tau_{R,ij} + C_{ij} = P_{ij} + D_{ij} - \varepsilon_{ij} + \pi_{ij} + \alpha_{ij} \quad (210)$$

where:

C_{ij} : stress convection

P_{ij} : stress production

D_{ij} : stress diffusion

ε_{ij} : stress dissipation

π_{ij} : transport due to turbulent pressure strain interactions

α_{ij} : transport due to system rotation.

Variable D_{ij} requires further closure to model the turbulent diffusion component, as well as π_{ij} and ε_{ij} . In Eq. (210), the production term and the transport due to rotation are kept the same. A gradient diffusion is assumed to model the diffusive term. The dissipation related to ε is calculated from the standard $k-\varepsilon$ model. The pressure fluctuations due to eddies' interactions with each other and the interactions between eddies and different mean velocities flow regions are included in the pressure strain interactions. Overall, it decreases shear stresses and makes the normal stresses more isotropic and it does not alter the total turbulent kinetic energy. The Launder model is the most commonly used [10].

3.3.3. Near wall modelling

The presence of walls greatly affects the turbulent flows. The mean velocity affects the no slip boundary condition at the wall. The fluctuations in the tangential velocity are reduced by viscous damping very near the wall. However, the production of turbulent kinetic energy due to high gradients in mean velocity quickly increases the turbulence in the outer part of the near wall region. The solutions are considerably impacted by the near wall modelling since the main source of mean velocity and turbulence are walls. There exist large gradients in the solution variables in the near wall region. Therefore, to obtain correct results accurate modelling is required in the near wall region for wall bounded flows [9]. As was discussed, the $k-\varepsilon$ models and RSM models are valid if applied for the regions far from the wall. On the other hand, $k-\omega$

model can be applied through the wall provided near wall mesh resolution is adequate. For clarity, the reader is referred to FIG. 15 for a representation of the various near wall regions. Traditionally there are two approaches i.e., wall function, and enhanced wall treatment that are used for modelling the near wall region.

3.3.3.1. *Wall functions*

This approach does not resolve between the viscous sublayer and buffer layer. Instead, to bridge the region affected by viscosity between the wall and the fully turbulent region it uses semi empirical relations also known as wall functions. The need to revise the turbulence model to accommodate the presence of the wall is eliminated by using wall functions. As in this approach the near wall region, where there exist the large gradients in the solution variables, does not require resolution, in high Reynolds number flows it significantly saves computation time. Since the approach is economical, robust, and reasonably accurate it is prevalent. For the treatment of industrial flow problems near the wall, this approach is a practical choice. The hypothesis underlying the approach becomes invalid where the low Reynolds number effects are persistent in the flow domain and hence the approach becomes insufficient for such conditions. Near wall models applicable under the viscosity affected region are required in such conditions and may be applied up to the wall. Based on the method proposed by Launder and Spalding, the standard wall functions are used for many industrial problems [9].

3.3.3.2. *Enhanced wall treatment*

In the enhanced wall treatment model, it resolves the near wall region completely from the turbulent region to the viscous sublayer.

To indicate both ε and the turbulent viscosity in the computational mesh cells near the wall, this two layer approach is used. This approach subdivides the whole domain into two regions: viscosity affected region and a fully turbulent region. The turbulent Reynolds number Re_y that depends on the wall distance separates the two regions and is defined as:

$$Re_y = \frac{\rho y k^{0.5}}{\mu} \quad (211)$$

where the boundary for the fully turbulent regions lies at $Re_y > 200$. In this region, the $k-\varepsilon$ or the RSM models are employed, while in the viscosity affected region ($Re_y \leq 200$) one equation models such as the one by Wolfstein are employed [16].

Differences between wall function approach and enhanced wall treatment approach alongside the respective computational meshes in the near wall region are illustrated in Fig. 17.

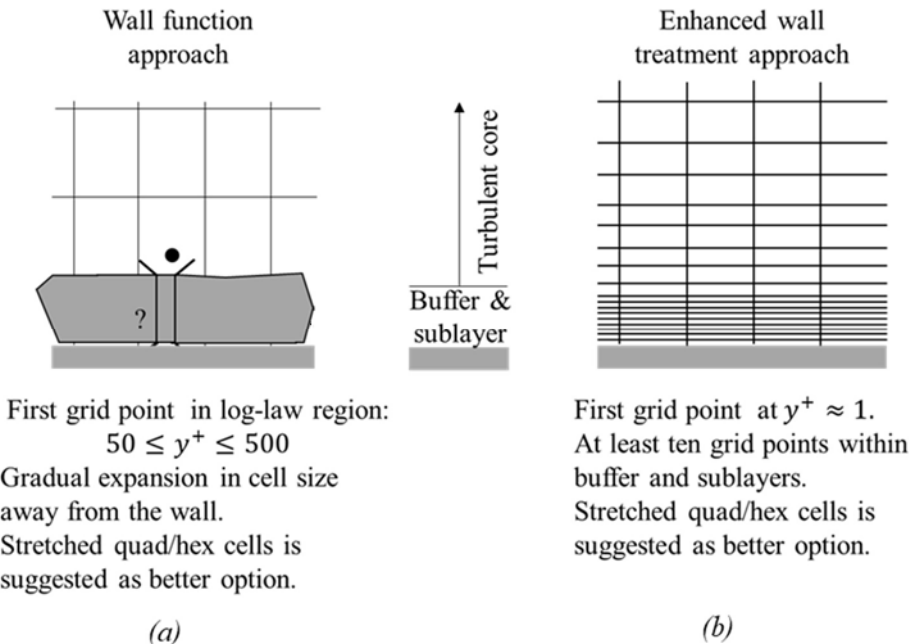


FIG. 17. (a) Meshing guidelines for near wall regions when employing the wall function approach or (b) enhanced wall treatment approach (conceived from [10]).

4. FUNDAMENTALS OF TWO PHASE FLOW MODELLING

This section describes the modelling options and their classification based on the space and time filtering or based on the averaging of the fundamental governing equations. Various flow processes to be modelled by closure relations are linked to each of these methods and the applicability of each of these methods to a specific flow regime is discussed.

4.1. OVERVIEW OF TWO PHASE FLOW MODELLING APPROACHES

Two phase CFD, also known as computational multi fluid dynamics is applied to the analysis of nuclear reactors in which two phase flow features are relevant either by design e.g., in boiling water reactors (BWRs), or in safety relevant scenarios, such as undesired flow boiling in the pressurized water reactors (PWRs). Modelling the flow configurations in steam–water two phase flow is very complex, and myriads of model options are available in the vast domain of computational multi fluid dynamics, with various treatments of turbulence and interfaces between the fluid phases. For an open medium, considering only the Eulerian approaches there are five different methods that can be used: RANS, pseudo DNS, and three types of space filtered methods.

4.1.1. Review of single phase computational fluid dynamics methods

This section describes a classification of one phase CFD. Three main categories of single phase CFD simulations are RANS, LES, and DNS models, and are compared in TABLE 1.

The RANS models are widely accepted for nuclear reactor applications. Summary on the selection of the models according to the application in reactor safety analysis are provided by the OECD Working Group for the Analysis and Management of Accidents (OECD–WGAMA) [17].

TABLE 1. OVERVIEW OF SINGLE PHASE TURBULENCE METHODS

Modelling method / Modelling aspect	RANS	LES	DNS
Ensemble or time averaging	Yes	Used by some methods (detached eddy simulation, very large eddy simulation, scale adaptive simulations)	No
Spatial filtering	No	Yes	No
Eddy resolution	Generally, all eddies modelled, but largest eddies (e.g., vortex shedding) may be simulated with URANS	Large eddies are simulated, small eddies are modelled	All eddies simulated
Closure requirements	Closure required for Reynolds stress tensor, turbulent diffusion of scalars, wall functions	Closure required for: turbulent diffusion of momentum and scalars, wall functions	None
Modelling complexity	Large	Intermediate	Small
Modelling locality and universality	Small	Intermediate	Large

4.1.1.1. *Reynolds averaged Navier–Stokes methods*

Although time averaging and ensemble averaging of local instantaneous equations (mass momentum and energy) when applied in RANS, are different, these can be considered as equivalent (ergodicity) in analysing the steady or quasi steady flows. Given that the closure (assumption) laws for Reynolds stress are validated against time averaged measured flow parameters, it is considered that RANS model is time averaged. In time averaged equations eddies are transported by the mean flow and therefore both time and space resolution in Eulerian approach are affected.

The most widespread RANS models (i.e., $k-\varepsilon$ models) are based on two equation turbulence model with Boussinesq approximation. There is a number of variations of two equation turbulence modelling approach such as but not limited to $k-l$, $k-\omega$, shear stress transport, RNG $k-\varepsilon$, and nonlinear $k-\varepsilon$. RANS was initially devoted to steady flows but, it was seen that it may be applied to unsteady flows in its URANS formulation if the time scale of the mean flow is larger than the time scale of the largest eddies. The RANS method can predict large scale Von Karman alleys if numerical scheme does not induce too much of artificial numerical viscosity.

4.1.1.2. *Eddy-resolving methods*

To predict large eddies, in case of insufficiently fine computational grid, a space filter is applied to the basic balance equations known as super grid scale. However, the effects of smaller eddies are modelled in a statistical way, presenting the basis of LES. The detached eddy simulation and very large eddy simulation belong to the same class of eddy-resolving methods, also referred to as scale resolving methods.

The scale adaptive methods are on the other hand, hybrid methods between URANS and LES where the LES method requires transient calculation with fine meshing in 3D space. Since the high order space discretization schemes and high order time integration methods are needed, it makes LES method much more computationally intensive than RANS method.

4.1.1.3. Direct numerical simulation

Direct numerical simulation means that solution is obtained without any averaging or filtering. In case of a turbulent flow, it is therefore required to have very fine meshing to be able to capture the smallest eddies at the Kolmogorov scale. Therefore, the approach is computationally expensive, and it is limited to simple cases.

4.1.1.4. Considerations of locality and universality of modelling methods

Since the RANS and LES methods require the averaging of filtering procedure, both methods thus also require the closure laws. The modelling of relevant physics processes depends only on local flow variables such as velocity, density, and internal energy, inclusive of their time and space local derivatives. As an example, RANS and LES approaches both capture the Reynolds stresses and turbulent heat fluxes. The wall functions are the only exception to the principle of locality since the meshing can be relatively coarse in high shear regions close to the wall because the closure terms depend on the distance to the wall. The principle of locality is more relevant to LES than RANS method, meaning that in LES models, the effects of small eddies close to a given point of flow need to be modeled, while in RANS method, the effects of largest eddies on local physics have to be modelled. Therefore, different RANS models are suggested for different flows such as but not limited to boundary layer, wake, mixing layer, or jet. In that respect the LES models tend to be more universal. When using the RANS method, the local models are more geometry dependent compared to LES. However, it is worth noticing that DNS provides a full application of the principle of locality given the molecular transfers are the only ones present.

4.1.2. Two phase flow features and averaging procedure

4.1.2.1. Two phase flow features

Three main categories of prediction techniques, similar to RANS, LES, and DNS can be as well identified using computational multi fluid dynamics to describe two phase flow. However, the additional complexities call for yet an extended list of modelling options [18].

A two phase flow exhibits various types of moving interfaces between gas and liquid and is also a juxtaposition of a mean flow and turbulent eddies. This limit Eulerian open medium models with the treatment of mass momentum and energy equation with:

- Averaging or filtering turbulent scales (similarly to single phase CFD);
- Usage of phase averaging or field averaging technique;
- Interface treatment (interface tracking, recognition, filtering, and statistical treatment).

How various averaging procedures affect description of a complex two phase flow is illustrated in Fig. 18 that shows a complex stratified flow with three interface types:

- Free surface (an interface with a large extension of space);
- Bubbles interface (closed surfaces with limited extension of space);
- Drops interface (closed surfaces with limited space extension).

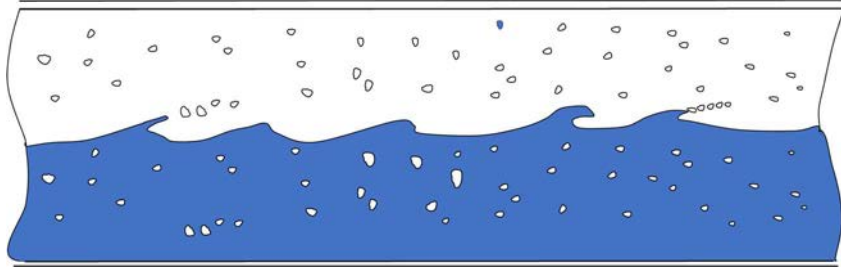


FIG. 18. Complex gas liquid flow, i.e., stratified flow with a breaking free surface resulting in bubbles and droplet entrainment.

Between interfaces, mass transfer (vaporization or condensation), momentum transfer and heat transfer exist that further split the space domain into fluid fields as follows:

- Continuous liquid field: limited by possible free surfaces and/or bubble interfaces;
- Continuous gas field: limited by possible free surfaces and/or bubble interfaces and is opposite to the liquid field;
- Bubble field or N_b several bubble fields if different bubble shapes or size are grouped into different fields;
- Droplet field or N_d several droplet fields if different droplet shapes or size are grouped into different fields.

Thus, there may be up to $2+N_b+N_d$ fields (i.e., 2 continuous fields + N_b bubble fields + N_d droplet fields). In addition to mass transfers by vaporization or condensation, the other mass transfers mechanisms are:

- Continuous liquid field→droplet field: by entrainment of drops from free surface waves;
- Droplet field→continuous liquid field: by fall of drops to free surface;
- Continuous gas field→bubble field: by capture of gas (breaking waves);
- Bubble field→continuous gas field: by bubble burst at free surface;
- Bubble field↔droplet field: from a single bubble field to multiple bubble fields (bubble breakup) or from multiple bubble fields to a single bubble field (bubble coalescence);
- Droplet field↔droplet field: from a single droplet field to multiple droplet fields (droplet breakup) or from multiple droplet fields to a single droplet field (droplet coalescence).

To describe local structure of two phase flow at certain point in space and time, only a few local flow configurations can be identified as follows:

- Continuous liquid field (single phase liquid);
- Continuous gas field (single phase gas);
- Continuous liquid field–bubble field (dispersed bubbly flow);
- Continuous gas field–droplet field (dispersed droplet flow);
- Continuous liquid field–continuous gas field (separate phase flow);
- Continuous liquid field–continuous gas field–droplet field (complex two phase flow);

- Continuous liquid field–continuous gas field–bubble field (complex two phase flow when continuous liquid, continuous gas, and bubbles are present in the space and/or time domain);
- Continuous liquid field–continuous gas field–droplet field–bubble field (complex two phase flow when continuous liquid, continuous gas, droplets and bubbles are present in the space and/or time domain as illustrated in Fig. 18).

Any CFD method or model describing the two phase flow when uses a time or a space averaging or filtering may require identification of local interfacial structures. The same analysis can be applied to complex annular flows (including annular mist flows) because of the same types of interfaces, same fields, and same transfers. Equally complex two phase churn flow has the presence of both small bubbles and large distorted bubbles, as sketched in Fig. 19.

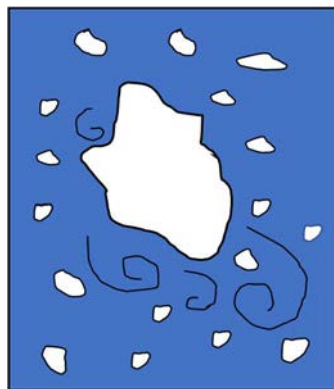


FIG. 19. Complex gas liquid flow, i.e., churn flow with small bubbles as well as large distorted bubbles.

4.1.2.2. Effect of spatial filter on two phase flow description

A space filter once applied to turbulent single phase flow creates certain loss of information about local flow structure as the smallest eddies are eliminated while the largest ones are kept. The same space filter applied to two phase flow affects interfaces, because in the space domain both liquid and gas could exist and exist with any kind of interface. In such a case, a volume fraction can be defined for each phase or for each field, as well as interfacial area density for each type of interfaces. To illustrate this, Fig. 20 shows how the space filtering affects description of complex stratified flows:

- *Subgrid interfaces vanish:* The only known parameters for smaller bubbles or drops are statistical or averaged values; their positions in space and time cannot be used to identify them (volume fraction, interfacial area density). If small bubble and drop interfaces are referred to as subgrid interfaces, then such subgrid interfaces will vanish throughout the filtering process.
- *Large interface discontinuities are smoothed:* When the space filter condenses the interface of big and deformed bubbles in churn flows, free surface in stratified flows, or film surface in annular flows, density discontinuity is replaced by density gradient. Large interface positions can be reconstructed using numerical methods, as shown in Fig. 20.
- *Subgrid waves of large interfaces vanish:* waves at free surface of small wavelengths or small scale interface deformations (such as distorted bubbles) are no more visible.

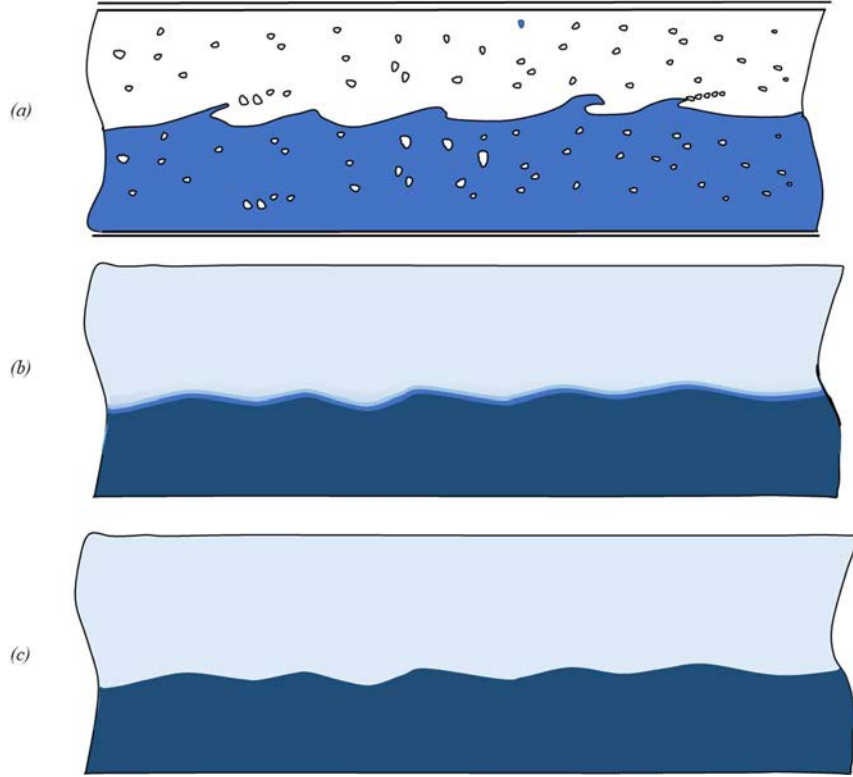


FIG. 20. Representation of loss of information in a complex flow field associated with application of spatial filter: (a) detail flow description, (b) application of spatial filter smoothens the interfaces, which are then best identified by strong field gradients leading to the loss of information pertaining smaller bubbles or droplets, (c) large scale interface reconstruction starting from spatially averaged field.

Subgrid processes (and their relationships and effects) that require modelling when employing a spatially filtered flow modelling method are summarized in FIG. 21.

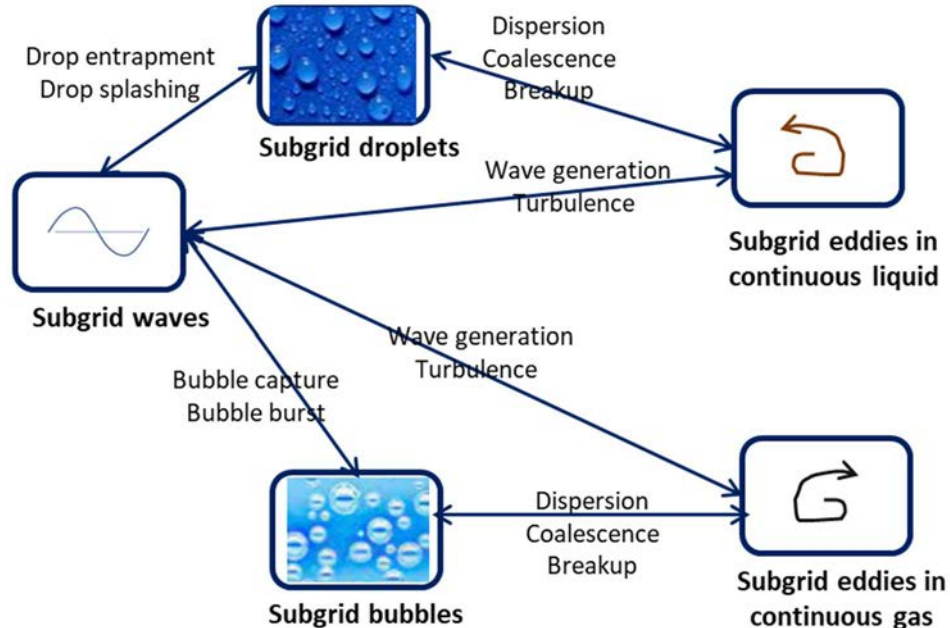


FIG. 21. Subgrid processes (and their relationships) that require modelling when employing a spatially filtered flow modelling method.

4.1.2.3. Effect of time or ensemble averaging on two phase flow description

When applying time averaging (or filtering) to turbulent single phase flow, the information about local flow features is lost (all eddies are eliminated as in RANS, or all eddies except the large ones are eliminated as in URANS). Similar loss of information appears on the interfaces when time filtering is applied as an average over a time period Δt , or space filtering (with an equivalent space filter of size $L = |\mathbf{u}|\Delta t$). This causes subgrid interfaces to vanish, large interface discontinuities to be smeared, and subgrid waves of large interfaces to vanish. This method is appropriate for complex stratified flows as shown in Fig. 18 with comparable loss of information as illustrated in Fig. 20. Given the space resolution depends on the magnitude and direction of local velocity \mathbf{u} it is neither uniform nor isotropic. This results in a much more complex and unclear closure issue. As an example, consider a bubble in a high velocity zone, with the size smaller than the filter scale $L = |\mathbf{u}|\Delta t$, becomes larger than L when comes to a low velocity zone in the simulated domain after passing through the subgrid domain. Hence, URANS is applicable only in a few quasi parallel flows with a preferential flow direction e.g., stratified, or annular flows in a duct. In such flow regimes large wavelengths are simulated while the large interface and small wavelength waves are filtered. It is worth mentioning that large wavelength waves (at free surface or film surface) may disappear while averaging in case of pure RANS for steady flow or URANS with the of a large time integration step Δt . Therefore, to have a clear difference among small interfaces (which may be statistically treated) and large interfaces (which can be predicted as filtered interfaces), space filtering is more effective than the time filtering.

4.1.3. Two phase computational fluid dynamics approaches

Depending on which operations are applied, different modelling approaches can be obtained. These choices allow to distinguish various methods accordingly. With specific reference to interface treatment, the following approaches can be distinguished:

- *Deterministic interfaces or simulated interfaces*: When space and time position is simulated or actually predicted without any simplification, it is referred as deterministic interface. This requires the use of an ITM;
- *Statistical interface*: When a space or time averaging or filtering procedure does not allow to predict its space and time position, it is referred as statistical interface. Quantities like a void fraction or an interfacial area density can only be used to predict statistical information on several interfaces. This is the case for small bubble and droplet interfaces as shown in Fig. 20;
- *Filtered interface*: When space and time position is predicted with some filtering of the smaller scale deformations, it is referred as filtered interface. This filtering may result either from space filter or from time averaging. The free surface in FIG. 20(c) is an example of a filtered interface.

TABLE 2 distinguishes five different types of Eulerian two phase CFD techniques for open media. The way the fundamental mass, momentum, and energy balance equations are handled varies amongst them. These are obtained by the application of the operations taken from the following list:

- Mass, momentum, and energy multiplication by phase indicator functions (for each of the two phases in a two fluid approach) or by the field indicator functions (for each of the $2 + N_b + N_d$ fields for a multi field method);

- Time filtering (i.e., averaging);
- Space filtering;
- Adoption of an interface tracking method (ITM) or an interface reconstruction technique either for some or all the interfaces.

Depending on which operations are applied, different modelling approaches can be obtained. These choices allow to distinguish various methods accordingly. With specific reference to interface treatment, the following approaches can be distinguished:

- *Deterministic interfaces or simulated interfaces*: When space and time position is simulated or actually predicted without any simplification, it is referred as deterministic interface. This requires the use of an ITM;
- *Statistical interface*: When a space or time averaging or filtering procedure does not allow to predict its space and time position, it is referred as statistical interface. Quantities like a void fraction or an interfacial area density can only be used to predict statistical information on several interfaces. This is the case for small bubble and droplet interfaces as shown in Fig. 20;
- *Filtered interface*: When space and time position is predicted with some filtering of the smaller scale deformations, it is referred as filtered interface. This filtering may result either from space filter or from time averaging. The free surface in FIG. 20(c) is an example of a filtered interface.

TABLE 2. CLASSIFICATION OF EULERIAN SIMULATION METHODS FOR TWO PHASE COMPUTATIONAL FLUID DYNAMICS

Method	Pseudo–DNS	LES with deterministic interfaces	Hybrid LES with filtered and statistical interfaces	LES with statistical interfaces	RANS/URANS with statistical and filtered interfaces
Category	Pseudo DNS	Eddy resolving	Eddy resolving	Eddy resolving	RANS/URANS
Time or ensemble averaging	No	No	No	No	Yes
Spatial filtering	No	Yes	Yes	Yes	No
Multiplication by indicator function	No	No	Yes	Yes	Yes
Interface treatment	Deterministic ITM	Deterministic ITM	Filtered and statistical ITM	Statistical with no tracking or reconstruction	Statistical and filtered with no tracking or reconstruction
Modelling effort	?	1	5	2	4
Modelling locality and universality	5	4	3	3	1

Modelling of wall transfers, interfacial transfers, inter field transfers and turbulent transfers depends on the method. Each method is described in the following subsections.

4.1.3.1. Pseudo DNS method

In the pseudo DNS method, space and time average equations are not used. However, to track the interface, ITM is required using one fluid approach. It is frequently necessary to use

additional models, for instance, to apply a film splitting criterion when two bubbles merge or to determine the contact angles at a triple solid-liquid-gas line. These additional models are the reason that pseudo DNS is used in place of DNS in two phase flow since certain very small scale physics is merely modelled and not solved. Because neither averaging nor filtering are applied, Pseudo DNS should be capable of simulating all interfaces.

4.1.3.2. Reynolds averaged Navier–Stokes method

The RANS method (as it applies to URANS as well) is by far the cheapest, most mature, and most adopted approach for two phase CFD modelling. In this method, all the turbulent scales and two phase intermittency scales are filtered. In addition, all the interfaces are statistically treated. This method is employed when the time scales of variation of the mean variables are longer than the longest time scales of turbulence and two phase intermittencies (time between passing of two interfaces at any given point). Large interfaces (free surface or film interface) can be thought of as filtered interfaces for stratified flows or annular flows. All two phase flow regimes are theoretically compatible with RANS if steady or quasi steady, and for the dispersed droplet flow or dispersed bubbly flow, the condition is easy to satisfy. For stratified flows and annular flows, the averaging process filters interfacial waves in an unclear manner: although the modelling of turbulent diffusion via RANS avoids the large eddies simulations, however, it does not avoid the irrotational waves (predicted by Kelvin-Helmholtz instabilities). As a result, both a filtered interface treatment and a statistical interface treatment are compatible with RANS and URANS. The intermittency caused by the passage of these bubbles' correlates to relatively long time scales for slug and churn flows with huge bubbles. RANS filters even these vast scales, therefore it cannot forecast this intermittency, but it can predict the typical behaviour.

4.1.3.3. LES with deterministic interface

This method combines a turbulent fluctuation filtering with an ITM at all the interfaces. It was first proposed for free surface flow by Liovic and Lakehal [19], [20], then pursued by Bois et al [21], Toutant et al. [22], [23], Magdeleine [24], Lakehal [25], [26]. Lakehal and Labois [27] reformulated the concept in a better way and referred it as a large eddy and interface simulation. An important requirement for deterministic interface is that all the phenomena having influence on space and time position of the interface needs to be simulated.

The interfaces with deformations on a smaller scale are affected by the turbulent fluctuations and the surface tension. Weber number limiting value i.e., We_{lim} defines the applicability limit of LES along with a deterministic interface, such that:

$$We = \frac{\rho u(l)^2 l}{\sigma} \leq We_{lim} \quad (212)$$

where σ is the fluid surface tension and $u(l)$ is the velocity scale of turbulent fluctuations for eddies of size l . The shape of an interface can only be affected by velocity fluctuations at a minimal length scale l , which corresponds to this limit. Below this threshold, the mechanical impacts of velocity fluctuations are outweighed by the effects of surface tension. For a particular turbulence spectrum, it may provide maximum value of the filter scale i.e., l_{filter} :

$$l_{filter} \leq \frac{We_{lim}\sigma}{\rho u(l_{filter})^2} \quad (213)$$

Alternatively, less restrictive limit is related to Laplace scale:

$$l_{filter} \leq \frac{1}{n} \sqrt{\frac{\sigma}{g\Delta\rho}} \quad (214)$$

where $\Delta\rho$ is the density difference between the two fluid phases, g is the strength of gravitational acceleration and n is to be determined, but typically in the 5–10 range. Considering no high turbulence density, Laplace scale associated to the smallest wavelength of capillary waves also known as free surface waves or film waves. When the denser phase is above the less dense phase, it is the first wavelength of an interface's deformation brought on by Taylor instability. If there are very small bubbles or droplets much smaller than the Laplace scale as there will be in boiling flow, the filter scale should provide a better description of the interfaces of the smallest bubbles of diameter d_{min} , which results in a limitation:

$$l_{filter} \leq \frac{1}{m} d_{min} \quad (215)$$

Magdeleine [28] claims that m can be taken as 6 at most without affecting the outcomes. Taking into account all these limitations, LES with deterministic interface approach is one to two orders of magnitude less computationally intensive than pseudo DNS, however, still very expensive. Therefore, it is rarely utilised to address issues at scales of engineering significance and is mostly used as a research tool, as a support for the modelling and validation of coarser techniques.

4.1.3.4. *LES with statistical interfaces*

An LES method is practically used with a filter scale smaller than the big eddy scale but larger than the two phase scale to enable a statistical treatment when the largest interfacial scale is relatively small and much smaller than the largest turbulent eddies. The idea was first developed by Lakehal et al [28], set the filtered two fluid equations and suggested including a bubble-induced diffusion model into Lilly and Germano's dynamic method. The authors formulated the so called Milleli criterion for the least permitted filter width, which according to their systematic sensitivity analysis should scale with the largest bubble diameter d_{max} as $l_{filter} > 1.5d_{max}$. Dhotre et al. [29], [30] and Niceno et al. [31], [32] applied this method to turbulent dispersed flow with some success. Such a method is computationally much less intensive than the other methods i.e., pseudo DNS and the LES with deterministic interface, however, it can only be applied to certain flow situations. Such situation includes dispersed bubble or dispersed drops. Nevertheless, this is not suitable in slug or churn flow where the largest bubbles and the largest eddies are of the size of the geometrical dimensions of the flow. This approach works with the two fluid model and multi-field models, which allow size groups to be applied to the dispersed bubbles or droplets.

4.1.3.5. *Hybrid LES with filtered statistical interfaces*

This method filters the smaller eddies and treats the small droplets or small bubbles statistically as illustrated in Fig. 20. The space filter removes the small bubbles that are statistically handled and thickens and filters the large bubble interface, which can be restored using a form simplification. There may be certain analyses for a two fluid model without a turbulence model that are similar to this method, even though it has not been defined and used with clarity

(Bartosiewicz et al. [33], [34]). D. Lakehal [26] discussed the difficulties of this method in comparison to LES with simulated interfaces. It may be a less computationally intense way of modelling the complex two phase flow e.g., churn or slug flow without filtering the large two phase structures. The closure problem, however, is quite complicated, and the current state of the art is not particularly advanced. Before obtaining a satisfactory modelling of all flow regimes, difficult challenges need to be addressed [35]. The two fluid approach and multiple field models are both compatible with this methodology. Reconstructing the large, filtered interfaces and modelling the mass transfers between continuous and dispersed fields may be aided by a four field model comprising a continuous gas field, a continuous liquid field, a dispersed bubble field, and a dispersed droplet field. This method has more closure terms than the LES with deterministic interfaces. It was found that many ITM-using applications approaches to LES type with deterministic interfaces which are hybrid methods. The ITM's interface tracking is poorly resolved, and simulated interfaces are filtered rather than deterministic. The modelling process should consider every influence brought on by subgrid waves at large interfaces.

4.1.3.6. Modelling locality and universality

The use of principle of locality of the modelling is similar in two phase CFD as in single phase CFD as the closure laws are described as functions of velocity, density, internal energy, l_{filter} and their derivatives (both spatial and temporal). However, this principle of locality cannot be applied to wall functions, as some of the closure terms in this case depend on the distance from the wall and interfacial function, which is like wall functions close to large interfaces between fluids. These allow the use of a rather coarse mesh in high shear regions close to a wall or close to a large interface, thereby reducing computational costs compared to the case where these high shear regions are resolved numerically via very fine meshes. When the processes to be described at any one place in space and time exclusively depend on the flow conditions nearby, principle of locality becomes increasingly relevant. Since the subgrid local turbulent viscosity in LES models primarily affects small eddies that are close to point P, the principle of locality in single phase CFD is better addressed by LES approaches than by RANS. In a two phase flow, there are small interfaces and large scale interfaces, free surface in stratified flow, and the film surface in annular flow. Henceforth, in the flow regimes with large interfaces, the principle of locality may only be reasonably applied in LES with deterministic or filtered interfaces.

4.1.4. Applicability limits of two phase computational fluid dynamics

The applicability along with the degree of maturity of the various two phase CFDs to every flow regime are summarized in TABLE 3 detailing whether an approach is routinely applied to the investigation of such flow type and is thus reasonably mature, if it is in principle possible to apply in spite of a lack of maturity, if it is impossible to apply due to intrinsic limitation, and whether it is computationally expensive or too expensive. It is to be emphasized that only RANS (or URANS) and LES with filtered and statistical interfaces can be used to simulate physical conditions where both two phase flow regimes may occur. The former, however, is more accomplished than the latter.

All flow regimes can be addressed by the pseudo DNS and LES with deterministic interfaces, but are practically constrained by the required computer resources, which are prohibitive in the majority of complex flow scenarios. Large interfaces cannot be treated by LES with statistical interfaces, and thus is inherently restricted to scattered flows.

Three popular flow regimes extensively simulated by various methods are: *i*) dispersed bubbly flow; *ii*) dispersed droplet flow (mist flow); *iii*) and the stratified flow. All currently used techniques have been used to model and simulate adiabatic bubbly flows, with the RANS two fluid appearing most frequently. For the purpose of predicting gas fraction profiles, efforts were made to model the forces acting on bubbles. Some progress was made to extend wall functions to two phase situations [36].

Boiling bubbly flows have also so far been simulated with the RANS two fluid methods in view of investigating departure from nucleate boiling. The prediction of bubble size was first made using algebraic models, then using interfacial area transport equation and later using a modelling of the poly dispersion. Wall transfer modelling was also investigated. Turbulence in the liquid phase is generally modeled with extensions of the $k - \varepsilon$ model to two phase conditions [37]. Dispersed droplet flows are modelled and simulated with RANS in the frame of dry out investigations. Such flows are also modelled with RANS for containment sprays simulation [38]. Free surface flows are simulated with pseudo DNS, LES with simulated interfaces, and URANS with filtered interface. One fluid with ITM is compared to two fluid model with an interface reconstruction method applied to the unstable free surface flow. Efforts are made to model interfacial transfers of momentum, heat, and mass. The subgrid wave profile, which can be treated as a roughness, need to be considered when free surface is treated as a filtered interface. Different models and codes are validated against steam–water condensing flow tests [18].

TABLE 3. DEGREE OF MATURITY OF EULERIAN METHODS FOR THE MODELLING AND SIMULATION OF DIFFERENT FLOW REGIMES

Approach Flow	Pseudo DNS	LES with deterministic interfaces	Hybrid LES with filtered and statistical interfaces	LES with statistical interfaces	RANS/URANS with statistical and filtered interfaces
Bubbly	Routinely applied	Routinely applied	Routinely applied	Routinely applied	Routinely applied
Slug–churn	In principle possible, Computationally too expensive	In principle possible, Computationally expensive	In principle possible	Impossible to apply	In principle possible
Annular	In principle possible, Computationally expensive	In principle possible, Computationally expensive	In principle possible	Impossible to apply	Routinely applied
Annular mist	In principle possible, Computationally too expensive	In principle possible, Computationally too expensive	In principle possible	Impossible to apply	In principle possible
Mist	Routinely applied	Routinely applied	Routinely applied	Routinely applied	Routinely applied
Stratified	Routinely applied	Routinely applied	Routinely applied	Impossible to apply	Routinely applied
Stratified mist	In principle possible, Computationally too expensive	In principle possible, Computationally too expensive	In principle possible	Impossible to apply	In principle possible
All regimes	Computationally too expensive	Computationally too expensive	In principle possible	Impossible to apply	In principle possible

4.1.5. Guidelines for the application of two phase computational fluid dynamics

A multistep methodology is necessary for application of two phase CFD to nuclear reactor analysis. Application of two phase CFD bring useful new simulation capabilities, but the degree of maturity strongly depends on the method employed. In every new application, choice of modelling options, a validation effort, and a clear application methodology to be followed to obtain reliable results must be considered. A general approach in using two phase CFD is illustrated in Fig. 22 as proposed in [39].

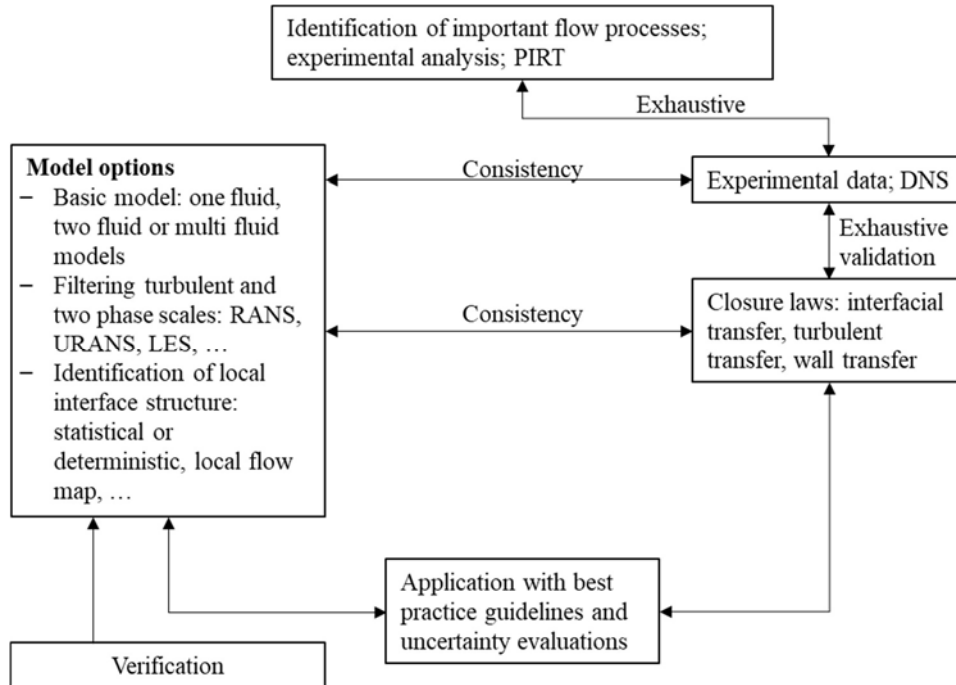


FIG. 22. General methodology dependencies for the application of two phase CFD to nuclear reactor analyses.

4.1.5.1. Identification of important flow processes

Many reactors analysis typically involve complex two phase phenomena in complex geometries. It is always needed to identify the thermal hydraulics phenomena of interest before selecting a code from the lot of available two phase CFD codes. CFD codes cannot be used as a black box to obtain a solution of complex problem without selecting the adequate options to provide the appropriate answer. The significance of each of these fundamental phenomena must be ranked for the reactor analysis. This can be done using a process identification and ranking table (PIRT) study. Identification of the phenomenon may be greatly aided by preliminary analysis of the experiments. Given the intrinsic complexity of any two phase flow, it is necessary to revisit this list of crucial operations multiple times. The relative significance of each phenomenon may change as a result of modelling and validation. Additionally, the study of some experimental data may bring to light previously undetected phenomena. The methodology could then be iterative.

4.1.5.2. Modelling choices

As already introduced, the main modelling choices consists of the field treatment options (i.e., one field per phase or multiple fields per phase, e.g., continuous and discontinuous fields for each phase), space and time filtering options, and interface treatment options. Any two phase

flow can be thought of as a juxtaposition of several phases and fields. In the absence of clear criterion to identify the limits of each field (phase), one may define that the field (phase) k indicator function $\chi_k(\mathbf{x}, t)$ which is equal to 1 or 0, depending on the field k presence at position \mathbf{x} at time t . The local instantaneous equations for mass, momentum, and energy may then be averaged after being multiplied by this indicator function. Then, for each of the N fields, the three balance equations for mass, momentum, and energy are averaged to provide a set of $3N$ field balance equations.

The CFD tools offer various models, to name a few are, one fluid homogeneous, two fluid, multi field models. For two phase flows, the separation of flows into several fields (as discussed above) is particularly necessary when there is a large variation of important parameters e.g., velocity, and temperature, among the fields. The most complex basic model for two-phase flow would have $2 + N_b + N_d$ fields and $3 \times (2 + N_b + N_d)$ basic balance equations, where N_b being the number of bubble fields, and N_d being the number of droplet fields. In many cases, it is not necessary to use such a complex model. The second important choice pertains to the type of averaging or filtering of the governing equations. The two fluid model is typically based on a time averaging of equations over a long enough time period as compared to turbulence time scales and two phase intermittency scales. This is completely in accordance with the conventional RANS equations used to model single phase flow turbulence. CFD of single phase turbulent flows can also be performed by alternative method i.e., URANS, LES, or very large eddy simulation when some large scale phenomena need to be deterministically treated. It is possible to extend these approaches to two phase CFD by splitting turbulent scales and two phase intermittency scales into the larger ones whereas a statistical description is applied to the smaller ones. Interfaces with a wide range of geometrical configurations exist for the two phase flows. There are locally closed interfaces for dispersed fields, such as bubbles and drops, and locally open interfaces for free surfaces, falling film interfaces, jet interfaces, and so on. A deterministic approach to an interface anticipates the position of the interface in space as a function of time and may call for an ITM, such as the volume of fluid (VOF) technique, front tracking method, level set method, lattice Boltzmann method, and others. The existence of interfaces is described statistically using averaged characteristics like volume fraction, interfacial area density, etc. To choose the best closure laws for the interfacial transfers in the case of a pure statistical approach, one might need to identify the local interfacial structure.

4.1.5.3. Closure laws selection

Closure laws should be adopted for modelling interfacial transfer phenomena (i.e., transfers of mass, momentum, energy), turbulent transfers as well as wall transfers. These phenomena range significantly in complexity; the following is a brief description of interfacial transfers.

For a large interface, an adequate model may require information of exact position of interface (by using an ITM or any other method). After the identification of local interfacial structure, the choice of adapted closure laws is possible. When available, mass momentum and energy interfacial transfers necessitate modelling and validation using so called separate effect tests. Whatever approach is used, modelling interfacial transfers is a fundamental question in two phase flow.

4.1.5.4. Verification and validation

To test the capabilities of a numerical technique and measure the accuracy of the resolution, numerical benchmarks may be required. The method is therefore applied to each of the selected

problems and gaps are identified at every step of the method for every problem. Considering a methodology is applied to many two phase flow situations, precise guidelines will be provided to CFD code users. This will help the users to choose the right options relevant for the specific application. Currently, only limited number of such best practice guidelines exist. To qualitatively validate the capability of a modelling approach to capture all the basic flow processes demonstration tests are necessary. And for the quantitative evaluation, model for models for interfacial, turbulent and wall transfer terms of the equations, validation tests including separate effect tests and global test are necessary. In some cases, DNS data can be utilised to support experimental validation. However, only fully validated DNS simulations may be used as numerical experiments.

4.1.6. Best practices guidelines

An example of practical guidance for the application of CFD tools to the analysis of thermal hydraulics for nuclear reactor safety is given by Mahaffy et al. [40] titled “Best Practice Guidelines for the Use of CFD in Nuclear Reactor Safety Applications”. The whole spectrum of subjects for accurate flow simulations is covered in this report. It includes sections on selecting simulation tools after properly defining the problem. The flow processes, as well as the turbulence and two phase flow scales to be addressed in the computation, are significant determinants in this choice. This method works for both single phase and multi phase simulations. It also describes techniques for the quantification and reduction of numerical errors. These were developed for single phase flows but are also applicable to multi phase flows; single and multi phase flow formulations are both based on conservation equations and thus mathematically similar. However, the presence of different phases, sharp interfaces, and an increased tendency to instability and unsteady state behaviour pose a significant additional challenge for multiphase flows. Due to the presence of such sharp interfaces, much finer grid resolution is often required than for corresponding single phase flows. On coarse grids, the higher affinity to physical instabilities may be suppressed, but it may appear after grid refinement. This property, combined with the additional model equations, results in extremely high computational demands for multiphase flows. An evaluation of CFD capabilities must ensure that various error types are properly recognized and addressed. For example, single phase studies have shown that model errors can only be quantified if numerical and systematic errors are reduced to an acceptable level. In an ideal situation, this would imply that solutions for grids and with time steps fine enough that numerical errors become negligible. This ideal separation of errors cannot always be achieved because it is not a simple task and would necessitate very large computing resources. These fundamental difficulties are exacerbated when multiphase flow physics and unsteady state are incorporated into numerical simulations.

4.1.6.1. Example guideline checklist

The following is a step-by-step procedure proposed for application of two phase CFD to a nuclear reactor analysis [39]. First is the identification of important flow processes:

- Identifying fundamental processes of interest that one would like to obtain from the application of a CFD code (e.g., fluid temperature, local heat transfer, peak pressure at a specific location);
- Identifying secondary processes that are coupled to fundamental processes of interest;
- Identifying several spatial dimensions that suffice the characterization of the processes of interest;

- Establishing spatial and temporal domain sizes required for characterization of the processes of interest;
- Assess how many different two phase flow regimes are expected to occur in the domain of interest;
- Assess whether phenomenon of interest can be best described by a transient or a steady state simulation;
- Assess minimum temporal scale (if the simulation is transient) and spatial scales (i.e., mesh size) required by simulation. While initial guesses can be made based on multiple conditions (ranging from the Courant condition to turbulence scale related conditions), this process is likely to be highly iterative depending on the nature of the processes to be resolved.

Secondly, the selection of fundamental modelling options, specifically the selection of suitable wall, interfacial and turbulent transfer models (for mass, momentum, energy) depending on the process to be investigated. Thirdly, if the material and temporal conditions of the investigation allow for it, a validation process would prove beneficial to further improve the modelling capabilities and the subsequent results obtained by the simulation. This validation process entails the following steps:

- Identification of available experimental data that covers the processes of interest;
- Assessment of whether selected models, with specific regard to wall, interfacial and turbulent transfer models, are covered by available experimental data;
- If any of the previous two steps are not satisfied and if temporal material conditions allow for it, the design of an experiment, from integral to separate effect tests, such as to provide further validation data would prove highly beneficial.

4.1.6.2. Consistency checks

Several choices are made during the successive steps of a general methodology, which necessitate some consistency checks. The following checks are particularly notable:

- Fundamental selection of several fields must be adapted to a physical situation or to an acceptable level of simplification. If the PIRT determines that specific behaviour of two fields is important, these must be treated separately;
- Experimental effect test validation matrix should include all identified flow processes;
- All interfacial, interfiled, turbulent, and wall transfers should be validated by the experimental effect test validation matrix;
- In the ideal scenario, the number of measured flow parameters in the experiments should be consistent to the complexity of the chosen model. Necessary condition for the validation of a model defined by a set of n equations having a set of principal variables X_i is that one should be able to measure n parameters giving the n principal variables;
- To provide a clear definition of principal variables and closure terms in equations, the averaging procedure must be specified. The filtering of turbulent scales and the intermittency of two phases must be fully consistent;
- Averaging of measured variables must be consistent with the averaging of the equations;
- Use of an ITM for interface treatment necessitates the simulation or deterministic treatment of all phenomena influencing the interface;

- Formulation of an appropriate interfacial transfer must be consistent with the interface treatment (deterministic, filtered, statistical) and with the identification of local interfacial structure.

4.1.6.3. Examples of common modelling errors

Due to availability of many modelling options in commercial CFD codes such as FLUENT, STARCCM+, CFX, or NEPTUNE_CFD [41], [42], it is possible that some inconsistent choices will be made. Most errors are due to inconsistent space and/or time resolution choices for interfacial, wall, and turbulent transfer modelling. Here are a few examples of common mistakes. A common error consists in adopting the interfacial transfers models devised for 1D system codes for simulations to be performed with 3D CFD codes. The interfacial transfer formulation in 3D modelling relates a local flux F_X of a quantity X to a difference between local phase variable X_k multiplied by a local transfer coefficient C_X , so that, for a system of two phases labelled e.g., l and v it follows:

$$F_X = C_{X,3D}(X_l - X_v) \quad (216)$$

The interfacial transfer formulation in 1D modelling is based on area averaged quantities. This area averaging is over the flow cross section perpendicular to the principal flow direction. Thus, by denoting the area averaged quantity X with $\langle X \rangle$, in 1D, it follows:

$$\langle F_X \rangle = C_{X,1D}(\langle X_l \rangle - \langle X_v \rangle) \quad (217)$$

Even if the flow is one directional e.g., in a pipe, there is no reason to expect $C_{X,1D} = C_{X,3D}$. These can differ by up to several orders of magnitude. It would be exact only in case of spatially uniform fields of X_l and X_v which cannot be generally the case in a 1D model since area averaging contains boundary layers along walls in which all variables have generally strong gradients. The same logic applies when discussing the errors committed when applying correlations developed to model phenomena in a porous medium to open media i.e., media that do not contain volume averaged structures are do not entail boundary layers. Similarly, the use of models for interfacial and wall transfers devised for porous media in open fluid (also called clear fluid, meaning regions that do not contain any volume averaged structures) is also incorrect. The volume averaging in a space domain containing solid structures homogenizes the wall transfer terms in a porous medium. In an open medium, the transfers with walls generally use the wall function method. Common issues can also be identified in 2D or 3D two fluid simulations without turbulence modelling. A time averaging over a long period of time covering two phase intermittency scales is included in the two fluid model. This averaging procedure filters all or a portion of the turbulence spectrum as a result, adding turbulent stresses (Reynolds stresses) and turbulent diffusion to the momentum and energy equations as previously shown. For instance, only the fluid meshes along the wall of a heated pipe with a two phase flow can be accurately heated by the wall, but the transfer to the core flow can only be accurately characterized by a turbulent transfer model in energy equations.

A common mistake might also lie in the adoption of models for interfacial coefficients devised for averaged or statistically treated interfaces when the underlying simulation is intended to be LES or DNS instead, meaning in scenarios in which the interfaces are deterministic.

4.1.7. Conclusive remarks

The huge variation of flow configurations in two phase flow (steam water), as well as the multitude of model options available in CFD codes, with various turbulence and interface treatments, make the selection of model options depending on the application rather complex. If there are many possible model option combinations, only a few of them provide consistent approaches. Several CFD applications with inconsistent approaches and some common errors are as follows [43]:

- Use of a 1D model for modelling interfacial transfers in 2D or 3D CFD models;
- Use of a 3D two fluid models without any turbulence modelling;
- Use of averaged interfacial transfer coefficients in a DNS or LES models.

Another common mistake is to believe that an interface is deterministic when ITM is used, when in fact it is a filtered interface with degraded prediction of interface movement and deformation. Because of this error, there is no modelling for subgrid waves at large interfaces. In general, many attempts to combine two fluid models for dispersed flow with an ITM for large interfaces use a partial modelling of all the processes that a hybrid LES with filtered and statistical interfaces should include. The fundamental steps in a two fluid CFD analysis are as follows:

- Selection of the time and spatial filtering approach, if any;
- Selection of an interface treatment method consistent with previously adopted filtering approach;
- Selection of phases and/or fields required by phenomena to be investigated;
- Selection of adequate closure laws.

4.2. INTERFACE RESOLVING TECHNIQUES

Interface resolving, also called interface tracking techniques, are developed to capture the shape and topology of fluid–fluid interfaces. Thus, detailed, and transient phenomena related to liquid–gas free surface can be simulated. For example, deformation of bubbles and droplets is directly calculated together with the interfacial area, as shown in Fig. 23 (a). Meanwhile, in case of Euler–Euler (also known as Eulerian, phase averaged, or two fluids) method, the bubble interface cannot generally be captured, and only distributions of averaged volume fraction are computed, as illustrated in Fig. 23 (b). From Fig. 23 (a) one can intuitively understand the possibility of ITM to reproduce the real bubbly flow for example shown in Fig. 23 (c). In Eulerian model, since the bubble surface is not captured, all dynamics related to bubble motion are modeled. e.g., drag, lift, turbulent dispersion, wall lubrication, bubble diameter, interfacial area concentration etc., which introduces modelling uncertainties into simulations.

The main advantage of ITM is that it can resolve local phenomena, while its principal drawbacks are fine mesh required to capture small scale bubbles and droplets, unsteady simulation required for most flows, and occasional occurrence of numerical artifacts such as spurious currents [44] and numerical coalescence (i.e. instantaneous merger of two different bubbles whenever parts of their interfaces end up in the same mesh cell). Thus, the computation using ITM requires large computational resources such as a cluster computer. The comparison of ITM and Eulerian model is reviewed by Yadigaroglu [45]. Several types of ITMs are VOF [46], level set [47], front tracking [48], phase field [49], arbitrary Langrangian-Eulerian [50], to name just a few. In VOF, the volume of liquid and/or gas in a control volume is tracked in

volume conservative manner. In the level-set method, a distance function is transported in accordance with the fluid flow. This distance function represents the distance of the fluid–fluid interface from a mesh cell. In a front tracking method, the interface is explicitly represented by segments in 2D or polygons in 3D, and transported together with the phase fraction.

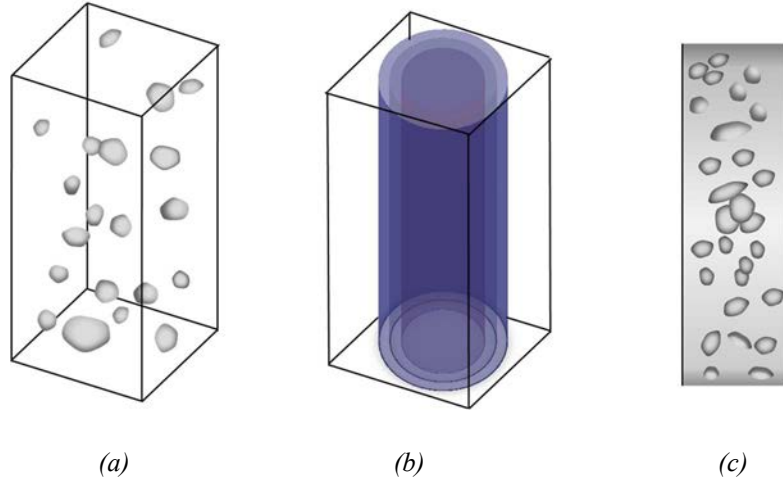


FIG. 23. Examples of bubbly flow: (a) computed with ITM; (b) computed with Eulerian method; (c) experimentally observed.

4.2.1. The volume of fluid method

4.2.1.1. Governing equations

The governing equations describing conservation of mass and momentum, namely the Navier–Stokes equations, are hereby recalled:

$$\frac{\partial}{\partial t} \rho + \nabla \cdot (\rho \mathbf{u}) = 0 \quad (218)$$

$$\frac{\partial}{\partial t} \rho \mathbf{u} + \nabla \cdot (\rho \mathbf{u} \otimes \mathbf{u}) = -\nabla p + \nabla \cdot (\mu_{eff} (\nabla \mathbf{u} + (\nabla \mathbf{u})^T)) + \mathbf{f}_b \quad (219)$$

where $\mu_{eff} = \mu + \mu_t$ is the effective viscosity, namely the sum of the molecular and turbulent viscosities assuming an eddy viscosity turbulence modelling. In a VOF method, density ρ and velocity \mathbf{u} represent weighted volume averages over both phases in each mesh cell. In practice, by defining a phase fraction α_i as fraction of volume V_i occupied by a phase i in a mesh cell of volume V , it follows:

$$\alpha_i = \frac{V_i}{V} \quad (220)$$

then, for a two phase system with phases labelled as l and v , by considering that $\alpha_v = 1 - \alpha_l$ for a two phase system and renaming $\alpha = \alpha_l$, it follows:

$$\rho = \alpha \rho_l + (1 - \alpha) \rho_v \quad (221)$$

$$\mathbf{u} = \frac{1}{\rho} (\alpha \rho_l \mathbf{u}_l + (1 - \alpha) \rho_v \mathbf{u}_v) \quad (222)$$

In contrast to Eulerian–Eulerian methods that solve conservation equations for both phases, in VOF method (and ITMs in general) a single continuity and momentum equations are solved and are thus representative of the overall two phase mixture mass and momentum conservation. Other mixture properties can be defined in a similar way, such as molecular viscosity of mixture:

$$\mu = \alpha\mu_l + (1 - \alpha)\mu_v \quad (223)$$

However, other averages can be employed instead of the arithmetic one, such as harmonic average given by the following Eq. (224):

$$\frac{1}{\mu} = \frac{\alpha}{\mu_l} + \frac{(1 - \alpha)}{\mu_v} \quad (224)$$

or an arithmetic average based on the continuity of tangential stresses (i.e., momentum conservative) at the interface given by the following Eq. (225):

$$\frac{\rho}{\mu} = \frac{\alpha\rho_l}{\mu_l} + \frac{(1 - \alpha)\rho_v}{\mu_v} \quad (225)$$

Regarding body force source term \mathbf{f}_b in Eq. (219), in VOF method it typically includes both gravity and surface tension forces. To consider the effect of buoyancy, the Boussinesq approximation is introduced to body force via density difference between liquid and vapor. The continuum surface force model by Brackbill [51] is usually used to represent the surface tension effect. The other surface tension model is continuum surface stress model [52], in which the force is introduced to the momentum equations via a stress tensor rather than the body force vector. The problem known as the spurious current can be seen in both models: continuum surface force and continuum surface stress models. By substituting ρ with ρ_l, ρ_v according to Eq. (221), and assuming that the flow is incompressible in the sense that the phasic densities are constant, the continuity equation can be reduced to:

$$\frac{\partial}{\partial t}\alpha + \nabla \cdot (\alpha\mathbf{u}) = 0 \quad (226)$$

In finite volume method, the (volume integral of the) divergence of $\alpha\mathbf{u}$ is calculated in terms of face sums of the value of $\alpha\mathbf{u}$ at mesh cell faces, meaning that it depends on the selected spatial discretization schemes. These are expanded later, as the phase fraction equation has some additional constraints on its solution, as the value of the phase fraction should always be bounded between 0 and 1. The choice of the spatial discretization scheme typically affects the solution behavior in terms of a tradeoff between boundedness and solution accuracy (numerical diffusion).

4.2.1.2. Phase fraction advection discretization

The difficulty with transport equation of the phase fraction, Eq. (226), lies in the errors associated with discretization of advection term. As an example, in 2D model, the transport of square phase fraction distribution (i.e., an idealized bubble with an initially square shape) is prescribed as uniform velocity field. The initial condition and the prescribed velocity are represented in Fig. 24 (a). Periodic boundary conditions are applied to all side boundaries. The time discretization is explicit, while the time step is set to have a Courant number of 0.25. The

solution using upwind scheme with a Superbee flux limiter (overall second order) is shown in Fig. 24 (b).

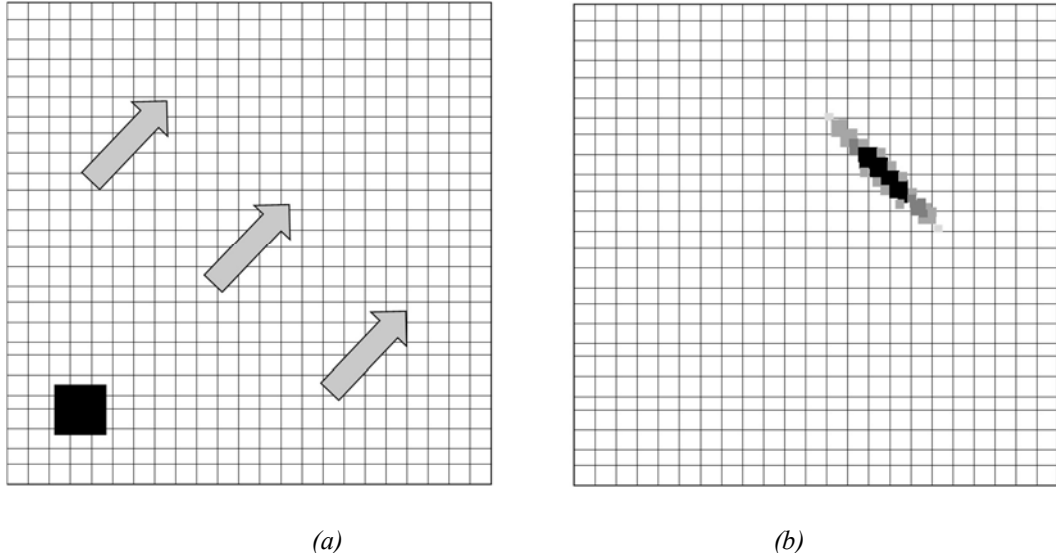


FIG. 24. (a) Initial phase fraction distribution (arrows indicating direction of uniform velocity field), (b) Final phase fraction distribution after certain time, subsequently to advection by uniform velocity field.

The problems of the solution phase fraction field are deformation of the shape and diffusion of the phase fraction distribution, meaning that the phase fraction gradient becomes smoother. These are the results of numerical errors that arise from the choice of spatial discretization made for the advective term. To avoid these, i.e., the deformation and diffusion, two types of VOF methods are proposed, the geometric and the algebraic VOF.

In geometric VOF, the value at the surface of the control volume is calculated based on the geometry of the interface. In case of piecewise linear construction approach [53], the interface topology is simplified to be a flat plane/line, as sketched in Fig. 25 (a). Based on Fig. 25 (b), the geometric shape coloured blue is transported in accordance with the velocity defined in each control volume. Since total area of the geometric shapes does not change, total mass is strictly satisfied. After the transport of the phase fraction, i.e., Fig. 25 (b), the interface topology is lost, yet the value of α is updated as sketched in Fig. 25 (c). Then, based on the α , the new interface topology is created, which is called reconstruction, as shown in Fig. 25 (d). The implementation of geometric VOF [54], although based on geometry only, is algorithmically complicated, but it is nonetheless implemented in commercial codes such as ANSYS Fluent.

The solution for 2D transport of the square using geometric VOF is displayed in Fig. 26. The condition of simulation is same as in previous case shown in Fig. 24 (a). The square is still deformed as it becomes rounded, but the deformation is smaller than that seen in Fig. 24 (b).

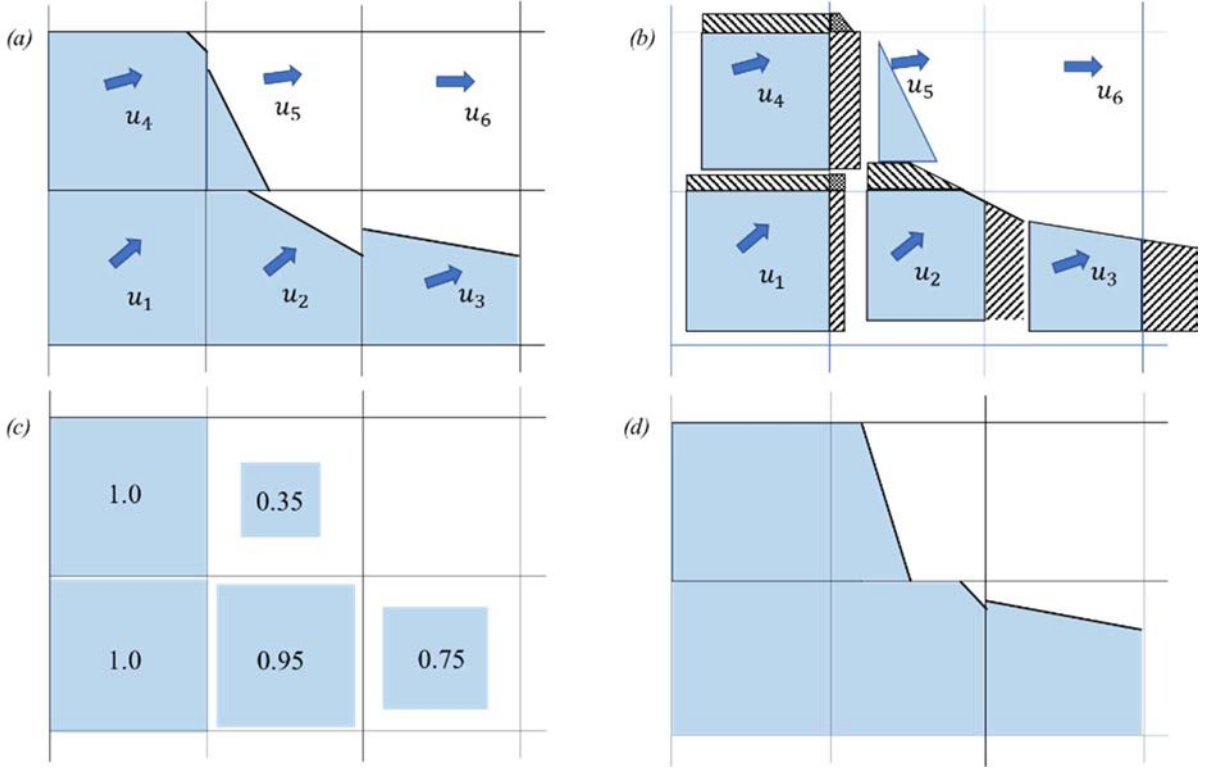


FIG. 25. Steps in the application of piecewise linear construction approach in 2D: (a) initial conditions wherein the interface in each cell is modelled by a linear segment, (b) transport of the phase polygons across mesh borders according to the velocity field, (c) update of the phase fraction values based on step (b), (d) reconstruction of new interface topology in each cell.

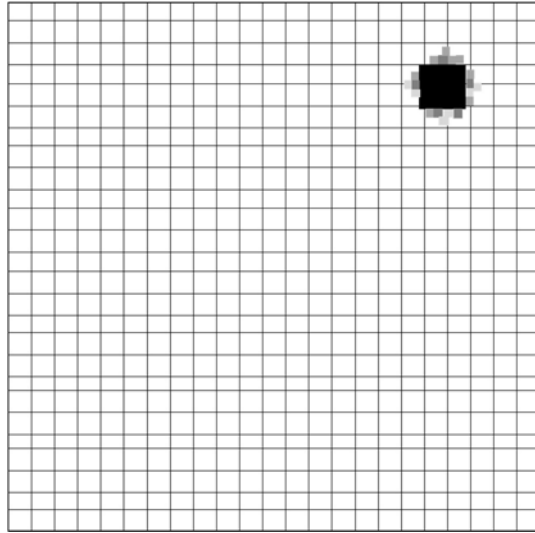


FIG. 26. Final phase fraction distribution after certain time, subsequently to advection by uniform velocity field starting from the conditions depicted in Fig. 24 (a).

The strategy to solve transport equation for the volume fraction without resorting any geometrical reconstructions is based on higher order spatial discretization schemes such as but not limited to high resolution interface capturing scheme [55], compressive interface capturing scheme for arbitrary meshes [56], constrained interpolation profile scheme [57], tangent of hyperbola for interface capturing [58]. The mass conservativeness is ensured by the schemes listed above. Compared to geometric VOF, the programming of these schemes is rather simple

when compared to the complex geometrical treatment for interface advection and reconstruction that geometric VOF entails. However, the smearing of a transported phase fraction shape can still occur in algebraic VOF approaches. To avoid this, a so called sharpening equation can be introduced in order to keep the interface thickness constant without changing the interface shape. This typically consists of an additional equation for phase fraction that is solved after the phase fraction conservation equation, Eq. (226). The actual implementation and reasoning that lies behind the construction of such sharpening equations vary between computer codes [59].

4.2.1.3. Surface tension modelling

In a continuum surface force model, the surface tension (that appears in f_b in Eq. (219)), is defined as:

$$\mathbf{f}_\gamma = \gamma \kappa \nabla \alpha \quad (227)$$

where γ is the value of the surface liquid tension and κ is a curvature calculated with:

$$\kappa = -\nabla \cdot \mathbf{n} = \left(\frac{\nabla \alpha}{|\nabla \alpha|} \right) \quad (228)$$

where \mathbf{n} is the surface normal of the interface between the two phases in each cell where an interface exists. It can be seen that the calculation of the curvature implies calculation of the gradient of the phase fraction, which typically changes from unity to null in the span of one or two mesh cells (particularly for sharp interfaces), as represented in Fig. 27. This means that calculated curvature typically suffers from numerical errors, which are greater for sharper interfaces, and the resulting errors give rise to so called spurious currents. These currents consist of actual momentum sources caused by an imbalance between pressure gradient and surface tension force. To reduce these errors, different approaches exist [60], [61].

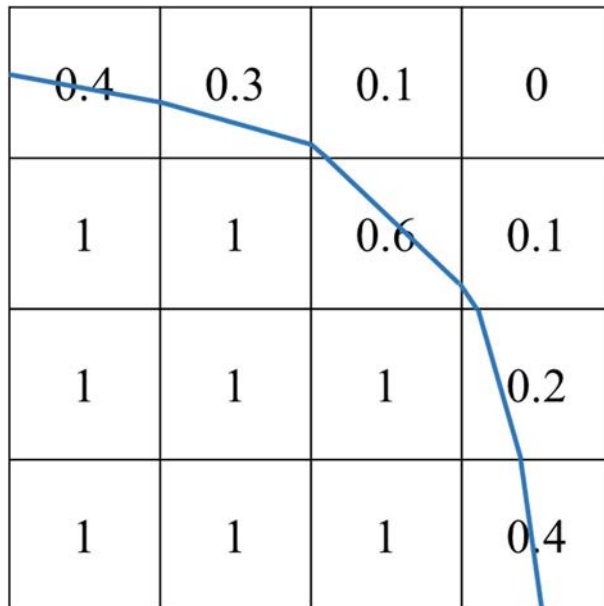


FIG. 27. Example of a fraction distribution in the computational cells around VOF interface.

4.2.2. Volume of fluid method for phase change

4.2.2.1. Governing equations

In case of boiling flows, the governing equations are modified to take the phase change into account. This manifests itself in the form of additional source terms in the continuity equation (to represent mass exchange) and in momentum equation (to represent momentum exchange associated with the phase change). By denoting with \dot{m} the mass exchange per unit volume, per unit time from the liquid phase l to the vapour phase v , by recalling that $\alpha = \alpha_l$, the mass conservation equation for the liquid phase therefore becomes:

$$\frac{\partial}{\partial t} \alpha \rho_l + \nabla \cdot (\alpha \rho_l \mathbf{u}) = -\dot{m} \quad (229)$$

Considering constant density flows, the phase fraction equation becomes:

$$\frac{\partial}{\partial t} \alpha + \nabla \cdot (\alpha \mathbf{u}) = -\frac{\dot{m}}{\rho_l} \quad (230)$$

which is formally identical to Eq. (226) except for a source term on the right hand side. It is worth noting that even for constant density flows, the divergence of the mixture velocity is not null if phase change occurs. To show this, by considering that $\alpha_v = 1 - \alpha_l = 1 - \alpha$, the vapour phase fraction conservation equations become:

$$\frac{\partial}{\partial t} (1 - \alpha) + \nabla \cdot ((1 - \alpha) \mathbf{u}) = \frac{\dot{m}}{\rho_v} \quad (231)$$

By subtracting the liquid phase fraction equation from the vapor phase fraction equation, it follows:

$$\nabla \cdot \mathbf{u} = \left(\frac{1}{\rho_v} - \frac{1}{\rho_l} \right) \dot{m} \neq 0 \quad (232)$$

Regarding the momentum equation, it is equal to Eq. (219) with the modification that the source term \mathbf{f}_b is inclusive of a momentum change due to the phase change. More specifically, it is inclusive of a recoil force \mathbf{f}_r due to the interface motion due to phase change, so that:

$$\mathbf{f}_r = \left(\frac{1}{\rho_v} - \frac{1}{\rho_l} \right) \dot{m}^2 \mathbf{n} \quad (233)$$

which also highlights the fact that such force is in the direction of the interface surface normal. While an energy equation is not typically entailed by the Navier–Stokes equations, an energy equation is nonetheless required when simulating phase change phenomena, as these are typically thermally driven phenomena. While there are many ways in which an energy equation might be formulated, a considered energy equation is with respect to mixture enthalpy $h = c_p(T - T_0)$, with T being mixture temperature, c_p mixture heat capacity and T_0 arbitrary reference temperature. Then, an enthalpy equation can be formulated with respect to the mixture temperature as:

$$\frac{\partial}{\partial t} (\rho c_p T) + \nabla \cdot (\rho c_p T \mathbf{u}) = \nabla \cdot (\kappa_{eff} \nabla T) + \dot{q} \quad (234)$$

with $\kappa_{eff} = \kappa + \kappa_t$ being the effective mixture thermal conductivity, given by the sum of turbulent and molecular mixture thermal conductivities and \dot{q} being the heat source associated with phase change. This source term is generally modelled as:

$$\dot{q} = -\dot{m}L \quad (235)$$

where L is the latent heat of evaporation and \dot{m} represents the liquid to vapour mass transfer rate as defined before, which is positive for evaporation and negative for condensation. The mass transfer rate can be computed in different ways, although the most popular is with heat conduction limited model. In this model, the mass transfer compensates for heat flux imbalances across the interface:

$$\dot{m} = \frac{\dot{q}_{il} + \dot{q}_{iv}}{L} \quad (236)$$

where \dot{q}_{il} and \dot{q}_{iv} represent heat flux from the liquid bulk to the interface and from the vapour bulk to the interface, respectively, in each computational cell. The interfacial heat fluxes are computed in each mesh cell as follows:

$$\dot{q}_{il} = \frac{S}{V} \kappa_l \mathbf{n} \cdot \nabla T \quad (237)$$

$$\dot{q}_{iv} = -\frac{S}{V} \kappa_v \mathbf{n} \cdot \nabla T \quad (238)$$

where S is the interface area in the computational cell, \mathbf{n} its surface normal and V the cell volume, as sketched in Fig. 28. This model is consistent with the fact that phase change occurs only in interfacial cells, the cells where $0 < \alpha < 1$, as $S = 0$ in mesh cells that do not contain an interface. It should be noted that heat conduction limited models are more readily employed in Euler–Euler multiphase treatments, wherein the definition of interfacial heat flux can take advantage of the actual phase temperature fields, instead of a mixture temperature such as in a VOF approach.

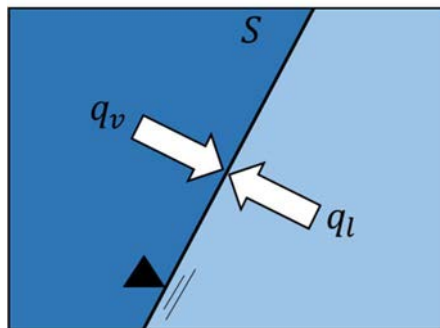


FIG. 28. Representation of heat fluxes from the bulk of each phase to the interface in an interfacial cell of volume V with total interface area S .

4.2.2.2. Nucleation site modelling

When simulating boiling starting from a single phase scenario, there is no numerical interface across which the mass transfer can be computed. Physically, in case of nucleate/heterogeneous boiling [62], vapor bubbles start to grow from nucleation sites, which are cavity or small gas trapped on wall. Since the cavities or the small gas bubbles trapped on walls are generally far

smaller than the computational mesh size, these cannot be directly resolved. Thus, it is necessary to use a mechanistic model, a nucleation site model. In this model proposed by Sato and Niceno [63] the location of nucleation sites along with nucleation activation temperature for each site is prescribed a priori on the heat transfer surface. When temperature at a particular nucleation site equals to its activation temperature value, a small vapor bubble (also known as seed bubble) is formed at the site. The seed bubble is assumed to be initially hemispherical in shape, the radius being typically one cell width of the underlying grid. The locations of nucleation site are set randomly using the random number generators. The activation temperature for each site is given in such a way that the given activation temperature agrees with correlation for nucleate site density, as per Kocamustafaogullari and Ishii [64], Hibiki and Ishii [65].

4.3. EULERIAN–EULERIAN METHOD

4.3.1. Introduction

The Eulerian–Eulerian method is a CFD method developed to model multiphase flows with the ability to provide reasonably accurate predictions of such flows at affordable computational cost. The multiphase flows can be regarded as a tessellation of single phase flow domains joined together through an interface at which mass, momentum and energy are transferred from one phase to the other. Each domain may have different properties, like density and viscosity, and may be in different thermodynamic states (hence, multiphase). Examples are bubbly flows in reactor primary cooling systems, oil/water flows in the petrochemical industry, stratified flows including those that can be observed in loss of coolant accidents [66] or particle/droplet flows like clouds, aerosols or pollutants in the atmosphere as can potentially be released during severe nuclear accidents. An example of different flow regimes of importance to nuclear engineering applications is exemplified in Fig. 29. In these applications, engineers would like to have tools to make predictive statements of the outcomes of such flows in terms of system performance, durability, robustness, efficiency, or impact. More specifically, in nuclear context, accurate modelling of such flows is pivotal in computationally driven optimization and safety assessments of reactor components, at both normal operation and during the accident conditions. The Eulerian–Eulerian method offers a platform to achieve such goals. From a macroscopic point of view, two phase interface is almost infinitesimally thin (it has some finite thickness, as for example modeled in diffuse interface methods). Thus, interfacial transfer processes are generally associated with length scale, which is prohibitively expensive to resolve with numerical method. Even if interfacial processes are considered in an averaged way, i.e., modelled from macroscopic perspective rather than from first principles, the multiphase structures that emerge in realistic flows still remain out of reach of contemporary computing power to be directly simulated as such. Interface resolving techniques, as suggested by their name, are designed to resolve multiphase structures. However, their use remains limited to simplified domains and/or to subproblems of realistic applications, always at moderate Reynolds numbers to allow for affordable mesh resolution. The challenge of modelling multiphase flows bears a resemblance with the challenge of modelling turbulent flows; in both problems one is limited by prohibitively small length and time scales that cannot be resolved directly. As for turbulent flows, averaging, as leveraged in the RANS or LES frameworks, is a way out of the computational impasse, the key idea being that computational requirement is exchanged with modelling effort (and, of course, associated modelling uncertainty). In the same spirit, the Eulerian–Eulerian method makes a similar trade off, by applying averaging to multiphase flows so that multiphase behavior is modeled. The Eulerian–Eulerian method formulation by considering the so called local instant formulation (LIF) to which the averaging is applied, gives rise to multiphase closure terms. In turn, those closure terms, capturing the

interfacial transfer processes of which an explicit formulation is lost in the averaging of the LIF, is described and includes an introduction to the treatment of interfacial mass, momentum and energy transfer models, as well as poly disperse size distribution models designed to describe the behavior of populations of bubbles, droplets or particles. The adequate modelling of multiphase closure terms stands at the heart of the Eulerian–Eulerian method and is, in fact, an area of research to which much scientific study is currently still dedicated.

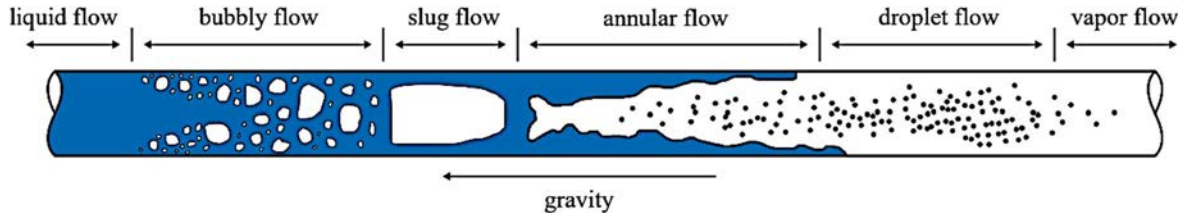


FIG. 29. Schematic of multiphase flow regimes encountered during boiling in a channel with heated walls.

4.3.1.1. Motivation and description of problems of interest in nuclear engineering

Typical designs of conventional water cooled nuclear reactor cores, such as in PWRs or BWRs, generally consist of vertically positioned fuel pin assemblies suspended in a primary coolant. The fuel pins generate heat because of fission, which is transferred to the primary coolant through the cladding of the fuel pins. The flow inside the core is from bottom to top. Fig. 29 shows a schematic overview of the multiphase flows that can be encountered during boiling in such a nuclear reactor core. More specifically, Fig. 29 portrays a simplified heated cylindrical subchannel conduit in which the primary coolant flow is from left to right so that gravity points from right to left. Realistic subchannels would have all sorts of complicated geometric features, such as vanes to promote flow mixing, assembly supports or wires with which fuel pins are wrapped to prevent damage from pin vibrations. Here, however, such complexities are not considered but an idealized conduit, which is sufficient to qualitatively explore typical subchannel flow phenomena. Fig. 29 considers scenario in which there is a sufficient heat transfer to the coolant to cause the boiling. This is, in principle, a desired situation in BWRs at normal operation, but highly undesired in PWRs, which keep the coolant at high pressure to avoid just that. Even so, also in PWRs boiling may occur in the core during accident scenarios, for example when the system is depressurized due to pipe breakage. In any case, the design and operation of the reactor should be such that sufficient heat is removed from the core to prevent dangerously high temperatures of the core inventory. Per Fig. 29, subcooled liquid enters the conduit and is heated. At some point, the onset of nucleate boiling point is reached. Microscopic bubbles are formed at the wall of the conduit, remain attached until grown sufficiently big to detach from the whole as a result of hydrostatic forces acting on it. While heat is being transferred from wall to liquid coolant, at some point in the conduit steam may evaporate onto the bubbles, which is called the onset of vapor generation. As temperatures increase, the coolant may reach and surpass the saturation temperature. From that point onward, boiling is much more significant, and bubbles may be formed not just at the wall but also in the fluid itself because of the onset of nucleate significant boiling. This leads to rapid growth of bubbles, which can migrate freely to the core of the conduit to coalesce into bigger bubbles and even form slugs. Higher up in the conduit the rapid formation of vapor leads to an increase in volume. In turn, the flow accelerates and starts to form a core of continuous steam enveloped by a film of liquid at the wall. Such flow is called annular flow. The film can be wavy, intermittently entraining steam or forming droplets which are then suspended in the steam, and which can evaporate or re-entrain back into the film. When there is enough heat put into the coolant that

the liquid film disappears, dry out of the conduit is established. This is an extremely dangerous situation, because the heat transfer from cladding to steam is much lower than from cladding to liquid coolant, thus resulting in a sharp increase of core inventory temperatures potentially leading to a meltdown. The heat flux at which dry out occurs is referred to as the CHF and is a key safety parameter of the nuclear reactor design. Assuming that the situation is stable, the droplets may still be suspended in the steam which, eventually, will evaporate altogether, leading to single phase superheated steam flow. The situation sketched in Fig. 29 displays a transition from single phase subcooled liquid (water) flow to single phase superheated vapor (steam) flow, by means of several multiphase flow regimes: bubbly, slug, annular and droplet flow.

4.3.1.2. Eulerian multiphase modelling methods

Four possible Eulerian modelling techniques applicable to core boiling problem are described in this section. FIG. 30 (a) depicts fully resolving modelling approach. In theory, one can model core boiling from first principles. In that case, all relevant length and time scales must be resolved, much like in DNS applied to turbulent flows. Clearly, this approach is superior in its accuracy, but it is prohibitively expensive. In practice, fully resolved approach is thus not very effective. Nevertheless, it is useful as fundamental starting point for the development of coarser models, resulting in a hierarchy of models that have a direct relationship with first principles and in which the assumptions and approximations that are made are mathematically clear. Fig. 30 (b) depicts a so called multiple flow regime Eulerian–Eulerian method [67]. For the flow in the core conduit, a spatial and temporal averaging of that flow over short space and time intervals can be imagined, possibly supplemented by ensemble averaging of different realizations of the same flow. In that case, small multiphase structures would no longer be visible as such, but would rather be smeared. It can be seen in Fig. 30 (b) that bubbles and droplets are no longer present as discrete elements but are rather captured by some sort of concentration or droplet density indicator. On the other hand, larger structures such as slugs or films would still prevail and can be captured using fully resolved like methods. Multiple flow regime Eulerian–Eulerian methods have only recently been under development and form a hybrid modelling approach leveraging accurate resolved techniques for structures that can be captured on coarse grids, and using conventional Eulerian–Eulerian method for structures that cannot be resolved.

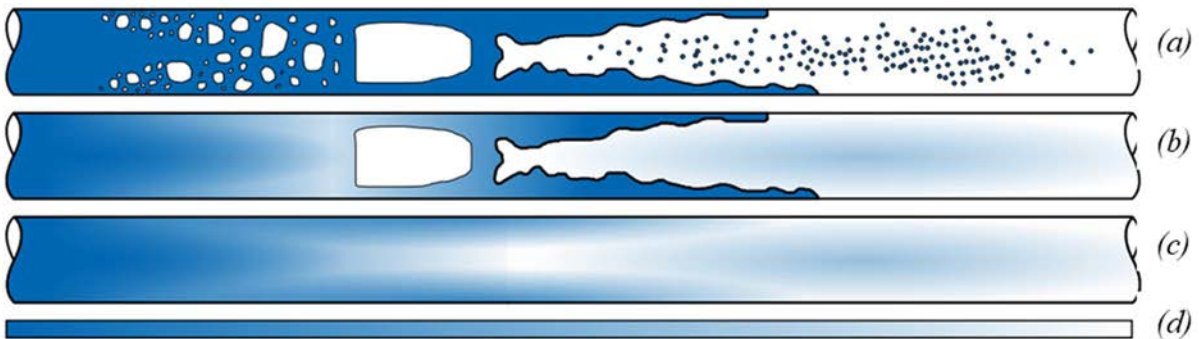


FIG. 30. Schematic overview of possible modelling techniques for the core boiling problem: (a) fully resolved, (b) multiple flow regime Euler–Euler, (c) Euler–Euler and (d) 1D thermal hydraulics system code.

Fig. 30 (c) represents a standard Eulerian–Eulerian method. By further reducing the model complexity compared to multiple flow regime Eulerian–Eulerian method, one can apply a full temporal averaging (and a partial spatial averaging as imposed by a coarse computational grid).

This would result in 3D representation of a flow field in which all multiphase structures are averaged. As a result, the interfacial mass, momentum, and energy transport need to be modeled by incorporation of appropriate source terms in their respective conservation equations. These source terms are subject to prevailing multiphase flow regime, which is no longer immediately obvious but can potentially be inferred from spatial gradients in the flow fields. The Eulerian–Eulerian method offers an affordable balance between accuracy and cost for many real world industrial multiphase problems. The multiple flow regime Eulerian–Eulerian methods rely heavily on the models that are originally developed in the Eulerian–Eulerian framework. Fig. 30 (*d*) presents a type of thermal hydraulics representation attainable by 1D Eulerian analysis, which is commonly adopted in the system codes. A full spatial averaging along the cross section of the conduit then can be applied. This would result in 1D description of the flow, in which special geometric features of the conduit itself can no longer be incorporated as is. Moreover, whereas in Eulerian–Eulerian models the prevailing flow regime could be inferred from 3D spatial information, this is no longer the case for thermal hydraulics system codes, thus fully relying on empirical flow regime maps. The thermal hydraulics system code approach is almost exclusively the only method used in the nuclear industry to model complete reactor systems. It is relatively fast, allowing for fast evaluations of a range of flow scenarios.

This discussion helps to position Eulerian–Eulerian methods within the hierarchy of multiphase Eulerian methods. The conclusions extend readily to multiphase flow problems other than boiling in a core. Next, before embarking on the actual model development, we first consider what Eulerian means and how it relates to Lagrangian multiphase methods as a further extension of what was discussed in Section 2.2.

4.3.1.3. Eulerian and Lagrangian modelling strategies

The Eulerian description of a system is attributed to Leonhard Euler (1707–1783). It generally considers a system from a fixed reference frame and involves fields of variables. The Lagrangian description of a system, on the other hand, is attributed to Joseph–Louis Lagrange (1736–1813) and considers a system with respect to a moving reference frame attached to that system. The two phase Eulerian–Eulerian method, as the name suggests, thus adopts an Eulerian description for both phases. This method, however, is also used by interface resolving models (like VOF or level set as discussed in other chapters), but these are, perhaps quite ambiguously, not part of the Eulerian–Eulerian class of methods. What is characteristic to Eulerian–Eulerian method is that the two phase structures, which are usually of a dispersed nature, are unresolved as the result of averaging or filtering. The terminology of Eulerian, Lagrangian and resolved, unresolved gives rise to four types of two phase modelling strategies:

- *Resolved Eulerian*. The system is described from Eulerian point of view and two phase interface is resolved. Usually, in addition to the mass, momentum and energy conservation equations, an indicator function advection equation is solved. This holds for so called one equation models like VOF or level set. The indicator function determines the phase which locally prevails. The interface is localized, and interfacial mass and energy transfer can be modeled. Resolved Eulerian methods are relatively straight forward in their use for highly deforming interfaces, as the computational grid can remain fixed throughout the course of the simulation.
- *Resolved Lagrangian*. Two phase structures, like particles, are fully resolved and an equation of motion for each particle is solved by an integration of the forces acting on the structure. The carrier phase is often still treated with Eulerian model. Resolved Lagrangian methods are useful for when the typical size of two phase structures is larger

than the smallest length scales of the turbulent flow (i.e., the Kolmogorov length scale). In that case it is important that the wake induced by flow around the structure is modeled, which means that the structure must be resolved. The resolved Lagrangian approach is attractive when the two phase structure does not deform much, e.g., in the case of solid particles, or bubbles and droplets that have high sphericity as a result of large surface tension.

- *Unresolved Lagrangian.* In dispersed two phase flow regimes where the typical length scale of the dispersed structures is smaller than the Kolmogorov length scale, the effect of the dispersed structures on the carrier phase, and vice versa, can be appropriately modeled by considering the structures as unresolved point particles. For each particle, a Lagrangian equation of motion is then solved considering a number of forces that act on the particle. As such, all mass, momentum, and energy transfer are subgrid. Unresolved Lagrangian methods are useful for particle laden flows like particulate flows or aerosol flows, with many disperse elements. Non sphericity of the particles can be included in the subgrid transfer models.
- *Unresolved Eulerian.* Finally, by extension of the former, unresolved Eulerian methods treat the two phase structures in an unresolved way too, but from the Eulerian point of view. The unresolved Eulerian method is synonymous to Eulerian–Eulerian method. In comparison to the other three modelling frameworks, Eulerian–Eulerian method is probably the most generic in the sense that it can deal with a large array of two phase flow regimes at relatively large scale, by it does not explicitly track anything like Lagrangian methods. Nevertheless, this may come at the price of relatively large modelling uncertainty.

4.3.2. Eulerian–Eulerian modelling theory

The general Eulerian–Eulerian method formulation is derived in this section starting from the LIF. The LIF is not very practical in its direct use but offers solid mathematical foundation for the derivation of the Eulerian–Eulerian method formulation.

4.3.2.1. Local instantaneous formulation

A volume Ω shown in Fig. 31 is composed of gas with the volume Ω_g and liquid of volume Ω_l . The gas and liquid volumes are strictly separated by an interfacial surface Γ_i , and do not overlap. Using separation of phases, the state of each phase in terms of local instant variables can be defined as $F_k(\mathbf{x}, t)$, where F is the variable of interest, subscript k denoted either liquid phase l or gas phase g , \mathbf{x} is a position vector in the chosen coordinate system and t is the time. The variable F_k is only defined if phase k is present at (\mathbf{x}, t) . For convenience, it is set to zero otherwise. In Ω_k , a phase k of mass density $\rho_k(\mathbf{x}, t)$, phase k velocity $\mathbf{u}_k(\mathbf{x}, t)$, phase k pressure $p_k(\mathbf{x}, t)$ and phase k internal energy $e_k(\mathbf{x}, t)$ are defined so that the standard single phase conservation equations for mass, momentum, and energy are:

$$\frac{\partial}{\partial t} \rho_k + \nabla \cdot (\rho_k \mathbf{u}_k) = 0 \quad (239)$$

$$\frac{\partial}{\partial t} \rho_k \mathbf{u}_k + \nabla \cdot (\rho_k \mathbf{u}_k \otimes \mathbf{u}_k) = -\nabla p_k + \nabla \cdot \boldsymbol{\sigma}_{d,k} + \rho_k \mathbf{g} \quad (240)$$

$$\frac{\partial}{\partial t} \rho_k e_k + \nabla \cdot (\rho_k e_k \mathbf{u}_k) = -\nabla \cdot \dot{\mathbf{q}}''_k + \nabla \cdot (\boldsymbol{\sigma}_k \cdot \mathbf{u}_k) + \rho_k \mathbf{g} \cdot \mathbf{u}_k + \dot{q}_k \quad (241)$$

wherein $\sigma_{d,k}$ is the deviatoric stress tensor defined in Eq. (51), $\dot{\mathbf{q}}''_k = \kappa_k \nabla T_k$ is the heat flux, $\sigma_k = -p_k \mathbb{I} + \sigma_{d,k}$ is the total stress tensor and \dot{q}_k is a volumetric heat source term. For each phase, these equations need to be closed using constitutive equations. More precisely, an equation of state has to be introduced which relates density to pressure and temperature, such as the ideal gas law or an incompressible equation of state. In turn, the temperature must be related to the internal energy, which is usually done with a heat capacity coefficient. Finally, mechanical, and energetic constitutive equations need to be introduced. Examples are the Newtonian assumption for momentum diffusion, setting the shear stress proportional to the gradient of velocity, or Fourier's law for heat diffusion, setting the heat flux proportional to the gradient of temperature. It is assumed here that these relations are known. Further discussion is out of scope, and the reader is referred to Bird et al. [68] for more details.

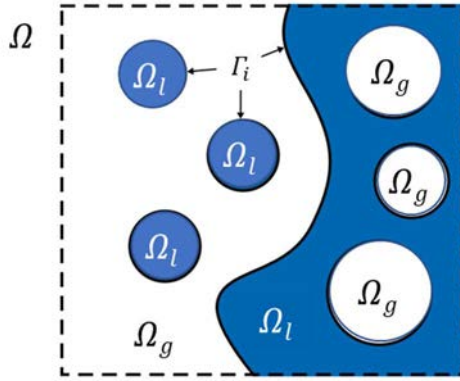


FIG. 31. Schematic of two phase system of total volume Ω (gas volume Ω_g and liquid volume Ω_l are bounded by interface Γ_i).

While the interface Γ_i does not contain any mass, it does have a velocity \mathbf{u}_i with which it propagates throughout the domain. Moreover, it can have an interfacial energy \mathbf{u}_i . Across the interface, which locally has a normal \mathbf{n}_k pointing into phase k , we have a mass conservation equation:

$$\sum_{k \in (g,l)} \dot{m}''_k = 0 \quad (242)$$

where

$$\dot{m}''_k = \rho_k \mathbf{n}_k \cdot (\mathbf{u}_k - \mathbf{u}_i) \quad (243)$$

where \dot{m}''_k thus represents the net mass influx ($\text{kg}/\text{m}^2/\text{s}$) into phase k . The Eq. (243) states that whenever the velocity of the fluid in the immediate neighborhood of the interface is different than the velocity of the interface itself, mass transfer is occurring. Similarly, momentum conservation at the interface can be stated in terms of a balance of forces per unit interface area (i.e., in terms of pressures) as:

$$\sum_{k \in (g,l)} (\dot{m}''_k \mathbf{u}_k - \mathbf{n}_k \cdot \sigma_{d,k}) + \Delta p_\gamma = 0 \quad (244)$$

where the first term under the summation accounts for pressure associated with the transfer of mass, the second term accounts for pressure due to mechanical stress and the third term is the

pressure due to the surface tension (given by the Young–Laplace equation). Note that if there is no phase change, a non-zero surface tension term must be balanced by a difference in mechanical stress across the interface, in order to satisfy Eq. (244). An interfacial energy conservation equation can as well be formulated. However, since the interface may hold non zero energy e_i (unlike momentum, because it has zero mass), the interfacial energy conservation equation becomes an advection equation for \mathbf{u}_i :

$$\frac{\partial}{\partial t} e_i + \mathbf{u}_i \cdot \nabla \mathbf{u}_i = \sum_{k \in (g,l)} (\dot{m}'_k e_k - (\mathbf{n}_k \cdot \boldsymbol{\sigma}_{d,k}) \cdot \mathbf{u}_k + \Delta p_\gamma \cdot \mathbf{u}_k) \quad (245)$$

where the first term represents the energy transfer associated with mass transfer, the second term is the energy transfer due to mechanical stress, the third one is due to heat flux (e.g., conduction) and the last one is due to surface tension. Note that the field e_i may act as a buffer in which energy is stored or from which energy can be extracted.

The set of equations Eq. (240) through Eq. (245), complemented by the required constitutive equations/laws, is a fully closed system that may be solved numerically. However, in the following section it is shown how to use it as a mathematical foundation for the derivation of the Eulerian–Eulerian method, by making use of volume averaging.

4.3.2.2. Volume averaging

In most cases, the LIF is much too complicated for realistic situations, because multiple deformable interfaces are complicated to capture accurately, all time and length scales need to be resolved and significant discontinuities of properties may lead to numerical instabilities. However, the detail that is offered by the LIF is typically not needed, particularly for engineering purposes. Thus, by proper averaging of the LIF a model reduction can be achieved which eliminates the three challenges associated with the LIF. In turn, instead of solving for local instant fields $F_k(\mathbf{x}, t)$ we reduce the problem to be defined in averages \overline{F}_k , where the overline, or bar, denotes an averaging operator. A spatial averaging operator is defined over an arbitrary domain Ω_s (which might be a volume as well as a surface, e.g., a cross section perpendicular to a flow direction) as follows:

$$\overline{F}_k(t) = \frac{1}{|\Omega_s|} \int_{\Omega_s} F_k(\mathbf{x}, t) d\mathbf{x} \quad (246)$$

The result of averaging over the cross section of a subchannel is shown in Fig. 30 (d). A temporal averaging operator, on the other hand, is given by:

$$\overline{F}_k(\mathbf{x}) = \frac{1}{|\Omega_t|} \int_{\Omega_t} F_k(\mathbf{x}, t) dt \quad (247)$$

in which Ω_t is the temporal domain (i.e., time interval) over which the average is taken. The result of temporal averaging is shown in Fig. 30 (c). Finally, we can also apply a spatial filtering operator, as defined by:

$$\overline{F}_k(\mathbf{x}_a, t_b) = \frac{1}{|\Omega_{s,a}|} \frac{1}{|\Omega_{t,b}|} \int_{\Omega_{s,a}} \int_{\Omega_{t,b}} F_k(\mathbf{x}, t) dx dt \quad (248)$$

with a, b being indices of the spatial and temporal subdomains of Ω_s, Ω_t under consideration. A straightforward example in a computational setting would be a single mesh cell as a spatial subdomain of the overall spatial domain of interest and a single time step as a temporal subdomain of the overall time domain of interest. As previously discussed in Section 2.6, the nature of the finite volume method (based on which most Eulerian–Eulerian method are numerically developed) consists of an integration over discrete volumes and time steps, much like the filtering operation described in Eq. (248).

Averaging in two phase systems, however, is more complex than simply applying the averaging operators to the conservation equations. It is convenient to define special two phase averaging operators which apply certain weighting to distinguish between the phases. In this way, separate conservation equations can be derived for each phase. Such averaging operators are needed in order to keep the conservation equations for the averages interpretable and meaningful. $M_k(\mathbf{x}, t)$ representing the instantaneous indicator function of phase k is defined as follows:

$$M_k(\mathbf{x}, t) = \begin{cases} 1 & \text{if phase } k \text{ is present at } (\mathbf{x}, t) \\ 0 & \text{otherwise} \end{cases} \quad (249)$$

The average phase k volume and/or time fraction (depending on the definition of the averaging operator) is defined as:

$$\alpha_k = \overline{M_k} \quad (250)$$

The quantity α_k is important as it describes how much fraction of phase k there is in the averaging domain. Using the indicator function, more formally the generic phase k quantity F_k can be written as follows:

$$F_k(\mathbf{x}, t) = M_k(\mathbf{x}, t)F(\mathbf{x}, t) = \begin{cases} F(\mathbf{x}, t) & \text{if phase } k \text{ is present at } (\mathbf{x}, t) \\ 0 & \text{otherwise} \end{cases} \quad (251)$$

Thus, F_k can be understood as an instantaneous value of a global field F filtered by the presence of phase k . To clarify this with an example, fluid velocity is taken as an example. At a physical level, each point in space and time (\mathbf{x}, t) is characterized by the presence of a single phase. Thus, one can think of the velocity field \mathbf{u} as a single field that, at each point in space and time (\mathbf{x}, t) , describes the velocity of a fluid phase that occupies that point in space and time. Conversely, one can imagine separate velocity fields \mathbf{u}_k , one for each fluid phase, that describe the velocity of phase k at each point in space and time, such that the field is different than zero only within the spatial and temporal subdomains that are occupied by phase k . Using these results, the phase average of phase k becomes:

$$\overline{\overline{F}_k} = \frac{\overline{M_k F_k}}{\overline{M_k}} = \frac{\overline{F_k}}{\alpha_k} \quad (252)$$

This special two phase averaging operator, called phase average or intrinsic average, expresses the average of F by only taking into account F whenever phase k is present at the point (\mathbf{x}, t) that belongs to the spatial and temporal subdomains of interest to the averaging. A very simple example would be a two phase system in which the gas phase has constant temperature T_g and the liquid phase has constant temperature T_l . The phase average of temperature T , i.e., T_k , is then equal to T_g for $k = g$ and to T_l for $k = l$. In the same spirit as the phase average, the mass weighted average is defined as follows:

$$\hat{F}_k = \frac{\rho_k F_k}{\bar{\rho}_k} = \frac{\overline{\rho_k F_k}}{\overline{\bar{\rho}_k}} \quad (253)$$

The reason for weighting F with density ρ is that the quantities represented by F are generally expressed in specific terms (i.e., per unit mass), so that mixture values can be calculated as:

$$\hat{F} = \frac{\sum_k \alpha_k \overline{\rho_k} \hat{F}_k}{\sum_k \alpha_k \overline{\rho_k}} \quad (254)$$

4.3.2.3. Two fluid model: averaging the local instantaneous formulation

With these operators as tools, the LIF conservation equations can be averaged for each phase k . As an illustration, the averaging is discussed for the mass conservation equation, Eq. (239). Applying the averaging operator, and assuming that this operator is commutative (e.g., the divergence of the average is the average of the divergence), it follows:

$$\frac{\partial}{\partial t} \overline{\rho_k} + \nabla \cdot (\overline{\rho_k} \overline{\mathbf{u}_k}) = 0 \quad (255)$$

Considering relationship between the average and the phase average established by Eq. (252) it follows that $\overline{\rho_k} = \alpha_k \overline{\bar{\rho}_k}$, and using the mass weighted average $\overline{\rho_k \mathbf{u}_k} = \alpha_k \overline{\bar{\rho}_k} \hat{\mathbf{u}}_k$. Introducing these two relationships in the averaged mass conservation equations it is possible to show that:

$$\frac{\partial}{\partial t} \alpha_k \overline{\rho_k} + \nabla \cdot (\alpha_k \overline{\bar{\rho}_k} \hat{\mathbf{u}}_k) = \Lambda_k \quad (256)$$

where Λ_k represents an interfacial mass transfer term which appears whenever a liquid–gas interface falls within the spatial and temporal subdomains used for the averaging. When inspecting Eq. (256), it can be observed that this form is very similar to the phase k LIF mass conservation equation Eq. (239). It is convenient, because it has products of averages and not averages of products (unlike the original averaged mass conservation equation, Eq. (255)). This is purely a result of the choice of the phase density ρ_k and phase velocity $\hat{\mathbf{u}}_k$. Conversely, if the averaged mass conservation equation is to have a form like Eq. (256) in which the products of averages exist, then the density has to carry the meaning of a phase average and the velocity the meaning of a mass weighted average. In the same way as for the mass conservation equation, the phase k averaged momentum and energy conservation equations can be derived [69]. The phase k averaged momentum equation is given by:

$$\begin{aligned} \frac{\partial}{\partial t} \alpha_k \overline{\bar{\rho}_k} \hat{\mathbf{u}}_k + \nabla \cdot (\overline{\bar{\rho}_k} \mathbf{u}_k \otimes \mathbf{u}_k) \\ = -\alpha_k \nabla \overline{\bar{p}_k} + \nabla \cdot (\alpha_k (\overline{\sigma_{d,k}} + \boldsymbol{\sigma}_{t,k})) + \alpha_k \overline{\bar{\rho}_k} \mathbf{g} + \mathbf{M}_k \end{aligned} \quad (257)$$

with interfacial momentum transfer term \mathbf{M}_k and turbulent stress tensor $\boldsymbol{\sigma}_{t,k}$ which results from the application of the averaging operator to the non linearity of the convective term, the discussion of which is out of the scope for this section and for which the reader is referred to Section 3 or to Wilcox [70], or Durbin [71].

The phase k averaged energy equation is given by:

$$\begin{aligned} \frac{\partial}{\partial t} \alpha_k \overline{\rho}_k \hat{e}_k + \nabla \cdot (\alpha_k \overline{\rho}_k \hat{e}_k \hat{\mathbf{u}}_k) \\ = -\nabla \cdot \left(\alpha_k \left(\overline{\dot{\mathbf{q}}''}_k + \dot{\mathbf{q}}''_{t,k} \right) \right) + \nabla \cdot (\alpha_k \overline{\sigma}_{d,k} \cdot \mathbf{u}_k) + \alpha_k \overline{\rho}_k \mathbf{g} \cdot \hat{\mathbf{u}}_k \\ + E_k \end{aligned} \quad (258)$$

with an interfacial energy transfer term E_k and turbulent heat flux $\dot{\mathbf{q}}''_{t,k}$ for which a description is omitted here for the same reason as for $\sigma_{t,k}$. The set of mass, momentum and energy conservation equations, Eq. (256) through Eq. (258), for $k \in (g,l)$ constitute the popular Eulerian–Eulerian two fluid model. It is called that way because each fluid is modeled separately and is subject to its own set of conservation equations. These conservation equations are generally coupled to each other by the modelling choices underpinning the interfacial transfer terms. Upon comparison against the set of LIF conservation equations, Eq. (239) through Eq. (241), the following key differences can be observed:

- Conservation equations in Eulerian–Eulerian method are defined in terms of the rate of change of void fraction weighted quantities, $\alpha_k \overline{\rho}_k$, $\alpha_k \overline{\rho}_k \hat{\mathbf{u}}_k$ and $\alpha_k \overline{\rho}_k \hat{e}_k$, i.e., phase k mass, phase k momentum and phase k total energy, respectively. As a result of the averaging, a statistical coexistence of both phases is obtained. It is said that the two fluid model, and by extension the Eulerian–Eulerian method, allows for interpenetrating phases, as can also be observed in Fig. 30 (c). This is probably the most important concept of the Eulerian–Eulerian method; locally, the two phase flow is modeled as a mixture of phase concentrations.
- Averaging has introduced a turbulent momentum and heat flux, which must be modeled in a RANS or LES context, depending on the chosen averaging operator.
- Conservation equations are extended to include interfacial mass, momentum, and energy transfer terms Λ_k , \mathbf{M}_k and E_k . These transfer terms, often referred to as closure terms, model the effect of the averaged interfacial conservation equations that were explicitly available in the LIF, but were lost throughout the averaging process. Because of conservation, it follows:

$$\sum_{k \in (g,l)} \Lambda_k = 0 \quad (259)$$

$$\sum_{k \in (g,l)} \mathbf{M}_k = 0 \quad (260)$$

$$\sum_{k \in (g,l)} E_k = 0 \quad (261)$$

where Eq. (260) is valid only if neglecting surface tension forces [69].

The adequate modelling of multiphase closure terms stands at the heart of the Eulerian–Eulerian method. We note that much of the formal averaging notation used in Eq. (256) through Eq. (258), such as the overlines and hats, is dropped in many works so that the meaning of variables is only implied. Nevertheless, the set Eq. (256) through Eq. (258) constitutes the proper definition of the Eulerian–Eulerian method two fluid model and may be convenient in the interpretation of models in works that adhere to a less strict notation. The two fluid model treats each phase separately and, as such, reports phase specific quantities. However, in many engineering problems the behavior of the two phase mixture is of interest and not so much the behavior of individual phases. Fundamentally, the drift flux model considers the mixture, instead of two phases separately. This yields a simpler formulation than the two fluid model, however it requires drastic assumption which may not necessarily hold in situations where

coupling between the two phases, and thus explicit knowledge of phase specific quantities, is needed. As the basic idea of the Eulerian–Eulerian method is sufficiently illustrated by the two fluid model [69]. As was previously observed, the LIF is complicated due to presence of deformable interfaces, expensive due to the presence of small time and length scales and numerically challenging due to strong discontinuities in variables. These three drawbacks have effectively been removed by averaging, resulting in the two fluid or drift flux Eulerian–Eulerian methods. This comes with a need to develop suitable models for the closure terms needed to model turbulence and interfacial mass, momentum, and energy transfer. While the former is subject to classical turbulence modelling theory which can be studied mostly in a single phase setting, the latter is specific to the Eulerian–Eulerian method and requires much more attention. In the next Section, the modelling of interfacial transfer is described.

4.3.3. Interfacial transfer closure

The Eulerian–Eulerian method introduces a formulation in which phases are interpenetrating. Locally, there is a statistical coexistence of two phases in the sense that on average (referring to the choice of the averaging operator, namely time, space, ensemble, or mixed average) there are to some extent both phases present. In the two fluid model, each phase adheres to its own set of conservation equations which are coupled via interfacial mass, momentum, and energy transfer terms. These transfer terms should reflect the actual two phase physics that were filtered out in the averaging process. However, this is where a problem arises. Namely, from the two volume fractions α_k with $k \in (g, l)$, it is not necessarily possible to infer the actual two phase flow regime. For example, the averaged solution may be that of a slug flow but may also be that of a bubbly one. Most Eulerian–Eulerian method make an assumption on the two phase flow regime and adhere to that choice statically, and therefore, are tailored to the two phase flow regime that is to be expected a priori. More advanced methods will have some sort of regime map or other decision mechanism, based on which the models underpinning the interfacial transfer closures are dynamically adjusted to reflect the actual two phase flow regime. Eulerian–Eulerian methods are mostly used (but certainly not exclusively) for dispersed flows. Within that context, there are commonly used dispersed interfacial transfer closures for mass, momentum, and energy. Instead of using the subscripts g and l for two phases, the two phases are distinguished with more general subscripts c for the continuous phase (sometimes also referred to as carrier phase) and d for dispersed phase (e.g., bubbles and droplets). This makes the theory applicable to all types of dispersed flows like bubbly flow, droplet flow or solid particle flow.

4.3.3.1. Interfacial momentum transfer closure

The momentum transfer closure term \mathbf{M}_d captures the momentum transfer from the continuous phase onto the dispersed phase through the interface between two phases. Conversely, by extension of Eq. (260), \mathbf{M}_c captures the momentum transfer from the dispersed phase onto the continuous phase. A strategy in modelling \mathbf{M}_d is to consider the forces acting on a single dispersed particle (particle refers to bubbles, droplets, or solid particles altogether) and to then multiply those forces by the number of particles per unit volume, i.e., particle number concentration N . Assuming that dispersed particles are mono dispersed (i.e., having the same volume), by denoting the average particle volume with v , the number concentration is then given with:

$$N = \frac{\alpha_d}{v} \quad (262)$$

In case of poly dispersed size distribution, this relation still holds if v represents an appropriate average particle volume. Let $\mathbf{F}_d(\mathbf{x}, t)$ be the sum of all forces locally exerted from continuous phase to dispersed phase on a particle with volume v , then the interfacial momentum transfer term is given as follows:

$$M_d(\mathbf{x}, t) = N\mathbf{F}_d(\mathbf{x}, t) = \frac{\alpha_d}{v} \sum_i \mathbf{F}_{d,i}(\mathbf{x}, t) = \sum_i \mathbf{M}_{d,i}(\mathbf{x}, t) \quad (263)$$

in which $F_{d,i}(\mathbf{x}, t)$ for $i \in (1, \dots, N_f)$ are the N_f individual forces acting on a single particle, and $M_{d,i}(\mathbf{x}, t)$ are the respective individual momentum transfer terms.

Drag force

The most important force, by virtue of its relative magnitude, is the drag force. It expresses the resistance felt by a particle as it moves through the continuous phase. The drag momentum transfer term can be expressed as:

$$\mathbf{M}_{d,drag} = \frac{3}{4} C_D \frac{\alpha_d \rho_c}{d} |\mathbf{u}_c - \mathbf{u}_d| (\mathbf{u}_c - \mathbf{u}_d) \quad (264)$$

where d is particle diameter, ρ_c is continuous phase mass density and C_D is drag coefficient. The drag coefficient models the resistance of the particle against motion relative to the continuous phase, and it is a function of the object shape and the dispersed particle Reynolds number defined as:

$$Re_d = \frac{\rho_c |\mathbf{u}_c - \mathbf{u}_d| d}{\mu_c} \quad (265)$$

with continuous phase dynamic viscosity μ_c . The dispersed Reynolds number uniquely characterizes the flow dynamics around the particle, and therewith controls the effective drag coefficient. Fig. 32 shows the classical drag coefficient curve for a spherical particle as function of the dispersed Reynolds number [72].

A schematic depiction of the flow pattern transition around a spherical particle as a function of increasing dispersed Reynolds number is shown in Fig. 33. For very small Re_d , the flow is viscous and does not detach from the particle. Streamlines are smooth. This regime is called Stokes flow, and the drag coefficient is then known to be inversely proportional to the Reynolds number:

$$C_D = \frac{24}{Re_d} \quad (266)$$

which is a well known law analytically derived by Sir George Stokes in 1851. Substituting this expression into Eq. (264) and using the definition of Re_d , it is shown that the drag force is linearly proportional to the relative velocity difference between the phases $\mathbf{u}_c - \mathbf{u}_d$, and inversely proportional to d^2 . This linearity in the relative velocity allows for simple analytical solutions of, e.g., the sedimentation velocity of small particles. However, such solutions only hold in the linear Stokes flow regime. As Reynolds number increases, streamlines remain smooth with an asymmetry observed in the flow. This is associated with drag coefficient that is no longer inversely proportional to Re_d as seen in Fig. 32.

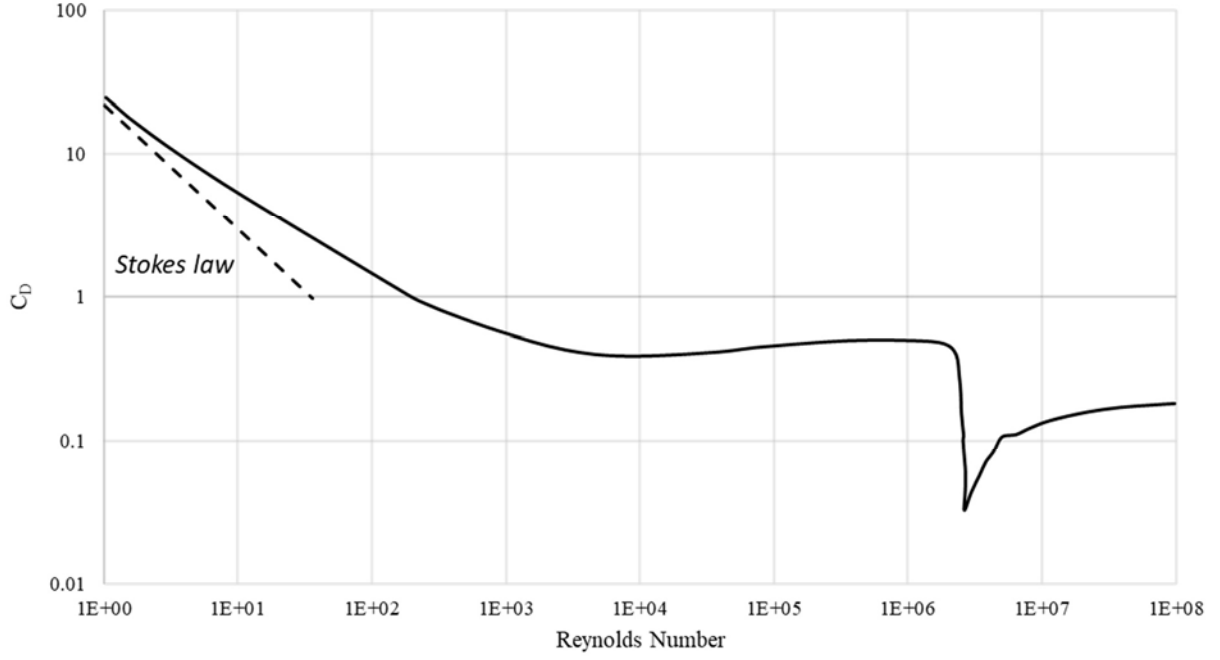


FIG. 32. Drag coefficient curve for a spherical particle (as presented in [72]).

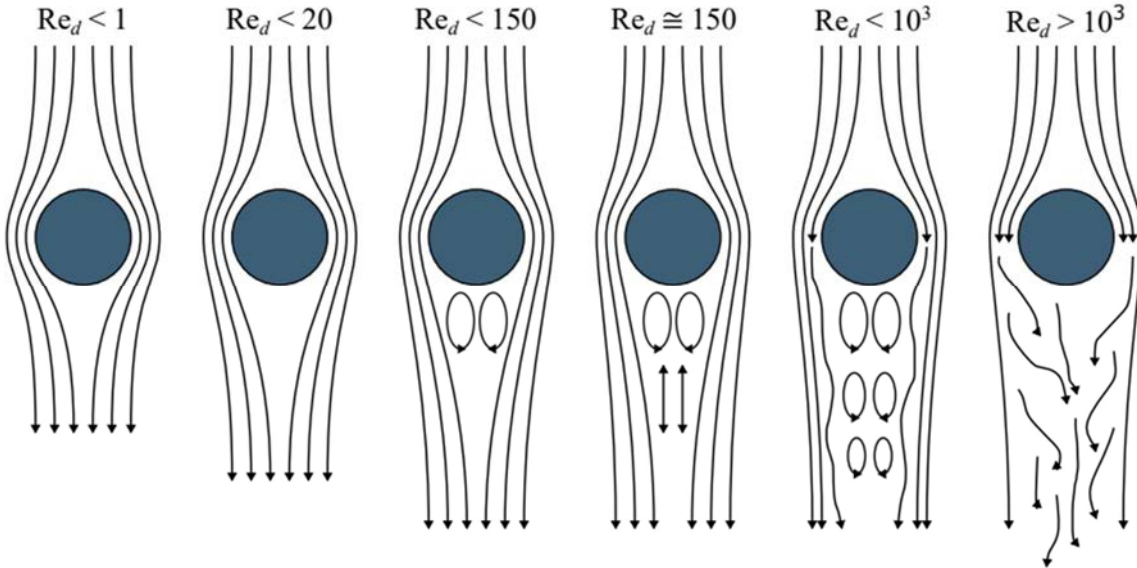


FIG. 33. Schematic of flow patterns around spherical particle as a function of dispersed Reynolds number Re_d .

For even larger Reynolds numbers, flow detachment occurs on the aft side of the particle, which induces stable recirculation in the wake of the particle as long as Reynolds number remains below roughly 150. Beyond that point, instability in the flow is observed at all Re_d values. First, still close to $Re_d = 150$, an oscillating motion of the wake occurs. This is associated with a further flattening of the (mean) drag coefficient curve as a function of Re_d . Towards $Re_d = 10^3$ multiple vortices may be formed as these are shed by the particle. A so called Von Karman vortex street is formed. Note that flow, up to this point, is laminar. The wake flow is unstable, but the Reynolds number is still sufficiently low to prevent transition into turbulence. The onset of this transition is beyond roughly $Re_d = 10^3$, where the wake will become fully turbulent. As

a result, the drag coefficient curve is fully flattened, with a drag coefficient of roughly 0.44. The boundary layer of flow is still laminar at the sphere's surface, and the flow is only turbulent in the wake. Somewhere around $Re_d = 420$, the laminar boundary layer becomes turbulent, and an extreme reduction in the drag coefficient is observed. This point is called the drag crisis. A golf ball has a dimpled surface to reduce the drag coefficient exactly for this phenomenon. The dimples cause instability in the boundary layer at the ball surface, triggering turbulence and therewith reducing the drag coefficient. Clift et al. [72] present a table of ten drag correlations that are each applicable in a distinct range in Re_d , therewith fully capturing the drag coefficient curve as shown in Fig. 32. However, such an accurate description of the drag coefficient curve is generally not needed. For many dispersed two phase systems, the Schiller–Naumann drag coefficient [73], given by:

$$C_D = \frac{24}{Re_d} (1 + 0.15 Re_d^{0.687}) \quad (267)$$

is sufficient. It is applicable up to a Reynolds number of 10^3 , which is usually not exceeded by bubbles or small particles. This captures empirically the deviation of the C_D curve from the Stokes drag curve.

Until now, only spherical particles are considered. In case of a bubbly flow, however, deformation of the bubbles may have an effect on the effective drag coefficient of such bubbles. A measure of the deformation of bubbles is the Eötvös number, given by:

$$Eo = \frac{|\rho_c - \rho_a| g d^2}{\gamma} \quad (268)$$

where γ is the surface tension and g represents gravitational acceleration. Generally, for small Eo numbers, particles tend to be spherical because of the surface tension. For large Eo , bubbles tend to deform subject to hydrostatic forces into ellipsoids, wobbly shapes, spherical cap shapes or even skirted shapes. Additionally, the Morton number (Mo) plays a role in the shape of a particle, as it brings in the effect of continuous phase viscosity. The Morton number is a non dimensional group which only depends on material properties and not on particle diameter or velocity and is thus constant for a given two-phase mixture. In yet another well known graph, Clift et al. [72] present a regime map for bubble shapes as a function of Eo , Mo and Re . More practically, Tomiyama et al. [74] present a drag coefficient correlation tailored to bubbly flows subject to bubble deformation. It is given by:

$$C_D = \max \left(\min \left(\frac{24}{Re_d} (1 + 0.15 Re_d^{0.687}), \frac{72}{Re_d} \right), \frac{8}{3} \frac{Eo}{Eo + 4} \right) \quad (269)$$

While this drag coefficient is known to not always be very accurate, it is remarkably popular in its use.

Lift force

In addition to drag force, particles can also experience a lift force lateral to the direction of relative velocity. As the particles generally have cylindrical symmetry along an axis in line with the direction of relative motion, such as spherical, ellipsoidal, spherical cap or skirted shapes,

lift force is not induced by particle shape as opposed to, for example, an air foil. Instead, lift force is caused by rotation of the continuous phase flow around the particle, or rotation of the particle itself. The latter, called the Magnus effect, is less relevant for bubbly flows. Rotation can be quantified by the vorticity, namely:

$$\boldsymbol{\omega}_c = \nabla \times \mathbf{u}_c \quad (270)$$

The so called Saffman lift force then takes the general form [75]:

$$\mathbf{M}_{d,lift} = C_L \alpha_d \rho_c (\mathbf{u}_c - \mathbf{u}_d) \times \boldsymbol{\omega}_c \quad (271)$$

where lift coefficient C_L , carrying similar meaning as drag coefficient. Fig. 34 presents a schematic of a particle embedded into a continuous phase velocity field with a gradient, inducing a lift force. This simple quasi 2D setting is useful in understanding the working principle of Eq. (271). Let the horizontal direction, from left to right, be denoted by x , and the vertical direction, from bottom to top, be denoted by y . The x component of the continuous phase velocity is assumed to be a linearly increasing function of y , i.e., $\partial u_{x,c}/\partial y = const > 0$, where $u_{c,x}$ denotes the component of \mathbf{u}_c in the x direction. All other gradients of the continuous phase velocity components are zero. Then, the only non zero component of the continuous phase vorticity $\boldsymbol{\omega}_c$ is its z component $\omega_{c,z}$, and is given by $\omega_{c,z} = -\partial u_{c,x}/\partial y$. The relative velocity vector $\mathbf{u}_c - \mathbf{u}_d$ is assumed to only have a non zero component in the x direction, which is set to be negative, mimicking the case of bubbly flow in our vertical conduit with $u_{d,x} > u_{c,x}$ due to bubble buoyancy. The cross product between the relative velocity vector and the continuous phase vorticity, as present in Eq. (271), can then be expressed as:

$$(\mathbf{u}_c - \mathbf{u}_d) \times \boldsymbol{\omega}_c = \begin{bmatrix} 0 \\ -(u_{c,x} - u_{d,x})\omega_{c,z} \\ 0 \end{bmatrix} = \begin{bmatrix} 0 \\ -(u_{c,x} - u_{d,x})\partial u_{c,x}/\partial y \\ 0 \end{bmatrix} \quad (272)$$

whose y component is the only non zero component, being always negative for this particular flow because $u_{c,x} - u_{d,x} < 0$ and $\partial u_{x,c}/\partial y > 0$. This implies that a positive lift coefficient C_L is associated with dispersed motion against the positive direction of the gradient and vice versa for a negative lift coefficient.

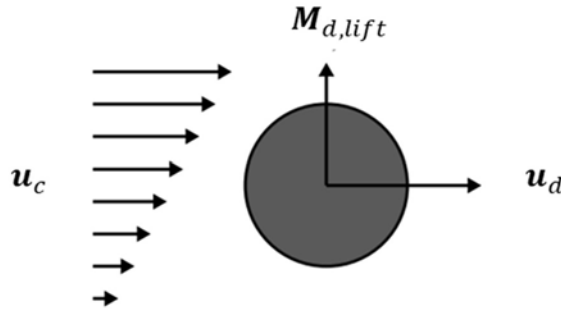


FIG. 34. Schematics of a particle embedded in a continuous phase velocity field with a gradient, inducing a lift force.

Extending this to wall bounded flows, in which the gradient of the (mean) streamwise velocity is positive in the direction away from the wall, a positive C_L thus implies wall ward dispersed motion for vertical wall bounded bubbly flow. Frequently used lift coefficients are the ones of

Drew [76] with $C_L = 0.5$ for weakly sheared inviscid flow, Zun [77] with $C_L = 0.3$ for single bubbles suspended in a tap water stream or Lopez de Bertodano et al. [78] with $C_L = 0.02$ and $C_L = 0.1$ to match different sets of experimental data for bubbly flows in vertical ducts. All these works consider relatively small spherical bubbles, resulting in positive lift coefficients with generally $0 < C_L < 0.5$. Another lift coefficient model, specifically tailored to bubbles, is that of Tomiyama et al. [79], given by:

$$C_L = \begin{cases} \min(0.288 \tanh(0.121 Re_d), f) & Eo \leq 4 \\ f & 4 < Eo \leq 10 \\ -0.27 & 10 \leq Eo \end{cases} \quad (273)$$

$$f = 0.474 - 0.0204 Eo - 0.0159 Eo^2 + 0.000105 Eo^3 \quad (274)$$

This model has, just like the Tomiyama drag model, a dependence on the Eötvös number and, as such, a dependence on the non sphericity of bubbles. Bubbles with small diameters have relatively small Eo and thus a positive C_L ; these bubbles move towards the wall in a wall bounded flow. Larger bubbles have a relatively larger Eo and thus deform much more. This leads to a lift coefficient inversion, giving a negative lift and moving bubbles away from the wall in wall bounded flow. In turn, such a lift force would improve heat transfer in our conduit, as steam is transported away from the wall, leading to quenching. Therefore, accurate modelling of the lift force is important in this type of settings.

Other forces

Apart from the drag and lift forces, there are many more interfacial momentum transfer closures that can play significant roles. While more complete discussion on such momentum transfer mechanism can be found in literature [80], the most relevant ones are briefly summarized as follows:

- *Virtual mass force*. When the continuous phase undergoes acceleration or deceleration, the dispersed phase will also accelerate or decelerate, as a result of drag. However, in addition to the mass of the particle that changes momentum, also an additional mass that is present in the wake of the particle must adjust its velocity. This can be modelled by giving the particle an added mass. In case of solid particles in a gas, this added mass is usually very small compared to the mass of the particle itself, so that the virtual mass force can be neglected. In case of a bubble in a liquid, however, the added mass can be significant.
- *Turbulent dispersion force*. In the formulation of Eulerian–Eulerian method, a filtering or averaging of turbulent structures is introduced. In the RANS framework, this leads to a steady solution for the mean flow. However, turbulence generally has a dispersive nature; it enhances mixing and tends to smear out sharp gradients in transported quantities such as temperature, but also dispersed phase concentrations. To model this behaviour, a turbulent dispersion force is included for which there are several models proposed in literature [78], [81]. These models propose a proportionality of a turbulent dispersion force to the amount of turbulence locally present (as expressed by turbulent kinetic energy or by turbulent viscosity) and to the negative gradient of dispersed void fraction, $-\nabla \alpha_d$, driving particles in the direction where their concentration is low. As such, the turbulent dispersion force has a smearing effect on the solution, reflecting the dispersive nature of turbulence.

- *Wall lubrication force.* The use of lift and turbulent dispersion may lead to nonphysical dispersed fraction peaks near the wall in wall bounded flows, because the Eulerian–Eulerian method is unaware of the spherical shape of particles and would thus predict particles overlapping with the wall. The volume fraction of a dispersed phase will always decrease towards zero near the wall, as particles only touch the wall in a single point. To counteract nonphysical dispersed fraction peaks, a wall lubrication force is introduced in many Eulerian–Eulerian method, particularly in bubbly flows. The wall lubrication force pushes particles away from the wall, and no longer mathematically overlap with the wall. Wall lubrication force models are often quite heuristic and depend on the wall distance y , decaying for $y/d > 1$. Some commonly used wall lubrication force models are those of Antal et al. [82] and Hosokawa et al. [83].

4.3.3.2. Interfacial energy and mass transfer closure

Mass and heat transfer are intimately connected with each other. Mass transfer between phases is caused by phase change, which is the result of heating or cooling. Conversely, if mass is changing phase, e.g., by evaporation or condensation, this will require or produce heat, respectively. In Eulerian–Eulerian method, the modelling of Λ_k as the phase k mass source and E_k as the phase k heat source always goes jointly, and we will therefore discuss the two together. Like interfacial momentum transfer, we may model E_k by considering the heat transfer rate from or to a single particle, and then multiplying that rate by the total number concentration of particles. Such a single particle is schematically shown in Fig. 35. The disperse particle is held at temperature T_d while the continuous phase is held at temperature T_c . The interface has temperature T_i , which is assumed to be at saturation temperature, i.e., the pressure dependent temperature at which phase change occurs between the two phases.

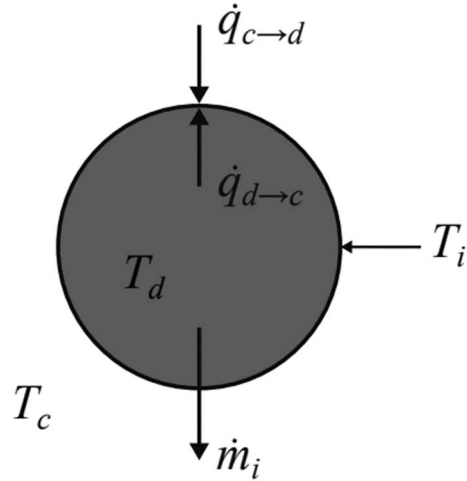


FIG. 35. Schematics of heat and mass transfer mechanisms acting on dispersed particle at temperature T_d suspended in a continuous phase held at temperature T_c ; interface is at temperature T_i .

Two heat transfer mechanisms can be identified. The first is the conductive heat transfer as a result of temperature differences across the interface, $\dot{q}_{\Delta T,k}''$, and the second is the heat transfer due to mass transfer, $\dot{q}_{m,k}''$. The total heat transfer rate to phase k is then given by:

$$E_k = \dot{q}_{\Delta T,k}'' + \dot{q}_{m,k}'' \quad (275)$$

Conductive heat transfer

The conductive heat transfer can be partitioned in two, i.e., from continuous phase to interface and from dispersed phase to interface. The conductive heat from continuous phase to the interface is given by:

$$\dot{q}_{c \rightarrow i}'' = h_c a_i (T_c - T_i) \quad (276)$$

with interfacial area density a_i giving the total amount of interfacial surface area per unit of volume locally available, and continuous phase heat transfer coefficient per unit of interfacial area h_c given by:

$$h_c = \frac{\kappa_c}{d} Nu \quad (277)$$

with continuous phase thermal conductivity κ_c and Nusselt number Nu . The Nusselt number signifies the enhancement of heat transfer due to convective flow and is therefore a function of the dispersed Reynolds number. A commonly used relation is the Ranz–Marshall [84] given by:

$$Nu = 2 + 0.6\sqrt{Re_d^3 \sqrt{Pr_c}} \quad (278)$$

with Pr_c the continuous phase Prandtl number giving the ratio between kinematic viscosity and thermal diffusivity of the continuous phase. For particles that are suspended in the continuous phase without any relative velocity (i.e., $Re_d = 0$), the Nusselt number reduces to 2. The interfacial area a_i can be computed from the product of the surface area of a single particle multiplied by the total number of particles. For spherical particles, this gives:

$$a_i = \frac{6\alpha_d}{d} \quad (279)$$

Analogously to Eq. (276), the conductive heat transfer from dispersed phase to interface is given by:

$$\dot{q}_{d \rightarrow i}'' = h_d a_i (T_d - T_i) \quad (280)$$

and dispersed phase heat transfer coefficient per unit of interfacial area h_d . In case of boiling flow, however, the bubble temperature can be assumed to be at saturation temperature, so that $T_d - T_i = 0$.

Heat transfer due to mass transfer

As stated above, the conductive transfer of heat from continuous phase to particle, or vice versa, is associated with mass transfer. If we assume that all the heat transferred to the interface is used for phase change, then:

$$\Lambda_i = \frac{\dot{q}_{c \rightarrow i}'' + \dot{q}_{d \rightarrow i}''}{L} \quad (281)$$

with L the latent heat, i.e., the heat required per unit of mass of phase change. When $\Lambda_i > 0$, there is a net supply of energy to the interface which is associated with evaporation and thus a

positive flux to the gas phase, which can be either continuous or dispersed depending on the problem. Conversely, when $\Lambda_i < 0$, there is a net removal of energy from the interface which is associated with condensation and thus a positive mass flux to the liquid phase. In the situation of bubbly flow, therefore $\Lambda_d = \Lambda_i$ and $\Lambda_c = -\Lambda_c$. Clearly, in the case of droplet flow, the situation would be reversed.

The heat transfer model given by Eq. (275) can now be completed. The conductive heat flux of phase k is simply given by the heat lost to the interface, i.e., $\dot{q}_{\Delta T,k}'' = -\dot{q}_{k \rightarrow i}''$. The heat flux due to mass transfer is given by the mass transfer rate multiplied by the specific enthalpy of phase k at saturation temperature, $h_k(T_s)$. This gives:

$$E_k = -\dot{q}_{k \rightarrow i}'' + \Lambda_k h_k(T_s) \quad (282)$$

where $\dot{q}_{k \rightarrow i}''$ is given by Eq. (276) or Eq. (280) and Λ_k by Eq. (281) in the case of bubbly flow.

Wall boiling model

So far, a single particle suspended in a continuous phase is considered, and from that the mass and heat transfer terms are derived based on the interfacial area concentration, which, in turn, could simply be related to the amount of dispersed phase volume available. Such a model is suitable for homogeneous boiling but fails to predict complicated boiling physics taking place at the wall of our conduit beyond the onset of nucleate boiling point, see Fig. 29. Traditionally, the so called RPI model (named after the Rensselaer Polytechnic Institute where it was considered) is used to include wall boiling physics into the Eulerian–Eulerian method. The RPI model partitions the heat flux in three contributions: single phase convection from wall to liquid, removal of heat by the evaporation of water onto bubbles, and heat flux due to the quenching at bubble nucleation sites. RPI like models, which make such a partition, depend on many parameters, including nucleation site density, the average bubble diameter with which bubbles depart from the wall and the bubble departure frequency. The reader is referred to Lahey et al. [85] for a recent overview of the modelling state-of-the-art in the field of wall boiling.

4.3.3.3. Dispersed size distribution models

The momentum and energy transfer closure models, it can be observed that closure models are heavily particle size dependent through parameters such as dispersed phase Reynolds number (proportional to d) and Eötvös number (proportional to d^2), or the interfacial area density (proportional to d^2). The simplest way of resolving this dependence is by assuming a constant dispersed phase diameter, implying that particles are mono dispersed. Alternatively, a simple so called isothermal diameter model can be used for compressible particles in the form of:

$$d = d_0 \sqrt[3]{\frac{p_0}{p}} \quad (283)$$

which signifies the fact that volume is inversely proportional to pressure for compressible fluids. Still, the user needs to specify pressure p_0 at which diameter equals d_0 . In practice, particle populations are almost never mono dispersed. Instead, certain sizes locally appear with certain likelihood, giving rise to a poly dispersed population of particles, also called the size distribution. The size distribution can be denoted by $n(d, x, t)$ and is defined such that the

product $n(d, \mathbf{x}, t)dd$ gives the total number of particles per unit of volume having a diameter in the interval $[d, d + dd]$ at (\mathbf{x}, t) . Fig. 36 (a) schematically shows size distribution function, and the area $n(d, \mathbf{x}, t)dd$ marked in blue. The size distribution $n(d, \mathbf{x}, t)$ is an Eulerian description of a spatially distributed collection of dispersed particles and, as such, aligns well with the spirit of Eulerian–Eulerian method in the sense that a statistical description is adopted, rather than a deterministic one. Note that here we base the size distribution on the particle size d , however, it can be also expressed in terms of particle volume v , particle mass m or any other size. The size distribution adheres to its own conservation equation, which can be derived by considering the physical phenomena which change $n(d, \mathbf{x}, t)$ in time. This conservation equation is referred to as the population balance equation, and is expressed as [86]:

$$\frac{\partial n(d)}{\partial t} + \nabla \cdot (\mathbf{u}(d)n(d)) + \nabla_d(G(d)n(d)) = J(d) \quad (284)$$

with $\mathbf{u}(d)$ being the disperse velocity distribution, $\nabla_d := \partial/\partial d$ denoting a gradient in the particle size space d , $G(d)$ a condensational growth term and $J(d)$ representing a collection of various source term that describe the generation or removal of particles of size d , such as nucleation, breakup, or coalescence. The explicit dependence on (\mathbf{x}, t) of the various variables has been omitted for simplicity. Population balance equations are notoriously difficult to solve, because of their dimensionality, i.e., their dependence on three spatial dimensions, one temporal dimension and, in addition, one internal dimension (here, d).

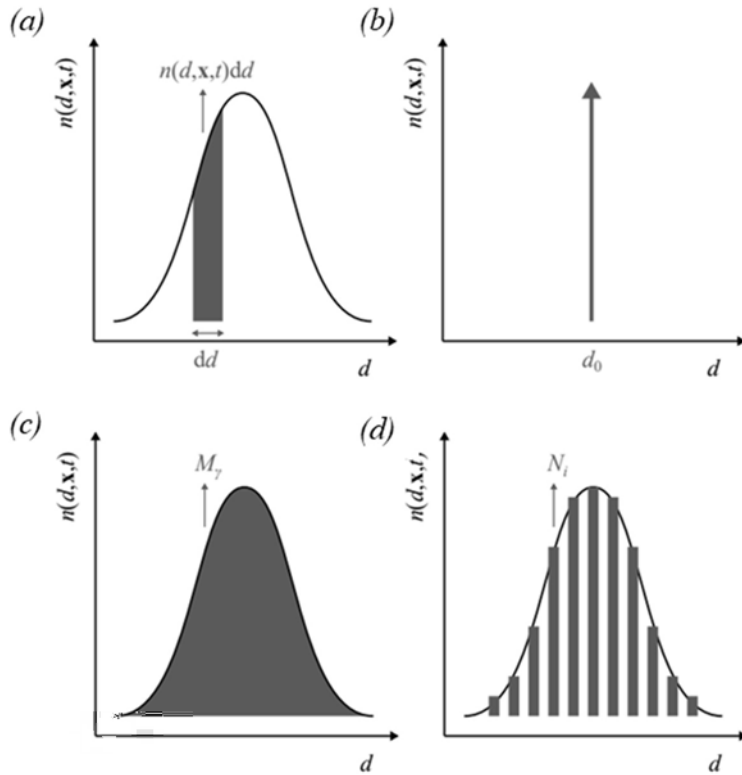


FIG. 36. Schematics representation of: (a) size distribution with highlight of a specific population within the distribution; (b) mono dispersed size distribution; (c) moment representation of a size distribution and (d) size group representation of a size distribution.

To solve a population balance equation, there are three main branches of size distribution methods. The first one, being the mono dispersed method. This is an extremely crude reduction

of the size distribution $n(d, \mathbf{x}, t)$ to be represented by a single size as $N(\mathbf{x}, t)\delta(d - d_0, \mathbf{x}, t)$ with the Dirac delta function δ , as sketched in Fig. 36 (b). More advanced methods are moment methods and size group methods, which are discussed next.

Moment methods

The a -th moment of a size distribution $n(d, \mathbf{x}, t)$ is defined by:

$$M_a = \int_0^\infty d^a n(d, \mathbf{x}, t) dd \quad (285)$$

and it is depicted in Fig. 36 (c). Some moments of the size distribution carry a relevant physical meaning. For example, the zero-th moment represents the total number concentration, the second moment multiplied by π is the interfacial area concentration a_i and the third moment multiplied by $\pi/6$ is the volume concentration α_d .

Each moment is governed by its own so called moment transport equation. The a -th moment transport equation can be derived from the population balance equation by multiplying it by d^a and taking the integral over the total domain of d^a . This yields:

$$\frac{\partial M_a}{\partial t} + \nabla \cdot (\mathbf{u}_a M_a) + \frac{a}{3\rho_d} \frac{\partial \rho_g}{\partial t} M_a = J_a \quad (286)$$

with \mathbf{u}_a being the a -th moment velocity and J_a the a -th moment source term. The third term on the left hand side represents change in the distribution due to compressibility of particles. It can be shown that when $a = 3$ and Eq. (286) is multiplied by $\pi/6$, the dispersed phase volume fraction equation, Eq. (256), is obtained, therewith establishing a consistent mathematical connection between the population balance equation and the two fluid model and, by extension, the Eulerian–Eulerian method.

Without going into details, it can be generally observed that models which describe the physical mechanisms underpinning J_γ , such as particle coalescence and break up, are dependent on moments of the size distribution. In most situations, we will have that:

$$J_a = J_a(M_0, M_1, \dots, M_a, M_{a+1}, \dots) \quad (287)$$

i.e., the source term of moment a depends on higher order moments $a' > a$. In turn, those higher order moments will depend on even higher order moments beyond them. This generates a closure problem.

To create closure, there are several subbranches in the field of moment methods. Probably the most intuitive approach is the presumed number density function approach, in which an assumption is made on the mathematical form of the size distribution (e.g., a log normal size distribution). This presumed number density function has some degrees of freedom, which must be closed by the same number of moment transport equations. In turn, when the form of the size distribution is known, any moment of that size distribution can be calculated readily. An example of such a method is the LogMoM method [87]. Another popular way of establishing moment closure is the quadrature method of moments, in which the problem is rewritten in terms of fictive particles, or nodes, that form a discretized size distribution. Each node consists of an abscissa and weight, from which, using quadrature rules, the moments can be

reconstructed. The number of nodes may increase or decrease adaptively. The reader is referred to Marchisio and Fox [88] for an extensive discussion on the family of such methods.

Size group methods

The concept of moment methods is quite abstract, in the sense that the size distribution is only known in terms of a finite set of integral moments. Perhaps more intuitively, size group methods make a full discretization of the size domain, much like how finite volume or finite element methods make a discretization of the space domain. The most straight forward size group methods make a fixed discretization on a number of N_s size intervals/sections/size groups. The total number concentration in such an interval is defined as:

$$N_i(\mathbf{x}, t) = \int_{L_i}^{U_i} n(d, \mathbf{x}, t) dd \quad (288)$$

with $[L_i, U_i]$ being the interval which is represented by size group i . Intervals are adjacent and non overlapping. These intervals cover some finite range of $d \in [0, \infty)$ which must be selected a priori. Next, we can approximate the full size distribution by a constellation of N_s mono dispersed size distributions, i.e.:

$$n(d, \mathbf{x}, t) \approx \sum_{i=1}^{N_s} N_i(\mathbf{x}, t) \delta(d_i - d, \mathbf{x}, t) \quad (289)$$

as schematically shown in Fig. 36 (d). The diameter d_i is called the representative diameter belonging to size group d_i . Particles within size group i are assumed to all have size d_i . Integrating the population balance equation over the interval $[L_i, U_i]$, and using Eq. (289), a conservation equation for each size group is obtained in the form of:

$$\frac{\partial N_i}{\partial t} + \nabla \cdot (\mathbf{u}_i N_i) = J_i \quad (290)$$

with \mathbf{u}_i being the velocity of particles in group i and J_i the rate of change of the number concentration of particles in group i due to condensational growth, coalescence, breakup, nucleation, etc. This source term can be calculated relatively intuitively, by considering the rates at which a particle of group i interacts with a particle of group j , $j \neq i$. A drawback of the size group method is that it requires N_s additional conservation equations to be solved. The number of size groups N_s is required to be sufficiently large to prevent numerical smearing of the size distribution in size space as a result of redistribution of particles due to J_i . Moreover, in principle each size group has its own transport velocity \mathbf{u}_i , which requires the two fluid model to be extended to an N fluid model in which each size group adheres to its own set of mass, momentum, and energy conservation equations. While this is an extremely accurate method to capture poly disperse two phase flows, it can also be computationally extremely expensive. A popular size group method is iMUSIG [89], which has recently also been implemented in the open source CFD platform OpenFOAM [90], [91] and is therewith freely accessible. A key benefit of iMUSIG is that it makes a distinction between size groups and velocity groups. A velocity group will contain at least one size group but may contain many more. Each velocity group has its own set of mass, momentum, and energy conservation equations. By assigning multiple size groups to the same velocity group, a dramatic reduction of the number of equations to be solved can be achieved, making the size group method much more computationally tangible. In some cases, it can be sufficient to use up to only two velocity

groups. Such an approach is able to capture the lift inversion as seen in the Tomiyama lift force model [79], by choosing one velocity group that represents particles with a diameter smaller than the inversion point, and one velocity group that represents particles that are larger.

4.3.4. Eulerian simulations of bubbly flow

In the previous Sections, the Eulerian–Eulerian method was derived, concluded that the Eulerian–Eulerian method requires interfacial transfer closure terms, and have subsequently introduced several such mass, momentum, and heat transfer closures terms. The simulation of bubbly two phase flow described in the TOPFLOW experiments by Prasser et al. [92], and using the two fluid model is implemented in the open source CFD package OpenFOAM. The OpenFOAM simulation examples are available in the literature and online [93]. The TOPFLOW experiments were performed in a circular vertical pipe in which both water and air are flowing upward. The air is added to the water from a circular inlet section as depicted in Fig. 37. As the bubbles are carried further downstream by the water, these will be redistributed in the domain to establish a new distribution along the radius of the pipe.

The TOPFLOW measurements include data on the bubble size distribution at both the inlet and the outlet, allowing for a detailed validation of the predictions of the Eulerian–Eulerian method. Computational fluid dynamics simulations of the TOPFLOW setting are performed using a quasi 2D wedge mesh imposing axi symmetric symmetry. The domain is mapped by uniformly sized cells with 30 cells in the radial direction and 500 cells in the axial direction, giving a total of 15,000 cells. The pipe has a radius of 100 mm and a length of 7.8 m. The multiphaseEulerFoam solver of OpenFOAM is used, which is OpenFOAM’s implementation of the two fluid model as previously discussed.

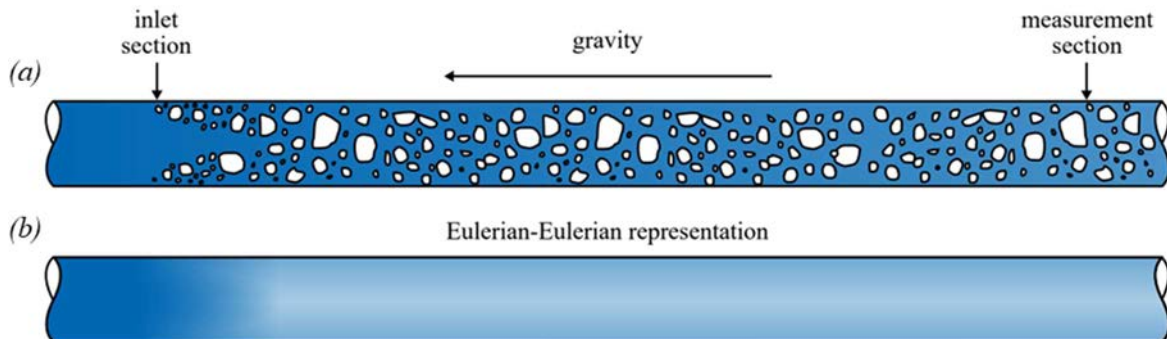


FIG. 37. (a) Schematics of the TOPFLOW experiment with inlet section and measurement section; (b) Eulerian–Eulerian representation. Gravity points from right to left and the flow is from left to right.

OpenFOAM allows the selection of many interfacial closure terms. In the case of TOPFLOW, the flow is adiabatic so that heat and mass transfer are assumed to be negligible, and the only selection is of suitable momentum closure models. For the drag force, the Ishii and Zuber [94] model is selected. For the lift force, the Tomiyama et al. [79] model is selected. Wall lubrication is modeled with the Frank [95] model and turbulent dispersion using the Burns et al. model [81]. Virtual mass was enabled with the virtual mass coefficient set to 0.5. Turbulence in both the continuous and dispersed phase is modeled using the two phase $k-\epsilon$ model of Behzadi et al. [96]. Bubble induced turbulence is modeled using the formulation of Lahey [97]. Poly dispersion is simulated using both a moment method and a size group method. The moment method relies on LogMoM, which establishes moment closure using the assumption that the size distribution has a log normal shape. This shape has three degrees of freedom: its height, its

width, and its displacement in diameter space. As such, three moment transport equations are solved, for which the zeroth moment, second moment and third moment are selected. However, the third moment, being the volume fraction, is already solved by the two fluid model so that only two additional moment transport equations must be solved. For the size group method, we use the fixed pivot technique (FPT) [98] which is implemented in OpenFOAM. The number of size groups is set to 30, and covers the size domain [0.5, 50] mm with size groups distributed uniformly in $\log(d)$ space. Because the flow is turbulent, bubbles are subject to coalescence and break up. This must be modeled, as both coalescence and breakup have a significant effect on the bubble size distribution and, therefore, on the two fluid solution via the right hand side closure terms. In both LogMoM and FPT, we use the same coalescence and breakup models. However, the way that the right hand side source terms J_y and J_i for LogMoM and FPT, respectively, are computed differ. For breakup, we use the model of Luo and Svendsen [99] and for coalescence we use the model of Prince and Blanch [100]. For FPT, these two models are readily implemented in OpenFOAM. For LogMoM, a custom and open source library is developed [93], which uses Gauss quadrature to compute the right hand side breakup and coalescence source terms.

Fig. 38 shows the solution of model in terms of the gas void fraction α_g and streamwise gas velocity $|\mathbf{u}_g|$, both at the measurement section of the TOPFLOW experimental setup and both as a function of the radial coordinate r . Shown are the experimental measurements of Prasser et al. [92] and the Eulerian–Eulerian method two fluid model predictions of FPT (triangles) and LogMoM (circles). The FPT and LogMoM show good agreement with each other, and also appear to match the experimental data reasonably. The two solutions are the result of a complex interplay of drag, lift, turbulent dispersion, wall lubrication, coalescence, and breakup. An interesting feature that can be observed is that while bubbles are injected from the wall (see Fig. 37 (a)), tend to migrate to the bulk region of the pipe towards small radii. This is the result of turbulent dispersion and lift force. The latter, as we have seen above, tends to be away from the wall for sufficiently large bubbles. The TOPFLOW facility was also used to perform experiments with wall peaking, which requires smaller bubbles than those observed in the current configuration.

The FPT and LogMoM methods allow to reconstruct the full bubble size distribution at the inlet and outlet. At the inlet, the size distribution is imposed by the numerical model. At the outlet, however, it is the outcome of the Eulerian–Eulerian method two fluid model and the used momentum closure and breakup/coalescence closure models.

Fig. 39 shows the average size distribution recorded at both the inlet and measurement sections of the pipe. It can be seen that at the inlet, the LogMoM method fails to reproduce the experimentally observed size distribution as a result of its presumed number density function (which is log normal while the measurements are certainly not).

The FPT, on the other hand, can be configured to represent any size distribution reasonably accurately, as long as a sufficiently large number of intervals is chosen. It can be seen that for the chosen 30 intervals, the FPT mimics the experimental input data almost perfectly at the inlet section. At the outlet section, it can be seen that the experimental measurements suggest a transition from an initially bimodal size distribution to a single modal one. Both the LogMoM and FPT model show good agreement with the experimental data, showing that the choice for a log normal size distribution is a reasonable one.

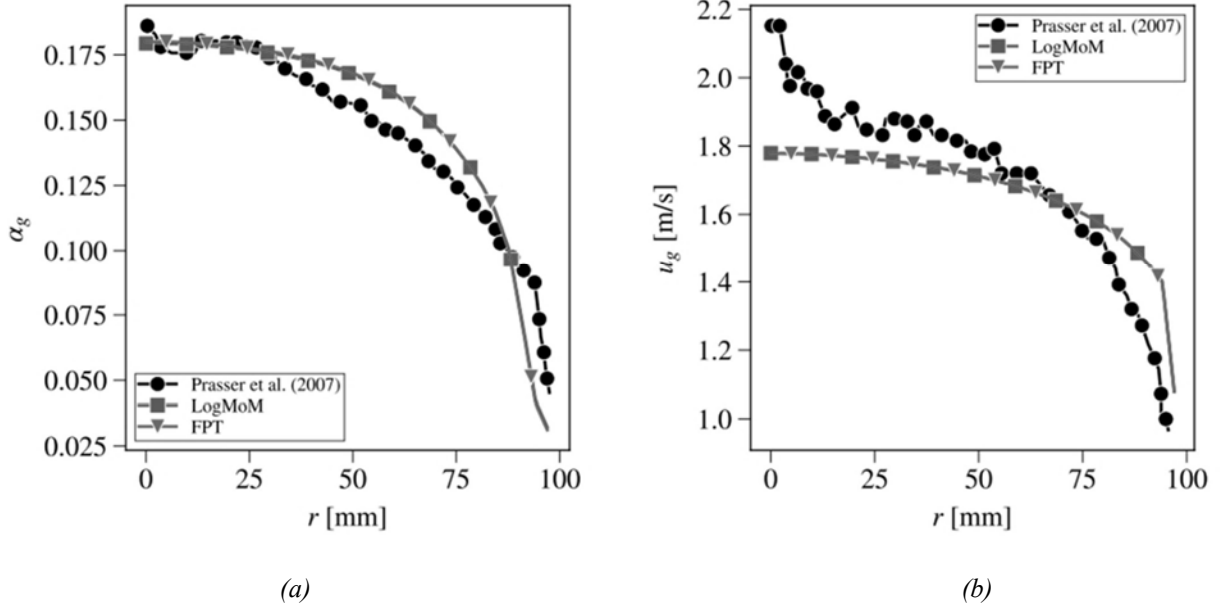


FIG. 38. (a) Radial profiles of gas void fraction and (b) streamwise gas velocity at the measurement section in the TOPFLOW experimental setup.

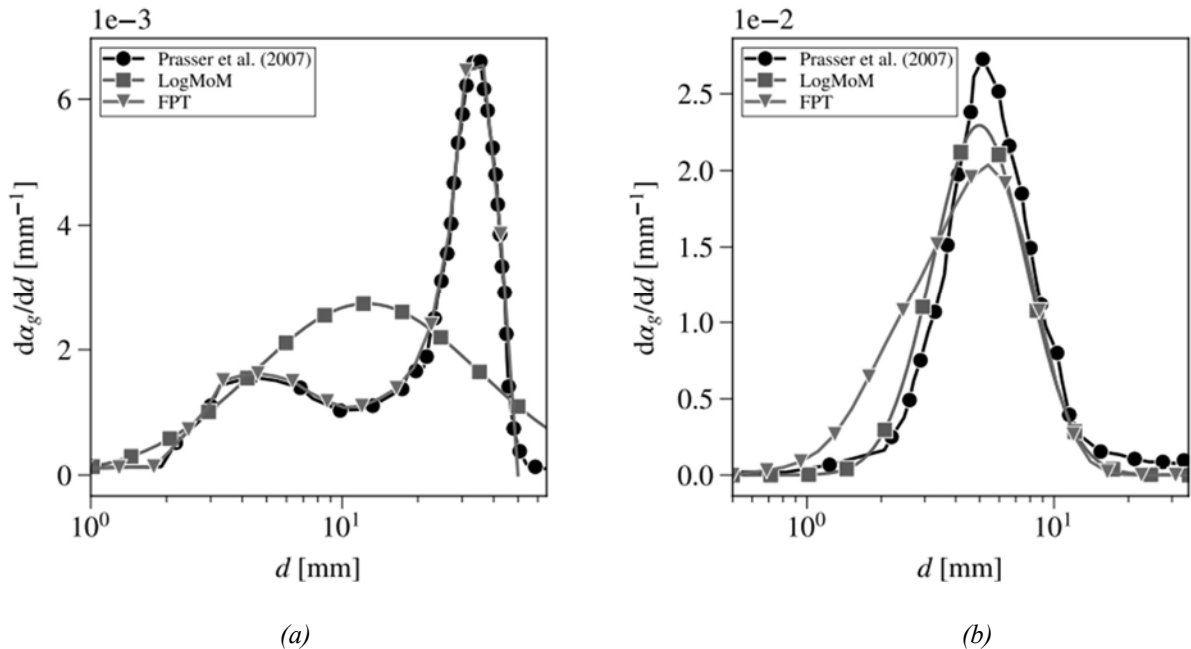


FIG. 39. (a) Bubble size distribution at the inlet section and (b) measurement section of the TOPFLOW experimental setup.

5. APPLICATION OF COMPUTATIONAL FLUID DYNAMICS TO REACTOR DESIGN AND ANALYSES

This chapter delves into further aspects pertaining to the application of CFD tools to the analysis of nuclear reactors. This is tackled from two different perspectives. First, it is addressed from the perspective of the numerical challenges associated with the simulation and investigation of advanced and innovative nuclear reactor concepts, which often transcend the scope of existing established simulation software. Secondly, it is tackled from the perspective

of large scale plant simulations, regardless of the particular underlying reactor technology, which require multi scale approaches in order to be performed.

5.1. COMPUTATIONAL FLUID DYNAMICS FOR INNOVATIVE REACTORS

5.1.1. Overview of advanced reactor concepts

The Generation IV International Forum (GIF) was established in the year 2000 as a cooperative international framework for carrying out research and development of the next generation reactors. The innovative nuclear reactors selected by this forum have the intention to deliver significant advances compared to water cooled reactors with respect to the efficiency of the use of nuclear fuel, the reduction of waste produced, and the economic performance, while meeting the stringent standards of safety and proliferation resistance. With these goals in mind, numerous reactor concepts were evaluated, and six reactor technologies were selected for further development. These include the supercritical water reactor, molten salt reactors, both molten salt cooled and fuelled, very high temperature reactors, liquid metal cooled reactors, primarily sodium and lead based alloys cooled and gas cooled fast reactors, as shown in Fig. 40 (a)–(f).

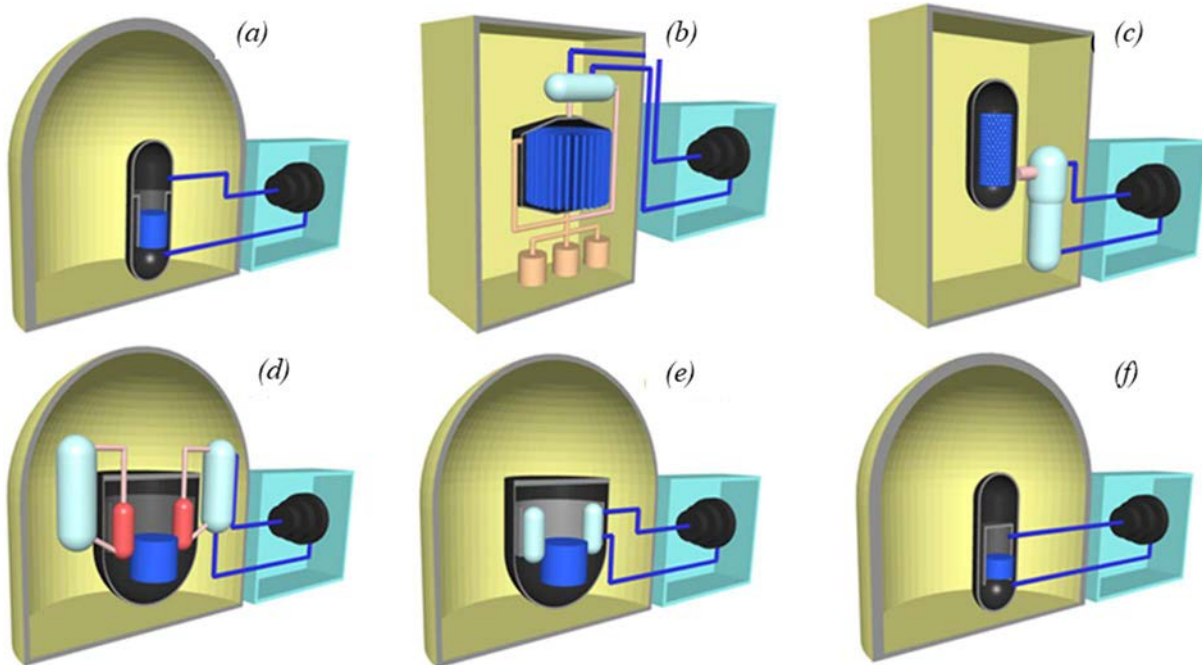


FIG. 40. Simplified overview of different innovative reactor concepts: (a) supercritical water reactor; (b) molten salt reactor; (c) very high temperature reactor; (d) sodium cooled fast reactor; (e) lead cooled reactor; (f) gas cooled reactor.

Innovative reactors typically employ coolants and moderators (if any) different than water. In summary:

- High melting points of liquid metals require pre heaters to keep the coolant liquid at operating conditions and are causing a risk of solidification (freezing) in accident situations, potentially blocking the coolant flow path;
- High boiling point may prevent coolant from forming voids which might affect neutron transport behaviour in nuclear reactor, while a low boiling point might increase the risk of voiding the core;

- High density may allow to design compact passive safety systems based on buoyancy forces but at the same time it may increase seismic and vibration risks;
- High specific heat capacity ensures storing a lot of energy in the coolant, increasing the margin to boiling and potential core voiding.

Modelling and simulation play a large role in the design support of innovative nuclear reactors as is the case for water cooled reactors. From a thermal hydraulics point of view, modelling and simulation is traditionally performed with system codes and sub channel codes. However, with increasing computer power and advancements in numerical algorithms, the use of 3D CFD is rapidly increasing. Fundamental challenges in the use of CFD for innovative reactors rise from the heat transport, especially for reactors cooled with so called non unity Prandtl number fluids, i.e., supercritical water cooled reactors, liquid metal cooled reactors, and molten salt reactors. Design specific challenges and CFD applications for various innovative reactor designs is discussed in the subsequent sections.

5.1.2. Computational considerations on turbulence modelling

As famously stated by Feynman in 1963, turbulence remains the most important unsolved problem in classical physics [101]. When considering applications of CFD to innovative nuclear reactor designs, turbulence and turbulent heat transfer modelling are fundamental challenges to be solved. The first challenge is related to the fact that many locations in a reactor require turbulence models which go beyond the widely used isotropic models, like the $k-\varepsilon$ and the shear stress transport $k-\omega$ turbulence models. A good example where these models fail, is illustrated in Fig. 41 for the axial flow in a grid spaced fuel assembly. Fig. 41 (b) show the measurements from Vonka [102], clearly indicating the secondary flow structures in a triangular lattice fuel assembly sub channel. Fig. 41 (a) represents the solution using an isotropic turbulence model, while Fig. 41 (c) shows the solution using an anisotropic turbulence model. It is clear the the isotropic turbulence model fails to capture the secondary flow structures, while the main (axial) flow structure (represented by colours) is captured by both models.

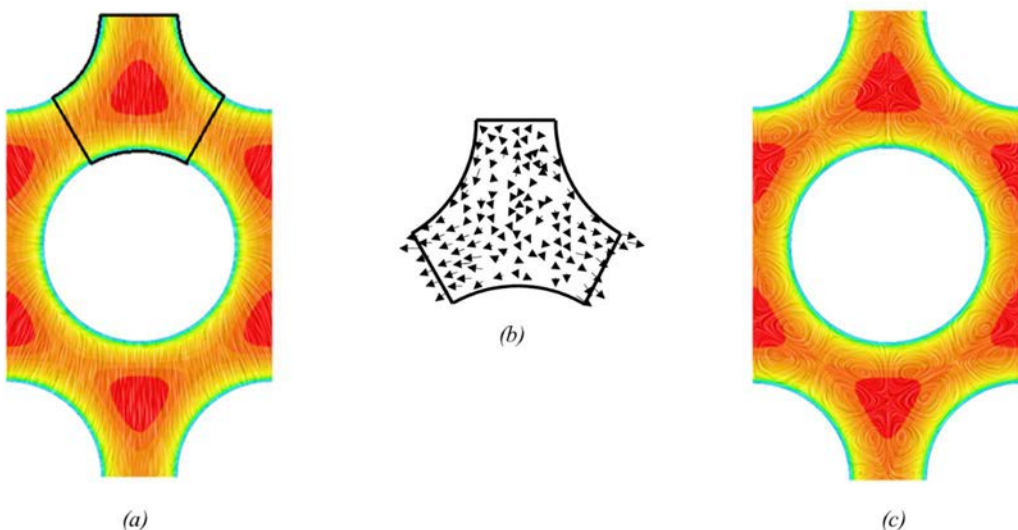


FIG. 41. Velocity distributions obtained by: (a) an isotropic turbulence model; (b) experimental measurements; (c) an anisotropic turbulence model (adapted from [102]).

While momentum transport is an important aspect, for many nuclear applications, heat transport is equally, if not more, important. Modelling of heat transport for non unity Prandtl number fluids like supercritical water, liquid metals, or molten salts, requires fundamentally different solutions than the Reynolds analogy which is nowadays implemented and used in CFD codes. Traditionally, most attention is paid to low Prandtl turbulence modelling for liquid metals. Grötzbach [103] provided a summary of the state of the art both in academic models as well as industrial modelling approaches. The latter was updated in Roelofs et al. [104] in which practical solutions for liquid metal forced convection heat transfer are considered. However, for nuclear applications, also the mixed and natural convection flow regimes will be important. A recent status update of international efforts into this direction is provided by Shams et al. [105]. Fig. 42 based on the information provided in that reference indicates that the international efforts on turbulence (heat transfer) modelling balance the robustness and accuracy. From this trend it can be concluded that the main effort in the coming years may be to combine anisotropic eddy viscosity turbulence models or Reynolds stress models with algebraic heat flux models. One such example is the development outlined by Shams et al. [106].

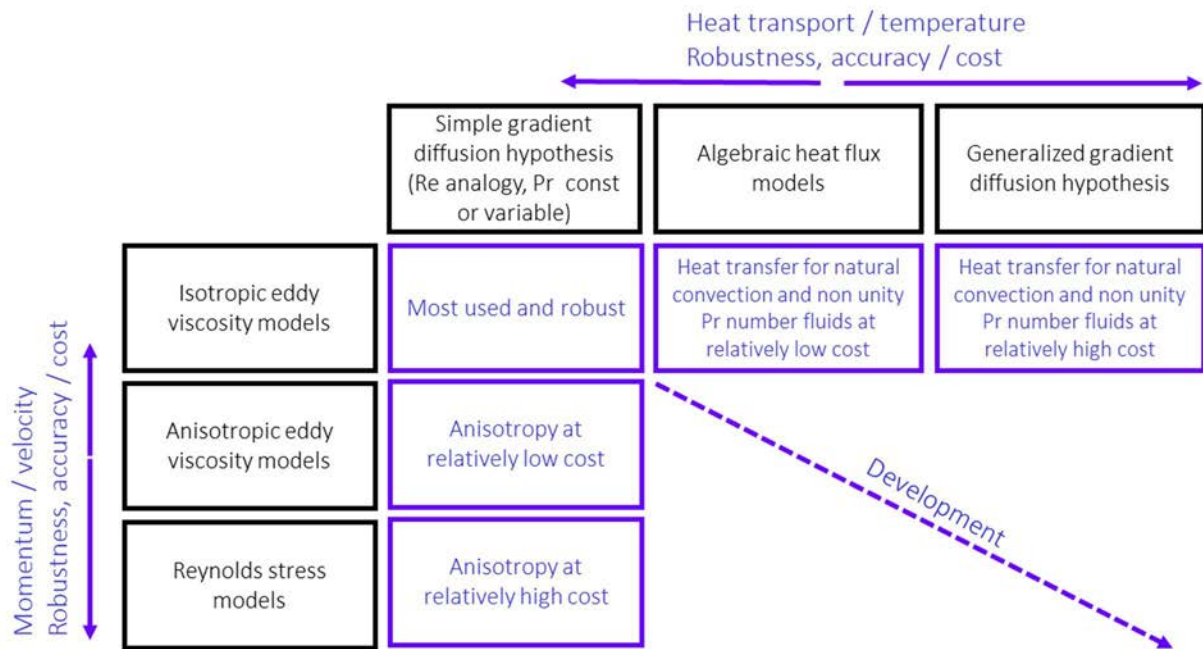


FIG. 42. Turbulent momentum and heat transport modelling matrix: robustness decreases, and accuracy increases from left to right across the columns, from top to bottom across the rows.

5.1.3. Reactor specific computational considerations

5.1.3.1. Supercritical water cooled reactors

One of the most peculiar aspects of water as a coolant at or after its supercritical point is its heat transfer properties, in the sense that, unlike liquid metals or molten salts, the Prandtl number shows a peak value at the critical temperature [107]. Additionally, other physical properties of supercritical water show a clear transition near the supercritical point [108].

An overview of the state-of-the-art of heat transport in supercritical water is provided in [109]. Modelling of a heat transfer requires taking into account strong variation in Prandtl number close to the (pseudo) critical temperature which is often taking place in a small temperature range. Apart from that, differences are observed between upward and downward flow in

experimental as well as numerical studies that are caused by the influence of a buoyancy. Because of this influence, the heat transfer might be enhanced or deteriorated. This issue is especially a challenge for the development of practical CFD turbulence models. Papukchiev et al. [110] assess such practical engineering CFD models. A general takeaway from their work is that two equation $k-\epsilon$ produce qualitatively good results in regions far from the pseudo critical conditions, but consistently overestimate the wall temperature trend in the vicinity of the pseudo critical threshold. On the other hand, two equation $k-\omega$ models usually underestimate the wall temperature trend. Algebraic heat transfer models seem to be an interesting choice to be made to improve the prediction quality. Unfortunately, considering all the operating conditions, there is no clear evidence that a single model is better than the others. Peeters et al., showed that local physical property variations can cause decreased or increased turbulent motions in heated or cooled supercritical fluids [108].

In addition to the mean profiles of density and molecular Prandtl number, fluctuations in density and molecular Prandtl number are important in understanding heat transfer to fluids at supercritical pressure [111]. In practice, this means that heat transfer to a fluid at supercritical pressure depends on physical properties of so called hot ejections and cold sweeps near the wall. Pucciarelli et al., explains how to apply an algebraic heat flux model for the calculation of a turbulent Prandtl number distribution in the energy equation [112]. Though this approach maintains a simple gradient approach, it leads to promising results.

A further important consideration regarding supercritical water reactors pertains to the core thermal hydraulics. The design of a supercritical water reactor is largely based on existing PWRs and especially BWRs. Description of current designs can be found in [113]. As an example, the European high performance light water reactor (HPLWR), is considered to illustrate that in order to avoid hot spots in the core reaching too high temperatures [114] via the mixing through a three-pass core concept, more details can be found in Ref. [115].

In this design, the coolant flows through the central part of the core in upward direction in a first stage called the evaporator. Subsequently, the coolant flows in a second stage downward through an annular section of the core, which acts as a first superheater. Finally, the coolant flows upwards in stage three through the outer part of the core which acts as a second superheater. In between, the flow is being mixed in the upper and lower mixing chamber. The upper and lower mixing regions are geometrically complex plena filled with connection tubes and headpieces connecting the evaporator stage and the superheater stages. In the first step of modelling, both mixing chambers are assumed to have constant properties. The optimized designs were checked in a second step in which the effect of variable properties and the large, expected variation of the Prandtl number were taken into account. The CFD simulations showed that due to the flow mixing, buoyancy effects did not have dominant influence.

5.1.3.2. Gas cooled reactors

Compared to LWRs, gas cooled reactors may employ different type of fuel. Generally speaking, very high temperature gas reactors may employ fuel in the form of graphite pebbles or in the form of graphite prismatic blocks, while others may employ traditional pin type fuel or plate type fuel. In this section, the focus is on pebble type fuel since the flow dynamics and heat transfer in such reactor cores is specifically challenging and has attracted the interest in using the CFD. However, this does not mean that there are no challenges for prismatic block, pin, or plate type fuel assembly designs.

The strategies for nuclear pebble bed simulations depends on the scale of geometric resolution as shown in Fig. 43 [116]. Detailed experimental data for the flow and heat transport in the heated randomly stacked pebble bed were unavailable at the time, so that numerical approach using high resolution CFD is an alternative. In this approach, the starting point was the flow around the single pebble in a single face cubic centered domain. Details of quasi-DNS data and true DNS data created from the artificial pebble bed domain in which pebbles don't touch one another can be found in Refs. [117]. Whereas the validation of the lower resolution CFD models, ranging from LES to RANS are detailed in Ref. [118]. For the purpose of validating lower resolution simulation models, the limited sized random beds are usually considered [116]. A study of the effect of the special pebble stacking near solid wall is given in Ref. [119]. Impressive demonstrations of CFD capabilities to that respect are found in [120]–[123].

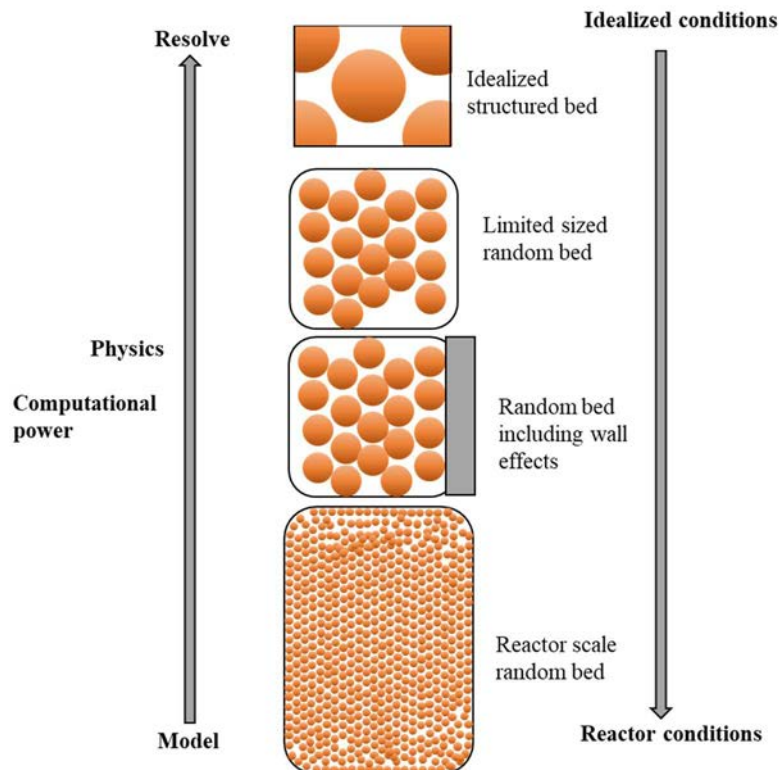


FIG. 43. Different strategies for nuclear pebble bed simulations and practical examples (adapted from [116]).

While the CFD simulation of the flow and heat transport in randomly stacked static pebble beds is already complex enough on its own, one should also consider that these pebbles are constantly moving in the reactor. These pebble movements can typically be simulated with finite element methods which need to be combined with CFD analyses for a clearer view on flow and heat transport phenomena. Furthermore, one should also notice that the pebbles, approximately the size of a tennis ball, contain fuel which is distributed in small, coated particles, approximately 1 mm diameter. The generated nuclear heat will be influenced by the configuration of the bed. This requires a multi physics approach coupling neutron transport codes to CFD. Such developments are ongoing. In addition to high resolution CFD approaches, lots of work is being dedicated to improving the existing lower resolution porous media approaches. These are typically employed in traditional nuclear system codes, as well as, occasionally, in CFD simulations which consider the complete primary system of a pebble bed reactor. Next to the core region, the core outlet region of high temperature gas cooled reactors is of great interest since the jets exiting the core at elevated but possibly different temperatures might give rise to

high cycle thermal fatigue issues, e.g., in the core support structures and the hot duct connecting the reactor vessel and the heat exchanger.

5.1.3.3. Liquid metal cooled reactors

Similarly, the simulation strategy for liquid metal cooled reactors ranges from subchannel to full core simulations as represented in Fig. 44. The modelling starts at subchannel level for which high resolution experiments and simulations serve as references, allowing to validate lower resolution modelling. Such approaches allow to model and validate a full scale fuel assembly, while based on that experience, an extrapolation can be made to full core simulations, in which the details of the pins are typically omitted and modelled through a porous medium approach, in the meantime simulating the inter wrapper flow between the fuel assemblies in full CFD.

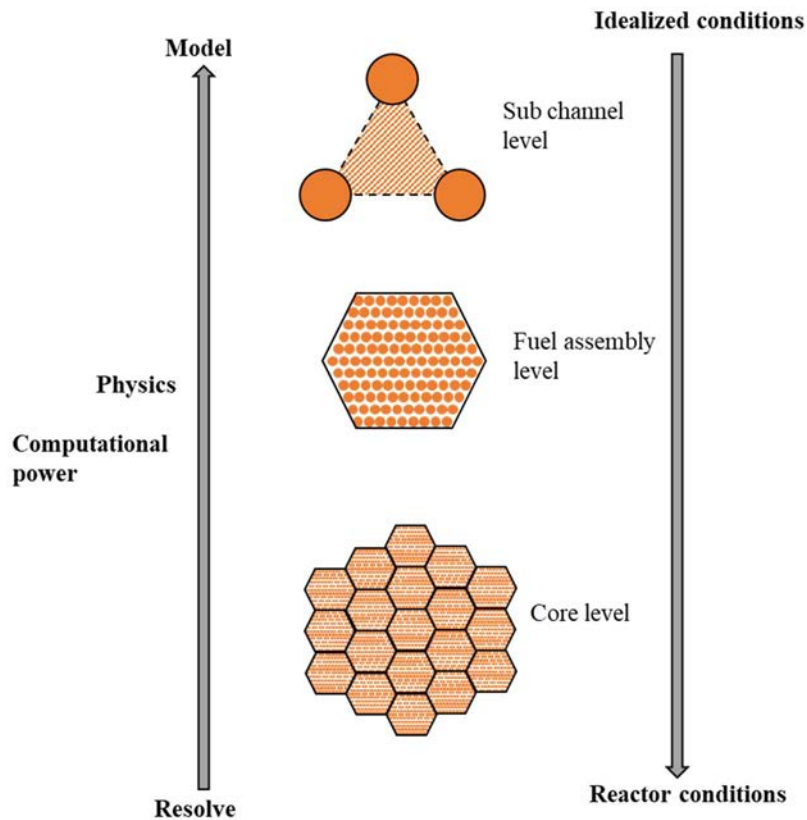


FIG. 44. Different scales for liquid metal cooled fast reactors analysis.

Significant efforts have been dedicated to validating CFD models for both wires wrapped as well as grid spaced liquid metal cooled reactor fuel assemblies. An overview for validation efforts of simulations of wire wrapped fuel assemblies can be found in Roelofs et al. [124]. These efforts typically concentrate on the prediction of pressure drop, flow and temperature field of fuel assemblies because of their design on the drawing board and under the expected operational conditions. However, validation of the simulation model should be expanded to various kinds of other conditions.

The possible occurrence and effect of vibrations needs to be assessed as well. Computationally this is difficult since it often involves a coupling between structural mechanics solver and CFD solver. It is well known that fuel assemblies typically are subject to some degree of deformation,

even under operational conditions. The effects of such deformations need to be studied if possible, and their onset as well. If one goes beyond operational conditions, the formation and especially the effects of local or global blockages in fuel assemblies deserve attention as well as the influence of the inter wrapper flow region in accidental transients.

Regarding the modelling of the pool, given the current computer power, reasonably detailed models consisting of millions of computational cells are standard and allow for steady state and (short) transient simulations [125]. The large components in a reactor pool, such as reactor core, the above core structure, heat exchangers, and pumps, require a geometric and modelling approximation by using porous medium methods combined with momentum and heat sources. In addition, several studies indicated that for a correct prediction of local temperatures, inclusion of heat transfer in internal structures through conjugate heat transfer is necessary.

Examples of pool thermal hydraulics CFD simulations and their results for various experimental facilities in support of liquid metal reactor designs as well as actual liquid metal reactor designs can be found in [126]–[133].

Full system thermal hydraulics is traditionally solved numerically with lumped parameter codes, also known as system codes. However, for many innovative nuclear reactor designs, these 0D or 1D codes have a significant drawback in their accuracy when solving for 3D flows in non conventional geometries, as those of the innovative reactors. One possibility is to model a complete system in CFD. However, this needs the implementation of models for large components which are readily available in system thermal hydraulics codes for the core, the pumps, and heat exchangers. Apart from that, the computational effort might become too large by modelling pipe systems in CFD. Another possibility is to couple existing system thermal hydraulic codes to CFD codes and use the benefits of both codes. Such a computational approach is called a multi scale approach. Several representative examples of such approaches can be found in Refs. [134], [135].

5.1.4. Summary

The CFD plays an important part in the design and safety assessment of nuclear reactors. The main future challenge is to integrate the application of CFD in the licensing process. This will require proper validation of the models and simulation approaches with suitable reference data, being a combination of experiments and high resolution simulations. This is also true for the modelling of innovative nuclear reactors which use different coolants rather than water. For such reactors, turbulent heat transfer raises specific challenges, since the widely applied Reynolds analogy is not valid for supercritical water, and liquid metals. Important challenges specific to the various innovative reactor types are:

- Modelling of heat transfer enhancement and deterioration in supercritical water cooled reactors;
- Modelling of pebble beds and bypass flows in gas cooled reactors;
- Multi scale modelling of the primary systems and energy conversion loops of liquid metal cooled reactors.

5.2. MULTI SCALE REACTOR SIMULATIONS

5.2.1. Overview of multi scale reactor simulation models and modelling scales

5.2.1.1. Modelling scales in reactor thermal hydraulics analysis

A wide range of fluid mechanics phenomena contribute to the thermal hydraulic behaviour of complex, large-scale systems such as nuclear reactors. In principle, these phenomena can be directly modelled using direct simulation of the Navier-Stokes equations. Nevertheless, such a reactor scale DNS approach is not feasible, given that such a model needs to span a range of spatial scales l and temporal scales t between:

- Microscopic scales based on molecular diffusion: $l < 10^{-6}$ m, $t \sim 10^{-6}$ s;
- Millimetric scales based on the smallest features in the core or heat exchangers: $l < 10^{-4} - 10^{-3}$ m;
- Large scales based on the reactor behavior itself, i.e., $l \sim 10$ m, $t \sim 10^6$ s for long transients.

An DNS model requires $\sim 10^{15} - 10^{18}$ mesh cells and up to 10^{10} time steps (depending on the reactor transient). While these estimates are rough, it seems likely that reactor scale direct simulations will not be feasible until the 2050 s at least. Averaging over turbulent fluctuations (as in RANS) reduces these estimates to $10^9 - 10^{10}$ mesh cells, around the edge of feasibility [136]. However, it probably takes a decade or so for this type of study to become common. While the large scale range remains an impediment to direct simulations, it does provide a path to an efficient way of modelling reactor thermal hydraulics. Almost always, small scale phenomena are locally complex, and only affect larger scales through statistical properties (average and variance). When these scales are separated, the overall effect of a given microscopical phenomenon on a larger scale can be accurately represented by a simple model describing its average behaviour. Such a model can in turn be constructed:

- Theoretically, by assuming that small scale behavior is self averaging (this assumption is at the root of most turbulence models);
- Experimentally, by performing analytical or intermediate scale experiments, to directly formulate a correlation for the phenomenon. These correlations are widely applied to model, at large scales, without dealing the small scale turbulent phenomena;
- Numerically, by performing small scale simulations of the local phenomena for all relevant input conditions (this is known as numerical experiment);
- By combining two or more of these methods.

Practically, this scale separation has also contributed to the wide variety of thermal hydraulics codes currently used to simulate nuclear reactor thermal hydraulics. For the smallest level, DNS CFD codes can directly simulate microscopic phenomena, however, practically, these are mostly limited to the simulation of smaller domains, typically of the size smaller than a single reactor subassembly.

For the larger scales, LES and RANS CFD codes can be used to model larger domains by employing turbulence models, as long as the domain under study can be meshed with the required precision without incurring exorbitant costs. At a further scale larger than that of RANS CFD codes, subchannel and so called coarse mesh CFD codes have been developed to model domains in which local geometric features are too complex to be meshed directly: this

is the case for complete core models, for which a detail geometrical meshing of mixing vanes (in LWRs) or wire wrappers (in sodium fast reactors (SFRs)) is prohibitive. In these codes, correlations are used to describe the effects of unresolved geometrical features. At the coarsest of scales, system thermal hydraulics (STH) codes have been developed to model the overall behaviour of a nuclear reactor (complete) for long transients, usually via a combination of 0D, 1D and 3D elements. At this scale, almost all physical phenomena need to be described by correlations.

5.2.1.2. *Interactions between scales*

The thermal hydraulics simulations usually involve modelling of large components (e.g., the core) or even a complete circuit (such as the primary circuit in PWR). Given practical limitations outlined in the previous section, these simulations must often be performed at the system scale. Because the simulation scale used in STH is relatively coarse, physical models must be used to describe all local phenomena that may impact a given transient of interest; however, establishing and validating these models can be challenging. The following are some examples of PWRs and liquid metal cooled reactors (LMRs).

In PWRs, coolant flow path is from the cold legs to the core inlet, via the downcomer and inlet plenum, and from the core outlet to the hot legs, via the outlet plenum strongly influences the reactor behaviour during asymmetric transients such as loss of coolant accidents, steam generator tube ruptures, or steam line breaks. For forced convection, mixing effects can be modelled in STH using experimentally validated mixing matrices. However, at a smaller flow rates or flow reversal conditions, flow patterns within these regions become complex and the mixing matrix approach is no more reliable [137].

LMRs mostly have pool type design for primary circuit to minimize loss of coolant accident risks and to provide a strong thermal inertia. Therefore, residual heat removal commonly relies on passive natural convection: which results in the large sodium plena around the core stratify, while the jets at the outlet of the core and heat exchangers transition from velocity to buoyancy driven flow. Heat exchanges between the hot and cold pools, as well as lateral cooling of the core assemblies, influence the natural convection regime. These phenomena have such a strong influence on natural convection that failing to account for them can result in a 50% overestimation of flowrate through the core [138]. Furthermore, convection loops between the core and its outlet plenum can contribute up to 30% of total decay heat removal.

Water cooled small modular reactors, such as NuScale design or NUWARD design, adopt an integrated primary circuit layout in which the core is located at the bottom of a large primary vessel; during natural convection, there is complex buoyant flow with large hot plume above the core for SFR. The traditional method for accounting for the effects presented thus far for these various reactor types at the system scale is to introduce conservative propositions into the modelling (for example, by assuming that mixing effects in the outlet plenum are as unfavourable as possible) along with the increase in the design margins as required. Recent advanced in numerical simulations have made it possible to simulate a number of these phenomena.

5.2.1.3. *Simulating multi scale phenomena*

Using available thermal hydraulics tools, two main approaches can be used to simulate local phenomena. The first method, referred to as a single scale approach, calls for a model of the

entire domain at the smallest scale necessary to describe all of the phenomena of interest (usually, a coarse CFD scale). The second option is to use a multi scale model in which each part of the reactor is modelled at the coarsest scale capable of describing the local phenomena of interest. Both of these methods are used for PWRs and LMRs.

The single scale approach has its pros and cons: the main advantage is that the existing numerical framework of a CFD code can be used (with its associated verification/validation matrix), whereas the disadvantage is that the whole domain (typically a reactor) must be modelled at CFD scale, including the regions of no interest. Additionally, existing models must be reprogrammed to include neutronics (for core power), pump and coarse scale heat exchange models, and subchannel pressure drop and/or mixing models. Once developed, these require verification and validation so to be consistent with the original code(s). The main benefit of a multi scale approach is that each scale can be modelled using the existing codes, remedying the need to use new models. To use them jointly as part of the multiscale model, these codes may need to be modified, which is one of the disadvantages of this approach. Typically, this involves creating a coupling interface with features that can control each code and exchange data with a different supervisor or master code. A new numerical scheme needs to be created for the overall coupled calculation, which is another drawback. This framework is anticipated to explain how scale interfaces are handled (for example, at the boundary between a system and a CFD domain); it should also converge to a multiscale solution that is consistent across scales, with no remaining inconsistencies between the solutions obtained by each code. Properties that conserve mass and energy are also very desirable. Once created, this coupling scheme needs to undergo the same level of validation and verification as the initial codes.

Several examples of implementation of abovementioned strategies are deployed as follows:

- Multi scale models of a complete loop/reactor coupling a CFD code (used to model a specific part of the circuit, such as a plenum) with a system code (used to model the rest of the circuit) [139];
- Multiscale models of an entire LMR core that couple a CFD model of the surrounding plenum to a subchannel model of the inside of the subassemblies [140]. In some instances, this kind of model is coupled with a system/CFD to create a three scale model of an entire reactor plenum. [141];
- Single scale CFD models of a complete reactor primary circuit using integrated coarse models (i.e., porous media based or 1D) for the core, heat exchangers and pumps.

In general, the multiscale approach is highly attractive as it is plausible to reuse the existing codes; and small algorithms implementing a code-to-code coupling can solve the problems in a relatively short time. Although the implementation of a verification and validation strategy typically necessitates the development of generic coupling. This generic coupling can be used for the modelling of both reactor cases and the experiments and further be used to validate a method. The development and verification of a coupled numerical scheme is potentially difficult and may require important or unexpected modifications as well as the development of a coupled model of a given experiment or reactor design can be undertaken ad hoc. To ensure that the validation studies can be extrapolated to the reactor applications, it is deemed crucial that this capability be present. Additionally, experiments that can take a long time are required to validate the effects predicted by a single scale or multiscale approach.

5.2.2. Multi scale coupling algorithms

This section describes multiscale coupling scheme using the existing codes, focusing on describing prevalent approaches and associated advantages and disadvantages.

5.2.2.1. Domain decomposition and domain overlapping

The search for an appropriate modelling scale for each domain of interest constitutes the first step in the development of a multiscale code coupling; in most cases, a PIRT like process results in the selection of the coarsest scale capable of representing all local phenomena that may have an impact on the system's overall behaviour. In turn, this procedure will result in the identification of:

- One or more (so called) fine domains, enclosing regions where local effects may occur, for which the obvious choices are subchannel or CFD codes;
- Coarse domain, enclosing the rest of the reactor or loop with possible inclusion of additional circuits and secondary loops, which should be modelled by a system code.

Once this choice is made, the actual domains for computation are then to be chosen; two choices are available.

- First option entails fitting each code's computational domain to the fine and coarse domains identified above in order to assign each of them to a single code. The interactions between codes in this so-called domain decomposition approach only occur at the boundaries between coarse and fine domains, which typically results in a simpler design for the coupling algorithm. Such an approach is schematically represented in Fig. 45 (a). However, this choice requires a tight coupling between the codes; considering the fact that the overall pressure field is strongly coupled in incompressible systems, needs to be shared between several codes. This makes the convergence more difficult in the coupling algorithm.

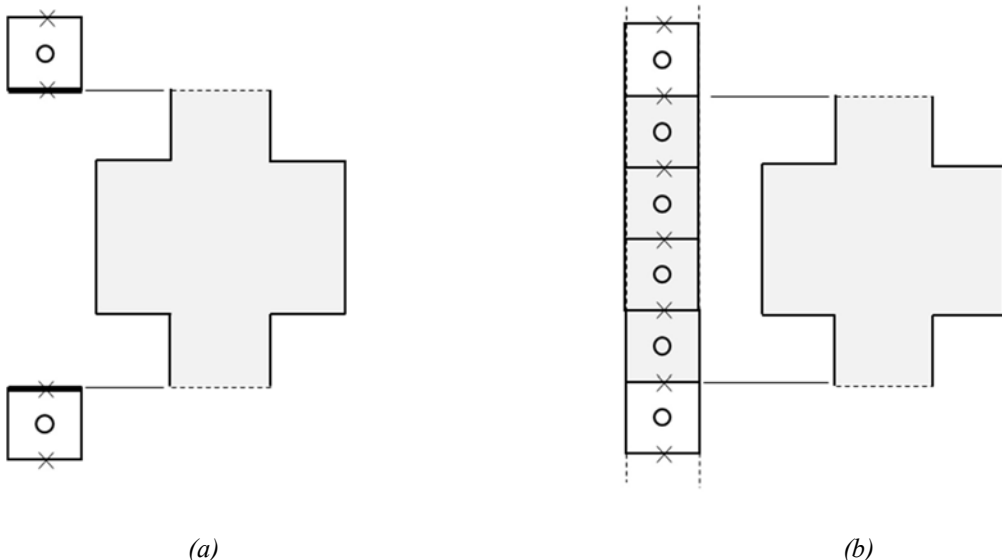


FIG. 45. (a) Domain decomposition and (b) domain overlapping approaches to multi scale coupling of a two scale system (adapted from [142]).

- Second choice consists of having a complete representation of a domain of interest in coarse computational domain, namely inclusive of the fine domain as well, modelled in some way. This is schematically represented in Fig. 45 (b).
- To produce an overall coupled calculation using this domain overlapping approach, the coarse results from the system code's fine computational domain must be overlaid with the results from the CFD/subchannel scale.

Compared to decomposition approach, the domain overlapping approach has its own advantages and disadvantages. As the system code computes the overlapped domain, exchanging coupling data at the fine domain's boundaries may not be sufficient. The coupling ensures that the outside part of the system scale computation is consistent with the findings obtained with the CFD/subchannel code in the overlapped domains. Furthermore, due to the additional complexity, an overlapped coupling is inherently more difficult to implement and verify than a decomposition coupling; whereas an error in the coupling algorithm usually results in easily visible defects in a decomposition coupling, an error in an overlapped coupling usually results in spurious use of system scale. This results in a significantly visible degradation of the coupled solution, which may be difficult to detect or track down. Some of the tight coupling issues associated with the decomposition approach are usually avoided by using an overlapped coupling. The pressure field calculations performed by the system and CFD codes are not tightly coupled in an overlapped coupling and can be implemented using the source terms. For this reason, numerical implementation of an overlapped coupling algorithm may indeed to be simpler. The system scale model used for coupled calculations is self sufficient in the overlapped approach to perform standalone calculations. This capability can be used to provide an initial state for the coupled calculation without the need for a different STH model (as coupled calculations are typically initialised from a STH steady state); it also enables easy comparison of differences between the coupled calculation and its original STH calculation.

Sections 5.2.2.2 and 5.2.2.3 deliberate on practical applications of overlapped and decomposition approaches in two specific cases: when the coupling boundary separate domains undergoing fluid exchanges and when the coupling interface is placed at a boundary between a solid and a fluid.

5.2.2.2. Coupling at hydraulic boundaries

The most common case of coupling in multi scale calculation is boundary between two fluid domains. Coupling strategy at such boundary, requires the following to constitutes a good start:

- A. Boundary needs to conserve mass, exiting flow from one the domains (STH or CFD) is equal to the flow coming into another domain (CFD or STH);
- B. Boundary needs to similarly conserve energy, transported enthalpy going out from one domain being equal coming into another domain;
- C. Boundary needs to ensure a consistent pressure field, so that both codes get the same pressure at the boundary. For incompressible flows, it is sufficient to ensure this equality up to a constant; hence, it is needed to ensure the consistency of the pressure differences between any two boundaries.

To guarantee a consistent multi scale calculation, this conservation approach is sufficient but not necessary. In fact, one may prefer a coupling algorithm in which one of these constraints is relaxed but which would nonetheless converge, in time and/or space, to a consistent result. In situations when numerous repetitions are required for the exact verification of certain criteria,

such non conservative techniques may be appealing. The implementation of matching inlet and outlet boundary conditions on the STH and CFD sides, with a pressure boundary condition on one side matching a flowrate boundary condition on the other, can ensure that conditions A and C are met for domain decomposition couplings. If code to code exchanges are utilized to ensure that the flowrate or pressure computed by one code at the boundary is used as a boundary condition on the other side, then conditions A and B can be satisfied. This is represented in FIG. 46 (a).

For the domain overlapping, STH code computed flow rates can be used as a boundary condition on the CFD side in order to guarantee A condition (for incompressible systems, it is sufficient to impose flowrate at all but one inlets/outlets). Pressures can be applied directly to the STH side to verify the pressure consistency C condition, resulting in a coupling algorithm akin to those used for domain decomposition; alternatively, source terms can be added inside the STH domain, as indicated in FIG. 46 (b).

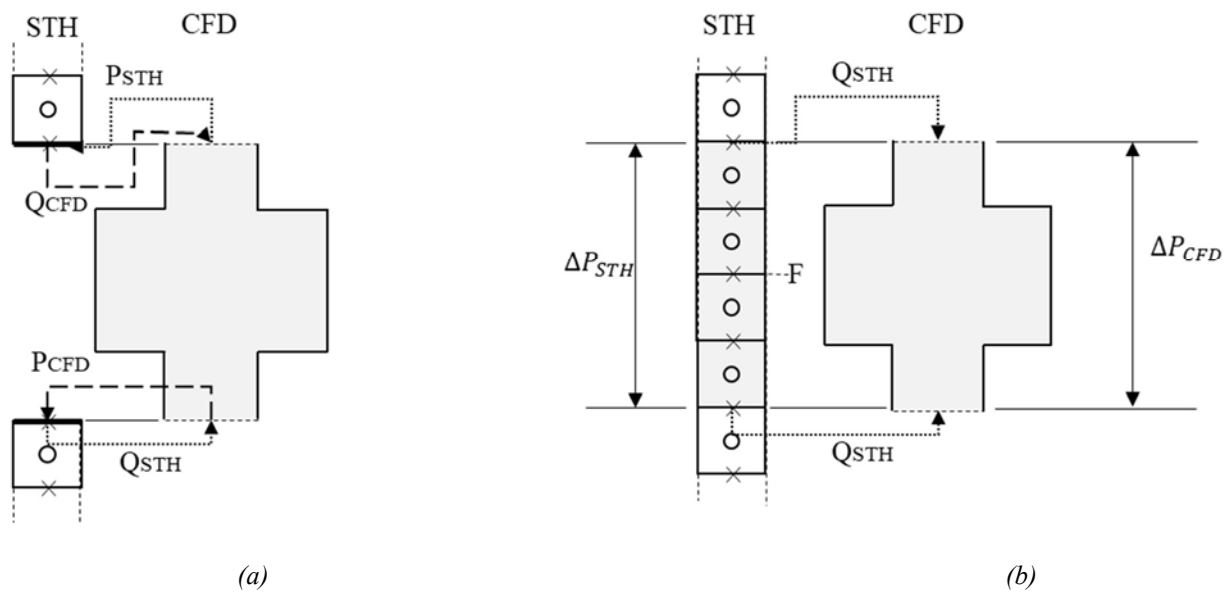


FIG. 46. Examples of hydraulic coupling strategies between system and CFD domain in (a) domain decomposition and (b) domain overlapping approaches (adapted from [142]).

The disparity in scales between the coarse and fine domains necessitates yet another consideration. The STH code typically computes (or requires) a single, average velocity to describe the flow at the boundary. In contrast, the CFD code computes (or requires) a 2D velocity profile at the boundary. As indicated by Fig. 47, this can lead to several problems.

If the velocity profile is imposed by the boundary condition on the CFD side, the simplest option is to impose a constant velocity equal to those computed by the system code. The flow leaving the boundary, however, won't develop in the CFD domain at that point. The most elegant way to address this is to impose a fully developed velocity profile that complies with the mass conservation condition on the CFD side. In order to reduce this developing flow effect, most users prefer to extend the CFD domain of their calculations by a few hydraulic diameters at the inlet/outlet. One may decide to include a flow development region outside of the coupled CFD domain in the domain overlapping approach, as represented in Fig. 47 (b), to allow the CFD flow to develop without affecting the overall computation procedure. Secondly, the CFD code may compute a velocity profile with local flow inversions if the boundary condition on the CFD side is of the imposed pressure type. Although it is possible to make such a profile consistent

with conservation conditions A, B, and C, it is undesirable because it cannot be accurately described on the STH side. Using flowrate boundary conditions as much as possible, especially in areas where two way flow may develop, is a common way to prevent this situation.

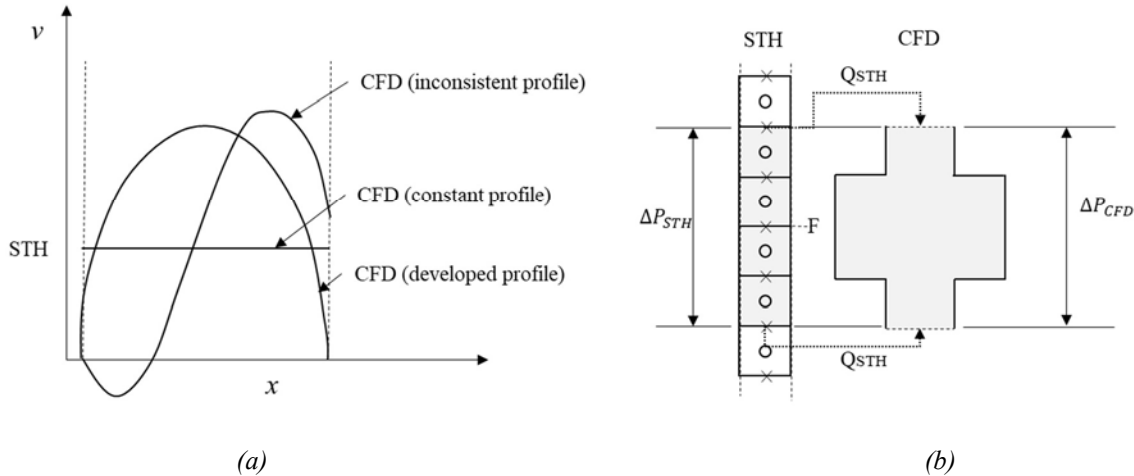


FIG. 47. Possible velocity profiles at a STH/CFD boundary satisfying the flowrate consistency condition. (a) Imposing constant velocity equal to those computed by the STH code results in non developed flow condition on the CFD side; (b) flow is already fully developed when it enters the coupled region (adapted from [142]).

The energy passing through the boundary must remain equal on the STH and system sides in order to satisfy the energy conservation condition C. This condition reads as follows when comparing the STH and CFD descriptions of the boundary:

$$H_{STH}v_{STH}S = \int_S H_{CFD}\mathbf{v}_{CFD} \cdot d\mathbf{S} \quad (291)$$

where S is the area of the boundary S , H_{STH} and v_{STH} are the advected liquid enthalpy and velocity across the boundary on the system side, respectively, and H_{CFD} and \mathbf{v}_{CFD} are their counterparts for the CFD side. This equation need to be fulfilled by the coupling algorithm via adjusting either H_{STH} (for CFD → STH flow) or H_{CFD} (for STH → CFD flow), considering discretization and advection schemes used by each code.

In common case where the system code uses a staggered grid discretization with an upstream convection scheme (such as RELAP, CATHARE, TRACE, etc.), this condition can be satisfied, as long as no two way flow occurs, by the scheme as described in Fig. 48. In this figure, the average temperature T_{CFD} is obtained by taking a flow weighted average of the temperature on the surface of the boundary on the CFD side; it can be imposed in the system code either by replacing the energy equation in the relevant mesh (if possible) or by adding heat source/sink terms to this equation. A more complex formulation is adopted if the system code uses a different advection scheme (such as a centred scheme). It can be noted that these hydraulic coupling interfaces lead to approximations in the momentum and energy equations at the boundary. Fig. 48 shows that the effects of heat diffusion in the meshes around the boundary are neglected. These effects are typically regarded as minor (except for the case for a liquid-to-wall coupling).

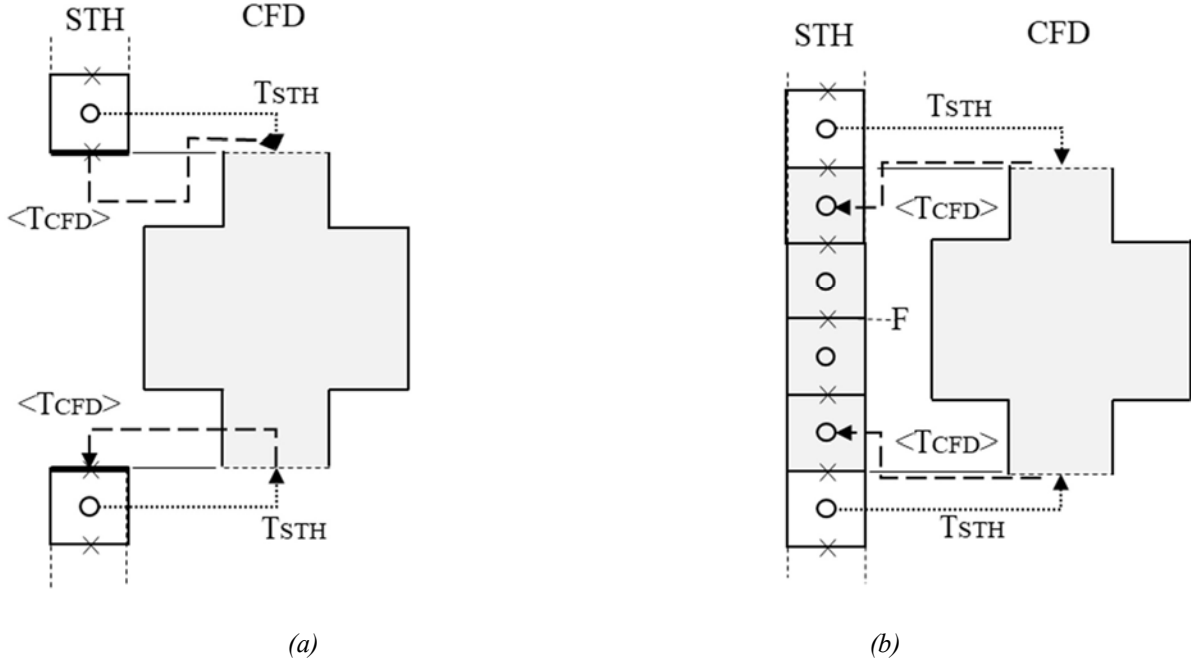


FIG. 48. Thermal coupling at a hydraulic boundary between a STH and a CFD code in (a) domain decomposition and (b) domain overlapping approaches (adapted from [142]).

5.2.2.3. Coupling at thermal boundaries

Heat conduction effects through the boundary are typically ignored at coupling interfaces at hydraulic boundaries. In rare cases, thermal exchanges between domains described by different codes may need to be modelled:

- To incorporate the CFD model of the primary circuit into a reactor model that includes descriptions of the intermediate heat exchangers and their secondary circuits, the heat transfers occurring at the intermediate heat exchanger must be modelled by a coupling between the CFD model of the intermediate heat exchanger primary side and the system model of the intermediate heat exchanger secondary side.
- Heat removal by the inter wrapper flow must be modelled in complete core models coupling a subchannel description of the inside of the subassemblies to a CFD model of the inter wrapper region. This is done by coupling the wrappers (modelled by the subchannel code) to the inter wrapper CFD.

The high surface to volume ratios of the exchange surfaces in these two geometries cause a strong coupling between the energy equations of the two codes involved, which can be difficult to model efficiently. Fig. 49 shows the decomposition and overlapping techniques' examples of coupling procedures at thermal coupling boundaries. In both situations, the STH or subchannel code computes the wall; the CFD domain meshes are connected to this wall by interpolating the wall temperature onto the CFD meshes and adding a source term to the CFD energy equation of the following form:

$$\Phi_{CFD} = h(T_{CFD}^L - T_{STH}^W) \quad (292)$$

where T_{STH}^W is the interpolated wall temperature of the system code, T_{CFD}^L is the liquid temperature in the CFD code and where the volumetric exchange coefficient h can either be

computed locally by the CFD code or globally by the system code (this is often the case in an overlapped coupling). The CFD code is in charge of calculating the heat flux through the wall when using this source term; at the subsequent iteration of the STH code, this heat flux is interpolated onto the STH mesh and imposed to the STH, substituting its own calculation.

The consistency of the heat flow in all CFD meshes relating to a single STH mesh might result in unphysical temperatures when computing the heat flux in the STH code and then applying this flux to the CFD domain. The CFD meshes with slower flow on the CFD side typically experience continual heat removal, resulting in temperatures that are lower than those on the secondary side. In the overlapped case, simply projecting the CFD domain's liquid temperature onto the overlapped domain at the next STH iteration is insufficient; while this method converges to a consistent solution, the heat fluxes calculated in the STH and CFD codes are equal, violating energy conservation. In the source term given by Eq. (292), the use of the STH wall temperature and the local wall-to-fluid heat exchange coefficient leads to a very strong coupling in liquid metal system, along with the associated timestep stability conditions. Instead, some system codes are able to provide the susceptibility of the wall heat flux to the liquid temperature of the adjacent mesh:

$$\Phi_{STH} = \Phi_0 + \xi(T_{STH}^L - T_0) \quad (293)$$

where the susceptibility coefficient ξ is typically one or two orders of magnitude less than the heat exchange coefficient h . Therefore, ξ can be used instead of h in the heat source term on the CFD side, together with an equivalent wall temperature (equivalent to Eq. (292)):

$$\Phi_{CFD} = \Phi_0 + \xi(T_{CFD}^L - T_0) = \xi(T_{CFD}^L - \tilde{T}) \quad (294)$$

$$\tilde{T} = T_0 - \frac{\Phi_0}{\xi} \quad (295)$$

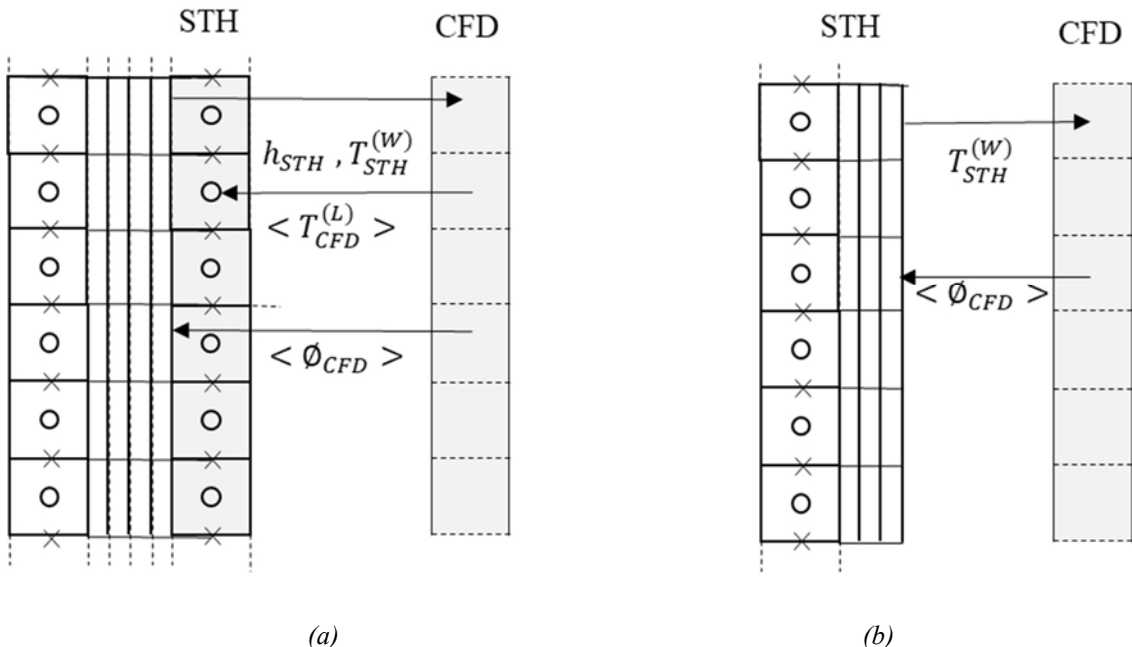


FIG. 49. Coupling strategies at thermal boundary between a STH and a CFD code in (a) overlapping and (b) domain decomposition approaches (adapted from [142]).

5.2.2.4. Time schemes and internal iterations

The previously discussed coupling strategies can be used to couple two or more codes, with the aim to simulate a given transient via a multi scale approach. This time advancement scheme for the algorithms can be:

- *Explicit scheme*: the coupling approach guarantees consistency between calculation domains before each timestep;
- *Implicit scheme*: the coupling algorithm guarantees consistency of the computation domains for each timestep.

The coupling algorithm often only needs to exchange data across codes before the start of each time step, after which each code runs independently for duration of time step. If both runs are successful, time can be advanced, and the coupled global scheme can proceed to the following time step. Data exchanges can also take place only at certain synchronization points, allowing the codes to run at different timesteps. This functionality is most frequently utilized to let the CFD code use bigger timesteps than the system code. A typical implicit coupling method performs iterations for each code at a predetermined time step, coordinating data exchanges between iterations until the coupling parameters (defined, for example, at the boundary) converge to common values. Iterations may be necessary in thermal boundaries until the wall temperature on the STH side converges; iterations may be necessary in hydraulic boundaries until the pressure field converges (in a decomposition approach) or the pressure differences between coupled boundaries converge (in the overlapping approach). These iterations add to the numerical cost; however, these are required for the coupling strategies discussed previously:

- As shown in FIG. 46 and Fig. 47, are necessary to ensure that pressure field consistent between the two codes is reached at the end of the timestep;
- Thermal coupling, described in Fig. 49, requires at least a second STH iteration to ensure the equality between heat fluxes on the system and CFD sides.

The most prevalent iterative scheme is first order iteration (such as Gauss-Seidel), which involves passing coupling information back and forth between the codes until convergence to common values. Variants where the STH code iterates more frequently than the CFD code can offer an intriguing trade off because STH iterations are typically less expensive than CFD iterations. These schemes can also employ acceleration methodologies as well. Nonetheless, the Gauss-Seidel algorithm's convergence speed may be insufficient in some cases. A second order system, like Newton-Raphson, cannot typically be implemented directly since the coupling interfaces of the codes do not make the matrix elements necessary for this approach available. However, discrete derivatives can still be used to create a Newton-Raphson matrix for the coupled boundary variables [143]; and Jacobi free Newton-Krilev-like techniques can be used to solve the Newton-Raphson system using the first order data of the codes.

5.2.2.5. Extension to two phase flows

When two phase flows are possible, mass conservation in the domain overlapping approach becomes much more difficult; imposing the flowrate at a single boundary, as shown in FIG. 46 (b) is no longer sufficient as boiling is attained in the domain while the overlapped STH domain remains liquid. Consequently, the domain overlapping approach is rarely used for two phase flows, and the domain decomposition approach is much more common. Because domain decomposition tends to require more iterations to obtain common pressure field compared to

domain overlapping, an efficient iteration algorithm is indispensable for the overall simulation to be efficient. In practice, implementing a complete Newton algorithm seems to be the best choice [137]. As shown in Fig. 47, the flow consistency effects are much more pronounced in two phase flows; a two phase mixture with $\alpha = 0.5$ in the STH code may correspond to a stratified flow, a slug flow or churn flow on the CFD side. Treating these flow effects in the CFD domain thus becomes especially important. As a consequence of these observations, two phase multiscale coupling is much less attempted, and much less mature field than its single phase counterpart.

5.2.3. Verification and validation of multi scale simulations

In the context of reactor safety applications, validation and qualification efforts often add up to a major part of the development of any new code. For multi scale simulations, these efforts have, until now, mainly been focused on LMR applications. This is because two major reactor projects have integrated multi scale simulations: (a) French ASTRID SFR project used as the reference simulation method for natural convection and asymmetric transients a multi scale MATHYS model and coarse CFD StarCCM+/CATHARE model, and (b) Belgian MYRRHA lead bismuth reactor project also uses, in a more exploratory role, a multi scale model and a coarse CFD model. These two applications provide the impetus to develop a full validation approach for LMR multi scale simulations, as a prelude to full verification, validation, and uncertainty quantification [144].

5.2.3.1. Analytical verification of coupling algorithms

Analytical validation has a unique interpretation in a coupled code than it does in a system or CFD code. Individual effects anticipated by a coupled model are, by definition, the output of a computation by one of the codes (included in the model); novel phenomena foreseen by a coupled code, such as those brought about by the interaction of multiple scales, are typically viewed as combined effects. In order to ensure that the coupling algorithm is valid at the coupling boundaries between the codes, it is sufficient to construct a number of analytical test cases that cover all possible types of coupling boundaries that the algorithm may encounter.

5.2.3.2. Small and intermediate scale experiments

A few small scale facilities are used to validate multi scale approaches. For example, the TALL–3D facility [145] is an experiment designed at KTH Royal Institute of Technology in Sweden to study the coupling between liquid lead bismuth eutectic (LBE) three leg loop and a cylindrical 3D test section subjected to local effects such as stratification and jet impingement. The facility is specifically intended to foster interactions in between local effects and the global loop scale; the 3D section is located in one of two hot legs, with the other hot leg having a simpler pipe geometry. Both legs compete for natural convection flows during loss of flow transients, resulting in strong oscillations. These oscillations are then heavily influenced by local effects in the 3D section. The coupled models of TALL–3D is described in [146], and summarized in TABLE 4.

The NACIE–UP facility at ENEA Brasimone [147] is an LBE loop that includes a 19 pin wire wrapped subassembly, an argon gas lift section which is used to induce forced convection in the loop, and a heat removal exchanger. Only subchannel or CFD codes can model local phenomena in the subassembly; detailed instrumentation is available to validate these local effects. These local effects are only expected to influence overall behaviour at the scale of the

entire loops through their averaged properties (such as the assembly pressure drop): thus, system scale models are expected to already provide good results. In this case, using a coupled model allows one to compare the correlation that would be used at the system scale to the CFD code prediction. Two different multiscale models are developed for NACIE–UP [148], as shown in Table 5.

TABLE 4. SUMMARY OF COUPLED MODELS BY DIFFERENT INSTITUTIONS FOR THE ANALYSIS OF TALL–3D FACILITY

Institution	STH	CFD	Domain scheme	Time scheme
KTH Royal Institute of Technology (Sweden)	RELAP5	StarCCM+	Overlapping	Implicit
Gesellschaft für Anlagen und Reaktorsicherheit (GRS), Technical University of Munich (TUM) (Germany)	ATHLET	ANSYS	Decomposition	Explicit
Atomic Energy Commission (CEA) (France), National Agency for New Technologies, Energy and Sustainable Economic Development (ENEA) (Italy)	CATHARE	TrioCFD	Overlapping	Implicit
Nuclear Research Center (SCK-CEN) (Belgium)	RELAP5	FLUENT	Decomposition	Implicit

TABLE 5. SUMMARY OF COUPLED MODELS BY DIFFERENT INSTITUTIONS FOR THE ANALYSIS OF NACIE–UP FACILITY

Institution	STH	CFD	Domain scheme	Time scheme
University Pisa (Italy)	RELAP5	FLUENT	Decomposition	Implicit
National Agency for New Technologies, Energy and Sustainable Economic Development (ENEA) (Italy)	CATHARE	TrioCFD	Overlapping	Implicit

The THEADES facility at Karlsruhe Institute of Technology [149] aims to validate lateral heat exchanges between each subassembly in the core and the surrounding liquid metal though hexagonal wrappers enclosing each subassembly; it consists of three LBE cooled 7 pin subassemblies. Its results have been used to validate the MATHYS subchannel/CFD coupling [141], as well as to validate RANS CFD models.

5.2.3.3. Integral effects experiments

Integral effects tests (IETs) are rare for LMRs compared to LWRs. The coupled and/or CFD approach offer a large potential advantage, because the use of subchannel and/or CFD allow to predict geometrical effects. The following liquid metal IETs are used for multiscale validation. The CIRCE experiment is a substantial scale, integral LBE designed to illustrate and investigate core cooling through natural convection in an LMRs. Installed and tested are several different test sections, such as CIRCE-ICE [150] in which a dipped heat exchanger is used to remove heat; CIRCE-HERO in which HERO steam generator is used to remove heat. The first implemented model of CIRCE-HERO was by NRG, using the SPECTRA STH code coupled with ANSYS-CFX for the CFD side, with a domain overlapping coupling approach and explicit time scheme [151]. The E-SCAPE experiment at SCK/CEN is a large scale LBE facility

designed in a 1 to 6 similarity with the MYRRHA reactor [152]. Aside from direct STH validation, this facility is used to validate a coupled model by SCK/CEN employing RELAP5 for the STH side, FLUENT for the CFD side, a domain decompositions scheme for coupling between the two codes and an implicit time scheme. At Japanese Atomic Energy Agency, the PLANDTL facility is a large sodium loop designed in similarity to the JSFR reactor; its simulated core is surrounded by large plenum simulating the hot pool. In the first version of this experiment, PLANDTL-1, the core consisted of 7 subassemblies [153]; a more recent version, PLANDTL-2 [154] has a core consisting of 55 simpler subassemblies. Both experiments can be used to validate coupling between different paths for decay heat removal in a LMR (via normal primary circulation, via recirculation loops between subassemblies and via inter wrapper flow around the subassemblies); these are used to validate system, multi scale and CFD models.

5.2.3.4. Reactor validation

Integral validation on reactor tests is the final, and often most complex part, of the validation database before reactor application. The PHENIX reactor was a 250 MWe oxide fueled SFR operated by CEA, France, from 1973 and 2009. During the last year of its operation various end of life tests were done, including a natural convection test [155] (featuring a loss of the primary pumps) and an asymmetric test (consisting of a sudden trip in one of the intermediate loops while remaining in forced convection). Table 6 shows multi scale models of PHENIX that are benchmarked and validated [156].

TABLE 6. SUMMARY OF COUPLED MODELS BY DIFFERENT INSTITUTIONS FOR THE ANALYSIS OF THE PHENIX REACTOR

Institution	STH	CFD	Domain scheme	Time scheme
CEA	CATHARE	TrioMC/CFD	Overlapping	Implicit
Karlsruhe Institute of Technology (KIT)	ATHLET	OpenFOAM	Decomposition	Sequential
NRG	SPECTRA	ANSYS-CFD	Overlapping	Explicit
Argonne National Laboratory	scale adaptive simulations	Nek5000	Overlapping	Implicit

The EBR-II reactor was a 20 MWe metal fuelled SFR operated by Department of Energy (DOE) and at Idaho National Laboratory (USA) from 1964 to 1994. From 1984 to 1986, it was used for an extensive shutdown heat removal test (SHRT) programme.

Two tests from this programme (POLF, SHRT-18, and ULOF, SHRT-45R) were analysed as part of an IAEA coordinated research project [157]; two additional tests (PLOHS and ULOHS) are analysed in the framework of an OECD GIF benchmark. Multi scale models of this reactor are under development at CEA, Japanese Atomic Energy Agency, and DOE. The FFTF reactor was a 400 MWth oxide fuelled SFR operated by DOE at Pacific National Laboratory (USA) between 1980 and 1992. In 1986, it underwent a series of passive safety tests; the most challenging of those tests, ULOF transient from 50% of nominal power, is analyzed in the framework of an IAEA coordinated research project.

5.2.4. Summary

Nuclear reactors are occasionally subject to transients where phenomena occurring at different scales start to interact: this can happen in large LWRs, but is quite common in pool type designs

such as LMRs or integral small modular reactors. Local effects in these reactors can influence global behaviour in a variety of situations, such as transition to natural convection and passive removal of decay heat power. In the presence of such situations, accurate modelling necessitates a method for incorporating the simulation of small, local effects into a model of the entire system. Multi scale models enable the construction of such a model while maximizing the use of existing codes for reactor thermal hydraulics at the system, subchannel, and CFD scales.

A multi scale model can reflect every part of the system at the description scale needed by the phenomena that should be modelled by coupling two or more of these codes, trying to eliminate the need to use a fine description of the entire domain. A coupling algorithm provides consistency across time between the various domains computed by each code, especially at the coupling boundaries separating two domains simulated at various scales; if this is the case, the multi scale calculation can predict global effects caused by the interaction of phenomena occurring at different scales. Practically, implementation of multi scale coupling remains a non trivial task. It is not always easy to ensure consistency at the coupling interfaces when the codes under consideration include data exchange interfaces.

The coupling strategies used to achieve consistency frequently necessitate an iterative process between the codes. This process can be especially costly in incompressible cases where the pressure field calculations of the codes are interdependent. This problem can be solved by using an overlapping approach, in which the system code contains the full computational domain; however, this method makes it more challenging to guarantee code-to-code consistency. Also, implementation of acceleration methods may also improve the convergence speed of the code-to-code iterations. Adapting these strategies to two phase flows is still an open problem. Eventually, it is expected that multi scale couplings will be used in the safety demonstration of advanced (future) reactors [144]. To achieve this, coupling strategies will need to undergo an extensive verification, validation, and uncertainty quantification.

6. UNCERTAINTY QUANTIFICATION AND ERROR ANALYSIS

This section summarizes some of the experiences gathered in the domain of uncertainty quantification of one phase CFD applied to nuclear reactor thermal hydraulics issues. Single phase CFD is used for design and safety analysis of LWRs. The WGAMA launched initiatives to promote the use of CFD for nuclear reactor safety analysis.

A list of safety issues for which CFD could be useful were identified. Recommended practice guidelines for single phase CFD have been written and the requirements for assessment are also addressed. By defining the conditions and requirements for having confidence in the predictions, these activities increase confidence in the application of CFD. However, no applicable methods are written about possible quantitative evaluation of prediction uncertainty, which is required in a best estimate approach.

The methodology for determining the uncertainty of CFD predictions applied to reactor thermal hydraulics is then reviewed in a new activity. Because there are available methods, a comparison with system codes may be useful. A comparison with system codes may be useful since available methods are rather mature.

6.1. APPLICATION OF SINGLE PHASE COMPUTATIONAL FLUID DYNAMICS

In this section the best practice guidelines are summarized [17], [18], [158]. The classification of identified problems of interest to uncertainty quantification in CFD is summarized in Table 7. With some overlaps, the data is roughly grouped into problems relevant to reactor core, primary circuit, and containment.

TABLE 7. PHENOMENA OF INTEREST TO UNCERTAINTY QUANTIFICATION IN CFD APPLIED TO REACTOR ANALYSIS

NRS problem	System classification	Accident classification	Flow type
Erosion, corrosion, deposition	Core, primary, secondary	Operational	Single and multi phase
BWR core instability	Core	Operational	Multi phase
BWR transition boiling	Core	Operational	Multi phase
BWR recriticality	Core	BDBA ¹	Multi phase
Reflooding	Core	DBA ²	Multi phase
Lower plenum debris coolability, melt distribution	Core	BDBA	Multi phase
Boron dilution	Primary circuit	DBA	Single phase
Mixing: stratification, hot leg heterogeneities	Primary circuit	Operational	Single and multi phase
Heterogeneous flow distribution	Primary circuit	Operational	Single phase
BWR lower plenum flow	Primary circuit	Operational	Single and multi phase
Water hammer condensation	Primary circuit	Operational	Multi phase
Pressurized thermal shock	Primary circuit	DBA	Single and multi phase
Pipe break	Primary circuit	DBA	Multi phase
Induced break	Primary circuit	DBA	Single phase
Thermal fatigue	Primary circuit	Operational	Single phase
Hydrogen distribution	Containment	BDBA	Single and multi phase
Chemical reactions	Containment	BDBA	Single and multi phase
Aerosol deposition, atmospheric transport	Containment	BDBA	Multi phase
Direct contact condensation	Containment, primary circuit	DBA	Multi phase
Bubble dynamics in suppression pools	Containment	DBA	Multi phase
Behavior of gas–liquid interfaces and surfaces	Containment, primary circuit	Operational	Multi phase
Special considerations for advanced reactors	Containment, primary circuit	DBA/BDBA	Single and multi phase

¹ BDBA: beyond design basis accident

² DBA: design basis accident

As far as single phase issues are concerned, it seems that the majority of these are related to turbulent mixing problems, such as temperature mixing or mixing of chemical components in a multi component mixture, boron dilution, mixing and stratification in the hot legs, lower plenum flows in BWRs, pressurized thermal shocks, thermal fatigue, hydrogen distribution, chemical reaction up to combustion and detonation, and special considerations for advanced reactor concepts. All these mixing phenomena may be simulated with both RANS and LES, with the consideration that RANS models require less computational time and are thus likely to be preferred [17].

The uncertainty evaluation of CFD need to be focused on mixing problems with density effects in steady state or in slow transients, since it covers most envisaged applications.

6.2. BEST ESTIMATE AND UNCERTAINTY APPROACH

6.2.1. Nuclear reactor thermal hydraulics analysis

Reactor safety assessment requires the analyses of complex problems related to various operating conditions. Two options to demonstrate the reactor safety are experimental and numerical simulations. The experiments require simplifications to reproduce realistic scenarios at a practical cost, and the computational tools cannot simulate the scenarios by solving the rigorous equations. It is only practical to conduct small scale experiments to study the phenomenon, and only an approximate system of equations can be solved to determine the time and/or space averaged parameters with errors due to numerical calculations and imperfections in the closure laws. Therefore, to address a problem, complex techniques such as PIRT analysis, a scaling analysis, the selection of a numerical simulation tool, the selection of scaled IET or combined effect tests and separate effect tests, the verification and validation of the tool, the application of the code to the safety issue of interest, and the use of an uncertainty method to evaluate the uncertainty of code prediction are necessary. This approach is shown in Fig. 50.

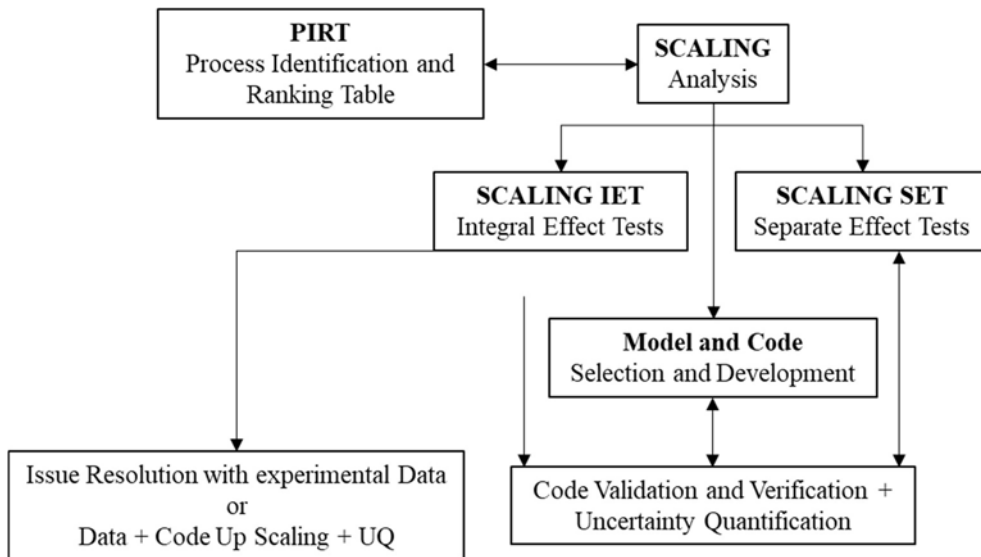


FIG. 50. Overview of the methodology for numerical simulation of a complex reactor thermal hydraulics phenomena.

6.2.2. Process identification and ranking table

Identification of phenomena is the process of collapsing a complicated thermal hydraulics scenario (dependent on several thermal hydraulic variables) into a set of simpler processes or phenomena that primarily depend on a limited number of thermal hydraulic quantities. During the physical analysis, it is useful to discern the dominant parameters, called figures of merit, from the parameters which have an influence on the figures of merit. The figure of merit can be scalar or a multidimensional value, or a dimensional less number (depending on the scenario). For any type of figure of merit, one has to give a required accuracy. This desired accuracy needs to be kept in mind when judging the pertinence of all later steps of the verification, validation and uncertainty quantification. Ranking refers to the practice of creating a hierarchy of identified processes based on their impact on the figures of merit. The PIRT is a recognized method detailed in Ref. [159]. Its use is suggested by OECD WGAMA best practice guidelines [17]. The main steps of the physical analysis based on PIRT are:

- Identify the analysis purpose and specify the details of reactor transient (or situation) of interest;
- Define the dominant parameters and figure of merit;
- List the involved physical phenomena and associated parameters. Identify and rank key phenomena (or the parameters associated to each phenomenon for a more accurate PIRT) with respect to their influence on the figure of merit. To enforce PIRT evaluation one can add the level of knowledge of each parameter (by this way one can highlight the weakness of the analysis based on what has a high influence coupled with a limited knowledge);
- Identify dimensionless numbers controlling the dominant phenomena and the representativeness.
- The PIRT can be derived from expert evaluation, experiment analysis, and sensitivity analyses carried out with the aid of simulation tools. WGAMA recommends performing sensitivity analyses to improve the justification in a nuclear reactor safety demonstration, although practically speaking, PIRT analysis traditionally in the US leans more largely on the first one (PIRT validation). As a result, it's critical to use testing and analysis to validate the PIRT. Sensitivity studies can be used for both the PIRT's final validation and to assess the relative importance of phenomena [160].

6.2.3. Scaling considerations

The word scaling can be used in several contexts with different meaning:

- With reference to experiments: scaling is the process of determining how and to what extent a physical process (such as a reactor transient) can be accurately simulated by an experiment at a smaller scale (or at different values of specific flow parameters, such as pressure and fluid characteristics);
- With reference to numerical simulation: Scaling is the process of illustrating how and to what extent a numerical simulation tool can be applied with sufficient confidence to the real or integral process after being validated on one or more reduced scale experiments (or at various values of some flow parameters like pressure and fluid properties).

The scaling uses information from a scaled experiment, as mentioned in Oberkampf and Roy [161]. The simulation tool is used to extrapolate from experiments to reactor situations (i.e.,

upscaling) and the degree of confidence on this extrapolation is part of the scaling. A single phase CFD tool's extrapolation to a reactor situation induces several aspects and raises several questions:

- How to ensure that a CFD code is capable of extrapolating from a reduced (smaller) scale validation trial to a full scale application;
- How to extrapolate the nodalization/meshing from the one used for the reduced scale validation experiment to a full scale application;
- How to extrapolate results for different experimental conditions (e.g., different values of non dimensional numbers).

The accuracy of the numerical simulation of the scaled experiments is defined by the error that must be determined when extrapolating to the reactor situation. As a result, scaling associated with CFD application is part of the uncertainty evaluation of the CFD code and is a necessary preliminary step in uncertainty evaluation. In 1991, the US NRC, developed a well known methodology known as hierarchical two tiered scaling [162]. This work established a theoretical framework as well as systematic procedures for conducting scaling analyses. This method is a progressive and hierarchized scaling system organized in two steps. The first is a *top down* step, and the second as a *bottom up* step. The top down step, which is organized at the system or plant level, is used to construct non dimensional groups using mass, energy, and momentum conservation equations derived from PIRT relevant systems. These non dimensional groups are employed to determine the scaling hierarchy, or which phenomena should be scaled first, as well as which phenomena must be considered in the bottom up analysis. The bottom up analysis is the second step in the hierarchical two tiered scaling process. To ensure that all pertinent phenomena are accurately represented in the governing equations, a thorough study is conducted at the component level. In the context of nuclear reactor analysis, the use of CFD is envisaged due to the limitations of system codes to simulate complex 3D flows. But this difficult request addressed to CFD requires rigorous approaches based on codes and methods to give confidence in the results of interest. The process, which is based on physical analysis and includes verification, validation, application to an industrial scale, and uncertainty quantification, serves to justify CFD results. It must be demonstrated that each phase of this process is consistent with the previous ones and with the simulations' ultimate purpose. To accomplish this uniformity, the physical study using PIRT devoted to a particular reactor scenario is essential. That view is in accordance with Oberkampf and Roy [161] and the best practice guidelines from OECD mentioned earlier. The PIRT is the basis of the scaling analysis, but it can also benefit the PIRT with the ranking of phenomena. When employing, for instance, the hierarchical two tiered scaling method with both top down and bottom up approaches, the PIRT may result in the scaling of experimental data of the IET type, and the scaling may also identify the requirement for separate effect tests (SETs). The selection of numerical tool (CFD code or a coupling of CFD with other thermal hydraulics codes) need to be consistent with PIRT; the selected physical model can describe the dominant processes. The chosen numerical tool must then be verified and validated using the selected SETs and IETs. Afterwards, code application towards a specific reactor transient requires to include a UQ step which may use code validation results. It will also be used to evaluate the impact of some sources of uncertainties.

6.2.4. Verification and validation

Code verification aims to assess the correctness of numerical implementation of a physical model defined by a set of governing equations. Code developers typically carry out the

verification, however occasionally independent verification is carried out by code users. Practically, verification consists in assembling and simulating idealized test cases that enable a comparison of simulation results against analytical or reference solutions.

Code validation uses comparisons between computational simulations and experimental data to assess the accuracy of the physical models used by the code. In a broad way, validation is done to give assurance that a code can accurately predict the values of important parameters. To ascertain the degree of uncertainty in certain of the code's constitutive laws, use the validation findings. Developers of the code or code users may perform the validation. Developmental assessment refers to the first, and independent assessment to the second. Typically, so called validation matrices are used in the validation process. A validation matrix is a collection of carefully chosen experimental data used for thorough, methodical code validation. The validation matrix usually includes SETs, IETs or combined effect tests, and nuclear power plant data. Separate effect tests are experimental procedures designed to examine a single physical process, either alone or in circumstances that permit measurements of the process's consequences. A constitutive relation can be independently validated using SET from other relations. IETs, on the other hand, are experimental tests that mimic the behaviour of a complex system by simulating all the interactions between different fluxes and heat transfer processes that take place in distinct system components. Through initial and boundary conditions, the IET for nuclear accident thermal hydraulics may model the entire primary cooling circuit and the accident scenario. The way in which validation results are employed is an important differentiating aspect between the various uncertainty quantification methodologies.

6.3. METHODS FOR UNCERTAINTY QUANTIFICATIONS

Reactor thermal hydraulics code uncertainty approaches were originally developed for system codes that mimic a variety of transients in a wide range of single phase and two phase flows. These approaches relied on either accuracy extrapolation techniques or the propagation of the uncertainty of the input parameters (so called uncertainty propagation methods) [163].

6.3.1. Uncertainty propagation based methods

The method using propagation of code input uncertainties for thermal hydraulics with a link to nuclear reactor analysis follows the pioneering idea of the code scaling and applicability uncertainty methodology, later extended by GRS [164]. It is the mostly commonly used class of methods. The first list of uncertain input parameters includes beginning and boundary conditions, material characteristics, and closure laws. For each input parameter, probability density functions are determined. Following that, each set of parameters is sampled in accordance with their probability functions, and reactor simulations are performed. According to the density function of each input parameter, all input parameters are simultaneously modified in the GRS proposal's Monte Carlo sampling. The Wilks theorem is frequently used to handle the outcomes of uncertainty propagation, possibly because it just requires a few assumptions. With a certain degree of confidence, this method enables one to predict the limits of the uncertainty range for any code. Even if slightly more code runs, typically 150 to 200, are advised to have a greater precision on the uncertainty ranges, the number of code runs needed for an adequate level of confidence is around 100. In general, the propagation of uncertainty necessitates numerous calculations to bring statistical estimators to convergence, which may be challenging with CFD due to the lengthy computation time. Fortunately, a rough estimate of the uncertainty coming from small datasets may be obtained using relatively straightforward

statistical procedures (e.g., bootstrapping). In terms of uncertainty propagation methods, there are mainly three groups of approaches:

- *Monte Carlo approaches*: use a rather large number of simulations wherein all input parameters are sampled from probability distribution functions representative of their uncertainty. The resulting probability distribution function of output variables is then established, while the accuracy is not dependent on the number of uncertain input parameters;
- *Metamodels*: some methods, to reduce the number of code simulations, take into account only important uncertain input parameters and run small number of calculations based on the variation of the input parameters to build a metamodel that can replace the code and determine the uncertainty on any code output at a low computational cost; the Monte Carlo method is used with these metamodels, with many thousands of runs. Metamodel usage, including Kriging and polynomial chaos expansion metamodels, gained popularity. These metamodels offer a mapping between erratic inputs and model outputs based on a small number of model assessments (i.e., simulations). These metamodels necessarily rely on assumptions and should be treated with caution when these assumptions are difficult to confirm.
- *Deterministic approaches*: In deterministic techniques, the whole probability distribution functions are not attempted to be propagated. It spreads statistical moments instead. The known statistical moments are represented by the deterministic samples that have been chosen. The uncertainty can be represented by two samples if just the mean and standard deviation, or the first and second moments, are known. These are selected in a way that ensures to have the specified mean and standard deviation. A Gaussian distribution's first four moments can be represented by three samples. More samples in the ensemble can be used to satisfy arbitrarily higher moments.

To determine the uncertainties of closure laws, preliminary research is necessary for the uncertainty propagation methods. For a better demonstration, statistical methods based on numerous validation computations can be used instead of expert judgement in this assessment. When data are provided that are susceptible to a single closure law, it may be simple to calculate the uncertainty band or PDF for each closure. Data are sensitive to a few closure laws very frequently in practice, and methods have been developed to compute uncertainty bands or probability density functions for several closure laws based on a number of data comparisons with predictions [165].

6.3.2. Accuracy extrapolation methods

For system codes, the methods identified as propagation of code output errors are based on the extrapolation of accuracy. One can mention the uncertainty methodology based on accuracy extrapolation (UMAE) [166] and the code with the capability of internal assessment (CIAU) approach [167], [168]. A thorough validation of system codes (on SETs and IETs both) allows measurement of code prediction accuracy in a wide range of situations. For UMAE and CIAU, Fourier transforms are used to define a metric for quantifying accuracy. The experimental database contains results from various scales, and assuming that the accuracy of code results is independent of scale, this accuracy can be extrapolated to reactor scale. Methods based on validation experiment extrapolation may only require one reactor transient simulation, but many preliminary validation calculations of integral test facilities are required.

6.3.3. Verification and validation standards

One of the most comprehensive standards for validation and verification is that by the American Society of Mechanical Engineers, known as ASME V&V20. According to this verification and validation standard in computational fluid dynamics and heat transfer, "the concern of V&V³ is to assess the accuracy of a computational simulation." This viewpoint is clearly compatible with the principle of extrapolation from validation experiments. Current industrial CFD models (non DNS) produce results from both a solved and modelled part of the Navier-Stokes equations. Even for complex flows, verification of correct equation solving is feasible, and once completed, physical model uncertainty is a legitimate concern. It is well known that different experiments produce significantly different model parameter values in calibration, indicating that the form and generality of the model itself must be investigated.

6.3.4. Methods comparison

Methods based on validation results extrapolation have a poor mathematical foundation, but their comparison to reality (even in scaled experiments) can provide insight into the impact of model inadequacy on full scale results. When simulations are compared to experiments, the impact of non modeled phenomena is also considered, which is not the case for uncertainty propagation. Obviously, regardless of the method used, transferring results from scaled experiments to full scale is nearly impossible to justify rigorously. It will be possible to define an exact model if the physical model uncertainty can be precisely estimated. Another distinction between propagation and extrapolation is the ability to perform sensitivity analysis. Sensitivity analyses can be performed using propagation by employing the results of uncertainty analysis for the previous runs. However, it is impossible with extrapolation based methods as these do not account for individual uncertainty sources. Knowing the main sources of code uncertainty is the first step toward code improvement. Benchmarking with system codes of methods from two different classes was carried out as part of the international projects launched by the OECD/CSNI [169]. For CFD, no relevant benchmark has been yet set up to compare different approaches.

6.4. APPLICATION OF AN UNCERTAINTY PROPAGATION METHOD

The method based on propagation of input uncertainties is broadly used for system codes. This method consists of performing Monte Carlo code runs without using a metamodel. Consequently, rather numerous codes run (in the order of hundreds) of the CFD code are needed, which raises a difficulty for CFD code applications. After these code runs, statistical quantities for the responses (such as percentiles or tolerance intervals) are obtained using the order statistics. Following the uncertainty analysis, a simple sensitivity analysis at the first order can be performed using the results of the code runs. There is no restriction on the number, and type of uncertain input parameters that can be considered. Also, initial and boundary conditions, as well as physical model parameters, can be specified. But it is also possible to consider different options of physical modelling (for example the turbulence modelling) and of numerical schemes (for example the convection schemes), if best practice guidelines do not give clear indications to the best option. It is done by the use of the so called categorical variables, more frequent for CFD codes than for system codes. A difficulty of the method is that it is compulsory to estimate the probability density functions of these numerous uncertain input parameters. More details are given in [170]. The method was applied to a simple case with experimental data, illustrated in FIG. 51. It comprises of a 2D square cold cavity, filled with air at 15 °C, and have a hot floor at temperature of 35 °C. Cold air at 15 °C enters the

cavity, and leaves the cavity from the bottom right hand corner. The flow is modelled as 2D, steady and presents buoyancy effects. It is calculated by the CFD code Trio_U developed by CEA with RANS $k - \varepsilon$ turbulence model.

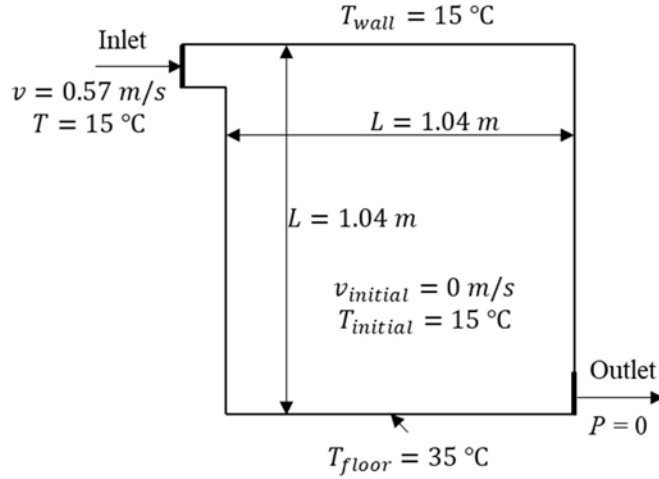


FIG. 51. Representation of the simulation domain with characteristic dimensions and boundary conditions.

The available experimental data consists of velocity profiles along the two axes at different positions in the domain. The input parameters that affect results are the parameters related to meshing, such as the mesh topology, mesh density in the cavity bulk as well as close to the walls, the choice of numerical discretization schemes and their parameters, the parameters related to physical modelling, such as fluid properties models (e.g. for density, viscosity, thermal conductivity, etc.) as well as wall laws for the turbulence model and turbulence model parameters, and initial and boundary conditions. Arbitrary uncertainties are assigned to these parameters. These are supposed to be distributed according to Gaussian distribution, with an assumed relative standard deviation of 5% unless experimental uncertainties are available (which is the temperatures and the inlet velocity). The different levels of the categorical variables are assumed to be equiprobable. A total of 100 code runs are performed, each with different sampling of the input parameters. The 100 values of the responses of interest (i.e., velocity and temperature profiles along certain axes at different locations) are ranked by increasing order and the third largest value (resp. the 98th highest value) is considered for the 2.5% percentile (resp. the 97.5% percentile). The possible issue regarding the potential non continuity of the probability distribution function of the responses (due to the presence of categorical variables is not met). All the values of the responses are different and ranking them by increasing order does not pose any problem.

The calculated profiles for the quantities of interest are compared against the experimental values in Fig. 52 for temperature and Fig. 53 for the velocity. The temperature results are satisfactory as the experimental results are entirely within the 95% confidence interval of the calculated results. As can be seen in Fig. 53 there are certain regions in which experimental results fall outside the confidence interval of the calculated results. Nonetheless, this serves as a reasonable case for illustrating the presented methodology.

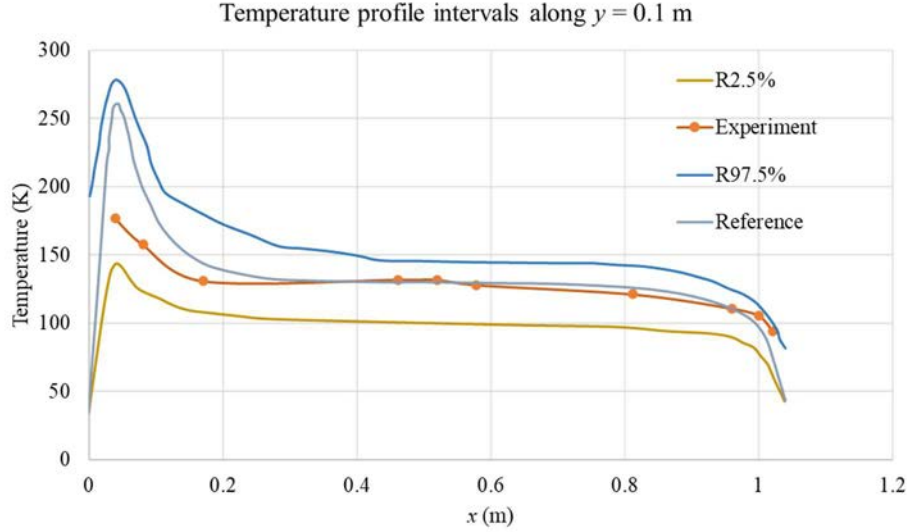


FIG. 52. Comparison of temperature profile and its 95% confidence interval against the experimentally measured temperature profile along the horizontal axis at height of 0.1m.

Despite the large number and variety of uncertain input parameters, the uncertainty bands do not completely encircle the experimental data. The first possible explanation is that the k - turbulence model used isn't the best fit for this scenario. A second explanation is that 2D modelling of the cavity inherently removes 3D effects from the analysis, which might be suspected, at this stage, to play a role. Additional explanation is that the ranges of variation of the input parameters (i.e., the variance of the Gaussian distributions for different input parameters) were arbitrarily determined and one can assume these were perhaps not wide enough.

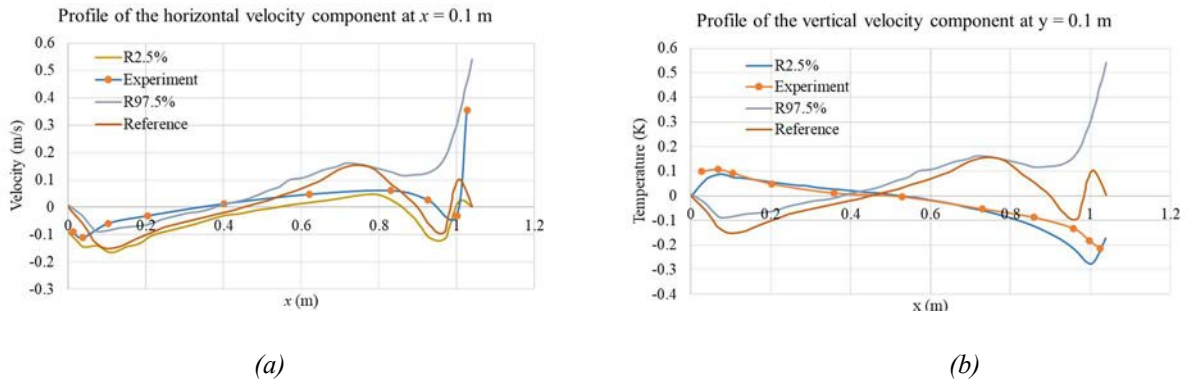


FIG. 53. Comparison of (a) horizontal velocity component profile and its 95% confidence interval against the experimentally measured profile along the vertical axis at length of 0.1 m; (b) vertical velocity component profile and its 95% confidence interval against the experimentally measured profile along the horizontal axis at a height of 0.1 m.

Overall, the advantages and drawbacks of this methodology are summarized as follows:

- The main advantage is the possibility to consider numerous and miscellaneous input parameters. Estimating an error band coming from the discretization error with a method such as Richardson extrapolation and grid convergence indices [171] would be perhaps

- better option, however, the discretization error does not represent all the potential sources of numerical uncertainties (e.g., the choice among different meshing options);
- An important issue not really addressed in the application case is the quantification of the uncertainty of the input parameters. This is for all the methods based on the propagation of input uncertainties.

The main drawback of the methodology is the high number of converged (i.e., successful) code runs.

6.5. UNCERTAINTY QUANTIFICATION VIA ACCURACY EXTRAPOLATION

The uncertainty method based on accuracy extrapolation (UMAE) was proposed by the University of Pisa, Italy, in the late eighties and then further developed [166]. In contrast to uncertainty propagation methods, the UMAE focuses on code output errors; information regarding accuracy is stored in a suitable validation database, and the accuracy from relevant integral experiments is extrapolated to the size of a power plant to determine the final uncertainty. In the application of the UMAE, an iterative process involving validation against experimental data achieves qualified nodalizations so that the related prediction accuracy meets given acceptance thresholds. Then, using similar criteria, a qualified nodalization for power plant analysis (also known as an analytical simulation model) is obtained, provided that the proper analysis shows that the phenomena observed in test facilities and predicted by the plant calculations are similar. User qualification is crucial in addition to nodalization qualification. With the qualified nodalization, a single calculation is more than sufficient for a given transient—the associated uncertainty is then found through accuracy extrapolation, using a relevant database which is supposed to have been acquired.

The accuracy evaluation is another key step, which involves appropriate metrics for quantification, and acceptance criteria. The accuracy evaluation tool in the framework of UMAE–CIAU is the fast Fourier transform based method [172], which characterizes, by appropriate figures of merit. The key steps of the UMAE methodology are summarized in [170]. The code with the CIAU was proposed in 1997 and further developed and applied ever since, with the resolve to overcome the limitation of other uncertainty methodologies.

The CIAU tool basically couples UMAE approach with RELAP5 and evaluate uncertainty (in the form of uncertainty bands enveloping the code results for selected target variables) associated with a specific transient calculation. The concepts used in the implementation and use of CIAU: UMAE qualification are as follows: the status approach for characterizing transient scenarios, the separation and recombination of time and quantity error, and the error filling and error extraction processes. To determine the status of the plant, the status approach uses an arbitrary set of relevant thermal hydraulics parameters representative of the selected scenario, as well as the time elapsed since the transient start. In other words, plant status is corresponding to a point in a multidimensional phase space.

One fundamental assumption is that all plant statuses within each discrete plant state have the same level of code prediction uncertainty for specified output variables. As a result, using an uncertainty evaluation method, a seven dimension matrix of quantity uncertainties and a vector of time uncertainties can be filled up (error filling process), forming a sort of uncertainty database that can be searched. As the uncertainty database is available, the application of the CIAU requires negligible computing effort and engineering judgement, which, on the other

hand, are embedded in the filling process. Some reflections for extending the UMAE–CIAU approach to CFD were summarized in the Ref. [170].

7. APPLICATIONS IN TRAINING AND EDUCATION

This chapter provides one example of how to structure the training course based on the contents provided in this publication. The scope of the course is structured such to provide the graduate students and professionals with theoretical foundations and examples for application of CFD modelling in nuclear engineering. The need for high fidelity nuclear reactor thermal hydraulic simulations has led to increased application of the CFD codes that are prevailing substitute of currently established 1D system thermal hydraulics codes and coarse mesh subchannel analyses codes. The course scope is aimed at discussing how the CFD constitutes the third approach in the philosophical study and development of the whole discipline of fluid dynamics. Combining the power of experimentation and theory, this approach has made possible the accounting of flow fields in complex geometries.

The suggested contents of the training course are derived from the virtual ICTP (Abdus Salam International Center for Theoretical Physics) and IAEA Joint Course on Theoretical Foundations and Applications of Computational Fluid Dynamics in Nuclear Engineering, conducted 13–17 January 2021.

The following sessions and lectures with hands-on examples may constitute the course suitable for various levels of background knowledge in the field:

- **Session 1:** History and theory of computational fluid dynamics
 - Basics of vector calculus and conservation equations (governing equations in fluid dynamics)
 - Solving the equations
 - **Hands on Session 1:** Quarter subchannel geometry and meshing
- **Session 2:** Basics of turbulence modelling
 - RANS and URANS modelling for turbulent flows
 - Turbulence resolving simulations: DNS, LES, and hybrid methods
 - **Hands on Session 2:** Quarter subchannel modelling options
- **Session 3:** Two phase CFD
 - Various modelling approaches in two phase flow
 - Interface resolving techniques
 - Eulerian – Eulerian approach
 - **Hands on Session 3:** Quarter subchannel simulation and post processing
- **Session 4:** Application of CFD codes in nuclear reactor design and analysis
 - Water cooled reactor (design basis accidents and other operation conditions)
 - CFD analysis of water cooled reactors severe accident phenomena
 - CFD analysis of innovative reactor concepts
 - Introduction to multi scale models
 - **Hands on Session 4:** CFD modelling challenges for problems related to nuclear reactors
- **Session 5:** Uncertainty quantification and error analysis

REFERENCES

- [1] INTERNATIONAL ATOMIC ENERGY AGENCY, Passive Safety Systems in Water Cooled Reactors: An Overview and Demonstration with Basic Principle Simulators, IAEA-TCS-69, IAEA, Vienna (2019).
- [2] ANDERSON, J. D., Fundamentals of Aerodynamics, McGraw-Hill, New York (2016).
- [3] CENGEL, Y. A., Fluid Mechanics Fundamentals and Applications, McGraw-Hill, New York (2013).
- [4] ANDERSON, J.D., Computational Fluid Dynamics: The Basic with Applications, McGraw-Hill, New York (1995).
- [5] PATANKAR, S.V., SPALDING, D. B., A calculation procedure for heat, mass and momentum transfer in three-dimensional parabolic flows, International Journal of Heat and Mass Transfer **15** 10 (1972) 1787, 1806.
- [6] ISSA, R. I., Solution of the implicitly discretised fluid flow equations by operator-splitting, Journal of Computational Physics **62** 1 (1986) 40, 65.
- [7] FERZIGER, J. H., PERIC, M., STREET, R. L., Computational Methods for Fluid Dynamics, Springer, Berlin (2002).
- [8] HOFFMAN, K. A., CHIANG, S. T., Computational Fluid Dynamics, Vol. 3, Engineering Education System, Wichita (2000).
- [9] ANSYS FLUENT Theory Guide 2013, USA (2011).
- [10] BAKKER, A., Applied CFD-Turbulence Modelling (2005).
- [11] SPALART, P., R., Comments on the Feasibility of LES for Wings, and on a Hybrid RANS/LES approach, Proceeding of First AFOSR International Conference on DNS/LES, Ruston, LA (1997).
- [12] FRISCH, U., Turbulence, Cambridge University Press, UK (1995).
- [13] SHIH, T., H., LIOU, W., W., SHABBIR, A., YANG, Z., ZHU, J., A new eddy-viscosity model for high Reynolds number turbulent flows model development and validation, Computers and Fluids **24** 3 (1995) 227, 238.
- [14] REYNOLDS, W. C., Fundamentals of Turbulence for Turbulence Modeling and Simulation, Stanford University, USA (1987).
- [15] WILCOX, D.C, Turbulence Modelling for CFD, DCW Industries, California (1993).
- [16] WOLDSTEIN, M., The velocity and temperature distribution of one-dimensional flow with turbulence augmentation and pressure gradient, International Journal of Heat and Mass Transfer **12** 3 (1969) 301, 318.
- [17] MAHAFFY, J., Best Practice Guidelines for the Use of CFD in Nuclear Reactor Safety Applications, Rep. NEA/CSNI/R(2014)11, OECD, Nuclear Energy Agency, (2015).
- [18] BESTION, D., et al., Extension of CFD Codes Application to Two-Phase Safety Problems – Phase 3, Nuclear Safety, Rep. NEA/CSNI/R(2014) 13, (2014)
- [19] LIOVIC, P., LAKEHAL, D., "Interface-turbulence interactions in large-scale bubbling processes, International Journal of Heat and Fluid Flow **28** (2007) 127, 144.
- [20] LIOVIC, P., LAKEHAL, D., Multi-physics treatment in the vicinity of arbitrarily deformable gas-liquid interfaces, Journal of Computational Physics **222** 2 (2007) 504, 535.

- [21] BOIS, G., et al., Towards Large Eddy Simulation of Two-Phase Flow with Phase-Change: Direct Numerical Simulation of a Pseudo-Turbulent Two-Phase Condensing Flow, 7th International Conference on Multiphase Flow, ICMF 2010, Tampa, FL, USA (2010).
- [22] TOUTANT, A., et al., Jump conditions for filtered quantities at an under resolved interface. Part 1: theoretical development, *International Journal of Multiphase Flow* **35** 12 (2009) 1100, 1118.
- [23] TOUTANT, A., et al., “Jump conditions for filtered quantities at an under resolved interface. Part 2: a priori tests, *International Journal of Multiphase Flow* **35** 12 (2009) 1119, 1129.
- [24] MAGDELEINE, S., DNS Up-Scaling Applied to Volumetric Interfacial Area Transport Equation, 7th International Conference on Multiphase Flow, ICMF 2010, Tampa, FL, USA (2010).
- [25] LAKEHAL, D., et al., Turbulence and heat transfer in condensing vapor-liquid flow, *Physics of Fluids* **20** 6 (2008) 065101
- [26] LAKEHAL, D., LEIS for the prediction of turbulent multifluid flows applied to thermal hydraulics applications, *Nuclear Engineering and Design* **240** 10 (2010) 2096, 2106.
- [27] LAKEHAL, D., LABOIS, M., A new modelling strategy for phase-change heat transfer in turbulent, *International Journal of Multiphase Flow* **37** (2011) 617, 639.
- [28] LAKEHAL, D., et al., Large eddy simulation of bubbly turbulent shear flows, *Journal of Turbulence* **3** 25 (2002) 1 ,21.
- [29] DHOTRE, M. T., et al., CFD simulation of bubbly flows: random dispersion model, *Chemical Engineering Science* **62** (2007) 7140, 7150.
- [30] DHOTRE, M. T., et al., Large eddy simulation of a bubble column using dynamic sub-grid scale model, *Chemical Engineering Journal* **136** (2008) 337, 348.
- [31] NICENO, B., et al., One equation sub-grid scale (SGS) modeling for euler-euler large eddy simulation (EELES) of dispersed bubbly flow, *Chemical Engineering Science* **63** (2008) 3923, 3931.
- [32] NICENO, B., et al., Euler-Euler large eddy simulation of a square cross-sectional bubble column using the Neptune CFD code, *Science and Technology of Nuclear Installations* **2009** (2008).
- [33] BARTOSIEWICZ, Y., et al., A Validation Case for the NEPTUNE_CFD Platform; Instabilities in a Stratified Flow. Experimental, Theoretical and Code to Code Comparison, NURETH-12, Pittsburgh, Pennsylvania, USA (2007).
- [34] BARTOSIEWICZ, Y., et al., A first assessment of the NEPTUNE_CFD code: Instabilities in stratified flow, comparison between the VOF method and a two-field approach, *International Journal of Heat and Fluid Flow* **29** (2008) 460, 478.
- [35] BESTION, D., The difficult challenge of a two-phase CFD model for all flow regimes, *Nuclear Engineering and Design* **279** (2014) 116, 125.
- [36] KREPPEL, E., et al., CFD modeling of adiabatic bubbly flow, *Multiphase Science and Technology* **23** 2-4 (2011) 129, 164.
- [37] KONCAR, B., et al., CFD modeling of boiling bubbly flow for departure from nucleate boiling investigations, *Multiphase Science and Technology* **23** 2-4 (2011) 165, 222.
- [38] ANGLART, H., CARAGHIAUR, D., CFD modeling of boiling annular-mist flow for dryout investigations, *Multiphase Science and Technology* **23** 2-4 (2011) 223, 251.
- [39] BESTION, D., Extension of CFD code application to two-phase flow safety problems, *Nuclear Engineering and Technology* **42** 4 (2010) 365, 376.

- [40] MAHAFFY, J., Best Practice Guidelines for the Use of CFD in Nuclear Reactor Safety Applications, Rep. NEA/CSNI/R(2014)11, OECD, Nuclear Energy Agency (2015).
- [41] BESTION, D., GUELFI, A., Status and perspective of two-phase flow modelling in the NEPTUNE multiscale thermal-hydraulic platform for nuclear reactor simulation, Nuclear Engineering and Technology **16** 1-3 (2005) 1, 5.
- [42] GUELFI, A., et al., NEPTUNE a new software platform for advanced reactor thermal hydraulics, Nuclear Science and Engineering **156** 3 (2007) 282, 324.
- [43] BESTION, D., From the direct numerical simulation system to system codes: Perspective for the multi-scale analysis of LWR thermal hydraulics, Nuclear Engineering and Technology **42** 6 (2010) 608, 619.
- [44] POPINET, S., Numerical models of surface tension, Annual Review of Fluid Mechanics **50** (2018) 49, 75.
- [45] YADIGAROGLU, G., Computational fluid dynamics for nuclear applications: from CFD to multi-scale CMFD, Nuclear Engineering and Design **235** 2-4 (2005) 153, 164.
- [46] HIRT, C. W., NICHOLS, B. D., Volume of fluid (VOF) method for the dynamics of free boundaries, Journal of Computational Physics **39** (1981) 201, 225.
- [47] SUSSMAN, M., SMEREKA, P., OSHER, S., A level set approach for computing solutions to incompressible two-phase flow, Journal of Computational Physics **114** (1994) 146, 159.
- [48] UNVERDI, S. O., TRYGGVASON, G., A front-tracking method for viscous, incompressible, multi-fluid flows, Journal of Computational Physics **100** (1992) 25, 37.
- [49] CAHN, J. W., HILLIARD, J. E., Free energy of a nonuniform system : Interfacial free energy, The Journal of Chemical Physics, **28** (1958) 258, 267.
- [50] FRANK, R. M., LAZARUS, R. B., Mixed Eulerian-Langrangian methods, Methods in Computational Physics **3** (1964) 47, 67.
- [51] BRACKBILL, J. U., KOTHE, D. B., ZEMACH, C., A continuum method for modeling surface tension, Journal of Computational Physics **100** 2 (1992) 335, 354
- [52] LAFAURIE, B., NARDONE, C., SCARDOVELLI, S., ZALESKI, S. ZANETTI, G., Modelling merging and fragmentation in multiphase flows with SURFER, Journal of Computational Physics, **113** (1994) 134, 147.
- [53] YOUNGS, D. L., “Time-dependent multi-material flow with large fluid distortion”, Numerical Methods for Fluid Dynamics, Academic Press, US (1982), 237-257 pp.
- [54] AULISA, E., MANSERVISI, S., SCARDOVELLI, R., ZALESKI, S., Interface reconstruction with least-squares fit and split advection in three-dimensional Cartesian geometry, Journal of Computational Physics **225** (2007) 2301, 2319.
- [55] MUZAFERIJA, S., PERIC, M., SAMES, P., SCHELIN, T., A Two-Fluid Navier-Stokes Solver to Simulate Water Entry, Proceeding of the 22nd symposium of naval hydrodynamics, Washington, DC (1998).
- [56] UBBINK, O., ISSA, R. I., A method for capturing sharp fluid interfaces on arbitrary meshes, Journal of Computational Physics **153** (1999) 26, 50.
- [57] YABE, T., XIAO, F., UTSUMI, T., The constrained interpolation profile method for multiphase analysis, Journal of Computational Physics **169** (2001) 556, 593.
- [58] XIAO, F., HONMA, Y., KONO, T., A simple algebraic interface capturing scheme using hyperbolic tangent function, International Journal of Numerical Methods in Fluids **48** 9 (2005) 1023, 1040.
- [59] OLSSON, E., KREISS, G., A conservative level set method for two phase flow, Journal of Computational Physics **210** (2005) 225, 246.

- [60] FRANCOIS, M., et al. A balanced-force algorithm for continuous and sharp interfacial surface tension models within a volume tracking framework, *Journal of Computational Physics* **213** (2006) 141, 173.
- [61] LOPEZ, J., et al., An improved height function technique for computing interface curvature from volume fractions, *Computer Methods in Applied Mechanics and Engineering* **198** (2009) 2555, 2564.
- [62] CAREY, V. P., *Liquid-Vapor Phase Change Phenomena: An Introduction to the Thermophysics of Vaporization and Condensation Processes in Heat Transfer Equipment*, 2nd ed., CRC Press, Taylor & Francis, Boca Raton (2007).
- [63] SATO, Y., NICENO, B., A depletable micro-layer model for nucleate pool boiling, *Journal of Computational Physics* **300** (2015) 20, 52.
- [64] KOCAMUSTAFAGULLARI, G., ISHII, M., Interfacial area and nucleation site density in boiling systems, *International Journal of Heat and Mass Transfer* **26** (1983) 1377, 1387.
- [65] HIBIKI, T., ISHII, M., Active nucleation site density in boiling systems, *International Journal of Heat and Mass Transfer* **46** (2003) 2587, 2601.
- [66] LUCAS, D., et al., On the Simulation of Two-Phase Flow Pressurized Thermal Shock (pts)", 12th International Topical Meeting on Nuclear Reactor Thermal Hydraulics, NURETH-12, USA (2007).
- [67] BESTION, D., The difficult challenge of a two-phase CFD modelling for all flow regimes, *Nuclear Engineering and Design* **279** (2014) 116, 125.
- [68] BIRD, R. B., STEWART, W. E., LIGHTFOOT, E. N., *Transport Phenomena*, John Wiley and Sons, New York (2006).
- [69] ISHII, M., HIBIKI, T., *Thermo-fluid Dynamics of Two-Phase Flow*, Springer Science and Business Media, New York (2010).
- [70] WILCOX, D. C., *Turbulence Modeling for CFD*, Vol. 2, DCW Industries LA Canada, CA (1998).
- [71] DURBIC, P. A., REIF, B. A. P., *Statistical Theory and Modeling for Turbulent Flows*, John Wiley and Sons, UK (2011).
- [72] CLIFT, R., GRACE, J. R., WEBER, M. E., *Bubbles, Drops and Particles*, Courier, Dover Publications, New York (2005).
- [73] SCHILLER, L., NAUMANN, Z., A drag coefficient correlation, *Zeitschrift des Vereins Deutscher Ingenieure* **77** 318 (1935) 323.
- [74] Tomiyama, A., et al., Drag coefficients of bubbles (2nd report: Drag coefficient for a swarm of bubbles and its applicability to transient flow), *Nippon Kikai Gakkai Ronbunshuu* **61** (1995) 61-588.
- [75] STAFFMAN, P.G.T., The lift on a small sphere in a slow shear flow, *Journal of Fluid Mechanics* **22** 2 (1995) 385, 400.
- [76] DREW, D.A., The force on a small sphere in slow viscous flow, *Journal of Fluid Mechanics* **88** 2 (1978) 393, 400.
- [77] ZUN., I., The transverse migration of bubbles influenced by walls in vertical bubble flow, *International Journal of Multiphase Flow* **6** 6 (1980) 583, 588.
- [78] DE BERTODANO, M. L., LAHEY, R.T., JONES, O.C., Phase distribution in bubbly two-phase flow in vertical ducts, *International Journal of Multiphase Flow* **20** 5 (1994) 805, 818.
- [79] TOMIYAMA, A., TAMAI, H., ZUN, I., HOSOKAWA, S., Transverse migration of single bubbles in simple shear flows, *Chemical Engineering Science* **57** 11 (2002) 1849, 1858.

- [80] SALNIKOVA, T., Two-Phase CFD Analyses in Fuel Assembly Sub-Channels of Pressurized Water Reactors under Swirl Conditions, PhD thesis, Technical University Dresden (2010).
- [81] BURNS, A.D., FRANK, T., HAMILL, I., SHI, J.M., et al., The Favre Averaged Drag Model for Turbulent Dispersion in Eulerian Multi-Phase Flows”, 5th International Conference on Multiphase Flow, ICMF, Vol. 4, Japan (2004), 1-17 pp.
- [82] ANTAL, S. P., LAHEY, R. T., FLAHERTY, J. E., Analysis of phase distribution in fully developed laminar bubbly two-phase flow, International Journal of Multiphase Flow, **17** 5 (1991) 635, 652.
- [83] HOSOKAWA, S., TOMIYAMA, A., MISAKI, S., HAMADA, T., Lateral Migration of Single Bubbles due to the Presence of Wall, Fluids Engineering Division Summer Meeting, Vol. 36150, Montreal, Quebec, Canada (2002) 855-860.
- [84] RANZ, W. E., Evaporation from drops, Chemical Engineering Progress **48** 3 (1952) 141, 146.
- [85] LAHEY, R. T., BAGLIETTO, E., BOLOTNOC, I. A., Progress in multiphase computational fluid dynamics, Nuclear Engineering and Design **374** (2021) 111018.
- [86] RAMKRISHNA, D., Population Balances: Theory and Applications to Particulate SYSTEMS in Engineering, Academic Press, USA (2000).
- [87] FREDERIX, E. M. A., COX, T. L. W., KUERTEN, J.G.M., KOMEN, E.M.J., Poly-dispersed modeling of bubbly flow using the log-normal size distribution, Chemical Engineering Science **201** (2019) 237, 246.
- [88] MARCHISIO, D. L., FOX, R. O., Computational Models for Polydisperse Particulate and Multiphase Systems, Cambridge University Press, USA (2013).
- [89] KREPPEL E., LUCAS, D., FRANK T., PRASSER, H.M., ZWART, P. J., The inhomogeneous MUSIG model for the simulation of polydispersed flows, Nuclear Engineering and Design **238** 7 (2008) 1690, 1702.
- [90] TEKAVCIC, M., MELLER, R., SCHLEGEL F., Validation of a morphology adaptive multi-field two-fluid model considering counter-current stratified flow with interfacial turbulence damping, Nuclear Engineering and Design, **346** (2021) 111223.
- [91] MELLER, R., SCHLEGEL, F. LUCAS, D., Basic verification of a numerical framework applied to a morphology adaptive multifield two-fluid model considering bubble motions, International Journal for Numerical Methods in Fluids, **93** 3 (2021) 748, 773.
- [92] PRASSER, H. M., et al. Evolution of the structure of a gas-liquid two-phase flow in a large vertical pipe, Nuclear Engineering and Design **237** 15-17 (2007) 1848, 1861.
- [93] FREDERIX, E.M.A., HABIYAREMYE, V., LogMOM OpenFOAM library, Nuclear Research and Consultancy Group, Netherlands, <http://github.com/edofrederix/LogMoM>.
- [94] ISHII, M., ZUBER, N., Drag coefficient and relative velocity in bubbly, droplet or particulate flows, AlChE Journal, **25** 5 (1979) 843, 855.
- [95] FRANK T., Advances in Computational Fluid Dynamics (CFD) of 3-Dimensional Gas-Liquid Multiphase Flows, NAFEMS Seminar: Simulation of Complex Flows (CFD)- Applications and Trends, Wiesbaden, Germany (2005) 1-18.
- [96] BEHZADI, A., ISSA, R.I., RUSCHE, H., Modelling of dispersed bubble and droplet flow at high phase fractions, Chemical Engineering Science **59** 4 (2004) 759, 770.
- [97] LAHEY, R.T., The simulation of multidimensional multiphase flows, Nuclear Engineering Design **235** 10-12 (2005) 1043, 1060.

- [98] KUMAR, S., RAMKRISHNA, D., On the solution of population balance equations by discretization- 1. A fized pivot technique, *Chemical Engineering Science*, **51** 8 (1996) 1311, 1332.
- [99] LUO, H., SVENDSEN, H.F., Theoretical model for drop and bubble breakup in turbulent dispersions, *AIChe Journal*, **42** 5 (1996) 1225, 1233.
- [100] PRINCE, M. J., BLANCK, H.W., Bubble coalescene and break-up in air-sparged bubble columns, *AIChe Journal* **36** 10 (1990) 1485, 1499.
- [101] FEYNMAN, R. P., LEIGHTON, R. B., SANDS, M., *The Feynman Lectures on Physics*, Vol. 1, Addison-Wesley, USA (1963).
- [102] VONKA V., Measurement of secondary flow vortices in a rod bundle, *Nuclear Engineering and Design* **106** (1988) 191, 207.
- [103] GRÖTZBACH, G., Challenges in low-Prandtl number heat transfer simulation and modelling, *Nuclear Engineering and Design* **264** (2013) 41,55.
- [104] ROELOFS, F., et al., Status and perspective of turbulence heat transfer modelling for the industrial application of liquid metal flows, *Nuclear Engineering and Design* **290** (2015) 99, 106.
- [105] SHAMS, A., et al., A collaborative effort towards the accurate prediction of turbulent flow and heat transfer in low-Prandtl number fluids, *Nuclear Engineering and Design* **366** (2020) 110750.
- [106] SHAMS, A., DE SANTIS, A., ROELOFS, F., An overview of the AHFM-NRG formulations for the accurate prediction of turbulent flow and heat transfer in low-Prandtl number flows, *Nuclear Engineering and Design* **355** (2019) 110342.
- [107] KASSEM, S., PUCCIARELLI, A., AMBROSINI, W., Insight into a fluid-to-fluid similarity theory for heat transfer at supercritical pressure: Results and perspectives, *International Journal of Heat and Mass Transfer* **168** (2021) 120813.
- [108] PEETERS, J., PECNIK, R., ROHDE, M., VAN DER HAGEN, T., BOERSMA, B., Turbulence attenuation in simultaneously heated and cooled annular flows at supercritical pressure, *Journal of Fluid Mechanics* **799** (2016) 505, 540.
- [109] JACKSON, J. D., Fluid flow and convective heat transfer to fluids at supercritical pressure, *Nuclear Engineering and Design* **264** (2013) 24, 40.
- [110] PAPUKCHIEV, A., ROELOFS, F., SHAMS, A., LECRIVAIN, G., AMBROSINI, W., Development and application of computational fluid dynamics approaches within the European project THINS for the simulation of next generation nuclear power systems, *Nuclear Engineering and Design* **290** (2015) 13, 26.
- [111] PEETERS, J., PECNIK, R., ROHDE, M., VAN DER HAGEN, T., BOERSMA, B., Characteristics of turbulent heat transfer in an annulus at supercritical pressure, *Physical Review Fluids* **2** (2017) 024602.
- [112] PUCCIARELLI, A., AMBROSINI W., Improvements in the prediction of heat transfer to supercritical pressure fluids by the use of algebraic heat flux models, *Annals of Nuclear Energy* **99** (2017) 58-67.
- [113] INTERNATIONAL ATOMIC ENERGY AGENCY, Status of Research and Technology Development for Supercritical Water Cooled Reactors, IAEA-TECDOC-1869, IAEA, Vienna (2019).
- [114] SCHULENBERG, T., et al., European supercritical water cooled reactor, *Nuclear Engineering and Design* **241** (2011) 3505, 3513.
- [115] WANK, A., STARFLINGER, J., SCHULENBERG, T., LAURIEN, E., Mixing of cooling water in the mixing chambers of the HPLWR – High Performance Light Water Reactor, *Nuclear Engineering and Design* **240** (2010) 3248, 3258.

- [116] SHAMS, A., ROELOFS, F., KOMEN, E.M.J., BAGLIETTO, E., Large eddy simulation of a randomly stacked nuclear pebble bed, *Computers and Fluids* **96** (2014) 302, 321.
- [117] SHAMS, A., ROELOFS, F., KOMEN, E.M.J., BAGLIETTO E., Quasi-direct numerical simulation of a pebble bed configuration. Part 1: Flow (Velocity) field analysis and Part 2: Temperature field analysis, *Nuclear Engineering and Design*, **263** (2013) 473, 499.
- [118] FICK, L., MERZARI, E., HASSAN, Y., Direct numerical simulation of pebble bed flows: Database development and investigation of low-frequency temporal instabilities, *Journal of Fluids Engineering* **139** (2017) 51301.
- [119] FICK, L., MERZARI, E., HASSAN, Y., Inertial effects and anisotropy for the flow in a domain of close packed spheres with a bounding wall, *Nuclear Technology*, **208** 3 (2022) 539, 561.
- [120] WU, H., GUI, N., YANG, X., TU, J., JIANG, S., Numerical simulation of heat transfer in packed pebble beds: CFD-DEM coupled with particle thermal radiation, *International Journal of Heat and Mass Transfer* **110** (2017) 393-405.
- [121] SHAVER D., NEAMS Thermal-Hydraulics Deep Dive, Thermal-Hydraulics Technical Area Deep Dive and Center of Excellence Workshop (Virtual).
- [122] BLANFORD E., et al., Kairos power thermal hydraulics research and development, *Nuclear Engineering and Design* **364** (2020) 110636.
- [123] YILDIZ, M., HASSAN, Y., MERZARI, E., Numerical simulation of the flow through a randomly packed pebble bed with small bed to pebble diameter ratio, *Transactions of American Nuclear Society* **123** 1 (2020) 1493, 1496.
- [124] ROELOFS, F., et al., CFD and Experiments for Wire-Wrapped Fuel Assemblies, 18th International Topical Meeting on Nuclear Reactor Thermal Hydraulics, NURETH18, Portland, USA (2019).
- [125] ROELOFS, F., GOPALA, V.R., JAYARAJU, S., SHAMS, A., KOMEN, E.M.J., Review of fuel assembly and pool thermal hydraulics for fast reactors, *Nuclear Engineering and Design* **265** (2013) 1205, 1222.
- [126] VAN TICHELEN, K., MIRELLI, F., GRECO, M., VIVIANI, G., E-SCAPE: A scale facility for liquid-metal, pool-type reactor thermal hydraulic investigations, *Nuclear Engineering and Design* **290** (2015) 65, 77.
- [127] ZWIJSEN, K., UITSLAG-DOOLAARD, H., ROELOFS, F., WALLENIUS, J., Thermal-Hydraulic Design Support and Safety Analyses of SEALER UK Demo, International Conference on Nuclear Engineering (ICONE28), Vol. 83785, American Society of Mechanical Engineers (2020).
- [128] VISSER, D., et al., CFD analyses of the European scaled pool experiment E-SCAPE, *Nuclear Engineering and Design* **358** (2020) 110436.
- [129] BHATIA, H., BIEDER, U., GORSSE, Y., GUENADOU, D., Thermal-Hydraulic Analysis of the Flow in the MICAS Experimental Facility using CFD, Computational Fluid Dynamics for Nuclear Reactor Safety Conference (OECD/CFD4NRS-8), Paris (2022).
- [130] VISSER, D., et al., CFD Analysis of the ALFRED Hot Plenum, FR22, Beijing, China (2022).
- [131] KOLOSZAR, L., PLANQUART, P., VAN TICHELEN, K., KEIJERS, S., Numerical simulation of Loss-of-Flow transient in the MYRRHA reactor, *Nuclear Engineering and Design* **363** (2020) 110675.
- [132] ZWIJSEN, K., DOVIZIO, D., MOREAU, V., ROELOFS, F., CFD modelling of the CIRCE facility, *Nuclear Engineering and Design* **353** (2019) 110277.

- [133] ZWIJSEN, K., MARTELLI, D., BREIJDER, P., FORGIONE, N., ROELOFS, F., Multi-scale modelling of the CIRCE-HERO facility, Nuclear Engineering and Design **355** (2019) 110344.
- [134] GERSCHENFELD, A., Towards more efficient implementations of multiscale thermal-hydraulics, Nuclear Engineering and Design **381** (2021) 111322.
- [135] TOTI, A., VIERENDEELS, J., BELLONI, F., Extension and application on a pool-type test facility of a system thermalhydraulic/CFD coupling method for transient flow analyses, Nuclear Engineering and Design **331** (2018) 83, 96.
- [136] FANG, J., et al., Feasibility of full-core pin resolved CFD simulations of small modular reactor with momentum sources, Nuclear Engineering Design **378** (2021) 111143.
- [137] YOON, H.Y., PARK, I.K., LEE, J.R., CHO, Y.J., LEE, S.J., Multi-Scale and Multi-Physics Nuclear Reactor Simulation for the Next Generation LWR Safety Analysis, 18th International Topical Meeting on Nuclear Reactor Thermal Hydraulics, NURETH-18, Portland, USA (2019).
- [138] GERSCHENFELD, A., “Multiscale and Multiphysics Simulation of Sodium Fast Reactors: from Model Development to Safety Demonstration”, 18th International Topical Meeting on Nuclear Reactor Thermal Hydraulics, NURETH-18, Portland, USA (2019).
- [139] BANDINI, G., et al., Assessment of systems codes and their coupling with CFD codes in thermal-hydraulic applications to innovative reactors, Nuclear Engineering and Design **281** (2015) 22, 38.
- [140] CONTI, A., et al., Numerical Analysis of Core Thermal-Hydraulic for Sodium Cooled Fast Reactors”, 16th International Topical Meeting on Nuclear Reactor Thermal Hydraulics, NURETH-16, USA (2015), 1006-1019 pp.
- [141] GERSCHENFELD, A., et al., “Development and Validation of Multi-Scale Thermal Hydraulics Calculation Schemes for SFR Applications at CEA”, International Conference on Fast Reactors and Related Fuel Cycles, Yekaterinburg, Russia (2017).
- [142] ROELOFS, F. (Ed.), Thermal Hydraulics Aspects of Liquid Metal Cooled Nuclear Reactors, Woodhead Publishing, Cambridge, UK (2018).
- [143] DEGROOTE, J., HAELTERMAN, R., VIERENDEELS, J., Quasi-Newton Techniques for the Partitioned Solution of Coupled Problems, In 7th European Congress on Computational Methods in Applied Sciences and Engineering, Greece (2016).
- [144] NATHALIE, M., et al., VVUQ of a thermal-hydraulic multi-scale tool on unprotected loss of flow accident in SFR reactor, EPJ N-Nuclear Sciences and Technologies **7** (2021) 3.
- [145] GRISHCHENKO, D., et al., The TALL-3D facility design and commissioning tests for validation of coupled STH and CFD codes, Nuclear Engineering and Design **290** (2015) 144, 153.
- [146] GRISCHCHENKO, D., et al., TALL-3D open and blind benchmark on natural circulation instability, Nuclear Engineering and Design **358** (2020) 110386.
- [147] DI PIAZZA, et al., Heat transfer on HLM cooled wire-spaced fuel pin bundle simulator in the NACIE-UP facility, Nuclear Engineering and Design **300** (2016) 256, 267.
- [148] PUCCIARELLI, A., GALLENI, F., MOSCARDINI, M., MARTELLI, D., FORGIONE., N., STH/CFD coupled calculations of postulated transients from mixed to natural circulation conditions in the NACIE-UP facility, Nuclear Engineering and Design **370** (2020) 110913.

- [149] PACIO, J., DAUBNER, M., FELLMOSER, F., WETZEL, T., Experimental study of the influence of inter-wrapper flow on liquid-metal cooled fuel assemblies, Nuclear Engineering and Design **352** (2019) 110145.
- [150] MARTELLI, D., FORGIONE, N., DI PIAZZA, I., TARANTINO, M., HLM fuel pin bundle experiments in the CIRCE pool facility, Nuclear Engineering and Design **292** (2015) 76, 86.
- [151] LORUSSO, P., et al., Total loss of flow benchmark in CIRCLE-HERO integral test facility, Nuclear Engineering and Design **376** (2021) 111086.
- [152] VAN TICHELEN, K., MIRELLI, F., Results on Thermal Hydraulic Experiments in the LBE-Cooled Pool Facility E-scape in Support of the MYRRHA Design and Licensing, 18th International Topical Meeting on Nuclear Reactor Thermal Hydraulics, NURETH-18, USA (2019), 1-11 pp.
- [153] KAMIDE, H., HAYASHI, K., ISOZAKI, T., NISHIMURA, M., Investigation of core thermos hydraulics in fast reactors-interwrapper flow during natural circulation, Nuclear Technology **133** 1 (2001) 77, 91.
- [154] ONO, A., TANAKA, M., MIYAKE, Y., HAMASE, E., EZURE, T., Preliminary analysis of sodium experimental apparatus PLANDTL-2 for development of evaluation method for thermal-hydraulics in reactor vessel of sodium fast reactor under decay heat removal system operation condition, Mechanical Engineering Journal **7** 3 (2020) 19, 00546.
- [155] TECHINE, D., et al., International benchmark on the natural convection test in Phenix reactor, Nuclear Engineering and Design **258** (2013) 189, 198.
- [156] UITSLAG-DOOLAARD, H., et al., Multiscale modelling of the Phénix dissymmetric test benchmark, Nuclear Engineering and Design **356** (2020) 110375.
- [157] INTERNATIONAL ATOMIC ENERGY AGENCY, Bechmark Analysis of EBR-II Shutdown Heat Removal Tests, IAEA-TECDOC-1819, IAEA, Vienna (2017).
- [158] SMITH, B. L., et al. Assessment of Computational Fluid Dynamics for Nuclear Reactor Safety Problems, Rep. NEA-CSNI-R—2007-13, OECD, Paris (2008).
- [159] WILSON, G. E., BOYACK, B. E., The role of PIRT process in experiments, code development and code applications associated with reactor safety analysis, Nuclear Engineering and Design **186** 1-2 (1998) 23, 37.
- [160] YURKO, J., BUNGIORNO, J., Quantitative phenomena identification and ranking table (QPIRT) for reactor safety analysis, Transactions of the American Nuclear Society **104** (2011).
- [161] OBERKAMPF, W. L., ROY, C. J., Verification and Validation in Scientific Computing, Cambridge University Press, UK (2010).
- [162] ZUBER, N., et al., Appendix D: Hierarchical, Two-Tiered Scaling Analysis; An Integrated Structure and Scaling Methodology for Severe Accident Technical Issue Resolution, NUREG/CR-5809, USA (1991).
- [163] D'AURIA, F., GALASSI, G. M., Scaling in nuclear reactor system thermal-hydraulics, Nuclear Engineering and Design **240** 10 (2010) 3267, 3293.
- [164] GLAESER, H., HOFER, E., KLOOS, M., SKOREK, T., Uncertainty and sensitivity analysis of a post-experiment calculation in thermal hydraulics, Reliability Engineering and System Safety, **45** 1-2 (1994) 19, 33.
- [165] DE CRECY, A., BAZIN, P., Quantification of the Uncertainties of the Physical Models of CATHARE 2, IAEA, (2004).
- [166] D'AURIA, F., DEBRECIN, N., GALASSI, G. M., Outline of the uncertainty methodology based on accuracy extrapolation, Nuclear Technology **109** 1 (1995) 21, 38.

- [167] D'AURIA, F., GIANNOTTI, W., Development of a code with the capability of internal assessment of uncertainty, Nuclear Technology **131** 2 (2000) 159, 196.
- [168] PETRUZZI, A., D'AURIA, F., Approaches, relevant topics, and internal method for uncertainty evaluation in predictions of thermal-hydraulic system codes, Science and Technology of Nuclear Installations **2008** (2007).
- [169] BAZIN, P., et al., BEMUSE Phase III Report: Uncertainty and Sensitivity Analysis of the LOFT L2-5 Test. Rep. NEA-CSNI-R-2007-04, OECD, Paris (2007).
- [170] BESTION, D., et al., Review of Uncertainty methods for CFD application to Nuclear Reactor Thermal hydraulics, NUTHOS 11-The International Topical Meeting on Nuclear Reactor Thermal Hydraulics, South Korea (2016).
- [171] ROACHE, P. J., Quantification of uncertainty in computational fluid dynamics, Annual Review of Fluid Mechanics **29** 1 (1997) 123, 160.
- [172] PROŠEK, A., D'AURIA, F., MAVKO, B., Review of quantitative accuracy assessments with fast Fourier transform based method (FFTBm), Nuclear Engineering and Design **217** 1-2 (2002) 179, 206.

CONTRIBUTORS TO DRAFTING AND REVIEW

Batra, C.	International Atomic Energy Agency
Bestion, D.	Commissariat à l'énergie atomique (CEA), France
Bojan, N.	Paul Scherrer Institute, Switzerland
Frederix, E.	Nuclear Research and Consultancy Group (NRG), Netherlands
Gerschenfeld, A.	Commissariat à l'énergie atomique (CEA), France
Giustini, G.	Imperial College London, United Kingdom
Jevremovic, T.	International Atomic Energy Agency
Kelm, S.	Forschungszentrum Jülich, Germany
Khuwaileh, B.	University of Sharjah, UAE
Manera, A.	Eidgenössische Technische Hochschule (ETH) Zürich, Switzerland
Merzari, E	The Pennsylvania State University, United States of America
Petrov, V.	Paul Scherrer Institute, Switzerland
Qureshi, K.	Pakistan Institute of Engineering and Applied Sciences (PIEAS), Pakistan
Radman, S.	École Polytechnique Fédérale de Lausanne, Switzerland
Rehman, H ur.	International Atomic Energy Agency
Riaz, W.	International Atomic Energy Agency
Roelofs, F.	Nuclear Research and Consultancy Group (NRG), Netherlands
Sato, Y.	Paul Scherrer Institute, Switzerland
Hassan, Y.	Texas A&M University, United States of America

Meetings

Consultancy Meeting on Theoretical Foundations and Application of Computational Fluid Dynamics in Nuclear Energy Course, 8–10 June 2021

Joint ICTP-IAEA Course on Theoretical Foundations and Application of Computational Fluid Dynamics in Nuclear Engineering, 13–17 September 2021



ORDERING LOCALLY

IAEA priced publications may be purchased from the sources listed below or from major local booksellers.

Orders for unpriced publications should be made directly to the IAEA. The contact details are given at the end of this list.

NORTH AMERICA

Bernan / Rowman & Littlefield

15250 NBN Way, Blue Ridge Summit, PA 17214, USA

Telephone: +1 800 462 6420 • Fax: +1 800 338 4550

Email: orders@rowman.com • Web site: www.rowman.com/bernan

REST OF WORLD

Please contact your preferred local supplier, or our lead distributor:

Eurospan Group

Gray's Inn House
127 Clerkenwell Road
London EC1R 5DB
United Kingdom

Trade orders and enquiries:

Telephone: +44 (0)176 760 4972 • Fax: +44 (0)176 760 1640

Email: eurospan@turpin-distribution.com

Individual orders:

www.eurospanbookstore.com/iaea

For further information:

Telephone: +44 (0)207 240 0856 • Fax: +44 (0)207 379 0609

Email: info@europangroup.com • Web site: www.europangroup.com

Orders for both priced and unpriced publications may be addressed directly to:

Marketing and Sales Unit
International Atomic Energy Agency
Vienna International Centre, PO Box 100, 1400 Vienna, Austria
Telephone: +43 1 2600 22529 or 22530 • Fax: +43 1 26007 22529
Email: sales.publications@iaea.org • Web site: www.iaea.org/publications



INTERNATIONAL ATOMIC ENERGY AGENCY
VIENNA